ANNÉE 2017





THÈSE / UNIVERSITÉ DE RENNES 1

sous le sceau de l'Université Bretagne Loire

pour le grade de DOCTEUR DE L'UNIVERSITÉ DE RENNES 1 Mention : Chimie

Ecole doctorale (Matière, Molécules et Matériaux - 3M)

présentée par

Jiangkun OUYANG

Préparée dans l'unité de recherche UMR 6226-CNRS-Institut des Sciences Chimiques de Rennes UFR « Sciences et Propriétés de la Matière » (SPM)

Helicenes for Chiral

Molecular Switches,

Magnetic Materials,

and Chiral Fullerene

Derivatives

Thèse soutenue à Rennes le 13 décembre 2017 devant le jury composé de : **Dr Federico CISNETTI** Maître de Conférences, Université Clermont Auvergne/ Rapporteur Dr Eric MANOURY Directeur de recherche CNRS, LCC Toulouse/ Rapporteur **Dr Narcis AVARVARI** Directeur de recherche CNRS, Moltech Anjou/ Examinateur Dr Joëlle RAULT-BERTHELOT Directeur de recherche CNRS, ISCR/Examinateur **Dr Patrick ROSA** Chargé de recherche CNRS, LCC Bordeaux/ Examinateur **Dr Jeanne CRASSOUS** Directeur de recherche CNRS, ISCR/ Directeur de thèse **Dr Ludovic FAVEREAU** Chargé de recherche CNRS, ISCR/Membre invité

For My Dear Mother "Jinlian ZHANG" For My Dear Father "Chengsheng YANG" For My Dear Grandmother "Chunxiu ZHANG" For My Dear Sister "Senli YANG" For My Brother-in-Law "Rong DENG" For My Niece "Yarui DENG" and Nephew "Haochen DENG"

> "Whatever is worth doing is worth doing well!" Lewis CARROLL

Pour ma vie compagnon dans le futur

"<u>Si tu aimes une fleur qui se trouve dans une étoile, c'est doux, la nuit, de</u> regarder le ciel. Toutes les étoiles sont fleuries."

Antoine de SAINT-EXUPERY

«Le Petit Prince»

Acknowledgements

How time flies! I can still remember the first day I arrived at the lab three years ago. Now I will finish my PhD study. Firstly, I would like to send my sincerest gratitude to my supervisor Dr. Jeanne CRASSOUS for her kindness, patience, enthusiasm, and abundant knowledge. I will never forget that she accepted me and provided me the opportunity to study my PhD in her group three years ago. During these three years, she taught me not only the chemistry and experiment, but also how to do research and a good presentation and write a thesis. Especially, she spent a lot of time in correcting my thesis.

I would especially like to thank my thesis committee whom I appreciate for accepting to referee my thesis: Dr. Federico CISNETTI, Dr. Eric MANOURY, Dr. Narcis AVARVARI, Dr. Joëlle RAULT-BERTHELOT, Dr. Patrick ROSA, Dr. Ludovic FAVEREAU.

I would thank all the collaborators, Dr. Fabrice POINTILLART, Dr. Boris Le GUENNIC, Prof. Olivier CADOR, Prof. Nazario MARTIN, Prof. Salvatore FILIPPONE, Prof. Rudolf PIETSCHNIG, Dr. Christophe LESCOP, Dr. Nicolas VANTHUYNE (Chiral HPLC separation), Dr. Thierry ROISNEL and Dr. Vincent DORCET (X-Ray crystallography), Rosa M. GIRON, and Sebastian HARTUNG.

I would also thank Dr. Ludovic FAVEREAU for teaching me chemistry knowledge and experiment technique. Equally, thank to Prof. Muriel HISSLER and Dr. Pierre-Antione BOUIT for their kind help in the lab.

My sincere thanks also go to Thibault REYNALDO for his help in ordering chemical compounds and solving technique problems, and to Cecile PERON who was always available to help me to deal with things about traveling and conference. Many thanks to Dr. Chengshuo SHEN for his huge help at the beginning of my PhD study. Thanks to Dr. Helena ISLA MATA for teaching me experiment skills.

I greatly appreciate to Dr. Nora HELLOU for sharing the same lab and helping me. Thanks to Dr. Nidal SALEH for that I continued part of his work. I would also thank all my dear labmates in PMM group: Dr. Matthew DUFFY, Anabella MOCANU, Kais DHBAIBI, Jonas HOFFMANN, Thomas DELOUCHE, Etienne GAUTHIER, Nesrine HAFEDH, Sondes RAOUAFI, Dr. Thomas DOMBRAY, Dr. Faouzi CHAHDOURA, Dr. Antoine MAUFROY, Dr. Thomas MALNOE, Dr. Sloane EVARISTE, Dr. Nicolas de RYCKE, Dr. Tereza VITVAROVA, Dr. Rozsa SZUCS,

Réka MOKRAI. It is really happy to meet you in the lab during my PhD study. I wish you all the best in the future.

I am grateful to Prof. Pierre-Henri DIXNEUF for inviting me to drink wine and driving me back. I wish to thank Prof. Christophe DARCEL, Prof. Henri DOUCET, and Dr. Jean-Baptiste SORTAIS for their interesting catalysis lessons. Many thanks to my neighbour lab for providing me convenience for UV-vis measurement.

I would like to thank my friends Changsheng WANG, Shengdong WANG, Feng YU, Duo WEI, Yuchao YUAN, Xinzhe SHI, Haoran LI, Haiyun HUANG, Zhuang ZHANG, Yixuan CAO, Weiheng HUANG, Shuxin MAO, Yaoyin LOU, Guangxing LIANG, Yanghai XU, Kedong YUAN, Xiaoyan HE, Le YU, Min FENG, Wenyan HE, Xiaolu MA, Ding WANG, Jingran HOU, Rui SANG, Yuya HU, Shi JIANG, Mian HE, Xiang LIU.

Finally, I would like to express my greatest appreciation to my family. My parents always supported and encouraged me during my PhD. They are my strong backing. Many thanks to my grandmother who raised me up also gave me encouragement. I hope she will always be healthy. I genuinely thank and appreciate my older sister and brother-in-law for helping me to take care of my parents and grandmother when I studied abroad. Thanks to my lovely niece and nephew for bringing me so much happiness.

Jiangkun OUYANG

31.10.2017

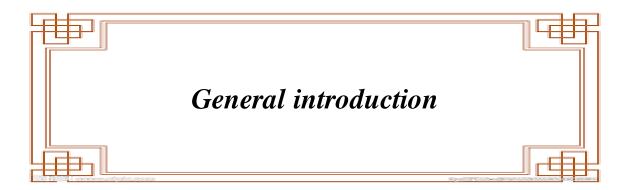
Abbreviations

Å: Angstrom	OLEDs: Organic light emitting diodes	
BINOL: 2,2'-dihydroxy-1,1'-binaphthyl	OR: Optical Rotation	
BuLi: Butyl Lithium	Rac: racemic	
CD: Circular Dichroism	RISC: Reverse intersystem crossing	
CIP: Cahn-Ingold-Prelog	ROESY: Rotating frame overhause effect	
CPL: Circular Polarized Luminescence	spectroscopy	
CP-PLED: circular polarized phosphorescence light emitting diode	R.T: Room Temperature RRM: reaction on racemic mixture	
DCC: dicyclohexyl carodiimide	SAM: self- assembled monolayer	
DMPC: 1,2-dimyristoyl- <i>sn</i> -glycero-3-	SIMs: single-ion magnets	
phosphorylcholine	SMMs: Single molecule magnets	
DTE: dithienylethene	SOC: Spin-orbital coupling	
ECD: Electronic circular dichroism	SQUID: Superconducting Quantum Interference	
<i>ee</i> : enantiomeric excess	Device	
hfac: 1,1,1,5,5,5-hexafluoroacetonate anion	TADF: Thermally activated delayed fluorescence	
HPLC: Hihg-Performance Liquid Chromatography	$T_{\rm c}$: curie temperature	
HOMO: Highest occupied molecular orbital	$T_{\rm N}$: Neel temperature	
	$T_{\rm B}$: blocked temperature	
HRMS: High resolution mass spectrometry	THF: Tetrahydrofuran	
ISC: Intersystem crossing	TMSA: trimethylsilylacetylene	
ILT: intra-ligand transition	UV-vis: Ultraviolat-visible	
LSVs: linear sweep voltammograms	UPy: 2-ureido-4[1H]-pyrimidinone	
LLCT: Ligand-to-ligand charge transfer	$U_{\rm eff}$: effective energy barrier	
LEECs: Light emitting electrochemical cells	Φ: Quantum yield	
LMCT: ligand-to-metal charge transfer transitions	ω: angular frequency	
LUMO: Lowest unoccupied molecular orbital	$[\alpha]_D^{23}$: Specific optical rotation	
MCT: metal centered transitions	$[\emptyset]_D^{23}$: Molar optical rotation	
MLCT: Metal-to-ligand charge transfer	ε: Molar absorption coefficient	
NMR: Nuclear Magnetic Resonance	χ _m : magnetic susceptibility	

Table of Contents

Chapter I General introduction: helicenes and applications	11
A General introduction	11
A.1 Chirality	11
A.2 Helicenes	14
B Conclusion	
C References	
Chapter II Photoresponsive chiral switches based on helicenes and gold complexes	
A General introduction: design of the project	35
A.1 Photoresponsive chiral switches based on helicenes	35
A.2 Photoresponsive gold complexes	
B Stiff stilbenes substituted with helicenes	
B.1 Bibliographic part	
B.2 Stiff stilbenes	
B.3 Photoisomerization mechanism of stiff stilbene	
B.4 Applications of stiff stilbene	40
B.5 Introduction of helicenes in light-driven chiroptical switches	
B.6 Results and discussion	50
B.7 Coordination tests	63
B.8 Conclusion	64
C Stiff stilbenes substituted with alkynyl-gold units	65
C.1 Generalities on gold(I) complexes	65
C.2 The gold-gold interaction and its applications in materials science	66
C.3 Results and discussion	69
C.4 Conclusion	
D Experiment part	
D.1 Synthetic procedures	
D.2 ¹ H NMR spectra of new compounds	
D.3 UV-Vis spectra of new compounds	
D.4 Crystal structures	101
D.5 Analytical chiral HPLC separation for compound 5c	104
E References	107

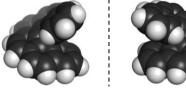
Chapter III First helicene-based Dy ^{III} single molecule magnets	111
A Introduction:	111
A.1 Definitions	111
B Design of chiral SMMs based on helicenes	128
C Results and discussion	130
C.1 Synthesis of ligands	130
C.2 Synthesis of Dy ^{III} SMMs	131
C.3 X-Ray diffraction analysis	131
C.4 Chiroptical spectroscopy	133
C.5 Magnetic properties	
D Experiment part	139
D.1 General Procedures and Materials.	139
D.2 Synthesis of complexes	139
D.3 Crystallography.	
D.4 Physical Measurements.	
D.5 Computational Details.	
E Conclusion	155
F References	156
Chapter IV Chiral fullerenes derivatives based on helicenes	159
A Introduction	159
A.1 General features of fullerenes	
A.2 Divergent reactions on racemic mixtures (Divergent RRM)	
B Design of the project	173
C. Result and discussion	175
D Conclusion	
E Experiment part	
E.1 General information	
E.2 Synthetic Procedures and Characterizations of helicene aldehydes	
E.3 Analytical chiral HPLC separation for compound 25	
E.4 Synthesis of chiral fullerene derivatives.	
F References	198
Résumé	201



RENNES 2017

General introduction

Chirality is widely found in nature and plays an important role in living systems. Helix is one kind of chirality found for example in DNA. Helicenes are unique synthetic molecules with helical topology; they are made-up of *ortho*-fused aromatic or heteroaromatic rings and display extended π -conjugation.



M-carbo[6]helicene P-carbo[

P-carbo[6]helicene

Figure 1 Molecular structures of *M*- and *P*-carbo[6]helicene.

The steric hindrance of terminal rings leads to chirality of helicenes, which endows helicenes with strong circular dichroism as well as high optical rotation values. Besides, helicenes possess good luminescence property, high chemical and thermal stability, and a unique chiral environment. Based on these features, helicenes derivatives are well applied and studied as chiroptical switches, spin filters, molecular recognition systems, circularly polarized luminescent (CPL) materials for organic light-emitting diodes (OLEDs) and asymmetric catalysts.

During my PhD study, I focused on new applications of helicenes, and developed novel photoresponsive chiral switches, magnetic materials, and chiral fullerenes derivatives based on helicenes.

In the first topic, I developed two parts of work based on so-called 'stiff stilbene' units that are known to reversibly interconvert between two *trans* and *cis* forms through light. The first part of the work corresponds to photoresponsive chiral switches based on helicenes, the other one to photoresponsive gold(I) complexes. The switchable processes were monitored by multi-NMR, UV-vis, CD, and optical rotation.



Figure 2 Helicene-based photoresponsive chiral switches (left) and photoresponsive gold complex (right).

The second topic dealt with the synthesis and characterization of helicene-bipyridine based Dy^{III} complexes as novel kinds of chiral single molecule magnets (SMMs). The study of their magnetic properties revealed that racemic and enantiopure single molecule magnets showed different magnetic properties. The racemic SMM displayed antiferromagnetic properties, while the enantiopure SMMs showed ferromagnetic properties.

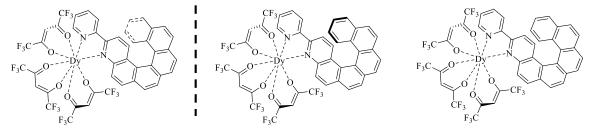


Figure 3 Enantiopure (left and middle) and racemic (right) Dy^{III} single molecule magnet based on a helicene-bipyridine ligand.

The third topic dealt with the preparation and characterization of a series of chiral fullerene derivatives based on helicenes, namely diastereomeric helicene-pyrrolidino[3,4:1,2][60]fullerenes. We developed the first use of the reversible sterodivergent cycloaddition of racemic helicenes onto [60]fullerene with its subsequent retro-cycloaddition as an efficient alternative strategy for the enantiomeric resolution of a helicene-carboxaldehyde.

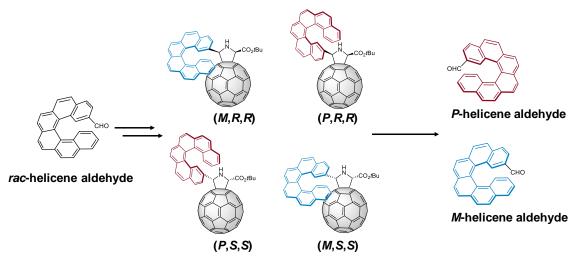
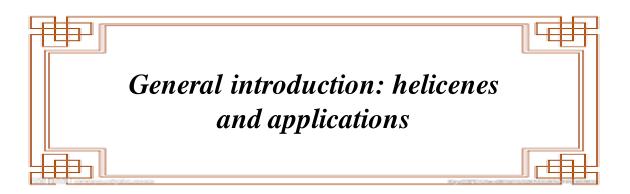


Figure 4 Helicene-based chiral fullerene derivatives.

Chapter I



RENNES 2017

A General introduction

In this chapter, I will mainly introduce the background of chirality¹⁻⁶ and helicenes chemistry including helicene history, optical properties, racemization, and applications. Recently, several reviews and a book about helicene chemistry have appeared. Herein, I will focus on the introduction of helicenes applications, especially those developed in our group. Some more information about helicenes can be seen in the references.⁷⁻¹²

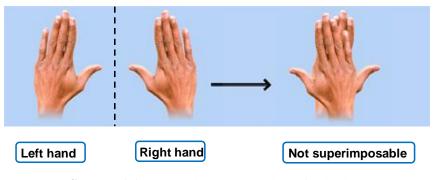
A.1 Chirality

The words of "chiral" and "chirality" derived from the Greek word, "cheir", which means "hand". The definition of the terms "chiral" and "chirality" were firstly introduced by William Thompson, Lord Kelvin, in 1884:¹

"I call any geometric figure, or group of points, chiral, and say that it has chirality, if its image in a plane mirror, ideally realized, cannot be brought to coincide with itself".¹³⁻

We have therefore a simple standard to distinguish which one is chiral or not. If it cannot be superposed on its mirror image, it possesses chirality (**Scheme 1.1**).

To nature life, chirality is pretty important. Most of biochemistry is chiral. DNA, proteins, amino acids, sugars, and many natural products such as steroids, hormones, and pheromones possess chirality.¹⁵ Nature has chosen a particular handedness (with L proteinogenic amino-acids and D sugars). Since our human body is homochiral, usually only one enantiomer of medicine is effective to us, while the antipode may lead to side-effects.



Scheme 1.1 Schematic representation of chirality. https://socratic.org/organic-chemistry-1/r-and-s-configurations/introduction-to-chirality-and-chiral-centers

A.1.1 Categories of chirality

In general, chirality can be divided into two categories.² The one is *Euclidean* or geometrical chirality. The other one is topological chirality or mechanically planar *chirality*. The former is the properties of rigid molecular objects that cannot be superposed on their mirror images by transition or rotation.² In chemistry, the molecules belonging to C_n , D_n , I, O, or T group are chiral (Figure 1.1).¹⁶ A review about classification of chiral molecules according to symmetry has been reported in 1974.³ However, topological *chirality* is a special case of chirality. It is realized when any presentation of its graph is topologically distinct from its mirror image, that is, cannot be converted into its mirror image by continuous deformation in three-dimensional (3D)-space (Figure 1.2).¹⁷ No molecular rigidity at all is required for topological enantiomers to remain distinct. This is the point which distinguishes Euclidean from topological chirality. For example, in [6] helicenes (Figure 1.3 a), deformations of benzene rings which are forbidden at room temperature are energetically allowed at high temperatures, thus racemization becomes possible; on the contrary, in the case of a trefoil knotted macrocycle (Figure 1.3 b), no continuous deformation, however easy it is, will never allow interconversion of its enantiomers.²

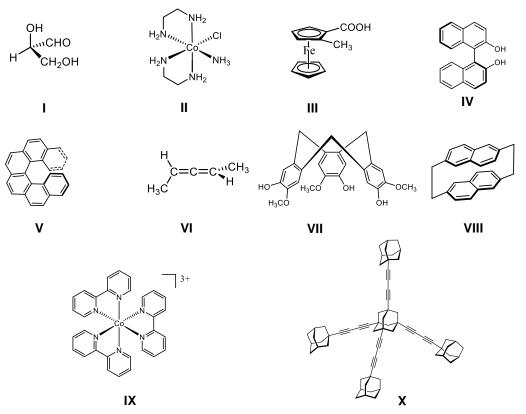


Figure 1.1 Several examples of molecules with Euclidean chirality, displayed in the order of increasing symmetry: *C*₁ (**I-III**), *C*₂ (**IV-VI**), *C*₃ (**VII**), *D*₂ (**VIII**), *D*₃ (**IX**), *T* (**X**).

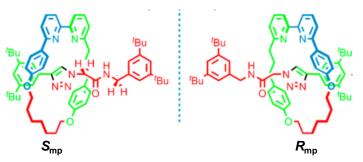


Figure 1.2 An example of topological chirality or mechanically planar chirality (Reproduced

from ref.¹⁷).

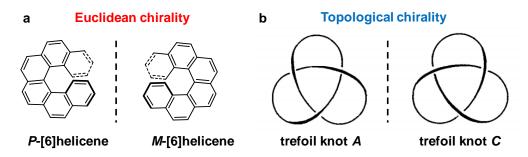


Figure 1.3 Difference between Euclidean chirality and topological chirality (Reproduced for ref.²).

A.2 Helicenes

The first helicenes were reported by Meisenheimer and Witte in 1903.¹⁸ But after that, in the next few decades, there has been little development about helicene. Then Newman and his coworkers developed the synthesis and separation methods in 1950s, and helicenes chemistry started to take off.¹⁹⁻²¹ Newman and Lednicer also introduced a simple nomenclature for helicenes in 1956.²⁰ For example, before helicene, a number, n, or Greek prefix in brackets was added. Accordingly, hexahelicene = [6]helicene. After that, helicene chemistry developed fast. In 1967, Martin's group reported the synthesis of carbo[7]helicene by photocyclization.²² With the same method, carbo[8] and [9]helicenes were prepared in 1968,²³ carbo[13]helicene in 1969,²⁴ as well as carbo[11], [12], [14]helicenes in 1975.²⁵ With increasing of number of rings, the synthesis of helicenes becomes difficult. In 2015, carbo[16]helicene, the longest to date, was reported by Fujita's group.²⁶ Some information about heterohelicenes (helicenes incorporating heteroatoms) can be found in references.^{7-8, 10-12, 27}

Helicene are helical compounds of *n* ortho-fused aromatic or heteroaromatic rings with π -conjugated. When $n \le 4$, the steric hinderance is not big enough to keep the helicene within one configuration, and two enantiomers can convert to each other fast. Thus, [4]helicenes are usually considered as non-chiral molecules. While n > 4, due to the steric hindrance of terminal rings, the helicenes wind into opposite directions and have a C_2 -symmetric axis (when unsubstituted) as well as the helicenes are not planar anymore. This feature endows helicenes with chirality even without asymmetric carbon centers or others chiral centers. Normally, [*n*]helicene has two enantiomers, which are noted as *P* (right handedness) and *M* (left handedness), respectively. This steric hindrance is also important for studying the racemization of helicene. When the ring numbers $n \ge 6$, the helicene are configurationally stable at room temperature. Some data about racemization of helicenes are presented in the following table (**Table 1.1**).

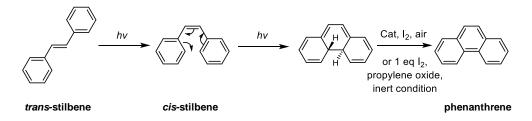
	$arDelta G^{ eq}$	${\it \Delta} H^{\not=}$	Temperature for
	(kcal/mol)	(kcal/mol)	measurement (K)
Thia[6]helicene ²⁸	23.7	Not mentioned	297
Carbo[5]helicene ²⁹	24.1	22.9	293
Carbo[6]helicene ³⁰	37.0	33.8	478
Carbo[7]helicene ³¹	~40	~40	290
Carbo[9]helicene ³¹	~40	~40	290
Carbo[11]helicene ³²	37.5	Not mentioned	503

Table 1.1 Gibbs free energy ΔG^{\neq} , enthalpy of activation ΔH^{\neq} , and temperature for racemization of different helicenes.

A.2.1 Synthesis of helicenes

Photocyclization is a main method for the synthesis of helicenes. At the beginning of helicene chemistry, the synthesis of helicene was very difficult and time consuming, which limited its development. Photocyclization was first used in 1964 for the construction of helicene by Mallory and his coworkers.³³

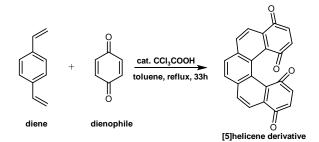
The photocyclization process contains three steps (**Scheme 1.2**): the first step is an isomerization of *trans*-isomer of a stilbenic system under irradiation; the second step is a conrotatory electrocyclization of *cis*-stilbene derivatives, as well as forming a 1,3-cyclohexadiene ring; the last step is oxidation, forming phenanthrenic final product. In the last step, two protons are removed by oxidation with I₂, which is reduced into HI. Then, the HI is oxidized by oxygen and returns back to I₂. In some cases, stoechiometric amount of I₂ are employed to photocyclization in present of propylene oxide under inert condition. The propylene oxide acts as a consumer of HI.^{8, 10-12, 34-36}



Scheme 1.2 Photocyclization process for preparing phenanthrene derivatives.

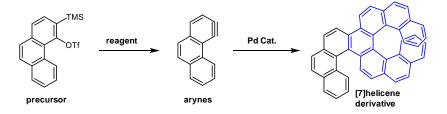
There are many other strategies to synthesize helicenes. For example, in 1990, Katz' group employed a Diels-Alder reaction to construct a [5]helicene, in which the terminal

rings are paraquinone units (**Scheme 1.3**).³⁷⁻³⁸ Then, they applied this method to prepare [7]helicene derivatives.³⁹



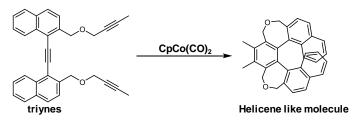
Scheme 1.3 Synthesis of [5] helicene derivative by Diels-Alder reaction.

In 1999, Pérez and Guitián *et al.* developed a palladium-catalyzed intermolecular [2+2+2] cyclotrimerization of arynes for the synthesis of helicenes (**Scheme 1.4**).⁴⁰ Later on, they employed the same way to construct [4]helicene, [5]helicene, even [7]helicene derivatives.⁴¹⁻⁴⁴



Scheme 1.4 Synthesis of helicene by palladium-catalyzed intermolecular [2+2+2] cyclotrimerization.

Starý and Stará' group reported CpCo(CO)₂-catalyzed intermolecular [2+2+2] reaction for synthesis of helicene-like molecules from triynes starting material (**Scheme 1.5**).⁴⁵ Later on, they developed Ni(0) or Co(I) catalysis systems to prepare carbo[5], [6], and [7]helicene derivatives.⁴⁶⁻⁴⁹



Scheme 1.5 Synthesis of helicene-like molecule by cobalt-catalyzed intermolecular [2+2+2] cyclotrimerization.

Some more examples about synthesis of helicene derivatives can be seen in the recent published reviews and book.^{7-8, 10-12}

A.2.2 Chiroptical properties of helicenes

Two important factors to evaluate chiral compounds are optical rotation and circular dichroism. Optical rotation is the rotation of the plane of a linearly polarized light as it passes through chiral materials, because of different speeds of left and right circularly polarized light in chiral materials. Optical rotation is denoted by α . In most cases, optical rotation of solution is proportional to the concentration of solution and cell length. Moreover, α is related to the wavelength, the solution and the temperature. Thus, specific rotation, [α], at certain wavelength λ , at the temperature *T*, is defined as:^{1,4}

$$[\alpha]_{\lambda}^{T} = \frac{\alpha}{l \cdot c}$$

, where α is optical rotation, *l* is the path length and *c* is the concentration of solution. Usually, the temperature, *T*, is 20 °C, and the wavelength, λ , is sodium D line at 589 nm.

Circular dichroism corresponds to the different absorption of left- and right-handed circularly light. The CD spectra reflects the wavelength dependence of $\Delta \varepsilon$, which is defined as,

$$\Delta \varepsilon = \varepsilon_L - \varepsilon_R$$

, where ε_L and ε_R are molar absorption coefficients of left- and right- hand circular polarized light. The unit of $\Delta \varepsilon$ is mol⁻¹ dm³ cm⁻¹. $\Delta \varepsilon$ obeys the Beer-Lambert law.

$$\Delta \varepsilon = \frac{\Delta A}{c \cdot l}$$

, where the ΔA is the difference between absorption of left- and right-hand polarized light. When the concentration is unknow, ellipticity, θ (in millideg), is apply to present the CD data.

$$\theta$$
 (millideg) = 32982 · ΔA

Thus, the ΔA can be presented by the equation as follow,

$$\Delta \varepsilon = \frac{\theta}{32982 \cdot c \cdot l}$$

For helicenes, the optical rotations (**Table 1.2**) and CD signals (**Figure 1.4**) are very strong. With the number of aromatic rings increasing, the optical rotation will increase.

Helicenes usually have two typical strong bands at around 200 L.mol⁻¹.cm⁻¹. For *P*-helicene isomers, there are a negative ${}^{1}B_{a}$ band in the shorter wavelength and a positive ${}^{1}B_{b}$ band in the longer wavelength. For *M*-Helicene isomers, mirror-images are obtained. These signatures can be regarded as a symbol to recognize the absolute configuration of helicene derivative.

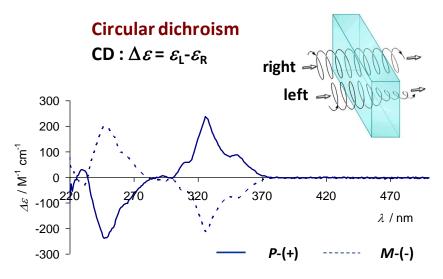


Figure 1.4 CD spectra of *P*-carbo[6]helicene and *M*-carbo[6]helicene.

Table 1.2 Optical rotations of some helicenes.⁵⁰⁻⁵¹

Compounds	$[\alpha]_D^{25}$ (°cm ³ dm ⁻¹ g ⁻¹)	$[\phi]_D^{25} (^\circ \mathrm{cm}^2 \mathrm{dmol}^{-1})$
P-carbo[6]helicene	+3640 (CHCl ₃)	+11900
P-carbo[7]helicene	+5900 (CHCl ₃ , <i>c</i> 6×10 ⁻²)	+22300
P-carbo[8]helicene	+7170 (CHCl ₃ , <i>c</i> 4.3×10 ⁻²)	+30600
P-carbo[9]helicene	+8100 (CHCl ₃ , <i>c</i> 6.07×10 ⁻²)	+38700

 $[\phi]_D^{25}$ is specific rotation; $[\phi]_D^{25}$ is molar rotation.

A.2.3 Applications of helicenes

A.2.3.1 Chiroptical switches

Molecular switches can be interconverted by external stimulus, such as chemical reaction, light, pH, temperature, redox, coordination, and host-guest interaction, from one state to another state, and the conversion process is reversible. This transfer process usually leads to the change of output signal, for example, UV-vis absorption, emission properties, color, circular dichroism, optical rotation, electric properties, etc. When the output signals are chiroptical signals, this kind of switches are normally called chiroptical switches. From the source of stimulus, chiroptical switches can be divided into several categories, such as photoresponsive chiroptical switches (see Chapter 2), pH-responsive chiroptical switches, redox-responsive chiroptical switches, and so on.

Due to helicene's strong signal of circular dichroism response and optical rotation, helicene derivatives are suitably employed for chiroptical switches.⁵² Our group also performed some work about chiroptical switches. In 2012, our group developed an efficient organometallic helicene-based redox responsive chiroptical switches (**Figure 1.5**).⁵³ The electro-active Ru center allows reversibility of helicene's chiroptical properties to be performed without modifying the ortho-fused π -system. Our group also did some other redox chiroptical switches based on helicene-tetrathiafulvalene (TTF) derivatives, helicene quinones, in collaboration with the groups of N. Avarvari and F. Diederich respectively (**Figure 1.6a,b**).⁵⁴⁻⁵⁷

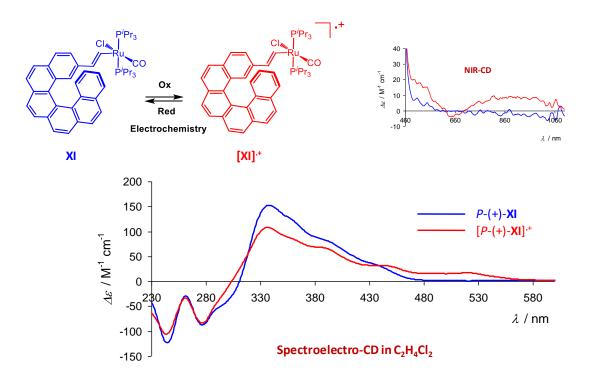


Figure 1.5 Helicene-based redox responsive chiroptical switches.

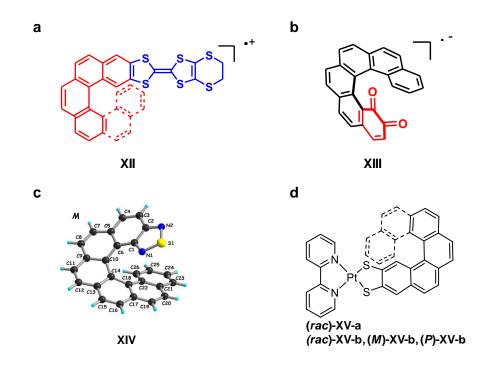


Figure 1.6 Some examples of redox-chiroptical switches with helicenes (**a**,**b**) and emissive/CPLactive helicene derivatives (**c**,**d**).

In 2016, our group reported Iron alkynyl helicenes (**Figure 1.7**). Through redox stimulus, the authors can tune chiroptical signal in IR and Near-IR spectral region. This kind of switches can be used for telecommunications applications because the M helicenes can change their optical rotation at 1.5 microns from a negative value to a positive one, without modifying the chemical structure but just by removing one electron.⁵⁸

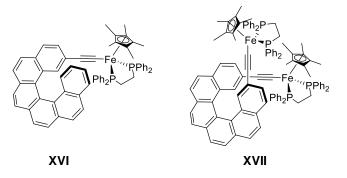
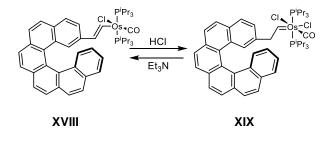


Figure 1.7 Mono-Fe^{II}-helicene complex (left) and bis-Fe^{II}-helicene complex.

In 2014, our group prepared helicene derivatives behaving as pH-triggered chiroptical switches. The helicene-grafted vinyl-osmium complex can be changed to the carbene-osmium form by adding HCl. It can recover back through adding Et₃N (**Scheme 1.6**).⁵⁹



Scheme 1.6 Helicene-based pH-responsive chiroptical switches.

In 2015, our group developed another two helicene-based pH-responsive chiroptical switches based on cycloplatinated helicene-bipyridine systems.⁶⁰ By adding 18-crown-6•HBF₄•H₂O and Na₂CO₃, we can realize the transformation between pyridine and pyridinium form (see chapter 2) along with the change of circular dichroism, circularly polarized luminescence (*vide infra*), and optical rotation.

In 2016, our group reported a coordination-driven chiroptical switches based on bishelicenic terpyridine (**Figure 1.8**). The conformation of ligand is strongly modified upon binding to Zn(II) ion. The process leaded to large changes in chiroptical properties.⁶¹

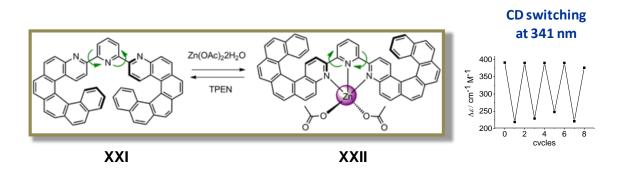


Figure 1.8 Helicene based coordination-driven chiroptical switches (Reproduced from ref.⁶¹).

In 2017, our group developed a dual responsive chiroptical switch (**Figure 1.9**), which were not only responsive to light, but also replied to redox.⁶² This switch acts as a NOR logic gate. More information about helicene-based photoresponsive chiroptical switches can be found in Chapter 2.

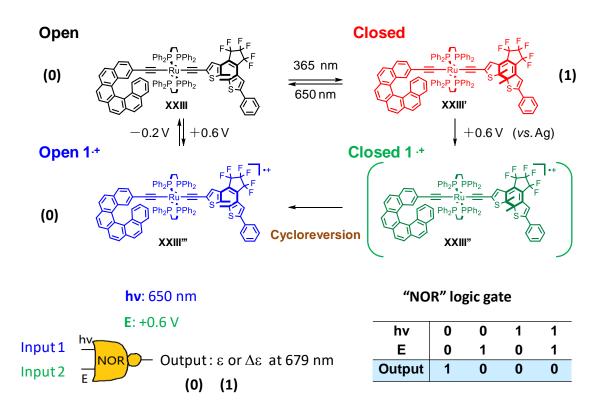


Figure 1.9 Dual redox and photoresponsive chiroptical switch.

A.2.3.2 Spin filter

In 2016, Naaman's group reported organic spin filters based on helicenes. They investigated the chirality-induced spin selectivity of monolayer of helicene films through

measurement of a current in an AFM experiment with a magnetic tip and found that the spin selectivity of P and M enantiopure helicenes was opposite (**Figure 1.10**).⁶³ This type of research topic is currently developing fast.

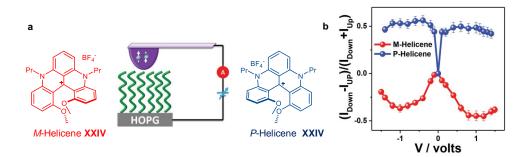


Figure 1.10 a) Schematic represent of magnetic conductive probe atomic force microscopy (mCP-AFM) measured by using Fe (magnetic) tip and molecular structures of *M*-Helicene **XXIV** (left) and *P*-Helicene **XXIV** (right); b) Spin polarization as a function of applied bias for *P*- Helicene **XXIV** I and *M*-Helicene **XXIV** films adsorbed on highly oriented pyrolytic graphite (HOPG) substrate. (Reproduced from ref.⁶³)

A.2.2.3 Circular polarized luminescence (CPL)

The first circular polarized luminescence (CPL) phenomenon was observed from a chiral crystal of sodium uranyl acetate, Na[UO₂(CH₃COO)₃], in 1948. After that, circular polarized luminescence has become a powerful tool of chiral molecular structures. In CPL spectra, we usually measure the difference in luminescence intensity (ΔI) of left-circular polarized light (I_L) versus right-circular polarized light (I_R). This difference is defined as follows:

$$\Delta I = I_L - I_R$$

Due to the difficulties of determination of absolute emission intensities, one usually reports the CPL in terms of the ratio of the difference in intensity. ⁶⁴

$$g_{lum} = \frac{\Delta I}{\frac{1}{2}I} = \frac{I_L - I_R}{\frac{1}{2}(I_L + I_R)}$$

The factor of one-half is included to make the definition of g_{lum} consistent with the definition of the related quantity in circular dichroism (CD).⁶⁵

$$g_{abs} = \frac{\Delta \varepsilon}{\varepsilon} = \frac{\varepsilon_L - \varepsilon_R}{\frac{1}{2}(\varepsilon_L + \varepsilon_R)}$$

where ε is the average molar absorption coefficient, ε_L and ε_R are the molar absorption coefficients for left and right polarised light.

Theoretically, g_{lum} is approximated by $4|m| \cos \theta / |\mu|$, where *m* and μ are the magnetic dipole transition moment and electric dipole transition moment, respectively, and θ is the angle between *m* and μ . Usually high anisotropic factor values are obtained for magnetic dipole-allowed and electric dipole-forbidden transitions.⁶⁶

CPL is different from CD. CD is related to the structural properties of the ground state of a system, while CPL reflects the structural information of the excited state of a system. The sign and magnitude of CPL are influenced by intensity of helical twist in organic compounds, the nature of ligand field in complexes and other factors. For example, chiral lanthanide complexes are known to display very large glum values (more than 1) due to their formally $f \rightarrow f$ Laporte forbidden transitions.⁶⁶

Organometallic helicene derivatives attracted increasing interest of chemists in the last decades. In the heavy metal fused helical π -conjugated systems, the photophysical properties can be significantly modified for the spin-orbit coupling, which could lead to the innovative applications such as circular polarized luminescence, responsive chiral polymers, or chiroptical switches. As following examples, we will focus on the circular polarized luminescence of helicenes complexes.

In 2014, our group reported the enantiopure mono- and bis-cycloplatinated helicenes (**Figure 1.11**).⁶⁷ Due to efficient spin-orbit coupling from heavy metal platinum, the cycloplatinated helicenes exhibited strong phosphorescence at room temperature. In addition, compounds **XXVIIa,b,c** displayed circular polarized luminescence (CPL) properties with g_{lum} value as high as 10⁻², which is one order of magnitude more than those of organic helicenes. The thiadiazole-helicene and helicene–dithiolene platinum bipyridine complex depicted in **Figure 1.6c,d** also display luminescence and/or CPL activity ($g_{lum} \sim 10^{-4}$).⁵⁶⁻⁵⁷

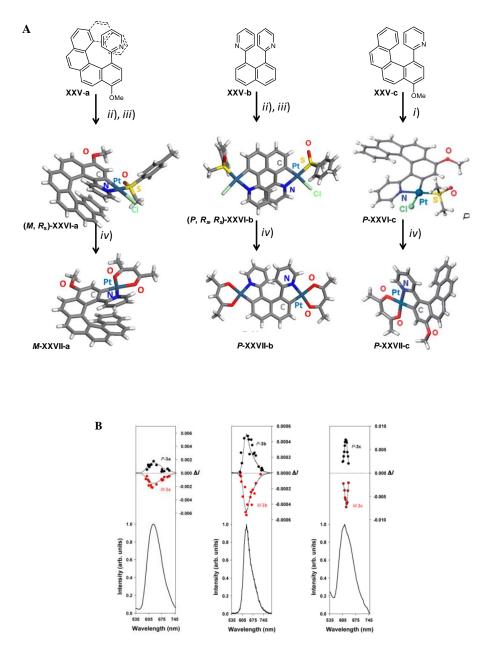


Figure 1.11 A) Synthesis of enantiopure platinahelicenes. i) $PtCl_2(DMSO)_2$, toluene, Na_2CO_3 , Ar, reflux, overnight, resolution by chiral HPLC; ii) (R_s , R_s)- $PtCl_2(p-tolyl-MeSO)_2$, toluene, Na_2CO_3 , Ar, reflux, overnight; iii) column chromatography and/or crystallization; iv) pentane-2,4-dione, toluene, Na_2CO_3 , Ar, reflux, 2 h, X-ray crystallographic of *M*-**XXVII-a**, *P*-**XXVII-b**, *P*-**XXVII-c**. B) CPL of platinahelicenes.

Recently, our group reported helicene-NHC-Iridium complexes (NHC:N-heterocyclic carbene) which display long-lived circular polarized phosphorescence (**Figure 1.12**).⁶⁸ These complexes showed light-green emission with circular polarization and long lifetimes which was related to both the conformation of helicenes ligands (*P/M*) and iridium stereochemical structure (Δ/Λ). Through quantum calculations, it was found that the

properties were attributed to extended π -conjugation of helicene-NHC ligand and efficient communication between these ligands and the Iridium metal center.

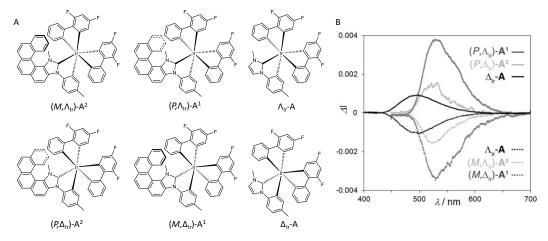


Figure 1.12 A) structures of Iridium complexes Λ_{Ir} -A, Δ_{Ir} -A, (M,Λ_{Ir}) -A², (P,Λ_{Ir}) -A¹, (M,Δ_{Ir}) -A¹, and (P,Δ_{Ir}) -A²; B) CPL spectra of Λ_{Ir} -A, Δ_{Ir} -A, (M,Λ_{Ir}) -A², (P,Λ_{Ir}) -A¹, (M,Δ_{Ir}) -A².

A.2.2.4 Molecular recognition

Helicenes possess good luminescence property, and can be employed as luminescent sensors for molecular recognition. For example, as early as in 1983, Nakazaki's group reported helicene-based crown ethers, which were applied to chiral recognition toward racemic guest molecules (**Figure 1.13**).⁶⁹⁻⁷⁰ Later on, lots of work about helicene in molecular recognition were reported.

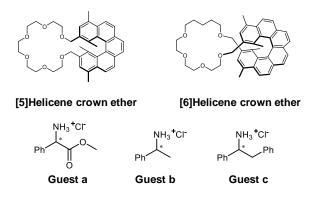


Figure 1.13 Helicene crown ethers (up) and guest molecules (down).

A.2.2.5 Chiral organic Light-Emitting Diodes (OLEDs), transistors and OPVs

Because of helicenes' good chemical and thermal stability, potentially high quantum yield of fluorescence and phosphorescence, helicenes are good candidates for organic electronics.⁷¹⁻⁷⁴ For example, in 2013, Fuchter, Campbell, and their co-workers group

applied *P*- and *M*-1-aza[6]helicene as chiral dopant of an emissive π -conjugated polymer to prepare an circular polarized light emitting diode (CP-PLED), which displayed high levels of circular polarized electroluminescence (CP-LE) (**Figure 1.14**).⁷⁵ In 2016, they also applied platinahelicene complex⁶⁷ to construct a circular polarized phosphorescent OLEDs (CP-PHOLED), which achieved both a display-level brightness and a high *g*_{EL} factor (**Figure 1.15**).⁷⁶ Besides, Liu's and Hatakeyama's group developed racemic helicene-based OLEDs too.⁷⁷⁻⁸⁰

In 2013, Fuchter, Campbell, and their co-workers also applied enantiopure 1aza[6]helicene to construct circular polarized light-detected organic field-effect transistors.⁸¹ They found a highly specific photoresponse to circular polarized light, which is related to the handedness of the helicene units (**Figure 1.16**).

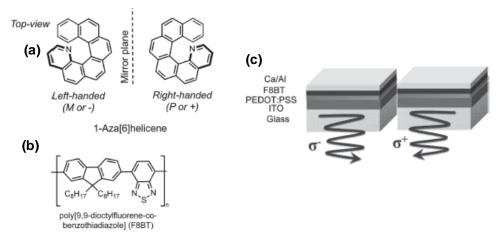


Figure 1.14 a) molecular structure *M*- and *P*-1-aza[6]helicene; b) Molecular structure of the lightemitting polymer F8BT; c) Single-layer PLED device structure consisting of a 1-aza[6]helicenedoped F8BT thin fi lm sandwiched between a PEDOT:PSS-coated ITO anode and a Ca/Al cathode; right- and left-handed + and - circularly polarized electroluminescent polymer emission was respectively generated from (+)- and (-)-1-aza[6]helicene-doped devices. (Reproduced from ref.⁷⁵)

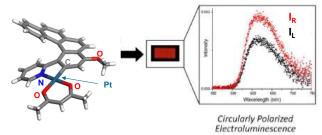


Figure 1.15 Crystal structure of platinahelicene *P***-XXVII-c** (left); circular polarized electroluminescence (right) (Adapted from ref.⁷⁶)

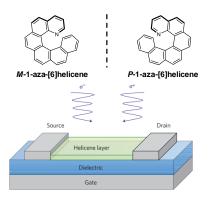


Figure 1.16 Molecular structures and device structure of the circularly polarized light-detecting OFET. (Reproduced from ref.⁸¹)

Our group recently reported organic photovoltaics (OPVs) based on a carbo-[6]helicene substituted with naphthalimide groups through ethynyl bridges (and poly(3-hexylthiophene P3HT used as an electron donating polymer).⁸² The authors found that when the enantiopure form of this π -helical non-fullerene acceptor was applied in the device, it displayed higher power conversion efficiencies than the racemic form, with higher electron mobilities in the solid state (**Figure 1.17**)

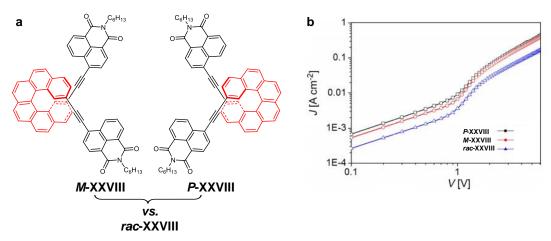


Figure 1.17 a) molecular structure of helicene derivatives; b) Electron mobility μ_e of *rac*-(blue), *P*-(black), *M*-(red) **XXVIII** based devices (Reproduced from ref.⁸²).

A.2.2.6 Asymmetric catalysis

Due to the unique chiral environment of helicenes, they can be used as asymmetric catalysts. In 1997, Reetz's group reported the first example of helicene applied in catalysis. The authors prepared 2,15-bis(diphenylhphosphino)[6]helicene, which was used as a ligand in enantioselective hydrogenation of itaconic acid ester.⁸³ Later on in 2003, Yamaguchi's group used a bishelicenol phosphite ligand and Rh complex to catalyze the

same reaction and got a quantitative yield and 96% ee value (**Figure 1.18**).⁸⁴ Some more examples about helicene-like chiral auxiliaries in asymmetric catalysis can be seen in the review article reported by Marinetti *et al.*⁸⁵

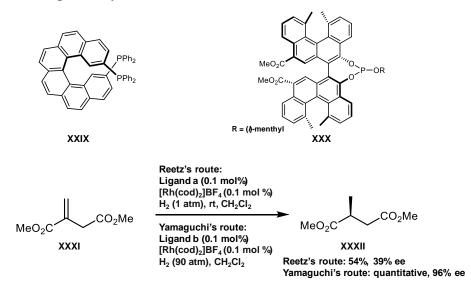
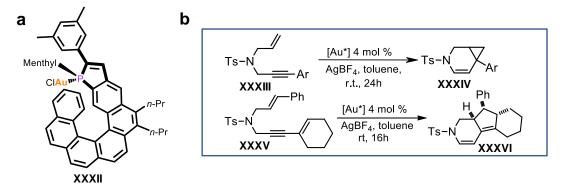
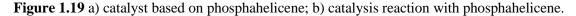


Figure 1.18 The asymmetric hydrogenation of dimethyl itaconate catalyzed by Reetz's route and Yamaguchi's route.

In 2014, Voituriez, Marinetti and their co-workers used phosphahelicenes as chiral ligands in enantioselective gold catalysis and got high *ee* value (>90%) (**Figure 1.19**).⁸⁶⁻⁸⁷





In 2017, Starý and Stará's group applied NHC helicene in Ni(0)-catalysed enantioselective [2+2+2] cycloisomerization of triynes and obtained model helicene products with 86% *ee* (**Figure 1.20**).⁸⁸

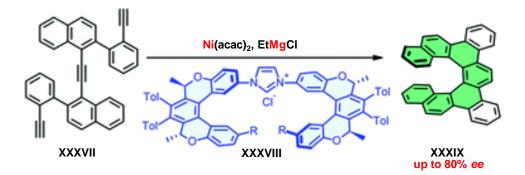


Figure 1.20 [2+2+2] cycloisomerization of triynes with NHC helicene derivative. (Reproduced from ref.⁸⁸)

Helicenes are also applied in biochemistry,⁸⁹⁻⁹⁹ assembly,¹⁰⁰⁻¹¹⁵ sensing,¹¹⁶⁻¹²² and so on. More information about helicene's application can be found in the recent book "Helicene Chemistry: From Synthesis to Application" written by Chen and Shen.⁷

B Conclusion

In summary, in this chapter, I introduced concept, classification of chirality, as well as history, racemization, synthesis, chiroptical properties, and applications of helicenes. I mainly focused on the applications of helicenes, including the chiroptical switches, spin filtering, circular polarized luminescence (CPL), molecular recognition, organic light-emitting diodes (OLEDs) and asymmetric catalysis. In the following chapters, I will present novel applications of helicenes I developed during my PhD work, *i.e.* as photoresponsive chiral switches, magnetic materials, and chiral fullerenes derivatives (**Figure 1.21**).

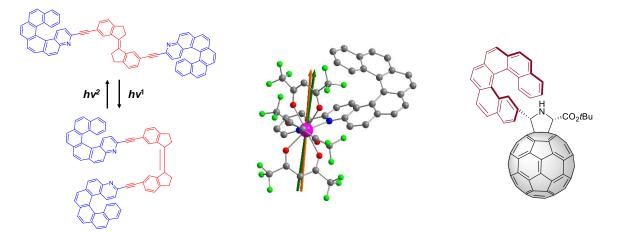


Figure 1.21 left) photoresponsive chiral switches; middle) single molecule magnets based on helicenes; right) chiral helicene grafted fullerene derivatives.

C References

1. Busch, K. W.; Busch, M. A., *Chiral analysis*. Elsevier: 2011.

2. Chambron, J.-C.; Dietrich-Buchecker, C.; Sauvage, J.-P., From classical chirality to topologically chiral catenands and knots. In *Supramolecular Chemistry I — Directed Synthesis and Molecular Recognition*, Springer Berlin Heidelberg: Berlin, Heidelberg, 1993; pp 131-162.

3. Farina, M.; Morandi, C., *Tetrahedron* **1974**, *30*, 1819-1831.

4. Berova, N.; Nakanishi, K.; Woody, R., *Circular dichroism: principles and applications*. John Wiley & Sons: 2000.

5. Riehl, J. P., *Mirror-image asymmetry: an introduction to the origin and consequences of chirality*. John Wiley & Sons: 2011.

6. Triggle, D. J.; Lough, W.; Wainer, I., *Chirality in Natural and Applied Science*. Blackwell: 2002.

7. Chen, C.-F.; Shen, Y., *Helicene Chemistry: From Synthesis to Applications*. Springer: 2016.

8. Shen, Y.; Chen, C.-F., *Chem. Rev.* **2012**, *112*, 1463-1535.

9. Saleh, N.; Shen, C.; Crassous, J., *Chem. Sci.* **2014**, *5*, 3680-3694.

10. Gingras, M., Chem. Soc. Rev. 2013, 42, 968-1006.

11. Gingras, M.; Felix, G.; Peresutti, R., Chem. Soc. Rev. 2013, 42, 1007-1050.

12. Gingras, M., Chem. Soc. Rev. 2013, 42, 1051-1095.

13. Mason, S. F.; Mason, S. F., *Chemical evolution: origin of the elements, molecules, and living systems*. Clarendon Press Oxford: 1991.

14. Knudsen, O., *Lord kelvin, baltimore lectures on mathematical physics ((1884), 1904).* 2005; p 748-756.

15. Hicks, J. M., *Chirality: Physical Chemistry*. American Chemical Society Washington, DC: 2002; Vol. 810.

16. Eliel, E. L.; Wilen, S. H., *Stereochemistry of organic compounds*. John Wiley & Sons: 2008.

17. Bordoli, R. J.; Goldup, S. M., J. Am. Chem. Soc. 2014, 136, 4817-4820.

18. Meisenheimer, J.; Witte, K., Eur. J. Inorg. Chem. 1903, 36, 4153-4164.

- 19. Newman, M. S.; Lutz, W. B.; Lednicer, D., J. Am. Chem. Soc. 1955, 77, 3420-3421.
- 20. Newman, M. S.; Lednicer, D., J. Am. Chem. Soc. 1956, 78, 4765-4770.
- 21. Newman, M. S.; Wise, R. M., J. Am. Chem. Soc. 1956, 78, 450-454.
- 22. Flammang-Barbieux, M.; Nasielski, J.; Martin, R., Tetrahedron Lett. 1967, 8, 743-744.

23. Martin, R.; Flammang-Barbieux, M.; Cosyn, J.; Gelbcke, M., *Tetrahedron Lett.* **1968**, *9*, 3507-3510.

- 24. Martin, R. H.; Morren, G.; Schurter, J., *Tetrahedron Lett.* **1969**, *10*, 3683-3688.
- 25. Martin, R.; Baes, M., *Tetrahedron* **1975**, *31*, 2135-2137.
- 26. Mori, K.; Murase, T.; Fujita, M., Angew. Chem. Int. Ed. 2015, 54, 6847-6851.
- 27. Martin, R. H., Angew. Chem. Int. Ed. 1974, 13, 649-660.
- 28. Wynberg, H.; Groen, M. B., J. Chem. Soc. D 1969, 964-965.
- 29. Goedicke, C.; Stegemeyer, H., Tetrahedron Lett. 1970, 11, 937-940.
- 30. Martin, R.; Marchant, M.-J., *Tetrahedron Lett.* **1972**, *13*, 3707-3708.
- 31. Martin, R.; Marchant, M.-J., *Tetrahedron* **1974**, *30*, 347-349.
- 32. Sehnal, P.; Stará, I. G.; Šaman, D.; Tichý, M.; Míšek, J.; Cvačka, J.; Rulíšek, L.;

Chocholoušová, J.; Vacek, J.; Goryl, G., Proc. Natl. Acad. Sci. 2009, 106, 13169-13174.

33. Wood, C. S.; Mallory, F. B., J. Org. Chem. 1964, 29, 3373-3377.

- 34. Katz, T. J., Angew. Chem. Int. Ed. 2000, 39, 1921-1923.
- 35. Urbano, A., Angew. Chem. Int. Ed. 2003, 42, 3986-3989.

36. Meurer, K. P.; Vögtle, F., Helical molecules in organic chemistry. In *Organic Chemistry*, Springer: 1985; pp 1-76.

37. Liu, L.; Katz, T. J., *Tetrahedron Lett.* **1990**, *31*, 3983-3986.

38. Katz, T. J.; Liu, L.; Willmore, N. D.; Fox, J. M.; Rheingold, A. L.; Shi, S.; Nuckolls, C.; Rickman, B. H., *J. Am. Chem. Soc.* **1997**, *119*, 10054-10063.

39. Paruch, K.; Katz, T. J.; Incarvito, C.; Lam, K.-C.; Rhatigan, B.; Rheingold, A. L., *J. Org. Chem.* **2000**, *65*, 7602-7608.

40. Pena, D.; Pérez, D.; Guitián, E.; Castedo, L., Org. Lett. 1999, 1, 1555-1557.

41. Pena, D.; Cobas, A.; Pérez, D.; Guitián, E.; Castedo, L., Org. Lett. 2000, 2, 1629-1632.

42. Peña, D.; Cobas, A.; Pérez, D.; Guitián, E.; Castedo, L., Org. Lett. 2003, 5, 1863-1866.

43. Caeiro, J.; Peña, D.; Cobas, A.; Pérez, D.; Guitián, E., *Advanced Synthesis & Catalysis* **2006**, *348*, 2466-2474.

44. Romero, C.; Pena, D.; Perez, D.; Guitian, E., J. Org. Chem. 2008, 73, 7996-8000.

45. Stará, I. G.; Starý, I.; Kollárovič, A.; Teplý, F.; Vyskočil, Š.; Šaman, D., *Tetrahedron Lett.* **1999,** *40*, 1993-1996.

46. Teplý, F.; Stará, I. G.; Starý, I.; Kollárovič, A.; Šaman, D.; Rulíšek, L.; Fiedler, P., *J. Am. Chem. Soc.* **2002**, *124*, 9175-9180.

47. Stará, I. G.; Alexandrová, Z.; Teplý, F.; Sehnal, P.; Starý, I.; Šaman, D.; Buděšínský, M.; Cvačka, J., *Org. Lett.* **2005**, *7*, 2547-2550.

48. Sehnal, P.; Krausová, Z.; Teplý, F.; Stará, I. G.; Starý, I.; Rulíšek, L.; Šaman, D.; Císařová, I., *J. Org. Chem.* **2008**, *73*, 2074-2082.

49. Teplý, F.; Stará, I. G.; Starý, I.; Kollárovič, A.; Šaman, D.; Vyskočil, Š.; Fiedler, P., *J. Org. Chem.* **2003**, *68*, 5193-5197.

50. Martin, R.; Marchant, M.-J., *Tetrahedron* **1974**, *30*, 343-345.

51. Newman, M. S.; Darlak, R. S.; Tsai, L. L., J. Am. Chem. Soc. 1967, 89, 6191-6193.

52. Isla, H.; Crassous, J., *Comptes Rendus Chimie* **2016**, *19*, 39-49.

53. Anger, E.; Srebro, M.; Vanthuyne, N.; Toupet, L.; Rigaut, S.; Roussel, C.; Autschbach,

J.; Crassous, J.; Réau, R., J. Am. Chem. Soc. 2012, 134, 15628-15631.

54. Biet, T.; Fihey, A.; Cauchy, T.; Vanthuyne, N.; Roussel, C.; Crassous, J.; Avarvari, N., *Chem. Eur. J.* **2013**, *19*, 13160-13167.

55. Schweinfurth, D.; Zalibera, M.; Kathan, M.; Shen, C.; Mazzolini, M.; Trapp, N.;

Crassous, J.; Gescheidt, G.; Diederich, F. o., J. Am. Chem. Soc. 2014, 136, 13045-13052.

56. Biet, T.; Martin, K.; Hankache, J.; Hellou, N.; Hauser, A.; Bürgi, T.; Vanthuyne, N.;

Aharon, T.; Caricato, M.; Crassous, J.; Avarvari, N., Chem. Eur. J. 2017, 23, 437-446.

57. Biet, T.; Cauchy, T.; Sun, Q.; Ding, J.; Hauser, A.; Oulevey, P.; Bürgi, T.; Jacquemin, D.; Vanthuyne, N.; Crassous, J.; Avarvari, N., *Chem. Commun.* **2017**, *53*, 9210-9213.

58. Shen, C.; Loas, G. h.; Srebro-Hooper, M.; Vanthuyne, N.; Toupet, L.; Cador, O.; Paul, F.;

López Navarrete, J. T.; Ramírez, F. J.; Nieto-Ortega, B.; Casado, J.; Autschbach, J.; Vallet, M.; Crassous, J., *Angew. Chem. Int. Ed.* **2016**, *55*, 8062-8066.

59. Anger, E.; Srebro, M.; Vanthuyne, N.; Roussel, C.; Toupet, L.; Autschbach, J.; Réau, R.; Crassous, J., *Chem. Commun.* **2014**, *50*, 2854-2856.

60. Saleh, N.; Moore, B.; Srebro, M.; Vanthuyne, N.; Toupet, L.; Williams, J. A. G.; Roussel, C.; Deol, K. K.; Muller, G.; Autschbach, J.; Crassous, J., *Chemistry – A European Journal* **2015**, *21*, 1673-1681.

61. Isla, H.; Srebro-Hooper, M.; Jean, M.; Vanthuyne, N.; Roisnel, T.; Lunkley, J. L.; Muller, G.; Williams, J. A. G.; Autschbach, J.; Crassous, J., *Chem. Commun.* **2016**, *52*, 5932-5935.

62. Shen, C.; He, X.; Toupet, L.; Norel, L.; Rigaut, S.; Crassous, J., Organometallics 2017.

63. Kiran, V.; Mathew, S. P.; Cohen, S. R.; Hernández Delgado, I.; Lacour, J.; Naaman, R., *Adv. Mater.* **2016**, *28*, 1957-1962.

64. Linfoot, C. L.; Leitl, M. J.; Richardson, P.; Rausch, A. F.; Chepelin, O.; White, F. J.; Yersin, H.; Robertson, N., *Inorg. Chem.* **2014**, *53*, 10854-10861.

65. Muller, G., Circularly Polarised Luminescence. In *Luminescence of Lanthanide Ions in Coordination Compounds and Nanomaterials*, John Wiley & Sons Ltd: 2014; pp 77-124.

66. Kumar, J.; Nakashima, T.; Kawai, T., J. Phys. Chem. Lett. 2015, 6, 3445-3452.

67. Shen, C.; Anger, E.; Srebro, M.; Vanthuyne, N.; Deol, K. K.; Jefferson, T. D.; Muller, G.;

Williams, J. A. G.; Toupet, L.; Roussel, C.; Autschbach, J.; Reau, R.; Crassous, J., *Chem. Sci.* **2014**, *5*, 1915-1927.

68. Hellou, N.; Srebro-Hooper, M.; Favereau, L.; Zinna, F.; Caytan, E.; Toupet, L.; Dorcet, V.; Jean, M.; Vanthuyne, N.; Williams, J. A. G.; Di Bari, L.; Autschbach, J.; Crassous, J., *Angew. Chem. Int. Ed.* **2017**, *56*, 8236-8239.

69. Nakazaki, M.; Yamamoto, K.; Ikeda, T.; Kitsuki, T.; Okamoto, Y., *J. Chem. Soc., Chem. Commun.* **1983**, 787-788.

70. Yamamoto, K.; Ikeda, T.; Kitsuki, T.; Okamoto, Y.; Chikamatsu, H.; Nakazaki, M., *J. Chem. Soc., Perkin Trans. 1* **1990**, 271-276.

71. Hatakeyama, T.; Hashimoto, S.; Oba, T.; Nakamura, M., *J. Am. Chem. Soc.* **2012**, *134*, 19600-19603.

72. Si, Y.; Yang, G., J. Mater. Chem. C 2013, 1, 2354-2361.

73. Kim, C.; Marks, T. J.; Facchetti, A.; Schiavo, M.; Bossi, A.; Maiorana, S.; Licandro, E.; Todescato, F.; Toffanin, S.; Muccini, M., *Org. Electron.* **2009**, *10*, 1511-1520.

74. Josse, P.; Favereau, L.; Shen, C.; Dabos-Seignon, S.; Blanchard, P.; Cabanetos, C.; Crassous, J., *Chem. Eur. J.* **2017**, *23*, 6277-6281.

75. Yang, Y.; da Costa, R. C.; Smilgies, D. M.; Campbell, A. J.; Fuchter, M. J., *Adv. Mater.* **2013**, *25*, 2624-2628.

76. Brandt, J. R.; Wang, X.; Yang, Y.; Campbell, A. J.; Fuchter, M. J., *J. Am. Chem. Soc.* **2016**, *138*, 9743-9746.

77. Sahasithiwat, S.; Sooksimuang, T.; Kangkaew, L.; Panchan, W., *Dyes Pigments* **2017**, *136*, 754-760.

78. Shi, L.; Liu, Z.; Dong, G.; Duan, L.; Qiu, Y.; Jia, J.; Guo, W.; Zhao, D.; Cui, D.; Tao, X., *Chemistry – A European Journal* **2012**, *18*, 8092-8099.

79. Hua, W.; Liu, Z.; Duan, L.; Dong, G.; Qiu, Y.; Zhang, B.; Cui, D.; Tao, X.; Cheng, N.; Liu, Y., *RSC Adv.* **2015**, *5*, 75-84.

80. Hirai, H.; Nakajima, K.; Nakatsuka, S.; Shiren, K.; Ni, J.; Nomura, S.; Ikuta, T.; Hatakeyama, T., *Angew. Chem. Int. Ed.* **2015**, *54*, 13581-13585.

81. Yang, Y.; da Costa, R. C.; Fuchter, M. J.; Campbell, A. J., Nat Photon **2013**, 7, 634-638.

82. Josse, P.; Favereau, L.; Shen, C.; Dabos-Seignon, S.; Blanchard, P.; Cabanetos, C.;

Crassous, J., *Chemistry – A European Journal* **2017**, *23*, 6277-6281.

83. Reetz, M. T.; Beuttenmüller, E. W.; Goddard, R., *Tetrahedron Lett.* **1997**, *38*, 3211-3214.

84. Nakano, D.; Yamaguchi, M., *Tetrahedron Lett.* **2003**, *44*, 4969-4971.

85. Aillard, P.; Voituriez, A.; Marinetti, A., *Dalton Trans.* 2014, 43, 15263-15278.

86. Aillard, P.; Voituriez, A.; Dova, D.; Cauteruccio, S.; Licandro, E.; Marinetti, A., *Chem. Eur. J.* **2014**, *20*, 12373-12376.

87. Yavari, K.; Aillard, P.; Zhang, Y.; Nuter, F.; Retailleau, P.; Voituriez, A.; Marinetti, A., *Angew. Chem.* **2014**, *126*, 880-884.

88. Sánchez, I. G.; Šámal, M.; Nejedlý, J.; Karras, M.; Klívar, J.; Rybáček, J.; Buděšínský, M.; Bednárová, L.; Seidlerová, B.; Stará, I. G., *Chem. Commun.* **2017**, *53*, 4370-4373.

89. Nakagawa, H.; Kobori, Y.; Yoshida, M.; Yamada, K.-i., *Chem. Commun.* **2001**, 2692-2693.

90. Nakagawa, H.; Yoshida, M.; Kobori, Y.; Yamada, K. i., *Chirality* **2003**, *15*, 703-708.

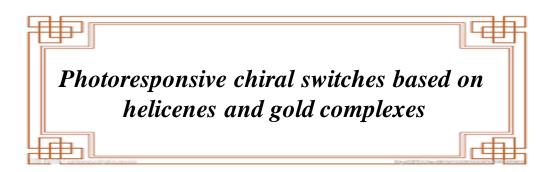
91. Honzawa, S.; Okubo, H.; Anzai, S.; Yamaguchi, M.; Tsumoto, K.; Kumagai, I., *Biorg. Med. Chem.* **2002**, *10*, 3213-3218.

92. Xu, Y.; Zhang, Y. X.; Sugiyama, H.; Umano, T.; Osuga, H.; Tanaka, K., *J. Am. Chem. Soc.* **2004**, *126*, 6566-6567.

93. Passeri, R.; Aloisi, G. G.; Elisei, F.; Latterini, L.; Caronna, T.; Fontana, F.; Sora, I. N., *Photoch Photobio Sci* **2009**, *8*, 1574-1582.

- 94. Shinohara, K.-i.; Sannohe, Y.; Kaieda, S.; Tanaka, K.-i.; Osuga, H.; Tahara, H.; Xu, Y.; Kawase, T.; Bando, T.; Sugiyama, H., *J. Am. Chem. Soc.* **2010**, *132*, 3778-3782.
- 95. Tsuji, G.; Kawakami, K.; Sasaki, S., *Biorg. Med. Chem.* **2013**, *21*, 6063-6068.
- 96. Latterini, L.; Galletti, E.; Passeri, R.; Barbafina, A.; Urbanelli, L.; Emiliani, C.; Elisei, F.;
- Fontana, F.; Mele, A.; Caronna, T., J. Photochem. Photobiol. A: Chem. 2011, 222, 307-313.
- 97. Li, M.; Feng, L. H.; Lu, H. Y.; Wang, S.; Chen, C. F., *Adv. Funct. Mater.* **2014**, *24*, 4405-4412.
- 98. Cauteruccio, S.; Bartoli, C.; Carrara, C.; Dova, D.; Errico, C.; Ciampi, G.; Dinucci, D.; Licandro, E.; Chiellini, F., *ChemPlusChem* **2015**, *80*, 490-493.
- 99. Santoro, A.; Lord, R. M.; Loughrey, J. J.; McGowan, P. C.; Halcrow, M. A.; Henwood,
- A. F.; Thomson, C.; Zysman-Colman, E., Chem. Eur. J. 2015, 21, 7035-7038.
- 100. Ernst, K.; Böhringer, M.; McFadden, C.; Hug, P.; Müller, U.; Ellerbeck, U., *Nanot* **1999**, *10*, 355.
- 101. Fasel, R.; Parschau, M.; Ernst, K. H., Angew. Chem. Int. Ed. 2003, 42, 5178-5181.
- 102. Fasel, R.; Parschau, M.; Ernst, K.-H., Nature 2006, 439, 449.
- 103. Barth, C.; Gingras, M.; Foster, A. S.; Gulans, A.; Félix, G.; Hynninen, T.; Peresutti, R.; Henry, C. R., *Adv. Mater.* **2012**, *24*, 3228-3232.
- 104. Balandina, T.; van der Meijden, M. W.; Ivasenko, O.; Cornil, D.; Cornil, J.; Lazzaroni, R.; Kellogg, R. M.; De Feyter, S., *Chem. Commun.* **2013**, *49*, 2207-2209.
- 105. Seibel, J.; Allemann, O.; Siegel, J. S.; Ernst, K.-H., *J. Am. Chem. Soc.* **2013**, *135*, 7434-7437.
- 106. Parschau, M.; Ernst, K. H., Angew. Chem. Int. Ed. 2015, 54, 14422-14426.
- 107. Ichinose, W.; Ito, J.; Yamaguchi, M., Angew. Chem. 2013, 125, 5398-5402.
- 108. Verbiest, T.; Van Elshocht, S.; Kauranen, M.; Hellemans, L.; Snauwaert, J.; Nuckolls, C.;
- Katz, T. J.; Persoons, A., Science 1998, 282, 913-915.
- 109. Nuckolls, C.; Katz, T. J., J. Am. Chem. Soc. 1998, 120, 9541-9544.
- 110. Shcherbina, M. A.; Zeng, X. b.; Tadjiev, T.; Ungar, G.; Eichhorn, S. e. H.; Phillips, K. E.;
- Katz, T. J., Angew. Chem. Int. Ed. 2009, 48, 7837-7840.
- 111. Saiki, Y.; Sugiura, H.; Nakamura, K.; Yamaguchi, M.; Hoshi, T.; Anzai, J.-i., *J. Am. Chem. Soc.* **2003**, *125*, 9268-9269.
- 112. Saiki, Y.; Nakamura, K.; Nigorikawa, Y.; Yamaguchi, M., *Angew. Chem. Int. Ed.* **2003**, *42*, 5190-5192.
- 113. Saito, N.; Kanie, K.; Matsubara, M.; Muramatsu, A.; Yamaguchi, M., J. Am. Chem. Soc. **2015**, *137*, 6594-6601.
- 114. Murguly, E.; McDonald, R.; Branda, N. R., Org. Lett. 2000, 2, 3169-3172.
- 115. Kaseyama, T.; Furumi, S.; Zhang, X.; Tanaka, K.; Takeuchi, M., *Angew. Chem.* **2011**, *123*, 3768-3771.
- 116. Weix, D. J.; Dreher, S. D.; Katz, T. J., J. Am. Chem. Soc. 2000, 122, 10027-10032.
- 117. Wang, D. Z.; Katz, T. J., J. Org. Chem. 2005, 70, 8497-8502.
- 118. Reetz, M. T.; Sostmann, S., Tetrahedron 2001, 57, 2515-2520.
- 119. Wallabregue, A.; Sherin, P.; Guin, J.; Besnard, C.; Vauthey, E.; Lacour, J., *Eur. J. Org. Chem.* **2014**, 2014, 6431-6438.
- 120. Li, M.; Li, X.-J.; Lu, H.-Y.; Chen, C.-F., Sensors Actuators B: Chem. 2014, 202, 583-587.
- 121. Storch, J.; Zadny, J.; Strasak, T.; Kubala, M.; Sykora, J.; Dusek, M.; Cirkva, V.; Matejka, P.; Krbal, M.; Vacek, J., *Chem. Eur. J.* **2015**, *21*, 2343-2347.
- 122. Zhou, L.-L.; Li, M.; Lu, H.-Y.; Chen, C.-F., Polym. Chem. 2016, 7, 310-318.

Chapter II



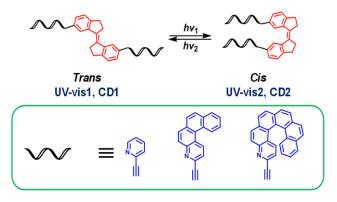
RENNES 2017

A General introduction: design of the project

In this chapter, we develop two parts of work based on so-called 'stiff stilbene' units that are known to reversibly interconvert between two *trans* and *cis* forms through light.¹ The first part of the work corresponds to photoresponsive chiral switches based on helicenes, the other one to photoresponsive gold(I) complexes. In the first part, we want to study the isomerization process of photochiral switches, and use the electronic circular dichroism (CD) to detect changes during the *cis-trans* photoisomerization process. In the other part, we want to take advantage of the different conformations of the stiff-stilbene *trans* and *cis* isomers and the reversibility of the photoconversion to tune the distance between gold metal centers and to tentatively switch on and off the gold-gold interaction by photo-irradiation.

A.1 Photoresponsive chiral switches based on helicenes

In order to prepare a novel series of photoresponsive chiral switches, we wanted to combine the stiff stilbene unit with helicene units (**Scheme 2.1**). Taking advantage of the photoresponsive properties of the stiff stilbene and of the strong chiroptical properties of the helicenes, we could realize light stimulus-responsive chiroptical switches. As shown in **Scheme 2.1**, the stiff stilbene has two distinct *trans* and *cis* isomers. When the switch transfers from one state to another one, the π -conjugated system will change, which may influence the properties of the whole system. That is, the absorption and chiroptical properties of the stiff stilbene. The readout process can be monitored by ultraviolet-visible (UV-vis) and CD spectroscopy.

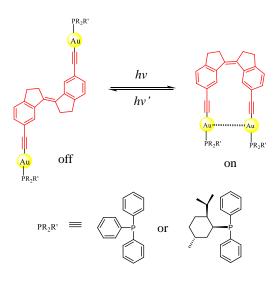


Scheme 2.1 Schematic representation of the photoresponsive switches studied.

In this chapter, a series of photoresponsive switches were prepared (**Scheme 2.1**). The compounds were well-characterized by multinuclear NMR spectroscopy and high resolution mass spectroscopy. The isomerization processes were monitored by ¹H NMR and UV-vis spectroscopy, and by CD spectroscopy in the case of enantiopure [6]helicene derivatives. In addition, due to the existence of nitrogen atoms in the switches, we anticipated that coordination would occur with metal ions. Especially, in the *cis* conformation of switches, two nitrogen atoms were expected to be close to each other, and could possibly coordinate to a metal center, which may block the *cis* conformation and prevent the isomerization process.

A.2 Photoresponsive gold complexes

Gold (I) complexes display a linear two-coordination geometry [AuXL], which has been known for a long time. They also show short intermolecular gold-gold interaction, which transforms the mono units into dimers, oligomers or multidimensional polymers.² In this chapter, we describe stiff stilbene dialkynyl ligands, which can react with gold (I) complexes [AuXL] and form Gold(I) alkynyl complexes. Gold(I) alkynyl complexes have wide range of applications, such as luminescence, optical switches, molecular recognition, electronic and catalysis.³ Herein, we want to develop a new type of photoresponsive gold complexes (Scheme 2.2), in which the distance between the gold atoms will be changed in the two different *cis* and *trans* conformation. We also want to check if there is gold-gold interaction in the *cis* form of the gold(I) alkynyl complexes. The gold complexes were well characterized by multinuclear NMR, UV-vis spectra, X-ray diffraction and so on. The isomerization process was monitored by ¹H NMR and ³¹P NMR spectroscopies. Under irradiation upon two different wavelength lights, the gold complex can achieve reversibility. This work was conducted in collaboration with Dr. Christophe Lescop (INSA Rennes), Sebastian Hartung and Prof. Rudolph Pietschnig (University of Kassel) through a Franco-German Procope PHC exchange.



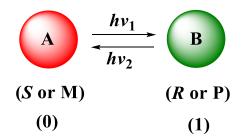
Scheme 2.2 Schematic representation of photoresponsive gold(I) alkynyl complexes studied.

B Stiff stilbenes substituted with helicenes

B.1 Bibliographic part

B.1.1 Generalities on molecular switches

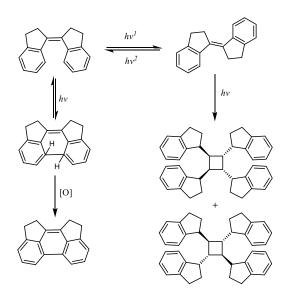
Molecular switches can be reversibly converted from one state to another by an external stimulus such as light, electricity, thermal or a chemical reaction.¹ During this conversion process, the changes of UV-vis spectra, emission intensity, circular CD, optical rotation (OR), color, pH, electronic properties and so on, are observed, which can be well applied in data storage, smart materials. Especially, the photoresponsive switches became a hot spot of chemistry research for its allowing remote activation and control without generating chemical waste to the systems.⁴ As one of photoresponsive switches, chiroptical photoresponsive molecules usually contain a class of photochromic compounds. The reversible isomerization usually leads to the chirality change in the system (**Scheme 2.3**).¹ It is well known that the living cells and organisms are examples of control of chirality in molecular, supramolecular, and macromolecular levels. So chiral optical switches can be applied in chiral recognition, information storage, organization self-assembly, catalysis, self-replication and so on.¹



Scheme 2.3 General scheme of chiral optical switches.

B.2 Stiff stilbenes

Stiff stilbene is one of the photoresponsive switch units, which was first reported by Majerus et al in 1967.⁵ In stiff stilbene, the rotation of the phenyl is hindered and this restriction may simplify the isomerization path, twisting around the central double bond.⁶⁻⁷ Stiff stilbene displays two distinct stable *trans* (*E*) and *cis* (*Z*) isomers, which show a high activation interconversion barrier of 43 kcal.mol⁻¹ (a half-life time of *ca*. 10³ year at 300 K) but can be readily interconverted by a photochemical process with a high quantum yield.⁸ Indeed, like stilbenes, stiff stilbene shows kinds of photochemical behavior in solution state, such as reversible *cis/trans* isomerization, cyclization of *cis*-stilbene and further oxidation, and dimerization of *trans*-stiff stilbene (**Scheme 2.4**).⁹

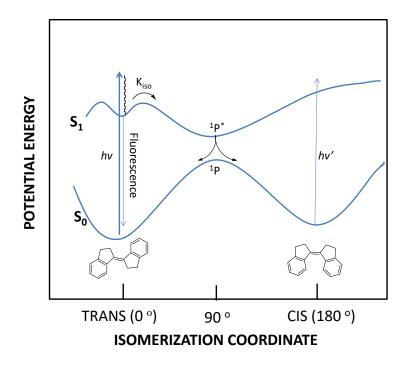


Scheme 2.4 Possible photochemical transformations of stiff stilbene.

B.3 Photoisomerization mechanism of stiff stilbene

Satile and his coworkers firstly proposed the mechanism for the photochemical isomerization of stilbenes.¹⁰⁻¹² In the first step of isomerization, the stilbene absorbs a

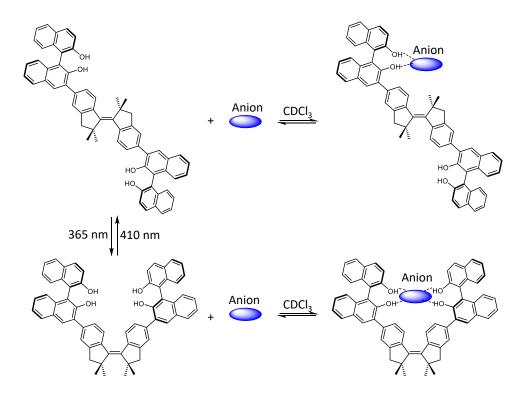
quantum of energy and is excited to the singlet or triplet state. Then, the solvent molecules undergo reorganization, and decrease the energy of system. The excited state decays by two ways: one is a radiative process such as fluorescence; another one is a non-radiative process, that is, photochemical deactivation.¹³ The modern generally accepted mechanism for describing the isomerization is based on an excited singlet potential surface which was proposed by Orlandi and Siebrand (Scheme 2.5).^{7, 14} Then it was proven by picosecond experiment.¹⁵ In stiff stilbene, the rotation of a phenyl group around the single bond is hindered, and this restriction may simplify the isomerization path, the isomerization can occur on the central double bond.⁶⁻⁷ In the ground state, there is a great energy barrier between *trans* and *cis* stiff stilbene. In the first excited state, the surface shows a minimum at the twisted conformation (refer to this state as ${}^{1}p^{*}$). This potential minimum resulted from the avoided crossing at the S_1 surface with a low energy doubly excited S_2 surface.⁸ On the *trans* side, there is a small barrier which is due to the twisting of ethylene bond, whereas, on the *cis* side, there is little or no barrier to twisting motion. When the *trans* or *cis* stiff stilbene reaches the twisted geometry (perpendicular geometry), the deactivation process to ground state is very fast. Once on the ground-state surface, the product molecules branches to cis or trans form.⁶ The solvent effects will influence the isomerization process of stiff stilbene. The first transient absorption of stiff stilbene was studied by Hochstrasser and co-workers in 1983. They found that the isomerization is strongly dependent on the viscosity of solvent.¹⁶ For *trans* stiff stilbene, an increase in viscosity in dilute solution leads to an increase in fluorescence efficiency and lifetime with a decrease in the efficiency of *trans* to *cis* photoisomerization.¹⁷⁻¹⁹ Stiff stilbene derivatives have been applied as anion receptors, molecular force probes, molecular rotors, catalysis, supramolecular polymers, photoresponsive proton gate, molecular motors and so on. The isomerization process is also influenced by substituents (vide infra).



Scheme 2.5 Potential energy diagram for the ground and first excited states along the isomerization coordinate in the case of stiff stilbene. Reproduced from ref.¹⁹

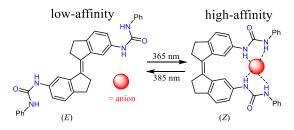
B.4 Applications of stiff stilbene

In 2007, the Shinmyozu's group reported the synthesis and photoswitchable properties of 2,2,2',2'-tetramethyl-stiff stilbene derivatives (**Scheme 2.6**).²⁰ Later on, they introduced 2,2'-dihydroxy-1,1'-binaphthyl (BINOL) group into the molecules to construct an axially chiral stiff stilbene used as a chiral molecular host.²¹ In this system, the authors introduced four methyl groups around the olefin which resulted in decreasing the energy barrier for photoisomerization. The photoisomerization processes were checked by ¹H NMR, UV-vis, and CD spectroscopy. The *trans-cis* and *cis-trans* photochemical interconversions were triggered by a wavelength corresponding to 365 nm and 410 nm respectively. The switches showed good resistance against photofatigue. After 10 cycles switching process, no decrease of absorption intensities was observed. Anion-binding properties were also checked. An 8-fold difference in binding chloride was observed and the *trans-*isomer turned out to be a better binding form.



Scheme 2.6 Scheme of photoswitchable process and complexes formation.

In 2017, Feringa's group reported an anion receptor derived from stiff stilbene (**Scheme 2.7**).²² The stiff stilbene was equipped with two urea units. The switches could selectively bind $CH_3CO_2^-$ and $H_2PO_4^-$, but showed different affinity in *trans* and *cis* isomers. The affinity could be varied by 365/385 nm light irradiation. In addition, the switches were tolerant to water.



Scheme 2.7 Photoswitching of anion binding.

In 2009, Boulatov's group reported a series of molecular force probes based on stiff stilbene.²³⁻²⁸ For example, it was applied to study the relation between kinetics of thiol/disulfide exchange and restoring force of molecules (**Figure 2.1**). The isomerization of stiff stilbene unit could change the conformation flexibility of the linker, which created kinds of strained macrocycles. The change of macrocycles' tension affected the kinetics of

substrate reaction. The authors measured the kinetics of reaction across a series of lengths of linker as a function of the restoring force of molecules in tension.²⁶

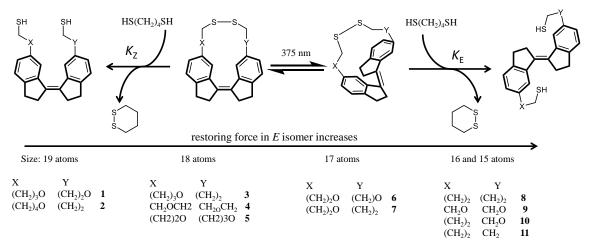
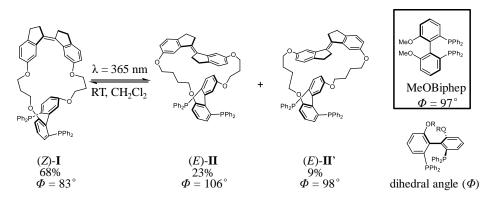


Figure 2.1 The series of macrocycles for measuring the kinetics of reaction. Reproduced from ref.²⁶

In 2014, Craig's group developed a chiral bis(phosphine) ligand fused with stiff stilbene unit (Scheme 2.8).²⁹ In this switchable catalytic system, the ligand geometry was distorted during switching process but without perturbing the electronic structure, which affected the catalyst activity and selectivity. The authors separated the *trans* and *cis* form ligands, then studied their catalytic activity and selectivity respectively (Table 2.1). For example, in the reaction of arylation with phenyl triflate, ligand in (*E*)-II form yielded III in high conversion and 79% *ee*, however, in (*Z*)-I form yielded a relative low conversion and 96% *ee*. While in the condition with (*E*)-II and 365 nm irradiation, 90% *ee* and 93% conversion of III were obtained. Through checking ³¹P-⁷⁷Se coupling constants of their corresponding phosphine selenides, the authors confirmed that the electronics at the phosphorus atoms in (*Z*)-I and (*E*)-II forms were the same, which revealed that geometric effects mainly led to the change of catalytic activity and selectivity. Trost's allylic alkylation was also studied.

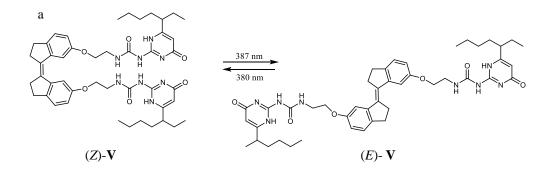


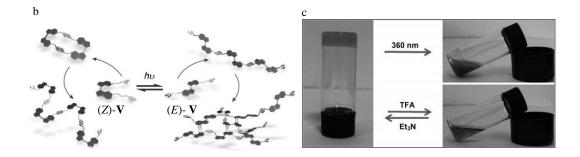
Scheme 2.8 Photostationary mixture and chiral bis(phosphine) ligand ((*E*)-II and (*E*)-II' are diasteromers). Reproduced from ref.²⁹

$ = \underbrace{\bigcup_{i=1}^{i}}_{\text{Benzene, } iPr_2\text{NEt}} \underbrace{\bigcup_{i=1}^{i}}_{\text{Benzene, } iPr_2\text{NEt}} \underbrace{\bigcup_{i=1}^{i}}_{\text{AU} \circ C, 24 \text{ h}} + \underbrace{\bigcup_{i=1}^{i}}_{\text{Benzene, } iPr_2\text{NEt}} + \underbrace{\bigcup_{i=1}^{i}}_{Benzene,$										
		S)-III	(<i>R</i>)- III	(<i>S</i>)- IV	(<i>R</i>)- IV					
Entry	ligand	Conv. [%]	III/IV	Total (S) products [%]	(S)-III ee [%]					
1	MeOBiphep	23	95:5	91	90					
2	(Z)-I	55	97:3	96	96					
3	(<i>E</i>)- II	95	98:2	88	79					
4	(<i>E</i>)- II + 365 nm	93	97:3	93	90					

Table 2.1 Summary of ligand screen in the Heck reaction of phenyl triflate and 2,3-dihydrofuran.

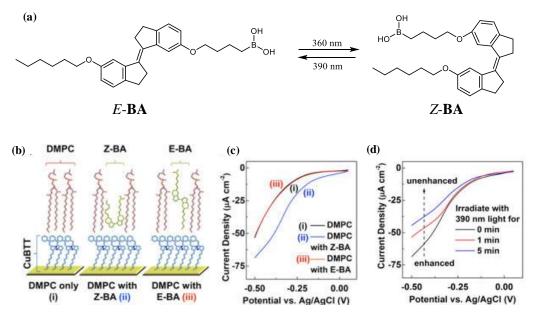
The Yang's group developed a series of supramolecular polymers based on stiff silbene units (**Scheme 2.9**).⁸ For example, the quadruple hydrogen-bonding group 2-ureido-4[1H]-pyrimidinone (UPy) was introduced into the stiff stilbene. Due to the high association constant of UPy and geometric difference of *trans* and *cis* isomers, the molecules showed different assembly process in *trans* and *cis* forms. In *trans* form, it generated supramolecular polymers, wheras, in *cis* form, it followed a ring-chain supramolecular polymerization. Besides, the supramolecular polymer gel was formed through π - π interaction from *E* isomer, which could be responsive to pH and light. Later on, they reported a series work about stiff stilbene, such as photoinduced transformation of metallacycle to metallosupramolecular polymers,³⁰ photoresponsive self-assembly³¹ and photoresponsive cryptand.³²





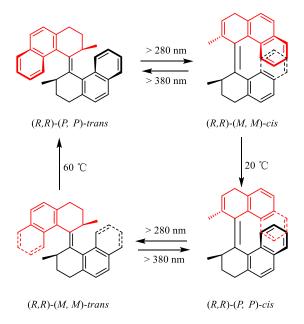
Scheme 2.9 a) Isomerization of the stiff stilbene derivatives; b) Schematic presentation of the assembly process of (*Z*)-V and (*E*)-V; c) stimulus-responsive behavior of the supramolecular gel. Reproduced from ref.⁸

In 2015, the Zimmerman's group reported a photoresponsive switch for transmembrane proton transfer (Scheme 2.10).³³ The stiff stilbene (Z and E-BA) was connected with a boronic acid group for proton transfer and an alkyl group for lipid incorporation. The authors checked the linear sweep voltammograms (LSVs) of O_2 reduction by a selfassembled monolayer (SAM) of CuBTT (Cu complex of 6-((3-(benzylamino)-1,2,4triazol-5-yl)amino)hexane-1-thiol) covered by a 1,2-dimyristoyl-sn-glycero-3phosphorylcholine (DMPC) monolayer with Z-BA, with E-BA and without switches. For Z-BA, the O₂ reduction current density is the same as in the case when 1,2-dimyristoyl-snglycero-3-phosphorylcholine (DMPC) is alone, which meant that Z-BA could not transfer proton, whereas, for E-BA, the O₂ reduction current density increased by 60%, which revealed that Z-BA could deliver proton transmembrane. Then, they tuned the O₂ reduction current density by irradiation with different wavelength lights.



Scheme 2.10 (a) structures of *E*-BA and *Z*-BA. (b) Hybrid bilayer membrane (HBMs) studies: (i) DMPC; (ii) DMPC and *Z*-BA; (iii) DMPC and *E*-BA. (c) Linear sweep voltammograms studies of three cases. (d) Linear sweep voltammograms of DMPC monolayer with *Z*-BA under irradiation with 390 nm. Reproduced from ref.³³

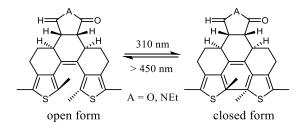
In 1999, Feringa's group firstly reported an overcrowded cyclic stilbene (**Scheme 2.11**).³⁴ Due to the steric interaction in the systems, the double bond is forced out of planarity, obtaining a helical structure, which played an important role in the functioning of these systems. Four different states exist, which can be interconverted in four steps with light and heat. In this way, unidirectional rotation around the double bond is achieved.³⁵ After that, they developed a series of molecular motors.^{1, 36-42} Ben L. Feringa received the Nobel Prize in 2016 for his work on Molecular Motors (together with Jean-Pierre Sauvage and Fraser Stoddart).



Scheme 2.11 Schematic representation of unidirectional 360 ° rotation for the first generation light-driven molecular motor.

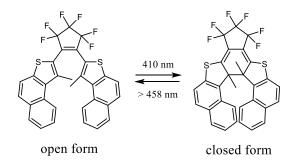
B.5 Introduction of helicenes in light-driven chiroptical switches.

Based on the idea of taking advantage of a photochromic unit to tune the chirality of a helicene-based structure, different chiroptical switchable helicene–like molecules have been reported. For example, in 1999, Dinescu and his coworkers reported helically locked 1,2-dithienylethenes (Scheme 2.12).⁴³ The open forms of switches were built on the rigid frame of dodecahydrophenanthrene. The overlapping of substituents and multi-ring locked structure endows the molecules with helicity. In the closed form, the molecular rigidity increases which provides a stabilization effect to the molecules after cyclization. The switching process included ring-closing and ring-opening which were triggered by wavelengths corresponding to the absorption bands of open ($\lambda = 310$ nm) and closed isomers ($\lambda > 450$ nm). Though the authors did not study the chiroptical properties of switching molecules, they achieved the reversibility of switches by checking the color changes upon different UV irradiation. The photochromic behavior of switches was monitored in an amorphous polymeric film. The cycle fatigue properties were also checked, and more than 10 cycles could be achieved in a degassed benzene solution.



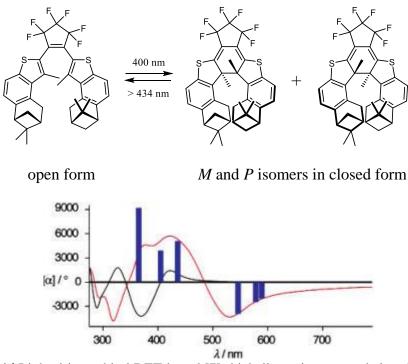
Scheme 2.12 Helical 1,2-dithienylethenes in open and closed forms.

In 2001, Neil R. Branda's group reported the dithienylethene (DTE) photochromo-fused helicene derivatives (**Scheme 2.13**).⁴⁴ These helical structures have open and closed states which can be converted by alternate irradiation with appropriate wavelength lights. Irradiated at 410 nm, switches were transferred to the closed state. However, the closed form helicenes are racemic. When tuning the light at a wavelength greater than 458 nm, the switches were transferred to the open state rapidly. The UV-vis spectra revealed the dramatic difference between open and closed forms. The authors resolved the crystal structures of open and closed forms of DET-based helicenes.



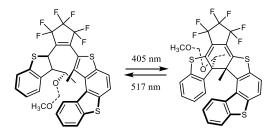
Scheme 2.13 DET-based [7]-thiahelicene in open and closed forms.

In 2005, Branda's group developed a family of chiral photochromic helicenes (**Scheme 2.14**).⁴⁵ They introduced bulky chiral pinene groups at the both terminal sides of molecules, which led to the ring-closing process from one side rather than from the other one, and resulted in one diastereoisomer rather than the other one. Under irradiation of light at 400 nm, a photostationary state was obtained with 40% of a single ring closed *M* isomer, which was proven by NMR spectra and Chiral HPLC. Due to the good selectivity during the ring-closing process and the large difference in how isomers interact with planar polarized light, ORD and CD were applied to monitor the switchable process. In ORD spectra, the strongest difference between photostationary state and ring-open form was at 373 nm ($\Delta[\alpha] = 8698 \text{ }^{\circ}\text{mL} \cdot \text{g}^{-1} \cdot \text{dm}^{-1}$).

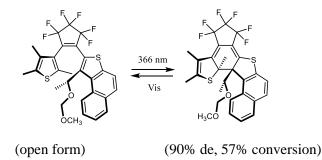


Scheme 2.14 Light-driven chiral DET-based [7]-thiahelicene in open and closed forms (up); ORD spectra of ring-open (black line) form and PPS (red line). Reproduced from ref.⁴⁵

In 2007, Yokoyama's group reported a family of dithienylethene (DTE) fused [5] and [7]thiahelicenes (**Scheme 2.15**).⁴⁶⁻⁴⁷ The authors introduced an asymmetric carbon into the switches as a stereogenic center, which led to a photoirradiation diastereoselectivity. In these two cases, the optical rotations between open form and photostationary state showed large differences. In addition, by analyzing the diastereoselectivity of ring-closing process, they found that there was a balance between stronger steric/electronic repulsion and 1,3-allylic strains.

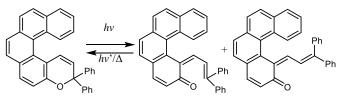


 $[\alpha]_{D} = 9^{\circ}$ (open form) $[\alpha]_{D} = -1370^{\circ}$ (photostationary state)



Scheme. 2.15 Chiral helicenoid diarylethenes developed by Yokoyama.

Some other chiroptical switchable helicene-like molecules without DTE were also reported. Moorthy group developed novel helical pyrones and chromenes (**Scheme 2.16**).⁴⁸ Under irradiation of the closed form, the o-quinonoid intermediates were generated, which led to the color and UV-vis absorption change. Later on, they reported a [6]helicene derivative, which was applied to optical data storage.⁴⁹



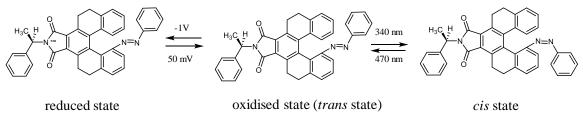
closed form

cis and trans open form

Scheme 2.16 Chromene-based helicene in closed and open forms.

Wang's group reported the dual modulation of helicene derivatives. An azobenzene and an imide group were introduced into the system, which were respectively responsive to light and electron (**Scheme 2.17**).⁵⁰ During the photomodulation process, the optical rotation changed dramatically between two photostationary states. In the electrochemical modulation process, the imide group was triggered by a redox reaction and large optical

signals were observed at 454 nm. The authors also checked the photoswitchable process in the solid state by fabricating a thin film.



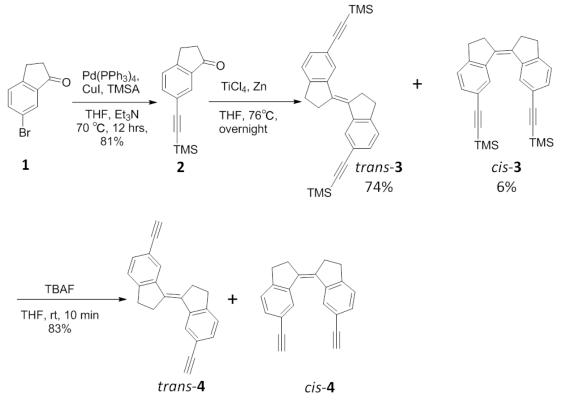
Scheme 2.17 Dual modulation of helicene-based switches.

B.6 Results and discussion

B.6.1 Synthesis and characterization of switches based on helicenes

In a first stage, the precursors *trans*- and *cis*-3 and *trans*- and *cis*-4 were prepared as described in Scheme 2.18. First, a Sonogashira coupling between commercially available 6-bromoindanone **1** and trimethylsilylacetylene (TMSA) yielded compound 6trimethylsilylethynyl-2,3-dihydro-1*H*-inden-1-one 2 with 81% yield, which was then subject to a McMurry coupling using titanium chloride and zinc in refluxing THF⁵¹ giving geometric isomers (*E*)- and (*Z*)-6,6'-bis-trimethylsilylethynyl-2,2',3,3'-tetrahydro-1,1'-bisindenylidene (trans-3 and cis-3 74:6, respectively from NMR) with 80% overall yield (Scheme 2.18). Separation through column chromatography enabled to obtain the main product *trans*-3 in chemically pure form while *cis*-3 was obtained as a 60:40 mixture with trans-3. Pure trans-3 was then transformed into (E)-6,6'-diethynyl-2,2',3,3'-tetrahydro-1,1'bis-indenylidene (*trans*-4) by a deprotection reaction with tetrabutylammonium fluoride (TBAF). Did the deprotection of *cis*-3 and *trans*-3 mixture, we could obtain mixture of *cis*-4 and *trans*-4 with a ratio of 60:40, which were difficult to be separated. Compounds *trans*-3 and *trans*-4 were fully characterized by NMR, mass spectrometry and X-ray crystallography (Figure 2.2). Indeed, single crystals of *trans*-3 and *trans*-4 were grown by slow diffusion of pentane vapors into CH₂Cl₂ solutions. Compound *trans*-3 is fully planar and shows a C-C=C-C dihedral angle of 1°; it displays a regular C=C double bond (C-C bond length 1.349 Å).⁵² In addition, it organizes in the solid state into dimers with CH- π interactions taking place between one CH₂ of a cyclopentene ring and the phenyl group of the neighboring molecule (CH-centroïd distance: 2.803 Å); these dimers then stack into columns along the y axis (see Figure 1b). Similarly, trans-4 is fully planar (C-C=C-C

dihedral angle of ~3.5°) and forms columnar stacks along the *z* axis through CH- π interactions (CH-centroïd distance: 2.872 Å).



Scheme 2.18 Synthesis of *cis* and *trans* compounds 3,4. *i*) Trimethylsilyl-acetylene, Pd(PPh₃)₄, CuI, THF, Et₃N, reflux, 12 hrs, 81%; *ii*) TiCl₄, Zn, THF, reflux, overnight, 80%; *iii*) TBAF, THF, rt,10 min, 83%.

The bis-alkynyl derivative *trans*-4 was then reacted with 2-bromo-pyridine **5a**, through a Sonigashira coupling under regular conditions (**Scheme 2.19**) thus giving access to (*E*)-6,6'-bis[(2-pyridyl)-ethynyl]-2,2',3,3'-tetrahydro-1,1'-bis-indenylidene *trans*-**6a** with 75% yield. Under similar conditions, the reaction starting from mixture of *trans*-**4** and *cis*-**4** yielded *trans*-**6a** and *cis*-**6a** with 10% and 23% yield, respectively. Compounds *trans*-**6a** and *cis*-**6a** were fully characterized by NMR and mass spectrometry. Their ¹H NMR spectrum display different signatures highlighting their different stereochemistry, especially regarding the dihydrocyclopentene protons H¹, H² that resonate at different chemical shifts (*trans*-**6a**: 3.2 ppm; *cis*-**6a**: 2.8 and 3.1 ppm, see **Figure 2.3**). Indeed, according to the literature,^{30, 33} when the product has a *trans* configuration, the protons H^{1,2} of the dihydrocyclopentene ring resonate as a broad signal in the range from 2.8 ppm to 3.4 ppm, while in the *cis* configuration, H^{1,2}

signals. Single crystals of *trans*-**6a** were grown by slow diffusion of pentane vapors into a CH₂Cl₂ solution. The X-ray diffraction study of the *trans*-**6a** olefine shows that it is fully planar (C-C=C-C dihedral angles 0.3°), and that it organizes in the solid state into columnar stacks along the z axis through π - π stacking between neighboring pyridyl and phenyl groups (centroïd-centroïd distance 3.763 Å).

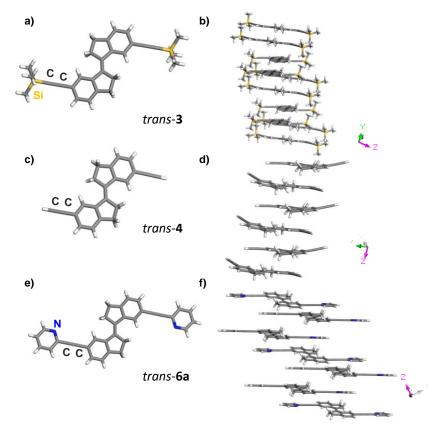
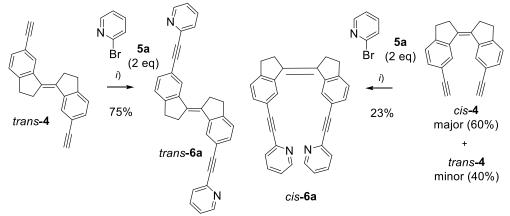


Figure 2.2 X-ray structures (a,c,e) and supramolecular organizations (b,d,f) of compounds *trans*-3,4,6a.



Scheme 2.19 Synthesis of *cis*- and *trans*-6a from respectively *cis*- and *trans*-4. *i*) Pd(PPh₃)₄, CuI, THF, Et₃N, rt, Ar, 2 hrs, dark.

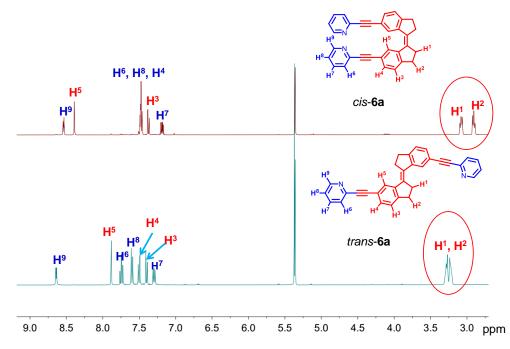
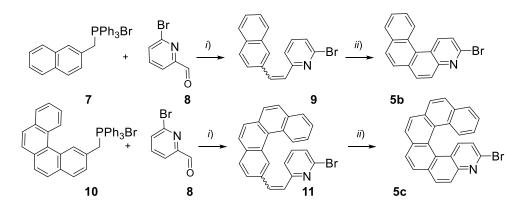


Figure 2.3 ¹H NMR (CD₂Cl₂, 400 MHz) spectra of the *trans*-6a and *cis*-6a at 298 K.

The synthesis of stilbenic derivative **6b** bearing two aza[4]helicene units was then examined. First, 3-bromo-4-aza[4]helicene **5b** was prepared in two steps according to **Scheme 2.20**, *i.e.* by a Wittig reaction between 2-methyl-naphthalene-phosphonium bromide **7** and 2-bromo-pyridine-6-carboxaldehyde **8**, yielding olefin **9** as a mixture of *cis* and *trans* isomers, followed by a photocyclization reaction with a 150 W mercury lamp (with 1 eq. of iodine and an excess of propylene oxide in toluene for one night) (19 % overall yield). Then the *trans*-**4** precursor was reacted with 2 equivalents of 3-bromo-4-aza[4]helicene **5b** under classical Sonogashira coupling conditions (**Scheme 2.21**) with 65 % yield. Surprisingly, the *cis*-**6b** compound was obtained instead of the expected *trans*-**6b** isomer. Indeed, the *cis* stereochemistry was clearly identified by NMR spectroscopy, both by ¹H and ROESY NMR. For example, the ¹H NMR spectrum displayed the two typical separated signals at 2.9 and 3.1 ppm for H¹ and H² protons. Furthermore, while correlation peaks were found between H² and H³ in the ROESY spectrum (**Figure 1.4**), no correlation was observed between H¹ and H⁵ as is usually observed in similar *trans* olefins.²¹ The real reason for this process is still unknown.



Scheme 2.20 1. *i*) n-BuLi, THF, rt, Ar, 5 hrs, 70-86% ; *ii*) hv, I₂ (1 eq.), propylene oxide (2 eq) toluene, rt, Ar, 14 hrs, 51-62%.

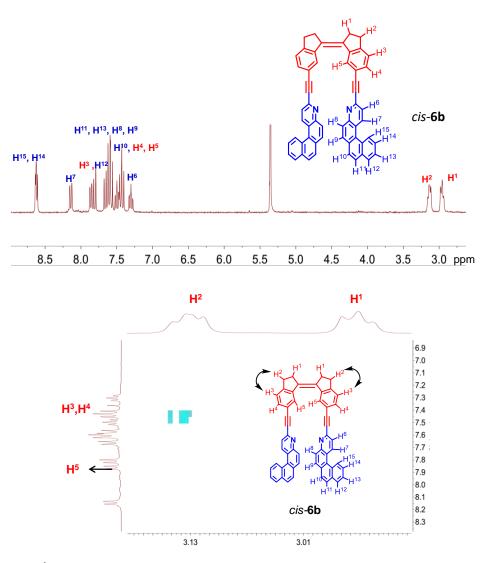
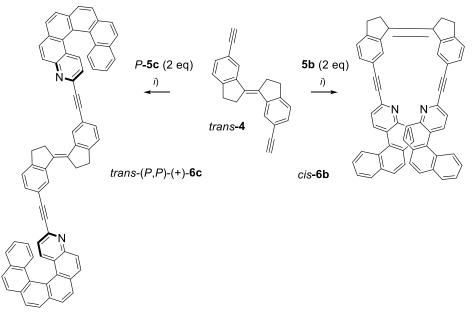


Figure 2.4 a) ¹H NMR spectrum (CD₂Cl₂, 400 MHz, 298 K) and b) part of the ROESY spectrum of the *cis*-**6b** stereoisomer.



Scheme 2.21 *i*) Pd(PPh₃)₄, CuI, THF, Et₃N, rt, Ar, 2 hrs, dark, 60-65 %.

The stilbenic system *trans*-6c containing two aza[6]helicene units was prepared using a similar strategy as for the bis-aza[4]helicene derivative **6b**, *i.e.* by reacting the precursor *trans*-4 with two equivalents of 3-bromo-4-aza[6]helicene (enantiopure P- or M-5c) through a Sonogashira coupling (performed in the dark). The helicene rac-5c was obtained in two steps from 2-methyl-benzo[c]phenanthrene phosphonium bromide following the same sequence as for **2b** (see Scheme 2.20). Enantiopure *P*- or *M*-5c were then obtained through HPLC resolution over a chiral stationary phase (see Experiment Part). Contrary to **5b** and certainly due to high steric hindrance, derivatives (P,P)- and (M,M)-**6c** were obtained as the pure *trans* stereoisomers, as illustrated by their ¹H NMR spectrum which display the H^{1,2} system as a broad characteristic signal around 3.2 ppm, and by the NOESY spectrum which this time depicts a correlation peak between H¹ and H⁵ protons in addition to the one for H^2 and H^3 protons (Figure 2.5). Enantiopure *cis* derivatives (*P*,*P*)- and (M,M)-6c were then obtained by a Sonogashira coupling between mixture of cis-4 and *trans*-4 and *P*- or *M*-5c in the dark (Scheme 2.22). We can obtain *trans* and *cis* derivatives at the same time, which can be separated by chromatographic column. Similar to *trans*-6a and cis-6a, the characteristic ¹H NMR peaks of the CH₂ of a cyclopentene ring in trans-(M, M)-6c and cis-(M, M)-6c appear at different regions (Figure 2.6). For trans-(M, M)-**6c**, the peaks are overlapped at 3.1 ppm, while for *cis*-(*M*, *M*)-**6c**, the peaks were separated in the region ranged from 2.8 to 3.1 ppm, which can allow us to distinguish them from ${}^{1}\text{H}$ NMR spectra and be regarded as typical changes for isomerization. The *trans-(P, P)-6c* and *cis-(P, P)-6c* show the same change. Furthermore, the spectra display the typical signal for the azahelicenic part, such as for instance the ddd (doublet of doublet of doublet) or unresolved triplet at 6.5 and 7.1 ppm for the protons H^{17} and H^{18} in the *cis* stereoisomer (see **Figure 2.6**).

a)

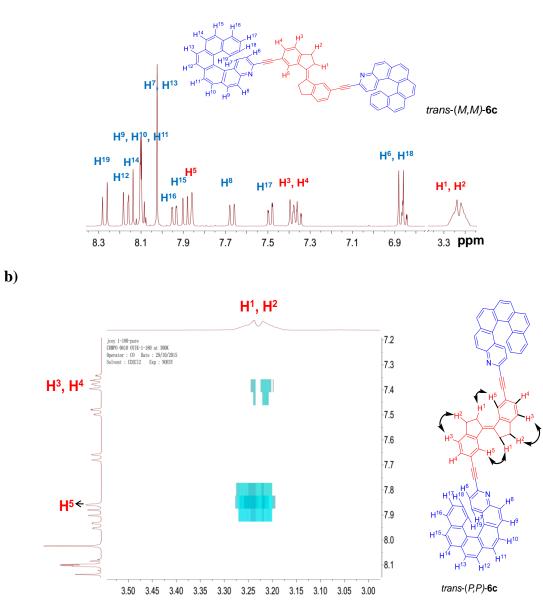
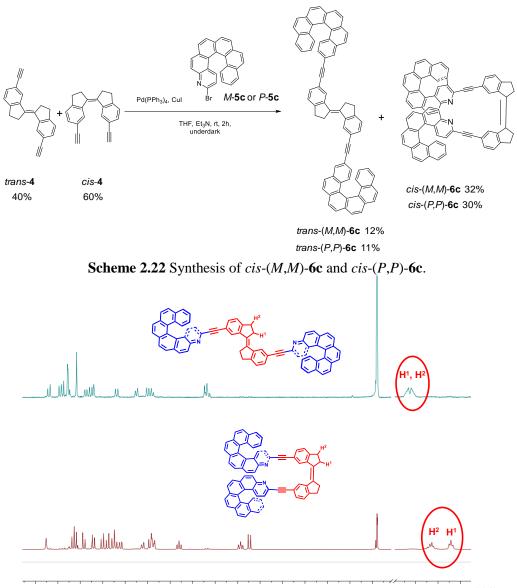


Figure 2.5 a) ¹H NMR spectrum and b) part of the ROESY spectrum of *trans-(M,M)*-6c stereoisomer (CD₂Cl₂, 400 MHz, 298 K).



8.4 8.2 8.0 7.8 7.6 7.4 7.2 7.0 6.8 6.6 6.4 6.2 6.0 5.8 5.6 5.4 3.2 3.0 2.8 **ppm**

Figure 2.6 ¹H NMR (CD₂Cl₂, 400 MHz) spectra of the *trans-(M, M)*-6c and *cis-(M, M)*-6c at 298 K.

B.6.2 Photochemical isomerization process of *trans*- and *cis*-6a.

The photochemical isomerization process of stilbenic system *trans*- and *cis*-**6a** was examined by ¹H NMR and UV-vis spectroscopy. Since stiff stilbene unit can undergo oxidative electrocyclization with oxygen, the photoisomerization process was performed in degassed diluted solutions. Besides, the intermolecular cycloaddition would occur at high concentration (see **Scheme 2.4**).⁵² After testing several kinds of wavelengthes, we found that, the *trans*-**6a** and *cis*-**6a** were responded to 365 nm and 420 nm wavelength light, respectively. A degassed dichloromethane- d_2 solution of *trans*-**6a** was irradiated with a 365

nm-wavelength light using the TLC analysis lamp in an NMR tube at room temperature. The whole process was monitored by ¹H NMR spectroscopy. We determined the ratio of *trans-* and *cis-*isomers by the integral intensities of proton signals of the five-membered ring in the stiff stilbene unit (*trans*, 3.2 ppm; *cis*, 3.1 ppm and 2.8 ppm). From the ¹H NMR spectra (**Figure 2.7**), it is seen that the *cis:trans* ratio increased with increasing of irradiation time. After 90 min, it reached the photostationary state with *cis:trans* ratio of 57:43.

The reverse process was also examined by ¹H NMR spectra. Indeed, after reaching the photostationary state, the wavelength was changed to 419 nm and the NMR tube was irradiated for 35 min. The ¹H NMR spectrum (**Figure 1.8**) showed that the *cis:trans* ratio slightly decreased with irradiation time and reached 34:66. From the ¹H NMR spectra, we did not observe the signals of degradation products, which indicated clean photoisomerization. Note that since the *cis*-**6a** isomer was obtained in small quantities, the isomerization of pure *cis*-**6a** was not examined by NMR.

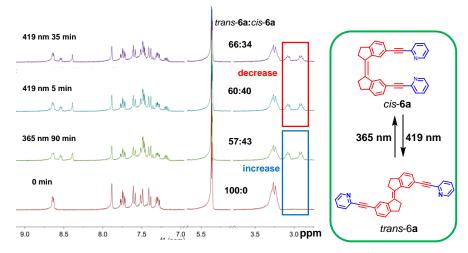


Figure 2.7 Reversibility of the switching activity observed by ¹H NMR spectra (CD₂Cl₂, 300 MHz, 298 K).

The isomerization process of *trans* and *cis*-**6a** were also studied by UV-vis spectroscopy in degassed dichloromethane solutions at 1.4-1.5 10^{-6} M concentrations (**Figure 2.8**). Under irradiation with a 365 nm-wavelength light, *trans*-**6a** underwent efficient *trans/cis* isomerization as seen by the change in the absorbance. After 60 minutes, it reached the photostationary state (*trans*-**6a**:*cis*-**6a** = 49:51 in the UV-vis conditions). From the UV-vis spectra in **Figure 2.8**, the major signals of *trans*-**6a** at 310 nm, 340 nm and 360 nm steadily decreased, whereas the signal at 380 nm increased gradually. Clear isosbestic points were observed which meant that the *trans/cis* isomerization was a unimolecular reaction. The photoisomerization of *cis*-**6a** was likewise investigated. From the UV-vis spectra, the opposite changes to *trans*-**6a** were observed. The signal at 310 nm, 340 nm and 360 nm increased gradually under irradiation with 420 nm-wavelength light. However, the signal at 380 nm decreased. Note that a *trans*-**6a**:*cis*-**6a** = 90:10 photostationary state was reached after 30 min under the UV-vis conditions, and that isosbestic point was observed at about 370 nm revealing that clean photoisomerization had occurred. We also studied the reversibility of *trans*-**6a** (**Figure 2.9**). Firstly, we used 365 nm wavelength light to irradiate *trans*-**6a** and made it to arrive at the *trans*-**6a**:*cis*-**6a** = 49:51 photostationary state. Then, we changed the wavelength to 420 nm, and irradiated the solution again. The UV-vis spectra displayed reversible isomerization process to a *trans*-**6a**:*cis*-**6a** = 51:49 mixture.

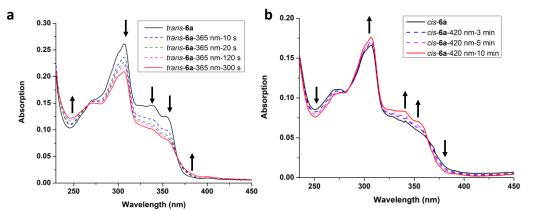


Figure 2.8 Photoisomerization process of a) pure *trans*-**6a** to *cis*-**6a** (irradiation with 365 nm wavelength light) and b) pure *cis*-**6a** to *trans*-**6a** (irradiation with 420 nm wavelength light) monitored by UV-vis spectroscopy in degassed CH₂Cl₂ solution.

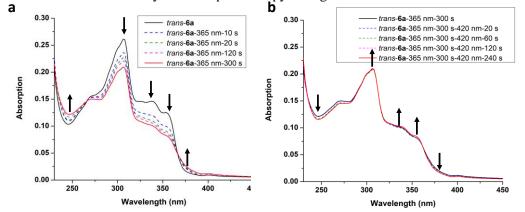


Figure 2.9 Reversibility of the switching activity of *trans*-**6a** observed by UV-vis spectra in degassed CH₂Cl₂ solution. a) UV-vis spectra of isomerization process under irradiation with 365 nm wavelength light; b) UV-vis spectra of reversible process under irradiation with 420 nm wavelength light.

B.6.3 Chiroptical properties of *trans-(P, P)-6c*, *cis-(P, P)-6c*, *trans-(M, M)-6c* and *cis-(M, M)-6c*.

The helicene units were grafted onto the switching stiff stilbene system, and the helicenes were chiral and showed huge optical rotations and strong circular dichroism. So the switches were also endowed with chiroptical properties. To obtain information on the relationship between the stereochemical structure and the chiroptical properties of *trans*and cis-6c isomers, CD spectra were studied in degassed dichloromethane (Figure 2.10). The CD spectra of trans-(P, P)-6c, trans-(M, M)-6c, cis-(P, P)-6c, cis-(M, M)-6c show almost complete mirror images and revealed the classical bisignate Cotton effect at 240 nm and 340 nm. For *trans-(P, P)-6c* and *cis-(P, P)-6c*, they both show negative bands at 240 nm followed by a positive band at 340 nm. This negative and followed by positive bisignate shape can be attributed to the typical helicene ${}^{1}B_{a}$ band (high energy) and ${}^{1}B_{b}$ bad (low energy),⁵³ which helps us to determine the absolute configuration of P and M-enantiomers of helicenes. The intensities of band for trans-(P, P)-6c, trans-(M, M)-6c, cis-(P, P)-6c and cis-(M, M)-6c enantiomers are almost twice stronger than P-3-bromo-4-aza-[6] helicene and M-3-bromo-4-aza-[6]helicene enantiomers, because each switch molecule contained two [6]helicene units. The specific rotations have also been measured and are summarized in Table 2.2.

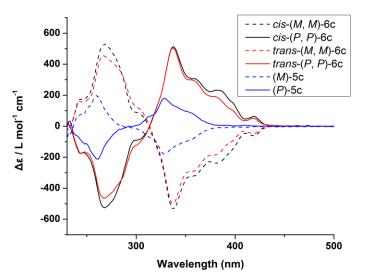
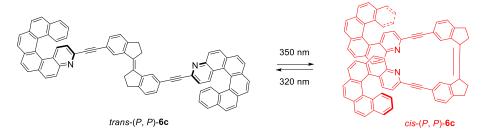


Figure 2.10 Circular dichroism spectra of *cis*-(*M*, *M*)-**6c** (black dash), *cis*-(*P*, *P*)-**6c** (black); *trans*-(*M*, *M*)-**6c** (red dash); *trans*-(*P*, *P*)-**6c** (red); *M*-3-bromo-4-aza[6]helicene (blue dash) and *P*-3-bromo-4-aza[6]helicene (blue).

Table 2.2. Specific rotation of enantiopure compounds **5c** and **6c** (CH₂Cl₂, $C \sim 5$. 10⁻⁵ M).

	(<i>M</i>)-5c	(P)- 5c	cis-(M,M)- 6c	cis-(P,P)- 6c	<i>trans-(M,M)-</i> 6c	trans-(P,P)- 6c
$[\alpha]_D^{23}$ (° dm ⁻¹ cm ³ g ⁻¹)	-7969	+7960	-4312	+4333	-4791	+4875

B.6.4 Photoisomerization process of trans-(P, P)-6c, cis-(P, P)-6c, trans-(M, M)-6c and cis-(M, M)-6c.



Scheme 2.23 Schematic representation of photoisomerization process.

The isomerization of the enantiopure bis-aza[6]helicenic systems was also checked by UV-vis and CD spectroscopy. The isomerization process triggered by photoirradiation was studied in degassed dichloromethane at 20 °C (**Scheme 2.23**). For example, the irradiation of *trans-(M, M)*-**6c** at 350 nm gave selective isomerization. The intensities of absorption of UV-vis spectra decreased continuously at 333 nm, 360 nm, 380 nm and 420 nm until a photostationary state was achieved after 60 min. Although the changes are modest compared to the strong intrinsic absorption of the helicenic systems, a clear isosbestic point was observed at 285 nm, which revealed that the isomerization from *trans-(M, M)*-**6c** to *cis-(M, M)*-**6c** was a unimoleular process. When irradiation of the *cis-(M, M)*-**6c** with 320 nm-wavelength light at 20 °C for 30 minutes, the opposite changes were observed. The UV-vis spectra of isomerization process of *cis-(M, M)*-**6c** and *trans-(M, M)*-**6c** were also studied (**Figure 2.11**).

Note that since the [4]helicenic compound **6b** had his conformation blocked in *cis*, after irradiation with 365 nm and other wavelength light, some precipitate appeared. It seemed impossible to perform the switching process.

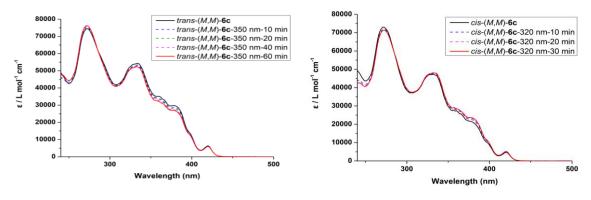


Figure 2.11 Left) UV-vis spectral changes of *trans-(M,M)*-**6c** in degassed dichloromethane upon 350 nm irradiation for 60 min; right) UV-vis spectral changes of *cis-(M,M)*-**6c** in degassed dichloromethane upon 320 nm irradiation for 30 min.

We also checked the CD spectra of solutions of switches before and after irradiation (**Figure 2.12**) From the CD spectra, for cis(M,M)-6c and cis(P,P)-6c, we can find that the intensities of band at 267 nm, 337 nm, 360 nm, 385 nm and 420 nm increased, while at 320 nm, the intensities increased slightly. An isosbestic point at 285 nm was observed. For *trans*-(*M*,*M*)-6c and *trans*-(*P*,*P*)-6c, the opposite changes were observed. These spectral changes show that, in addition to conformation changes, marked CD signal changes and observed which is interesting for applications as stimuli-responsive materials. Note however that the switching process would deserve to be improved. For example, we should add electron-donating groups such as methyls on the cyclopentene ring in order to improve the *trans* to *cis* interconversion.

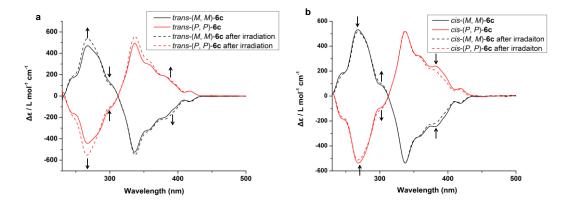


Figure 2.12 Circular dichroism (CD) spectra of a) *trans-(M, M)-6c* (black) and *trans-(P, P)-6c* (red) before (solid line) and after (dash line) irradiation at 350 nm and b) *cis-(M,M)-6c* (black) and *cis-(P,P)-6c* (red) before (solid line) and after (dash line) irradiation at 320 nm in degassed CH_2Cl_2 .

B.7 Coordination tests

Due to the existence of nitrogen atoms in the molecular switches, they can potentially coordinate to metal ions or protons. We thus tried to silver(I) or zinc(II) ions to model systems *cis-* and *trans-* **6a**, but the results appeared unsatisfactory. Indeed, when we added silver(I) ion into the solution of molecular switches **6a**, we found that some precipitates appeared and the signal of ¹H NMR spectra disappeared, probably leading to polymeric species, that were difficult to analyze. For zinc(II) ions, we found that there were no changes after addition, suggesting that the coordination to this type of bis(alkynyl-pyridyl) system is not efficient for coordination. Finally, we tried to use acid to protonate the nitrogen atoms. Fortunately, we found that we can tune the UV-vis absorption and emission properties of molecular switches by adding acid and base.

We chose 18-crown-6•HBF₄•H₂O acid⁵⁴ as the proton source, and sodium carbonate as the base. The protonation and deprotonation processes were monitored by UV-vis and fluorescence spectra (**Figure 2.13**). For *cis* and *trans* switches **6c** with [6]helicenic fragments, when adding excess of 18-crown-6•HBF₄•H₂O in dichloromethane (DCM) solution, the absorption band at 325 nm decreased, while the band at 380 nm increased, and a new broad absorption band appeared at 475 nm. The fluorescence of them were quenched after adding acid. Then adding sodium carbonate solid, we found that that UV-vis and fluorescence spectra were recovered. For *trans*-**6a**, we found that after adding acid, the band at 300 nm decreased, while the signal at 350 nm increased, and a new broad absorption band appeared at 400 nm. After adding sodium base, the UV-vis and fluorescence spectra recovered.

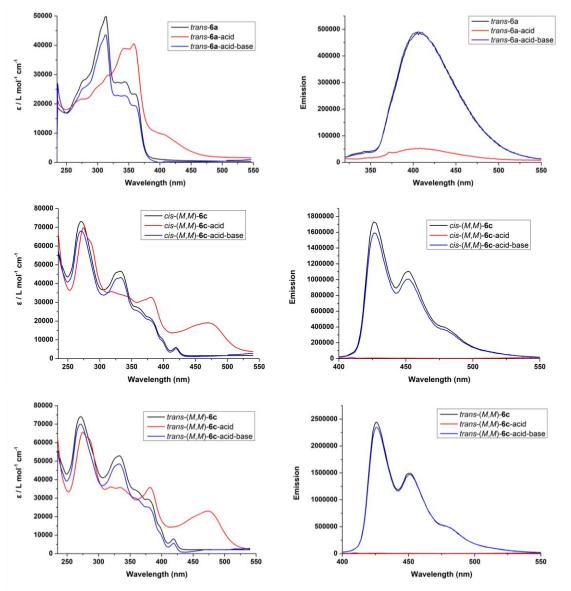


Figure 2.13 Left: reversibility of UV-vis spectra of *trans*-**6a**, *cis*-(*M*,*M*)-**6c** and *trans*-(*M*,*M*)-**6c**, right: reversibility of fluorescence spectra of *trans*-**6a**, *cis*-(*M*,*M*)-**6c** and *trans*-(*M*,*M*)-**6c** before adding acid (18-crown-6•HBF₄•H₂O)---black line; after adding acid (18-crown-6•HBF₄•H₂O)---red line; after adding base (sodium carbonate)---blue line.

Herein, we can tune UV-vis and emission properties of switches by adding acid and base. And the protonation and deprotonation process are reversible.

B.8 Conclusion

We have synthesized a series of novel photoresponsive chiral switches based on helicenes. They were characterized by multinuclear NMR spectroscopies, mass spectra, CD spectra and X-ray crystallography. The studies of their switching properties by ¹H NMR spectra, UV-vis spectra, and CD spectroscopies showed that they could be achieve

photochemical isomerization with good reversibility. Moreover, we could tune the chiroptical response of switches by changing the wavelength of light. We tested the coordination process of molecular switches, and found that 8-crown-6-HBF₄·H₂O acid and sodium carbonate base can tune the UV-vis absorption and fluorescence properties. In addition, the protonation and deprotonation process were reversible. The next and final step will be to study the influence of the protonation on the photochemical *trans-cis* process since we expect that the change in the electron richness of the system will have a strong impact. It is indeed what we have observed in the gold complex systems described below.

C Stiff stilbenes substituted with alkynyl-gold units

C.1 Generalities on gold(I) complexes

The symbol of gold (Au) derives from the Latin word *aurum*, which relates to Aurora, the goddess of drawn. The electronic configuration of gold (0) is $5d^{10}6s^1$, while for gold (I), it is $5d^{10}6s^0$ (closed-shell). Gold has some special characteristics, such as mechanical softness, high electrical conductivity, high thermal and chemical stability, and beautiful color, which makes it unique and widely applied.² Gold(I) complexes are among the most important part of gold chemistry. During the last two decades, gold(I) alkynyl complexes have attracted the chemists' interest for their rich luminescence properties. Gold(I) prefers a linear coordination. Besides, the linearity and π -unsaturation of the acetylide group can make the alkynylgold(I) complexes form metallic oligometric and polymetric materials (vide infra), which may display electrical conductivity, optical non-linearity, and liquid crystallinity properties. Luminescence is one of the most explored properties of alkynylgold(I) complexes. Che firstly reported the luminescence of alkynylgold(I) complexes in 1993.⁵⁵ Then, his group and Yam's group did extensive studies.⁵⁶⁻⁵⁸ Usually, there are two different emissive bands in the range between 400 to 600 nm, which are triplet emissions and displaying large Stokes shifts (250 - 350 nm).³ The introduction of gold(I) moiety leads to heavy-atom effect and improves the possibility of triplet emission at room temperature. Alkynyl-gold(I) complexes can be classified into four types: alkynyl-gold(I)phosphane complexes, alkynyl-gold(I)-isocyanide complexes, bis(alkynyl)-gold(I) complexes, and alkynyl-gold(I)-carbene complexes. They can be distinguished by the

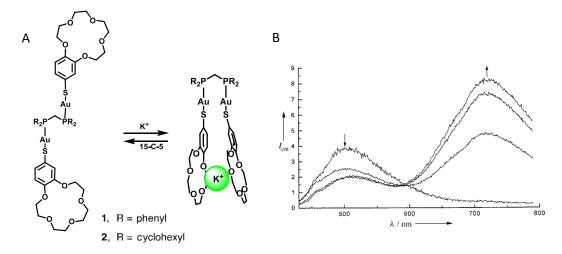
nature of the second ligand coordinated to gold center.³ Several reviews have been published, which are related to their interesting luminescence.⁵⁹⁻⁶¹

C.2 The gold-gold interaction and its applications in materials science

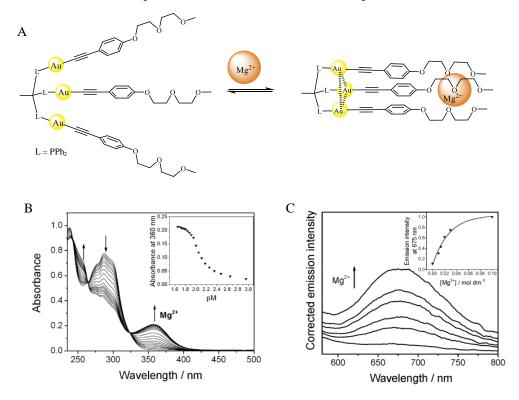
Gold is a heavy transition metal complex of group 11 and it displays relativistic effects that induce peculiar behavior such as gold-gold interaction. The Au-Au interaction was firstly named as aurophilic attraction by Schmidbaur in 1990. He defined it as "*the unprecedented affinity between gold atoms even with closed-shell electronic configurations and equivalent electrical charges*".^{59, 62} After that, it became a hot topic in gold chemistry. Gold-gold interactions are frequently observed in gold(I) complexes. Usually, in these cases, the distance between gold centers is in the range between 2.7 and 3.3 Å. This kind of attraction can modify molecular geometries or make molecules to form 1-Dimension, 2-Dimension, or 3-Dimension arrays, which usually results in some interesting properties, including optical behavior. The luminescence of coordination complexes may have several different origins, such as metal-to-ligand charge transfer transitions (ILT), ligand-to-metal charge transfers (LLCT) and metal centered transitions (MCT). However, in some cases, the emissive properties of gold complexes are related to gold-gold interactions.

In 1998, Yam's group reported a luminescent ion probe for potassium ion by switching on and off the gold-gold interactions (**Scheme 2.24**).⁶³ The molecules not only served as probe of potassium ion, but also as a molecular optoelectronic switch. In addition, the emission spectra provided proof for potassium ion induced gold-gold interaction. After that, her group developed several other systems to study gold-gold interactions.⁶⁴⁻⁶⁷

For example, in 2009, Yam's group developed a trinuclear alkynylgold(I) complex with three oligoether pendants, which selectively binds toward Mg²⁺ ion (**Scheme 2.25**).⁶⁵ The authors used UV-vis and emissive spectra to monitor the switching on/off process of gold-gold interaction, which depended upon the binding of Mg²⁺.

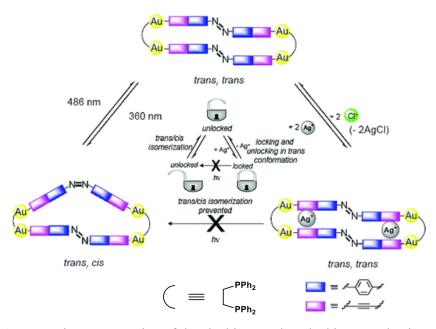


Scheme 2.24 A) Scheme of switchable process; B) Emission spectra upon addition of various concentrations of potassium ions in CH₂Cl₂/MeOH. Reproduced from ref.⁶³



Scheme 2.25 A) Proposed binding mode with Mg^{2+} ; B) UV-vis spectra of gold complex upon addition of Mg^{2+} cations; C) emission spectra of gold complex upon addition of Mg^{2+} cations. Reproduced from ref.⁶⁵

Some optical switches and logic gates based on gold(I) complexes were also reported. In 2007, Yam's group developed optical switches containing alkynylgold(I) moieties and azobenzene units (**Scheme 2.26**).⁶⁸ Under irradiation at 360 nm and 486 nm, the macrocycles can achieve the photoisomerization between *trans* and *cis* forms. When the alkynyl units coordinate to silver(I) centers, the isomerization process is inhibited. When the silver(I) ions are removed by AgCl precipitation, the isomerization process is recovered, which can be regarded as a dual-input lockable logic photoswitch. But in this part of work, the authors did not find the proof of gold-gold interaction.



Scheme 2.26 Schematic representation of the "locking" and "unlocking" mechanism. Reproduced from ref.⁶⁸

Gold-gold interaction has also been studied in our group. In 2016, our group developed a new kind of gold complexes based on helicenes (**Figure 2.14**). The authors prepared monometallic gold(I) complexes and bimetallic gold(I) complexes bearing phosphole ligands, including "U" form and "Z" form, which can enable and prevent aurophilic interaction, respectively.⁶⁹ The introduction of the gold(I) metal center influences the photophysical, electronic, and chiroptical properties of these gold(I) complexes. Through experimental and theoretical studies, they found that the ligand-to-ligand type charge transfers (LLCT) and the presence or absence of gold-gold interaction played important roles on the properties of these gold complexes. Indeed, the chiroptical properties (CD and OR) of the enantiopure bis-carbo[6]helicene scaffolds were examined in details and it was found that two helicenes were placed in the structure, that is in the case of **VIIIb** displaying no Au-Au interaction, the higher the chiroptical response was observed.

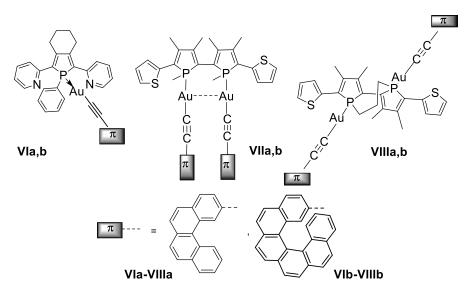


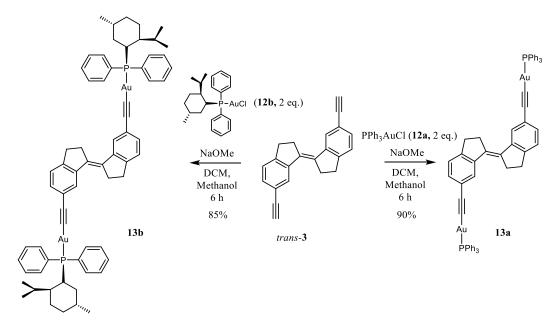
Figure 2.14 Mono-gold(I) complexes (**VIa,b**) and bimetallic "U" form gold(I) complexes (**VIIa,b**) and bimetallic "Z" form gold(I) complexes (**VIIIa,b**), bearing phosphole and helicene-alkynyl ligands.

As explained in **Scheme 1.2**, we wanted to explore if a photoswitchable stiff stilbene type derivative is able to establish Au(I)-Au(I) interaction in the *cis* form and to modify its photophysical properties (absorption, emission or chiroptical properties).

C.3 Results and discussion

C.3.1 Synthesis and characterization of photoresponsive gold complexes

The alkynyl-gold(I) complexes were prepared as described in **Scheme 2.27**. Dialkynyl *trans-3* reacted with Au(I) complexes **12a-b** with sodium methylate in the mixture solution of dichloromethane and methanol. After 6 h, the compounds **13a-b** were obtained with yield of 90% and 85%, respectively. Compounds **13a** and **13b** were fully characterized by NMR, UV-vis and X-ray crystallography. The precursors **12a** and **12b** were prepared as reported in the literature.⁷⁰⁻⁷¹



Scheme 2.27 Synthesis route of gold complexes of 13a and 13b.

Single crystals of *trans*-13a and *trans*-13b were grown by slow diffusion of pentane vapors into a CH₂Cl₂ solution. The X-ray diffraction studies of the *trans*-13a and *trans*-13b show that they are fully planar (Figure 2.15). Indeed, the C-C=C-C dihedral angles are 3.39° and 0.19°, respectively. For *trans*-13a, it organizes in the solid state into columnar stacks (Figure 2.16) along the z axis through π - π stacking between neighboring pyridyl and phenyl group (centroïd-centroïd distance 3.776 Å), while for *trans*-13b, there is C-H- π interaction between proton on cyclohexane group and phenyl in stiff stilbene unit (distance 2.789 Å). No gold-gold interaction was observed in the supramolecular assemblies. Indeed, in *trans*-13a, the shortest distance between gold metal centers is 8.147 Å. While in *trans*-13b, the shortest distance between gold metal centers is 10.722 Å.

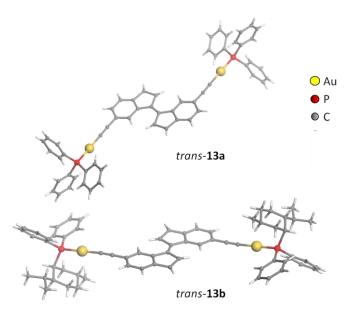


Figure 2.15. X-ray crystallographic structures of complexes *trans* isomers of 13a-b.

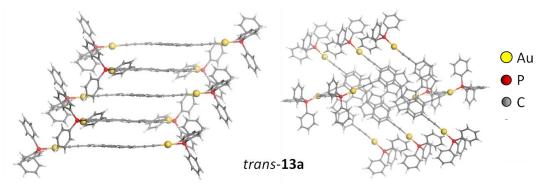


Figure 2.16. Supramolecular organization of *trans*-3a in the solid state.

C.3.2 Isomerization of gold complexes

The isomerization process of gold compound **13a** was first studied by ¹H NMR spectroscopy (**Figure 2.17**). The solution was degassed for 30 minutes and the whole process was conducted under argon atmosphere. Upon irradiation with a 365 nm-wavelength light, the compound **13a** underwent efficient *trans/cis* isomerization. After 15 minutes, it reached the photostationary state with a 40:60 *trans/cis* ratio. Then, we changed the light wavelength to 420 nm and irradiated the NMR tube again. After 20 minutes, it reached the another photostationary state again. The *trans*-**13a**/*cis*-**13a** ratio changed to 62:38 thus showing a reversible process. This process was also monitored by ³¹P NMR spectra (**Figure 2.18**). At the beginning, we could find only one signal at 42.3 ppm. After irradiation with 365 nm wavelength light for 15 minutes, the signal at 42.1 ppm increased gradually. When the wavelength was tuned to 420 nm, after 20 minutes irradiation, the

peak at 42.3 ppm increased again. This result proved that the isomerization process was reversible. Note however that a small signal at 42.2 ppm was also observed suggesting a slight decomposition in the NMR conditions.

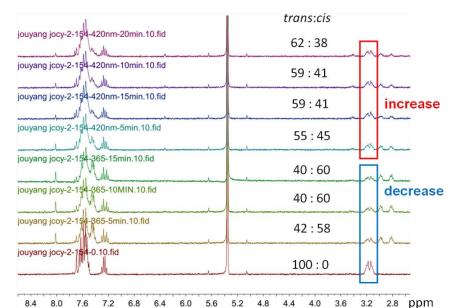
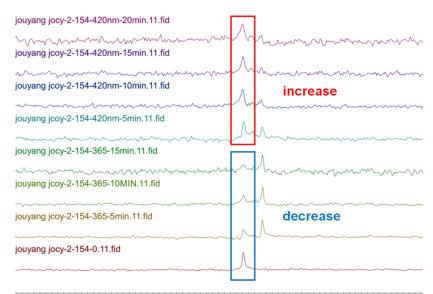


Figure 2.17 ¹H NMR (300 MHz) spectra of isomerization of compound **13a** with 365 nm and 420 nm in degassed CD₂Cl₂.



44.1 43.9 43.7 43.5 43.3 43.1 42.9 42.7 42.5 42.3 42.1 41.9 41.7 41.5 41.3 41.1 40.9 ppm

Figure 2.18 ³¹P NMR (121 MHz) spectra of isomerization of compound **13a** with 365 nm and 420 nm in degassed CD₂Cl₂.

The isomerization process was also checked by UV-vis spectroscopy (**Figure 2.19**). A degassed solution of compound **13a** at a concentration of 1.3×10^{-5} mol/L was prepared.

and the solution was irradiated at 365 nm-wavelength light for 60 seconds. From the UVvis spectra, we found that the intensity of absorption at around 300 and 350 nm decreased, while the band at 375 nm increased. Two isosbestic points around 270 and 370 nm were observed, which means that the isomerization process was unimolecular reaction.

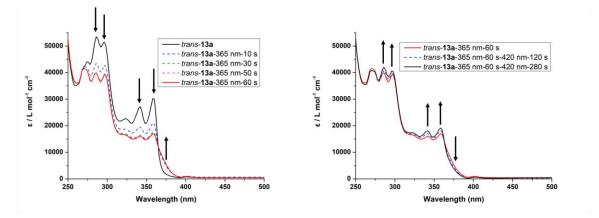
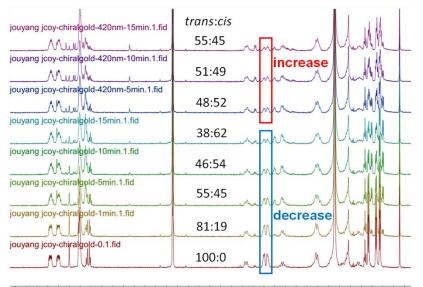


Figure 2.19 UV-vis spectra of isomerization of gold compound 13a with 365 nm and 420 nm in degassed dichloromethane.

The isomerization process of **13b** was also studied by ¹H NMR, ³¹P NMR and UV-vis spectra. Upon irradiation with a 365 nm-wavelength light, the compound **13b** underwent efficient *trans/cis* isomerization (**Figure 2.20**). After 15 minutes, it arrived at a photostationary state with a *trans/cis* ration of 38:62. Then, we changed the wavelength to 420 nm, and irradiated the NMR tube again, after 15 minutes, it reached another photostationary state. The ratio of *trans/cis* increased to 55:45, which proved that the isomerization process was reversible. ³¹P NMR spectra showed a similar trend (**Figure 2.21**). Before irradiation, there was only one signal at 38.1 ppm. After irradiation with 365 nm wavelength light for 15 minutes, the intensity of the peak at 37.9 ppm increased. Then, we tuned the wavelength to 420 nm, after 15 minutes, the peak at 38.1 ppm increased, and the signal at 37.9 ppm decreased, which also revealed that the isomerization process was reversible.

The isomerization process of a degassed dichloromethane solution of **13b** with concentration of 3.7×10^{-6} mol/L was examined by UV-vis spectroscopy (**Figure 2.22**). After irradiation with 365 nm wavelength light for 60 seconds, the band at 280 nm, 290 nm, 340 nm and 360 nm decreased. While the signal at 375 nm increased. And it reached a photostationary state. Subsequently, the light was changed to 420 nm. After irradiation for 330 seconds, it arrived at another photostationary state. And a reversible trend appeared.



9.0 8.5 8.0 7.5 7.0 6.5 6.0 5.5 5.0 4.5 4.0 3.5 3.0 2.5 2.0 1.5 1.0 0.5 0.0 ppm

Figure 2.20 ¹H NMR (300 MHz) spectra of isomerization of compound **13b** with 365 nm and 420 nm in degassed CD₂Cl₂.

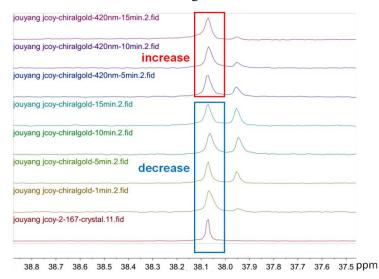


Figure 2.21 ³¹P NMR (300 MHz) spectra of isomerization of compound 13b with 365 nm and 420 nm in degassed CD₂Cl₂.

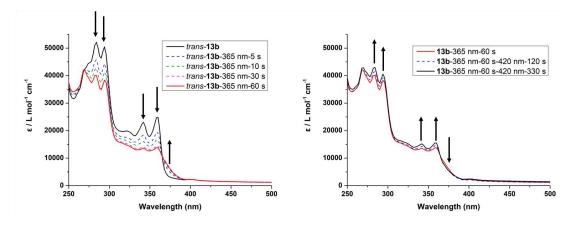


Figure 2.22 UV-vis spectra of isomerization of gold compound 13b with 365 nm (a) and 420 nm (b) in degassed dichloromethane.

The emissive properties of gold compounds *trans*-13a and *trans*-13b were also studied. Excitation of 13a and 13b was observed at 290 nm (Figure 2.23). The maximum emissive bands of gold complexes are both at 396 nm, which is assigned to metal-perturbed intraligand (IL) ${}^{3}[\pi \rightarrow \pi^{*}(C=C)]$ transition with some metal-to-ligand charge transfer (MLCT).^{3, 66, 72-73}

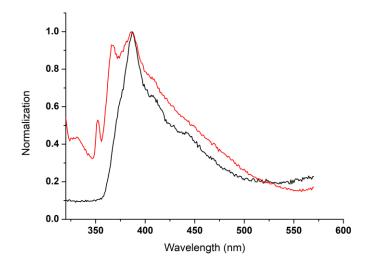


Figure 2.23 Emissive spectra of gold complexes 13a (black line) and 13b (red line).

In order to see if some gold-gold interaction can be established in the *cis* form, the *trans* to *cis* photochemical switching process of **13b** was followed by CD spectroscopy. We also checked the CD spectra of bis-gold(I) derivative **13b**, but no CD response in the UV-vis domain. Maybe the signal was too low to be detected. After irradiation at 365 nm, if there was some aurophilic interaction, a chiral CD response could have been induced thanks to

the chirality of the *cis* form. Unfortunately, for **13a**,**b**, here again, no CD was observed. It is therefore concluded here that in **13a**,**b** no gold-gold interaction can be present probably due to the steric hindrance of the phosphine ligands and the linear geometry around the gold atoms.

C.4 Conclusion

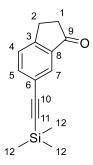
During my thesis, I have prepared photoresponsive gold-alkynyl complexes based on a stiff stilbene structure, which were characterized by multinuclear NMR spectra, UV-vis spectra, CD and fluorescence spectroscopy. Their isomerization process was studied and appeared efficient, highlighting the added value of having a heavy metal in such structure. Under irradiation with 365 nm and 420 nm wavelength light, the gold complexes can perform a reversible process, as observed by ¹H NMR, ³¹P NMR, and UV-vis spectroscopy. Such switchable properties of photoresponsive gold complexes may be used as logic gates and information storage materials. However, no gold-gold interaction could be established in the *cis* forms of **13a,b**. As a consequence, the chirality of the menthyl groups present in **13b** could not be transferred to the whole structure.

D Experiment part

D.1 Synthetic procedures

All experiments were performed under an atmosphere of dry argon using standard Schlenk techniques. Commercially available reagents were used as received without further purification. Solvents were freshly distilled under argon from sodium/benzophenone (tetrahydrofuran, diethyl ether) or from phosphorus pentoxide (pentane, dichloromethane). Preparative separations were performed by gravity column chromatography on basic alumina (Aldrich, Type 5016A, 150 mesh, 58 Å) or silica gel (Merck Geduran 60, 0.063-0.200 mm) in 3.5-20 cm columns. ¹H, ¹³C, and ³¹P NMR spectra were recorded on Bruker Ascend 300 or 400. Assignment of proton atoms is based on ¹H-¹H COSY experiment. Assignment of carbon atoms is based on HMBC, HMQC and DEPT-135 experiments. Mass analyses were performed by the CRMPO, University of Rennes 1. Specific rotations (in deg $\text{cm}^2 \text{ g}^{-1}$) were measured in a 1 dm thermostated quartz cell on a PerkinElmer Model 341 polarimeter. Circular dichroism (in M⁻¹ cm⁻¹) was measured on a Jasco J-815 Circular Dichroism Spectrometer (IFR140 facility - Biosit. Université de Rennes 1).

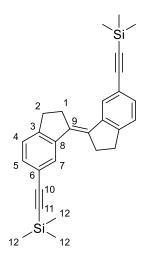
Synthesis of compound 2 (6-((trimethylsilyl)ethynyl)-2,3-dihydro-1H-inden-1-one)



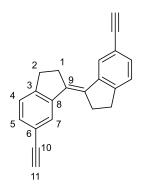
A solution of compound **1** (1.0 g, 4.7 mmol), copper(I) iodide (44.6 mg, 0.23 mmol), and tetrakis(triphenylphosphine)palladium (271.2 mg, 0.23 mmol) in a mixture of THF/Et₃N (10 mL/20 mL) was stirred under argon atmosphere. Then trimethylsilylacetylene (1.37 mL, 9.4 mmol) was added. The reaction was stirred at reflux for 12 hours. The solvent was removed by evaporation and the residue was purified by column chromatography (SiO₂, heptane/ethyl acetate = 8 : 1) to yield compound **2** as a light brown solid (875 mg, 81%). R*f* = 0.5 (heptane/ethyl acetate 4 : 1). ¹H NMR (CDCl₃, 300 MHz): δ 7.84-7.84 (s, 1 H, H^7), 7.64-7.67 (dd, J = 7.9 Hz, 1.6 Hz, 1H, H^5), 7.40-7.43 (dd, J = 7.9 Hz, 0.8 Hz, 1 H, H^4), 3.12-3.16 (m, 2 H, H^2), 2.68-2.72 (m, 2 H, H^1), 0.24 (s, 9 H, H^{12}). ¹³C NMR (CDCl₃, 75 MHz): 204.0 (1*C*⁹), 153.00 (1*C*³), 136.0 (1*C*⁵), 135.0 (1*C*⁸), 125.3(1*C*⁷), 124.7 (1*C*⁴), 120.6 (1*C*⁶), 102.0 (1*C*¹⁰), 93.3 (1*C*¹¹), 34.4 (1*C*¹), 24.0 (1*C*²), 2.0 (3*C*¹²). (M7-jcoy-1-128-C). HRMS: *m/z* calcd for C₁₄ H₁₆ONaSi: 251.08626 [M+Na]⁺, found: 251.0862 (0 ppm).

Synthesis of compound trans-3 ((E)-6,6'-bis((trimethylsilyl)ethynyl)-2,2',3,3'-tetrahydro-

1,1'-biindenylidene)



A 100 mL Schlenk flask was charged with Zn (256 mg, 4 mmol), degassed, and backfilled three times with Ar. Dry THF (5 mL) was added by a syringe and the reaction was stirred at 0 °C for 20 min then TiCl₄ (2 mL, 2 mmol) was then slowly added. The reaction was stirred at reflux for 2 hours. Then compound **2** (228.10 mg, 1 mmol) was added into the flask. The reaction was stirred under argon atmosphere at reflux for 12 hours. NH₄Cl solution was added to quench the reaction. The mixture was extracted with ethyl acetate (3 × 15 mL) and the combined organic layers were washed with brine and dried (MgSO₄). The solvent was removed and the residue was purified by column chromatography (SiO₂, heptane/ethyl acetate = 10 : 1) to yield compound *trans*-**3** (170 mg, 80%) as a light yellow solid. R*f* = 0.45 (heptane/ethyl acetate 10 : 1). ¹H NMR (CD₂Cl₂, 300 MHz): 7.66 (s, 2 H, H^7), 7.25-7.32 (m, 4 H, 2 H^4 and $2H^5$), 3.14 (br, 8 H, 4 H^1 and 4 H^2), 0.27 (s, 18 H, H^{12}). ¹³C NMR (CD₂Cl₂, 300 MHz): 150.1 (2 C^3), 145.0 (2 C^8), 137.4 (2 C^5), 132.7 (2 C^9), 129.5 (2 C^7), 126.8 (2 C^4), 123.0 (2 C^6), 107.6 (2 C^{10}), 94.8 (2 C^{11}), 33.8 (2 C^2), 33.0 (2 C^1), 1.6 (6 C^{12}).(M7-jcoy-1-135-C). HRMS: *m/z* calcd for C₂₈ H₃₂ Si₂ K: 463.16742 [M+K]⁺, found: 463.1674. **Synthesis of compound** *trans*-4 ((E)-6,6'-diethynyl-2,2',3,3'-tetrahydro-1,1'- biindenylidene)

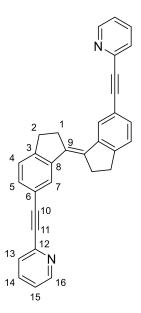


To a solution of **3** (140 mg, 0.33 mmol) in THF (5 mL) at room temperature, tetrabutylammonium fluoride (0.05 mL, 1M) was added. The mixture was stirred for 10 min, and then quenched with an aqueous NH₄Cl solution. The mixture was extracted with ethyl acetate (3 × 10 mL) and the combined organic layers were washed with brine and dried (MgSO₄). The solvent was stripped off and the residue was purified by column chromatography (SiO₂, heptane/ethyl acetate 6 : 1) to yield compound *trans*-**4** (77 mg, 83%) as a yellow solid. R*f* = 0.52 (heptane/ethyl acetate 6 : 1). ¹H NMR (CD₂Cl₂, 400 MHz): δ 7.72 (s, 2 H, H^7), 7.28-7.35 (dd, 4 H, J = 20.8 Hz, 4.4 Hz, H^4 and H^5), 3.14-3.15 (d, 8 H, J = 3.3, 4 Hz, H^1 and H^2), 3.11 (s, 2 H, H^{11}). ¹³C NMR (CD₂Cl₂, 100 MHz): δ 148.6 (2*C*³), 143.2 (2*C*⁸), 135.6 (2*C*⁵), 131.0 (2*C*⁹), 128.1 (2*C*⁷), 125.1 (2*C*⁴), 120.0 (2*C*⁶), 84.3 (2*C*¹⁰), 76.2 (2*C*¹¹), 31.9 (2*C*²), 31.1 (2*C*¹).(M7-jcoy-1-137) HRMS: *m*/*z* calcd for C₂₂ H₁₇: 281.13303 [M+H]⁺, found: 281.1330.

Synthesis of trans-6a

A solution of compound *trans*-4 (40 mg, 0.14 mmol, 1eq), copper(I) iodide (3 mg, 0.014 mmol, 0.1 eq), and tetrakis(triphenylphosphine)palladium (16 mg, 0.014 mmol, 0.1 eq) in a solution mixture (THF/Et₃N 5 mL/10 mL) was stirred under argon atmosphere at room temperature, then the brominated starting material **5a** (45 mg, 0.28 mmol, 2. eq) was added. The reaction mixture was stirred at room temperature under argon for 3 hrs. The solvent was stripped off and the residue was purified by column chromatography (SiO₂, dichloromethane/ethyl acetate = 4:1)

Compound *trans*-6a ((E)-6,6'-bis(pyridin-2-ylethynyl)-2,2',3,3'-tetrahydro-1,1'biindenylidene)

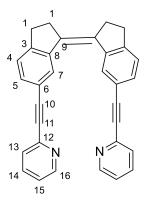


Yield 75%. $\mathbf{R}f = 0.31$ (heptane/ethyl acetate 3 : 1). ¹H NMR (CD₂Cl₂, 400 MHz): δ 8.60-8.61 (d, 2H, J = 4 Hz, H^{16}), 7.85 (s, 2 H, H^7), 7.69-7.73 (td, 2H, J = 7.7 Hz, 1.7 Hz, H^{14}), 7.55-7.57 (d, 2 H J = 7.8 Hz, H^{15}), 7.46-7.47 (d, 2 H, J = 7.7 Hz, H^5), 7.36-7.37 (d, 2H, J = 7.8 Hz, H^4), 7.25-7.28 (dd, 2 H, J = 7.0 Hz, 5.3 Hz, H^{13}), 3.20-3.23 (d, 8 H, J = 12.6 Hz). ¹³C NMR (CD₂Cl₂, 100 MHz): 150.7 (2 C^3), 149.5 (2 C^{16}), 144.1 (2 C^8), 143.9 (2 C^{12}), 136.6 (2 C^{14}), 136.3 (2 C^5), 131.5 (2 C^9), 128.4 (2 C^7), 127.7 (2 C^{13}), 125.8 (2 C^4), 123.3 (2 C^{15}), 120.8 (2 C^6), 90.1 (2 C^{11}), 88.5 (2 C^{10}), 32.6 (2 C^2), 31.7 (2 C^1). (M7-jcoy-1-159-pure, jouyang jcoy-2-trans-py-c) HRMS: m/z calcd for C₃₂ H₂₃ N₂: 435.18557 [M+H]⁺, found: 435.1853.

Synthesis of *cis*-6a

A solution of mixture of *cis*-4 and *trans*-4 (10 mg, 0.0.35 mmol, 1eq), copper(I) iodide (0.8 mg, 0.004 mmol, 0.1 eq), and tetrakis(triphenylphosphine)palladium (5 mg, 0.004 mmol, 0.1 eq) in the mixed solution (THF/Et₃N 5 mL/10 mL) was stirred under argon atmosphere at room temperature, then brominated starting material **5a** (11 mg, 0.07 mmol, 2 eq) was added. The reaction mixture was stirred at room temperature under argon atmosphere overnight. The solvent was removed by evaporation and the residue was purified by column chromatography (SiO₂, dichloromethane/ethyl acetate = 4 : 1).

Compound *cis*-6a ((Z)-6,6'-bis(pyridin-2-ylethynyl)-2,2',3,3'-tetrahydro-1,1'biindenylidene)

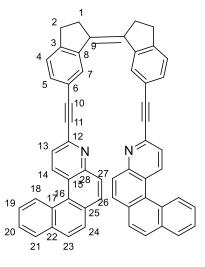


Yield 23%. R*f* = 0.35 (heptane/ethyl acetate 3 : 1). ¹H NMR (CD₂Cl₂, 400 MHz): δ 8.49-8.51 (dt, 2H, *J* = 4.9 Hz, 1.4 Hz, *H*¹⁶), 8.35 (s, 2 H, *H*⁷), 7.42-7.45 (m, 6 H, *H*⁵, *H*¹⁴, *H*¹⁵), 7.37-7.34 (d, 2 H, *J* = 7.8 Hz, *H*¹³), 7.13-7.16 (m, 2 H, *H*¹⁶), 3.02-3.06 (dd, 4 H, *J* = 7.9 Hz, 5.4 Hz, *H*²), 2.85-2.89 (dd, 4 H, *J* = 7.9 Hz, 5.4 Hz, *H*¹). ¹³C NMR (CD₂Cl₂, 100 MHz): 149.9 (2*C*¹⁶), 149.9 (2*C*³), 143.5 (2*C*⁸), 140.5 (2*C*¹²), 135.8 (2*C*¹⁴), 135.3 (2*C*⁵), 130.9 (2*C*⁹), 127.3 (2*C*⁷), 126.7 (2*C*¹³), 125.4 (2*C*⁴), 122.5 (2*C*¹⁵), 119.6 (2*C*⁶), 89.3 (2*C*¹¹), 87.9 (2*C*¹⁰), 34.6 (2*C*²), 30.7 (2*C*¹). (jkoy jcoy-1-cis-h-py) HRMS *m*/*z* calcd for C₃₂ H₂₃ N₂: 435.18557 [M+H]⁺, found: 435.1853.

Synthesis of *cis*-6b

A solution of compound *trans*-4 (120 mg, 0.42 mmol, 1eq), copper(I) iodide (8 mg, 0.21 mmol, 0.1 eq), and tetrakis(triphenylphosphine)palladium (25 mg, 0.04 mmol, 0.1 eq) in a solution mixture (THF/Et₃N 5 mL/10 mL) was stirred under argon atmosphere at room temperature, then the brominated starting material **5b** (263 mg, 0.84 mmol, 2 eq) was added. The reaction mixture was stirred at room temperature under argon for 3 hrs. The solvent was stripped off and the residue was purified by column chromatography (SiO₂, dichloromethane/ethyl acetate = 4:1).

Compound *cis*-**6b** ((Z)-6,6'-bis(4-aza[4] helicene-3- ylethynyl)-2,2',3,3'-tetrahydro-1,1' biindenylidene)

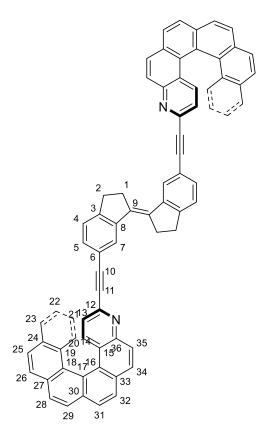


Yield: 65%. Rf = 0.29 (heptane/ethyl acetate = 3 : 1). ¹H NMR (CD₂Cl₂, 400 MHz): 8.57-8.60 (m, 4H, H^{18} , H^{19}), 8.09-8.12 (d, 2 H, J = 8.4 Hz, H^{14}), 7.76-7.84 (dd, 4 H, J = 16.4 Hz, 8.3 Hz, H^4 , H^{21}), 7.52-7.64 (m, 8 H, H^{20} , H^{23} , H^{26} , H^{27}), 7.37-8.49 (m, 6 H, H5, H^7 , H^{24}), 7.24-7.27 (t, 2 H, J = 7.1 Hz, H^{13}), 2.92-3.11 (dd, 8 H, J = 47.9 Hz, 7.2 Hz, H^1 , H^2). ¹³C NMR (CD₂Cl₂, 100 MHz) 150.2, 148.5, 135.4, 134.8, 133.1, 130.8, 130.7, 130.6, 129.3, 128.4, 128.0, 127.9, 127.5, 126.6, 126.3, 126.1, 125.9, 125.8, 125.6, 123.7, 123.56, 119.6, 90.5, 88.9, 34.4, 30.7. (M7-jcoy-1-157-C) HRMS: m/z calcd for C₅₆ H₃₅ N₂: 735.27947 [M+H]⁺, found: 735.2794.

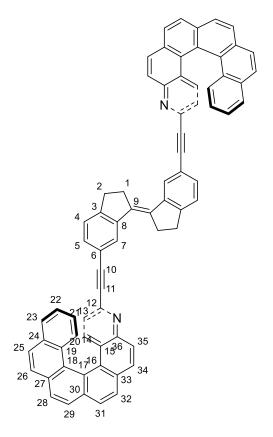
Synthesis of *trans*-(*P*,*P*)-6c and *trans*-(*M*,*M*)-6c

A solution of compound *trans*-4 (10 mg, 0.036 mmol, 1eq), copper(I) iodide (0.7 mg, 0.0036 mmol, 0.1 eq), and tetrakis(triphenylphosphine)palladium (4 mg, 0.0036 mmol, 0.1 eq) in a solution mixture (THF/Et₃N 2.5 mL/5 mL) was stirred under argon atmosphere at room temperature, then the brominated starting material *P*-3-Br-4-Azo[6]helicene *P*-5c or *M*-3-Br-4-Azo[6]helicene *M*-5c (30 mg, 0.07 mmol, 2 eq) was added. The reaction mixture was stirred at room temperature under argon for 3 hrs. The solvent was stripped off and the residue was purified by column chromatography (SiO₂, dichloromethane/ethyl acetate = 4:1).

Compound *trans-(P,P)-6c* ((E)-6,6'-bis(4-aza-(+)-[6] helicene-3- ylethynyl)-2,2',3,3'- tetrahydro-1,1' biindenylidene)



Yield: 60%. R*f* = 0.22 (heptane/ethyl acetate = 3 : 1). ¹H NMR (CD₂Cl₂, 400 MHz): 8.21-8.24 (d, 2 H, *J* = 8.9 Hz, H^{21}), 8.09-8.14 (dd, 4 H, *J* = 12.5 Hz, 8.5 Hz, H^{26} , H^{29}), 8.03-8.07 (m, 6 H, H^{31} , H^{32} , H^{34}), 7.98 (s, 4 H, H^{14} , H^{28}), 7.89-7.91 (d, 2 H, *J* = 8.0 Hz, H^{23}), 7.80-7.85 (m, 4 H, H^7 , H^{25}), 7.62-7.64 (d, 2 H, *J* = 8.5 Hz, H^{35}), 7.43-7.45 (dd, 2 H, *J* = 7.7 Hz, 1.1 Hz, H^{21}), 7.30-7.34 (m, 4 H, H^4 , H^5), 6.80-6.84 (m, 4 H, H^{13} , H^{22}), 3.16-3.18 (d, 8 H, *J* = 6.1 Hz, H^1 , H^2). ¹³C NMR (CD₂Cl₂, 100 MHz) 149.0, 147.5 (2 C^{23}), 143.2, 141.9, 135.6, 134.7, 133.3 (2 C^{20}), 132.2 (2 C^{21}), 131.7, 131,3 (2 C^{29}), 131.0 (2 C^{26}), 130.7 (2 C^{34}), 129.3 (2 C^{32}), 128.8 (2 C^{31}), 128.2, 127.9, 127.9, 127.8, 127.7, 127.4, 127.3, 127.1, 127.1, 126.1, 125.9 (2 C^{28}), 125.3 (2 C^{14}), 125.2 (2 C^5), 124.2 (2 C^4), 123.8, 122.3, 120.0 (2 C^{22}), 90.2, 88.5, 77.5, 32.0 (2 C^2), 31.12 (2 C^1). (M7-jcoy-1-176). HRMS: *m/z* calcd for C₇₂ H₄₃ N₂: 935.34207 [M+H]⁺, found: 935.3421. Specific rotation: +4875 ° cm³dm⁻¹g⁻¹ **Compound** *trans*-(*M*,*M*)-6c.((E)-6,6'-bis(4-aza-(-)-[6] helicene-3- ylethynyl)-2,2',3,3'- tetrahydro-1,1' biindenylidene)

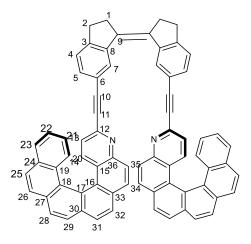


Yield: 58%. R*f* = 0.22 (heptane/ethyl acetate = 3 : 1). ¹H NMR (CD₂Cl₂, 400 MHz): 8.21-8.24 (d, 2 H, J = 8.9 Hz, H^{21}), 8.09-8.14 (dd, 4 H, J = 12.5 Hz, 8.5 Hz, H^{26} , H^{29}), 8.03-8.07 (m, 6 H, H^{31} , H^{32} , H^{34}), 7.98 (s, 4 H, H^{14} , H^{28}), 7.89-7.91 (d, 2 H, J = 8.0 Hz, H^{23}), 7.80-7.85 (m, 4 H, H^7 , H^{25}), 7.62-7.64 (d, 2 H, J = 8.5 Hz, H^{35}), 7.43-7.45 (dd, 2 H, J = 7.7 Hz, 1.1 Hz, H^{21}), 7.30-7.34 (m, 4 H, H^4 , H^5), 6.80-6.84 (m, 4 H, H^{13} , H^{22}), 3.16-3.18 (d, 8 H, J = 6.1 Hz, H^1 , H^2). ¹³C NMR (CD₂Cl₂, 100 MHz) 149.0, 147.5 (2 C^{23}), 143.2, 141.9, 135.6, 134.7, 133.3 (2 C^{20}), 132.2 (2 C^{21}), 131.7, 131,3 (2 C^{29}), 131.0 (2 C^{26}), 130.7 (2 C^{34}), 129.3 (2 C^{32}), 128.8 (2 C^{31}), 128.2, 127.9, 127.9, 127.8, 127.7, 127.4, 127.3, 127.1, 127.1, 126.1, 125.9 (2 C^{28}), 125.3 (2 C^{14}), 125.2 (2 C^{5}), 124.2 (2 C^{4}), 123.8, 122.3, 120.0 (2 C^{22}), 90.2, 88.5, 77.5, 32.0 (2 C^{2}), 31.12 (2 C^{1}).(M7-jcoy-1-180) HRMS: m/z calcd for C₇₂ H₄₃ N₂: 935.34207 [M+H]⁺, found: 935.3420. Specific rotation: -4791 ° cm³dm⁻¹g⁻¹

Synthesis of *cis*-(*P*,*P*)-6c and *cis*-(*M*,*M*)-6c

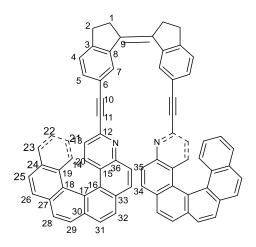
A solution of mixture of *cis*-4 and *trans*-4 (10 mg, 0.036 mmol, 1eq), copper(I) iodide (0.7 mg, 0.004 mmol, 0.1 eq), and tetrakis(triphenylphosphine)palladium (4 mg, 0.004 mmol, 0.1 eq) in the mixed solution (THF/Et₃N 2.5 mL/5 mL) was stirred under argon atmosphere at room temperature, then *P*-3-Br-4-Azo[6]helicene or I-3-Br-4-Azo[6]helicene (30 mg, 0.30 mmol, 2 eq) was added. The reaction mixture was stirred at room temperature under argon atmosphere overnight. The solvent was removed by evaporation and the residue was purified by column chromatography (SiO₂, dichloromethane/ethyl acetate = 4 : 1).

Compound cis(M, M)-6c



Yield: 32%. Rf = 0.24 (heptane/Ethyl acetate = 3:1). ¹H NMR (CD₂Cl₂, 400 MHz): 8.26 (s, 2 H), 8.04-7.99 (m, 4 H), 7.93 (d, J = 8.2 Hz, 2 H), 7.85 (d, J = 8.2 Hz, 2 H), 7.77 (d, J = 8.8 Hz, 2 H), 7.72 (d, J = 8.6 Hz, 2 H), 7.66 (t, J = 8.9 Hz, 4 H), 7.60 (dd, J = 7.9, 1.3 Hz, 2 H), 7.41(d, J = 7.8 Hz, 2 H), 7.37-7.27 (m, 6 H), 7.08 (ddd, J = 8.0, 6.8, 1.2 Hz, 2 H), 6.54 (ddd, J = 8.4, 6.9, 1.4 Hz, 2 H), 6.46 (d, J = 8.7 Hz, 2 H), 3.03 (t, J = 6.4 Hz, 4 H), 2.85 (t, J = 6.4 Hz, 4 H). ¹³C NMR (CD₂Cl₂, 100 MHz): 150.5, 147.7, 142.2, 141.1, 135.8, 134.9, 133.7, 132.4, 132.0, 131.6, 130.7, 129.5, 129.0, 128.6, 128.3, 128.2, 128.2, 127.9, 127.7, 127.6, 127.5, 127.4, 127.2, 126.4, 126.2, 126.0, 125.6, 124.3, 124.2, 122.6, 120.0, 90.3, 89.1, 35.2, 31.3, 30.0. HRMS: m/z calcd for C₇₂H₄₃N₂: 935.34207 [M+H]⁺; found:935.3416 (0 ppm). Specific rotation: -4312 ° cm³dm⁻¹g⁻¹.

Compound *cis*-(*P*, *P*)-6c



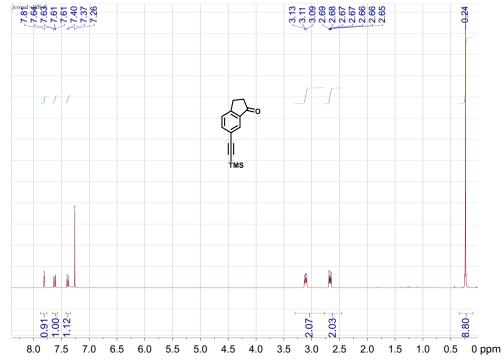
Yield: 30%. Rf = 0.24 (heptane/Ethyl acetate = 3:1). ¹H NMR (CD₂Cl₂, 400 MHz): 8.26 (s, 2 H), 8.04-7.99 (m, 4 H), 7.93 (d, J = 8.2 Hz, 2 H), 7.85 (d, J = 8.2 Hz, 2 H), 7.77 (d, J = 8.8 Hz, 2 H), 7.72 (d, J = 8.6 Hz, 2 H), 7.66 (t, J = 8.9 Hz, 4 H), 7.60 (dd, J = 7.9, 1.3 Hz, 2 H), 7.41(d, J = 7.8 Hz, 2 H), 7.37-7.27 (m, 6 H), 7.08 (ddd, J = 8.0, 6.8, 1.2 Hz, 2 H), 6.54 (ddd, J = 8.4, 6.9, 1.4 Hz, 2 H), 6.46 (d, J = 8.7 Hz, 2 H), 3.03 (t, J = 6.4 Hz, 4 H), 2.85 (t, J = 6.4 Hz, 4 H). ¹³C NMR (CD₂Cl₂, 100 MHz): 150.5, 147.7, 142.2, 141.1, 135.8, 134.9, 133.7, 132.4, 132.0, 131.6, 130.7, 129.5, 129.0, 128.6, 128.3, 128.2, 128.2, 127.9, 127.7, 127.6, 127.5, 127.4, 127.2, 126.4, 126.2, 126.0, 125.6, 124.3, 124.2, 122.6, 120.0, 90.3, 89.1, 35.2, 31.3, 30.0. HRMS: m/z calcd for C₇₂H₄₃N₂: 935.34207 [M+H]⁺; found:935.3416 (0 ppm). Specific rotation: -4333 ° cm³dm⁻¹g⁻¹.

Synthesis of gold complexes 13a and 13b.

A flask was charged with compound *trans*-4 (10 mg, 0.036 mmol) and sodium methoxide (7.7 mg, 0.144 mmol) under Argon atmosphere. The methanol (2 mL) was added, and the reaction was stirred for 2 hours at room temperature. Then the solution of gold precursor $12a^{71}$ (40 mg, 0.072 mmol) in dichloromethane was added into the flask. The reaction was stirred for 4 hours. Stop the reaction and do a filtration, removed the

solvent and collected the compound **13a** (42 mg, 90%). ¹H NMR (300 MHz). δ 7.60 (m, 28 H), 7.3 (m, 4 H), 3.16 (d, *J* = 12 Hz, 8 H). ¹³C NMR (75 MHz, CD₂Cl₂). δ 146.1, 143.0, 135.4, 134.3, 134.2, 131.6, 131.5, 130.8, 130.3, 129.5, 129.2, 129.0, 127.9, 124.6, 123.2, 32.0, 30.8. 31P NMR: 42.3 ppm.

A flask was charged with compound *trans*-**4** (10 mg, 0.036 mmol) and sodium methoxide (7.7 mg, 0.144 mmol) under Argon atmosphere. The methanol (2 mL) was added, and the reaction was stirred for 2 hours at room temperature. Then the solution of compound **12b**⁷⁰ (40 mg, 0.072 mmol) in dichloromethane was added into the flask. The reaction was stirred for 4 hours. Stop the reaction and do a filtration, removed the solvent and collected the compound **13b** (40 mg, 85%). ¹H NMR (300 MHz). 8.21-7.99 (m, 4 H), 8.01-7.85 (m, 4 H), 7.65 (s, 2 H), 7.48-7.36 (m, 12 H), 7.31-7.01 (m, 4 H), 3.56(dd, *J* = 14.5, 4.0 Hz, 2 H), 3.23-2.94 (m, 8 Hz), 2.72 (dd, *J* = 11.3, 2.0 Hz), 1.93(d, *J* = 11.8 Hz, 6 H), 1.77-1.55 (m, 4 H), 1.30-1.14 (m, 4 H), 0.90 (m, 2 H), 0.74 (d, *J* = 6.3 Hz, 6H), 0.56 (d, *J* = 6.2 Hz, 6 H), 0.48 (d, *J* = 6.2 Hz, 6 H), ¹³C NMR (75 MHz, CD₂Cl₂) δ 146.0, 143.0, 135.4, 134.9, 134.9, 134.8, 134.7, 132.5, 131.8, 131.6, 131.4, 131.1, 130.9, 130.8, 128.9, 128.87, 128.8, 128.7, 127.8, 124.6, 123.4, 48.5, 48.4, 38.1, 37.1, 36.7, 35.4, 32.1, 30.9, 29.9, 29.9, 28.3, 28.2, 26.9, 26.8, 22.3, 22.0, 21.9, 20.7, 13.8. ³¹P NMR: δ 38.1 ppm. Specific rotation: +14.3 ° cm³dm⁻¹g⁻¹.



D.2 ¹H NMR spectra of new compounds

Figure S1 ¹H NMR (300 MHz, CD₂Cl₂) sepectrum of compound 2 in CD₂Cl₂ at room temperature.

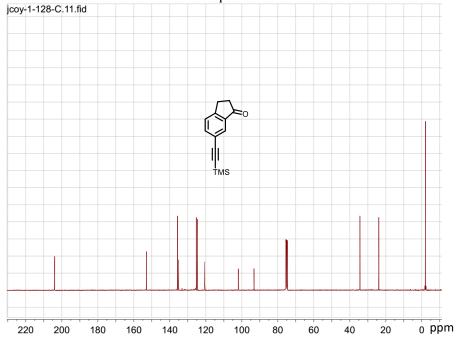


Figure S2 ¹³C NMR (75 MHz, CD₂Cl₂) spectrum of compound 2 in CD₂Cl₂ at room temperature.

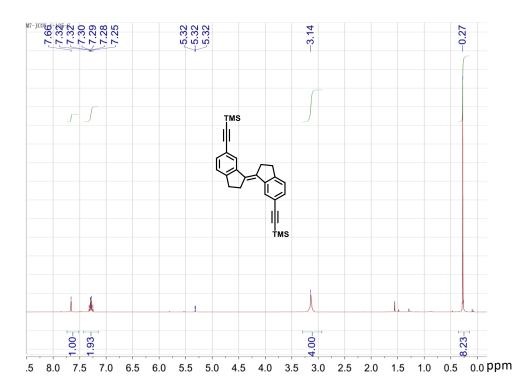


Figure S3 ¹H NMR (300 MHz, CD₂Cl₂) spectrum of compound *trans*-**3** in CD₂Cl₂ at room temperature.

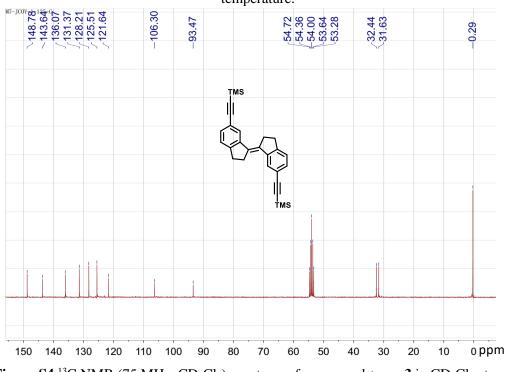


Figure S4 ¹³C NMR (75 MHz, CD₂Cl₂) spectrum of compound *trans*-**3** in CD₂Cl₂ at room temperature.

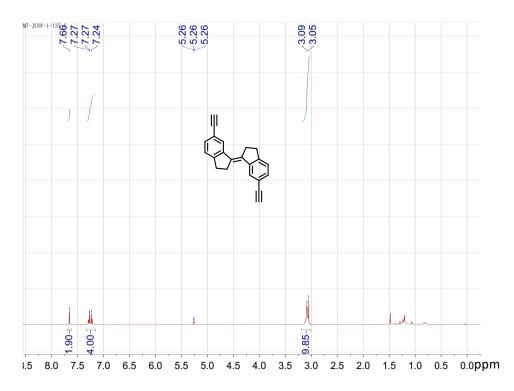


Figure S5 ¹H NMR (300 MHz, CD₂Cl₂) spectrum of compound *trans*-4 in CD₂Cl₂ at 298 K.

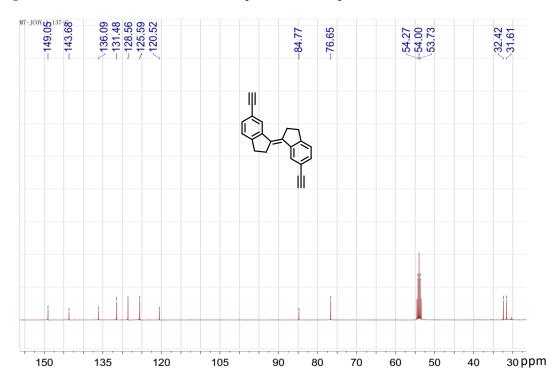


Figure S6¹³C NMR (75 MHz, CD₂Cl₂) spectrum of compound *trans*-4 in CD₂Cl₂ at room temperature.

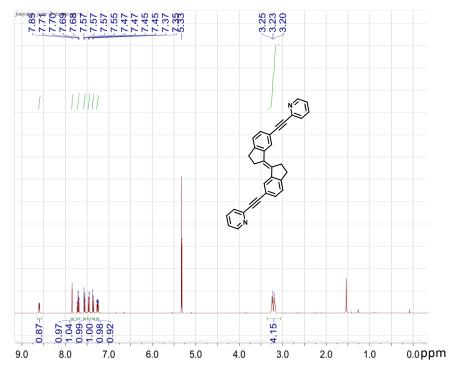


Figure S7 ¹H NMR (300 MHz, CD₂Cl₂) spectrum of compound *trans*-**6a** in CD₂Cl₂ at room temperature.

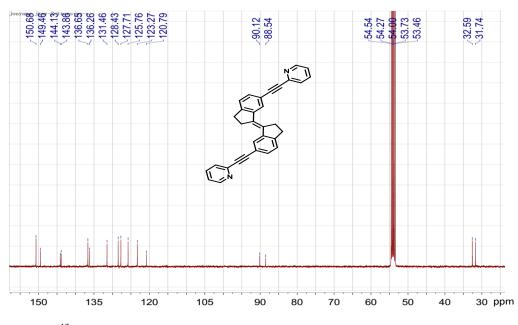


Figure S8 ¹³C NMR (75 MHz, CD₂Cl₂) spectrum of compound *trans*-**6a** in CD₂Cl₂ at room temperature.

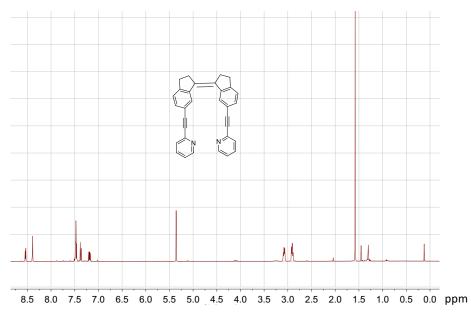


Figure S9 ¹H NMR (300 MHz, CD₂Cl₂) spectrum of compound *cis*-**6a** in CD₂Cl₂ at room temperature.

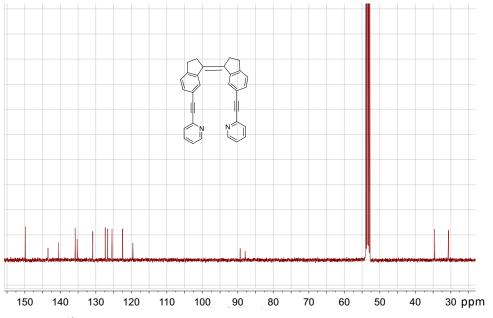


Figure S10 ¹³C NMR (75 MHz, CD₂Cl₂) spectrum of compound *cis*-**6a** in CD₂Cl₂ at room temperature.

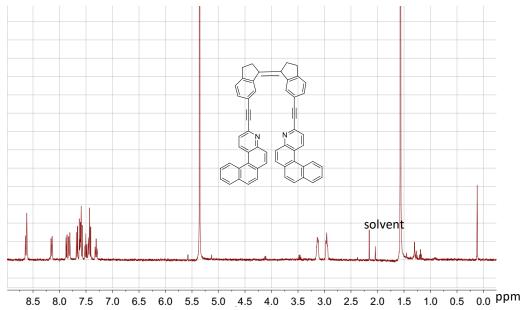


Figure S11 ¹H NMR (400 MHz, CD₂Cl₂) spectrum of compound *cis*-**6b** in CD₂Cl₂ at room temperature.

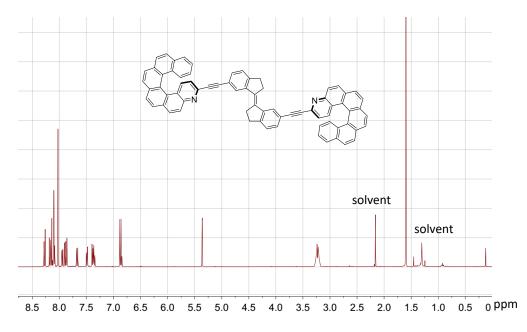


Figure S12 ¹H NMR (400 MHz, CD_2Cl_2) spectrum of compound *trans-(P,P)*-6c and *trans-(M,M)*-6c in CD_2Cl_2 at room temperature.

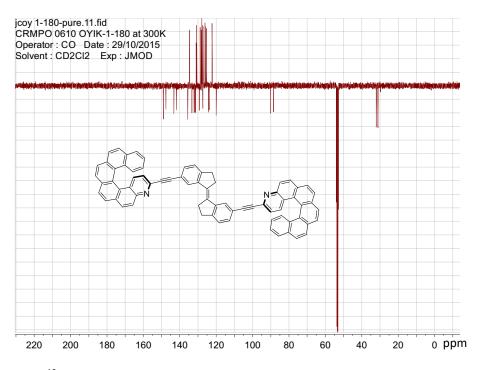


Figure S13 ¹³C NMR (100 MHz, CD_2Cl_2) spectrum of compound *trans-(P,P)-6c* and *trans-(M,M)-6c* in CD_2Cl_2 at room temperature.

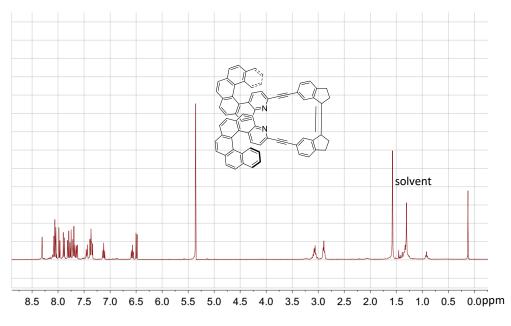


Figure S14 ¹H NMR (400 MHz, CD_2Cl_2) spectrum of compound *cis-(P,P)*-6c and *cis-(M,M)*-6c in CD_2Cl_2 at room temperature.

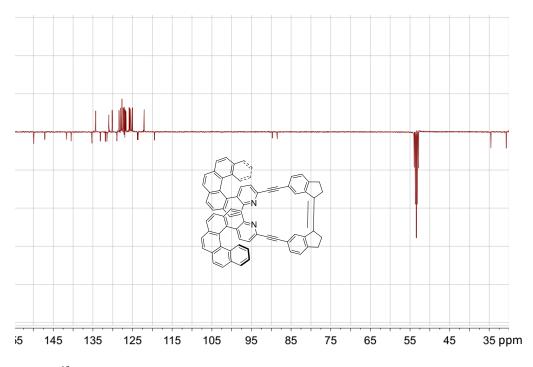


Figure S15 ¹³C NMR (100 MHz, CD_2Cl_2) spectrum of compound *cis-(P,P)-6c* and *cis-(M,M)-6c* in CD_2Cl_2 at room temperature.

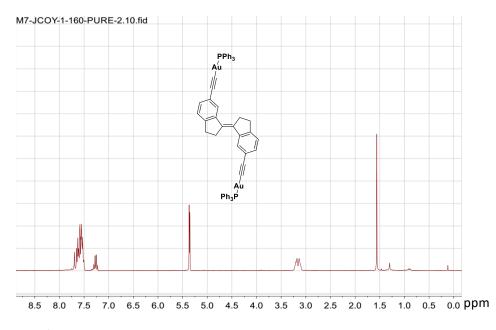


Figure S16 ¹H NMR (300 MHz) spectrum of gold complex 13a in CD₂Cl₂ at room temperature.

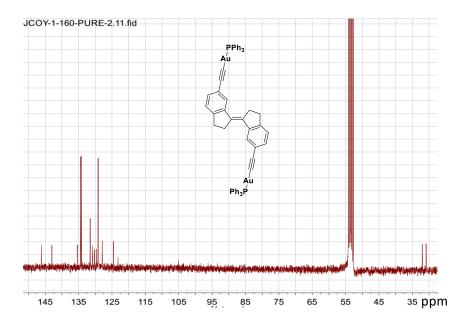


Figure S17 ¹³C NMR (75 MHz) spectrum of gold complex **13a** in CD₂Cl₂ at room temperature.

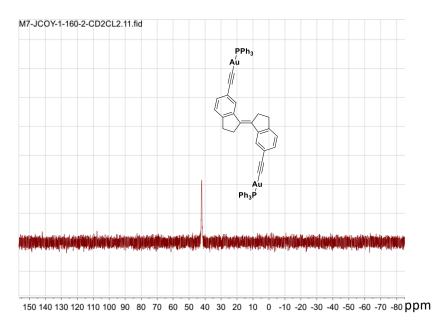


Figure S18 ³¹P NMR (121 MHz) spectrum of gold complex **13a** in CD₂Cl₂ at room temperature.

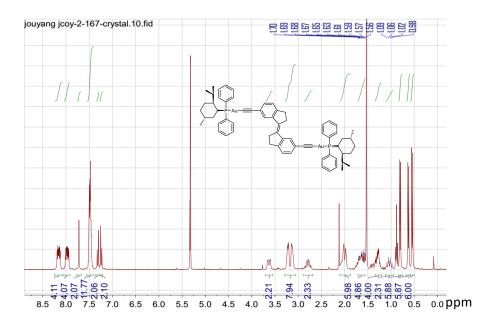


Figure S19¹H NMR (300 MHz) spectrum of gold complex 13b in CD₂Cl₂ at room temperature.

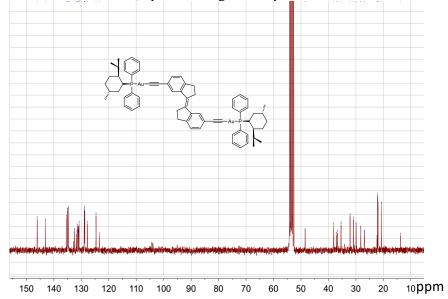


Figure S20¹³C NMR (75 MHz) spectrum of gold complex 13b in CD₂Cl₂ at room temperature.

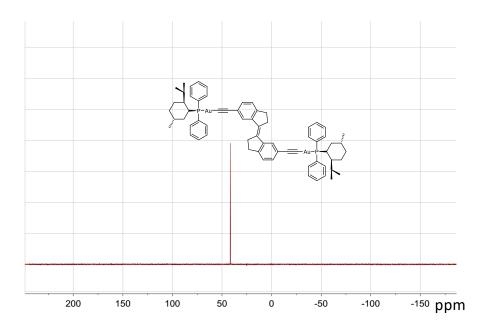


Figure S21 ³¹P NMR (121 MHz) spectrum of gold complex 13b in CD₂Cl₂ at room temperature.

D.3 UV-Vis spectra of new compounds

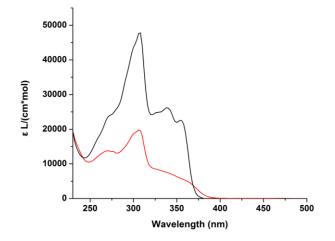


Figure S22 UV-vis spectrum of *cis*-6a (red line) and *trans*-6a (black line) in CH₂Cl₂ at room temperature.

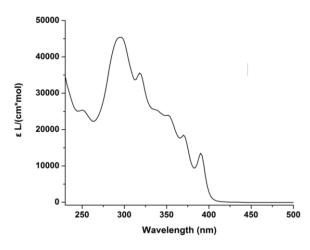


Figure S23 UV-vis spectrum of *cis*-6b in CH₂Cl₂ at room temperature.

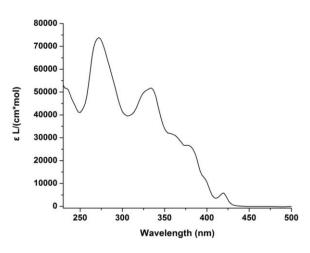


Figure S24 UV-vis spectrum of *trans-(P, P)*-6c in CH₂Cl₂ at room temperature.

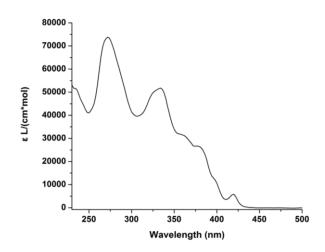


Figure S25 UV-vis spectrum of *trans-(M, M)-6c* in CH₂Cl₂ at room temperature.

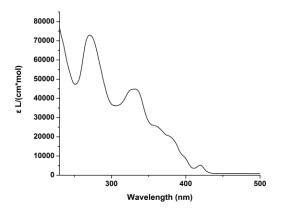


Figure S26 UV-vis spectrum of cis-(P, P)-6c in CH₂Cl₂ at room temperature.

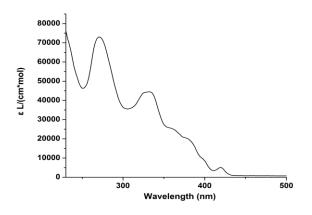


Figure S27 UV-vis spectrum of *cis*-(*M*, *M*)-6c in CH₂Cl₂ at room temperature.

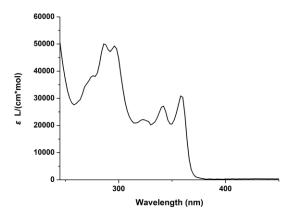


Figure S28 UV-vis spectrum of gold complex 13a in CH₂Cl₂ at room temperature.

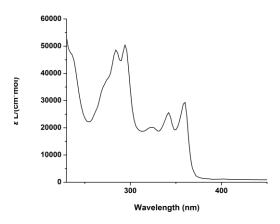


Figure S29 UV-vis spectrum of gold complex 13b in CH₂Cl₂ at room temperature.

D.4 Crystal structures

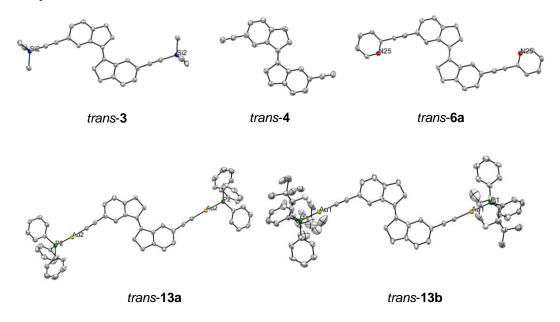


Figure S30 ORTEP plots of the molecular structures of *trans-3*, *trans-4*, *trans-6*, *trans-13a*, and *trans-13b* (all hydrogen atoms and solvent molecules are omitted).

	trans-3	trans-4	trans-6a	
Empirical formula	$C_{28}H_{32}Si_2$	$C_{22}H_{16}$	$C_{32} H_{22} N_2$	
Formula weight	424.71	280.35	434.51	
Temperature (K)	100(2)	250	150	
Wavelength (Å)	1.54184	1.54184	0.71073	
Crystal system	Monoclinic	Monoclinic	Monoclinic	
Space group	P-1	P 1 21/c 1	P 1 21/c 1	
a (Å)	5.8352(2)	12.1321(2)	16.3373(12)	
b (Å)	14.4408(6)	15.6354(3)		
<i>c</i> (Å)	15.8793(7)	7.7850(2)		
α (°)	111.756(4)	90	90	
β (°)	92.869(3)	95.064(2)		
γ (°)	93.262(3)	90		
Volume (Å ³)	1237.09(9)	1470.97(5)	2262.9(3)	
Z	2 1.140	4	4	
$ ho_{\text{Calculated}}$ (Mg/m ³)		1.266	1.275	
Absorption	1.371	0.541	0.074	
coefficient (mm ⁻¹)				
<i>F</i> (000)	456	592	912	
Crystal size (mm)	0.433 x 0.251 x	0.3327 x 0.2583 x	0.300 x 0.130 x	
	0.115	0.1991	0.070	
θ range for data	3.306 to 70.770	3.658 to 71.242	3.248 to 27.512	
collection (°)	7-h-5	-14≤h≤14	15-6-21	
Limiting indices	-7≤h≤5 -17≤k≤15	-14 <u>≤1</u> ≤14 -19≤k≤19	-15≤h≤21 -12≤k≤12	
	-17≤k≤13 -19≤l≤19	-19 <u>≤k≤</u> 19 -9≤l≤9	-12≤k≤12 -21≤l≤21	
Reflections collected	-19 <u><1</u>	-9 <u>≤1</u> ≤9 13177	-21 <u>≤1</u> ≤21 15492	
Reflections unique	4728 [R(int) =	2849 [R(int) =	5113 [R(int) =	
Reflections unique	0.0371	0.0237]	0.0895]	
Completeness	99.9 % (θ =	$100.0 \% (\theta =$	99.5 % ($\theta = \max$)	
completeness	67.684°)	67.684°)	<i>yy.b</i> // (0 = max)	
Absorption correction	Semi-empirical	Analytical	multi-scan	
F	from equivalents			
Refinement method	Full-matrix	Full-matrix	Full-matrix	
	least-squares on	least-squares on	least-squares on	
	F^2	F^2	F^2	
Data / restraints				
/ parameters	4728 / 0 / 272	2849/0/200	5113 / 0 / 308	
Goodeness-of-fit on	1.081	1.064	1.041	
F^2	1.001	1.004	1.041	
Final <i>R</i> indices $(I > I)$	$R_1 = 0.0426$	$R_1 = 0.0370$	$R_1 = 0.0772$	
$2\sigma_l$		M = 0.0070	M = 0.0772	
_01)	$wR_2 = 0.1118$	$wR_2 = 0.1089$	$wR_2 = 0.1758$	
<i>R</i> indices (all data)	$R_1 = 0.0504$	$R_1 = 0.0407$	$R_1 = 0.1304$	
	$wR_2 = 0.1287$	$wR_2 = 0.1123$	$wR_2 = 0.2056$	
Absolute structure				
parameter				
Extinction coefficient	0.0008(3)	0.0008(3)		
Largest diff. peak	0.272	0.160	0.515	
$(\mathbf{e} \cdot \mathbf{A}^3)$				
Largest diff. hole	-0.319	-0.123	-0.304	
$(\mathbf{e} \cdot \mathbf{A}^3)$				

Table S1. Crystal data and structural refinements of *trans*-3, *trans*-4, and *trans*-6a.

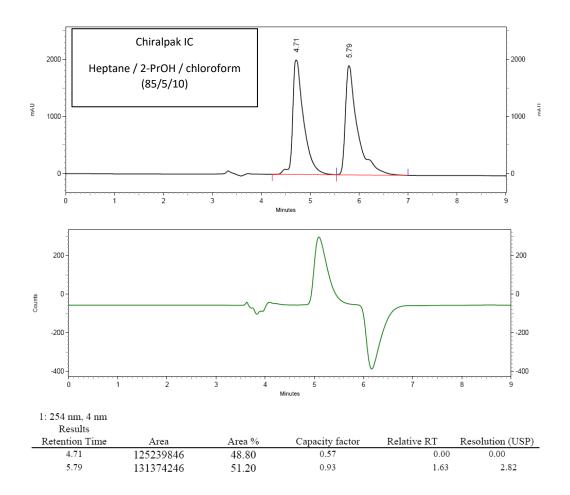
	trans-13a•CH2Cl2	trans-13b•2CH2Cl2
Empirical formula	$C_{59}H_{42}Au_2Cl_2P_2$	$C_{68}H_{72}Au_2Cl_4P_2$
Formula weight	1277.70	1486.93
Temperature (K)	150(2)	150(2)
Wavelength (Å)	0.71073	0.71073
Crystal system	Monoclinic	Orthorhombic
Space group	P21/n	Pcab
$a(\mathbf{A})$	20.1191(12)	17.887(2)
b (Å)	8.6443(5)	18.390(3)
c (Å)	29.6282(14)	19.363(3)
α (°)	90	90
β (°)	106.762(2)	90
γ (°)	90	90
Volume (Å ³)	4933.9(5)	6369.7(17)
Z	4	4
$\rho_{\text{Calculated}}$ (Mg/m ³)	1.720	1.551
Absorption coefficient (mm^{-1})	6.152	4.858
F(000)	2472	2944
Crystal size (mm)	0.16 * 0.12 * 0.09	0.15 * 0.10 * 0.08
θ range for data	1.06 to 6.42	2.21 to 27.55
collection (°)	1.00 to 0.42	2.21 10 27.55
Limiting indices	-24≤h≤25	-22≤h≤23
Emitting matces	$-24 \le n \le 25$ $-10 \le k \le 10$	-22 <u>s</u> 1 <u>5</u> 23 -23 <u>5</u> k <u>5</u> 23
	-10 <u>>k</u> <u>></u> 10 -35 <u><</u> <u><</u> 37	-25 <u><</u> k <u></u> 25 -25 <u><</u> l<25
Reflections collected	28983	57826
Reflections unique	10061	7316
Completeness	99.3 % ($\theta = \max$)	99.5 % ($\theta = \max$)
Absorption correction	multi-scan	multi-scan
Refinement method	Full-matrix	Full-matrix
Refinement method	least-squares on F^2	least-squares on F^2
Data / restraints	least-squares on P	least-squares on P
/ parameters	10061 / 0 / 586	7316/0/425
Goodeness-of-fit on F^2	1.041	1.161
Final <i>R</i> indices $(I > 2\sigma_I)$	$R_1 = 0.0448$	$R_1 = 0.0521$
	$wR_2 = 0.1038$	$wR_2 = 0.1027$
<i>R</i> indices (all data)	$R_1 = 0.0651$	$R_1 = 0.0866$
	$wR_2 = 0.1183$	$wR_2 = 0.1168$
Absolute structure parameter		
Extinction coefficient		
Largest diff. peak (e·Å ³)	2.057	2.150
Largest diff. hole (e·Å ³)	-1.703	-1.307

Table S2. Crystal data and structural refinements of *trans*-13a, *trans*-13b.

D.5 Analytical chiral HPLC separation for compound 5c

• The sample is dissolved in chloroform, injected on the chiral column, and detected with an UV detector at 254 nm and polarimeter. The flow-rate is 1 mL/min.

c	Mobile Phase	t1	k1	t2	k2	α	Rs
Chiralpak IC	Heptane / 2-PrOH / chloroform (85/5/10)	4.71 (+)	0.57	5.79 (-)	0.93	1.63	2.82



Semi-preparative separation for compound 5c

• Sample preparation: About 210 mg of compound 5c are dissolved in 23.5 mL of dichloromethane.

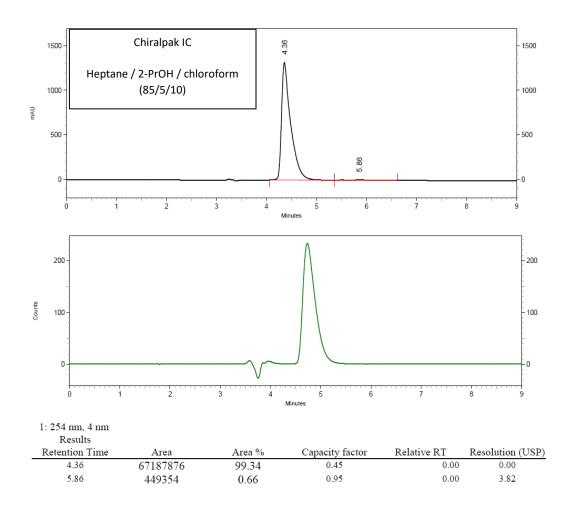
• Chromatographic conditions: Chiralpak IC (250 x 10 mm), hexane / 2-PrOH / chloroform ($\frac{85}{10}$) as mobile phase, flow-rate = 5 mL/min, UV detection at 254 nm.

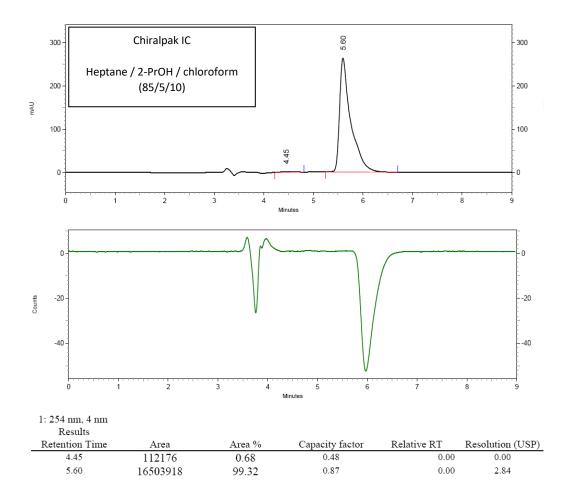
• Injections: 100 times 235 µL, every 5.3 minutes.

• Collection: the first eluted enantiomer is collected between 4.9 and 6.1 minutes, the second one between 7.7 and 10 minutes.

- First fraction: 75 mg of the first eluted ((+, polarimeter)-enantiomer) with ee > 98.5%
- Second fraction: 100 mg of the second eluted ((-, polarimeter)-enantiomer) with ee > 98.5%

• Chromatograms of the collected fractions:





E References

1. Feringa, B. L.; van Delden, R. A.; ter Wiel, M. K. J., Chiroptical Molecular Switches. In *Molecular Switches*, Wiley-VCH Verlag GmbH: 2001; pp 123-163.

2. Laguna, A., *Modern supramolecular gold chemistry: gold-metal interactions and applications*. John Wiley & Sons: 2008.

3. Carlos Lima, J.; Rodriguez, L., *Chem. Soc. Rev.* **2011**, *40*, 5442-5456.

4. Lukas, A. S.; Wasielewski, M. R., Approaches to a Molecular Switch Using

Photoinduced Electron and Energy Transfer. In *Molecular Switches*, Wiley-VCH Verlag GmbH: 2001; pp 1-35.

5. Majerus, G.; Yax, E.; Ourisson, G., Bull. Soc. Chim. Fr. 1967, 4143-&.

6. Waldeck, D. H., *Chem. Rev.* **1991**, *91*, 415-436.

7. Doany, F. E.; Hochstrasser, R. M.; Greene, B. I. In *Isomerization Intermediates In Solution Phase Photochemistry Of Stilbenes*, 1985; pp 25-31.

8. Xu, J.-F.; Chen, Y.-Z.; Wu, D.; Wu, L.-Z.; Tung, C.-H.; Yang, Q.-Z., *Angew. Chem. Int. Ed.* **2013**, *52*, 9738-9742.

9. Likhtenshtein, G., Stilbene Photophysics. In *Stilbenes*, Wiley-VCH Verlag GmbH & Co. KGaA: 2009; pp 67-98.

10. Saltiel, J., J. Am. Chem. Soc. 1967, 89, 1036-1037.

11. Saltiel, J., Stilbenes: Applications in Chemistry, Life Sciences and Materials Science. ACS Publications: 2010.

12. Gertz, L., Stilbenes: applications in chemistry, life sciences and materials science. WILEY-VCH Verlag GmbH & Co. KGaA., Weinheim, Germany: 2010.

13. Likhtenshtein, G., Stilbene Photoisomerization. In *Stilbenes*, Wiley-VCH Verlag GmbH & Co. KGaA: 2009; pp 99-136.

14. Orlandi, G.; Siebrand, W., Chem. Phys. Lett. 1975, 30, 352-354.

15. Doany, F. E.; Heilweil, E. J.; Moore, R.; Hochstrasser, R. M., J. Chem. Phys. 1984, 80, 201-206.

16. Rothenberger, G.; Negus, D. K.; Hochstrasser, R. M., J. Chem. Phys. **1983**, 79, 5360-5367.

17. Quick, M.; Berndt, F.; Dobryakov, A. L.; Ioffe, I. N.; Granovsky, A. A.; Knie, C.;

Mahrwald, R.; Lenoir, D.; Ernsting, N. P.; Kovalenko, S. A., J. Phys. Chem. B. 2014, 118, 1389-1402.

18. Saltiel, J.; D'Agostino, J. T., J. Am. Chem. Soc. 1972, 94, 6445-6456.

19. Whitten, D. G., Acc. Chem. Res. **1993**, 26, 502-509.

20. Shimasaki, T.; Kato, S.-i.; Shinmyozu, T., J. Org. Chem. 2007, 72, 6251-6254.

21. Shimasaki, T.; Kato, S.-i.; Ideta, K.; Goto, K.; Shinmyozu, T., *J. Org. Chem.* **2007**, *72*, 1073-1087.

22. Wezenberg, S. J.; Feringa, B. L., Org. Lett. 2017, 19, 324-327.

23. Yang, Q.-Z.; Huang, Z.; Kucharski, T. J.; Khvostichenko, D.; ChenJoseph;

BoulatovRoman, Nat. Nanotechnol. 2009, 4, 302-306.

24. Huang, Z.; Yang, Q.-Z.; Kucharski, T. J.; Khvostichenko, D.; Wakeman, S. M.;

Boulatov, R., Chem. - Eur. J., 2009, 15, 5212-5214.

25. Huang, Z.; Yang, Q.-Z.; Khvostichenko, D.; Kucharski, T. J.; Chen, J.; Boulatov, R., *J. Am. Chem. Soc.* **2009**, *131*, 1407-1409.

26. Kucharski, T. J.; Huang, Z.; Yang, Q.-Z.; Tian, Y.; Rubin, N. C.; Concepcion, C. D.;

Boulatov, R., Angew. Chem. Int. Ed. 2009, 48, 7040-7043.

27. Tian, Y.; Kucharski, T. J.; Yang, Q.-Z.; Boulatov, R., Nat. Commun. 2013, 4.

28. Kucharski, T. J.; Yang, Q.-Z.; Tian, Y.; Boulatov, R., *J. Phys. Chem. Lett.* **2010**, *1*, 2820-2825.

29. Kean, Z. S.; Akbulatov, S.; Tian, Y.; Widenhoefer, R. A.; Boulatov, R.; Craig, S. L., *Angew. Chem. Int. Ed.* **2014**, *53*, 14508-14511.

30. Yan, X.; Xu, J.-F.; Cook, T. R.; Huang, F.; Yang, Q.-Z.; Tung, C.-H.; Stang, P. J., *Proc. Natl. Acad. Sci.* **2014**, *111*, 8717-8722.

31. Wang, Y.; Xu, J.-F.; Chen, Y.-Z.; Niu, L.-Y.; Wu, L.-Z.; Tung, C.-H.; Yang, Q.-Z., *Chem. Commun.* **2014**, *50*, 7001-7003.

32. Xu, J.-F.; Chen, Y.-Z.; Wu, L.-Z.; Tung, C.-H.; Yang, Q.-Z., *Org. Lett.* **2014**, *16*, 684-687.

33. Li, Y.; Tse, E. C. M.; Barile, C. J.; Gewirth, A. A.; Zimmerman, S. C., *J. Am. Chem. Soc.* **2015**, *137*, 14059-14062.

34. Koumura, N.; Zijlstra, R. W. J.; van Delden, R. A.; Harada, N.; Feringa, B. L., *Nature* **1999**, *401*, 152-155.

35. Kassem, S.; van Leeuwen, T.; Lubbe, A. S.; Wilson, M. R.; Feringa, B. L.; Leigh, D. A., *Chem. Soc. Rev.* **2017**.

36. Chen, J.; Wezenberg, S. J.; Feringa, B. L., Chem. Commun. 2016, 52, 6765-6768.

37. Kistemaker, J. C. M.; Štacko, P.; Visser, J.; Feringa, B. L., Nat. Chem. 2015, 7, 890-896.

38. Eelkema, R.; Pollard, M. M.; Vicario, J.; Katsonis, N.; Ramon, B. S.; Bastiaansen, C. W.

M.; Broer, D. J.; Feringa, B. L., Nature 2006, 440, 163-163.

39. Zhao, D.; Neubauer, T. M.; Feringa, B. L., *Nat. Commun.* 2015, *6*, 6652.

40. Zhao, D.; van Leeuwen, T.; Cheng, J.; Feringa, B. L., *Nat. Chem.* **2017**, *9*, 250-256.

41. Wang, J.; Feringa, B. L., *Science* **2011**, *331*, 1429-1432.

42. Feringa, B. L., J. Org. Chem. 2007, 72, 6635-6652.

43. Dinescu, L.; Yuan Wang, Z., *Chem. Commun.* **1999**, 2497-2498.

44. Norsten, T. B.; Peters, A.; McDonald, R.; Wang, M.; Branda, N. R., *J. Am. Chem. Soc.* **2001**, *123*, 7447-7448.

45. Wigglesworth, T. J.; Sud, D.; Norsten, T. B.; Lekhi, V. S.; Branda, N. R., *J. Am. Chem. Soc.* **2005**, *127*, 7272-7273.

46. Okuyama, T.; Tani, Y.; Miyake, K.; Yokoyama, Y., J. Org. Chem. 2007, 72, 1634-1638.

47. Tani, Y.; Ubukata, T.; Yokoyama, Y.; Yokoyama, Y., *J. Org. Chem.* **2007**, *72*, 1639-1644.

48. Moorthy, J. N.; Venkatakrishnan, P.; Sengupta, S.; Baidya, M., *Org. Lett.* **2006**, *8*, 4891-4894.

49. Moorthy, J. N.; Mandal, S.; Mukhopadhyay, A.; Samanta, S., *J. Am. Chem. Soc.* **2013**, *135*, 6872-6884.

50. Wang, Z. Y.; Todd, E. K.; Meng, X. S.; Gao, J. P., *J. Am. Chem. Soc.* **2005**, *127*, 11552-11553.

51. McMurry, J. E., *Chem. Rev.* **1989**, 89, 1513-1524.

52. Oelgemöller, M.; Frank, R.; Lemmen, P.; Lenoir, D.; Lex, J.; Inoue, Y., *Tetrahedron* **2012**, *68*, 4048-4056.

53. Furche, F.; Ahlrichs, R.; Wachsmann, C.; Weber, E.; Sobanski, A.; Vögtle, F.; Grimme, S., *J. Am. Chem. Soc.* **2000**, *122*, 1717-1724.

54. Li, D.; Hong, X.; Che, C.-M.; Lo, W.-C.; Peng, S.-M., J. Chem. Soc., Dalton Trans. **1993**, 2929-2932.

55. Yam, V. W.-W.; Choi, S. W.-K., J. Chem. Soc., Dalton Trans. 1996, 4227-4232.

56. Lu, W.; Xiang, H.-F.; Zhu, N.; Che, C.-M., Organometallics 2002, 21, 2343-2346.

57. Chao, H.-Y.; Lu, W.; Li, Y.; Chan, M. C.; Che, C.-M.; Cheung, K.-K.; Zhu, N., *J. Am. Chem. Soc.* **2002**, *124*, 14696-14706.

58. Yam, V. W.-W.; Wong, K. M.-C., Luminescent Molecular Rods—Transition-Metal Alkynyl Complexes. In *Molecular wires and electronics*, Springer: 2005; pp 1-32.

59. Puddephatt, R., Chem. Soc. Rev. 2008, 37, 2012-2027.

60. Yam, V. W.-W.; Cheng, E. C.-C., Chem. Soc. Rev. 2008, 37, 1806-1813.

- 61. Schmidbaur, H., Gold Bull 1990, 23, 11-21.
- 62. Yam, V. W.-W, V.; Li, C. K.; Chan, C. L., Angew. Chem. Int. Ed. 1998, 37, 2857-2859.
- 63. He, X.; Lam, W. H.; Zhu, N.; Yam, V. W. W., *Chem-eur J* **2009**, *15*, 8842-8851.
- 64. He, X.; Cheng, E. C.-C.; Zhu, N.; Yam, V. W.-W., Chem. Commun. 2009, 4016-4018.

65. Yam, V. W.-W.; Cheung, K.-L.; Cheng, E. C.-C.; Zhu, N.; Cheung, K.-K., *Dalton Trans.* **2003**, 1830-1835.

66. Li, C.-K.; Lu, X.-X.; Wong, K. M.-C.; Chan, C.-L.; Zhu, N.; Yam, V. W.-W., *Inorg. Chem.* **2004**, *43*, 7421-7430.

67. Tang, H.-S.; Zhu, N.; Yam, V. W.-W., Organometallics 2007, 26, 22-25.

68. El Sayed Moussa, M.; Chen, H.; Wang, Z.; Srebro-Hooper, M.; Vanthuyne, N.;

Chevance, S.; Roussel, C.; Williams, J. A. G.; Autschbach, J.; Réau, R.; Duan, Z.; Lescop, C.; Crassous, J., *Chem. - Eur. J.*, **2016**, *22*, 6075-6086.

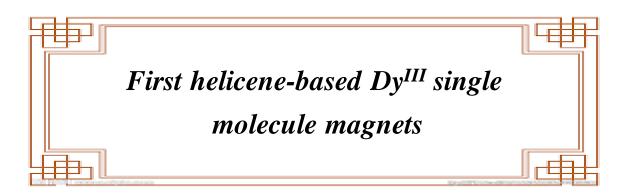
69. Whittall, I. R.; Humphrey, M. G.; Samoc, M.; Luther-Davies, B.; Hockless, D. C., J. Organomet. Chem. **1997**, 544, 189-196.

70. Harper, M. J.; Emmett, E. J.; Bower, J. F.; Russell, C. A., *J. Am. Chem. Soc.* **2017**, *139*, 12386-12389.

71. Li, D.; Hong, X.; Che, C.-M.; Lo, W.-C.; Peng, S.-M., J. Chem. Soc., Dalton Trans. **1993**, 2929-2932.

72. Irwin, M. J.; Vittal, J. J.; Puddephatt, R. J., Organometallics 1997, 16, 3541-3547.

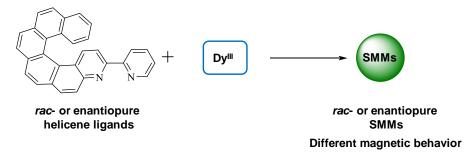
Chapter III



RENNES 2017

A Introduction:

In this chapter, we synthesized and characterized novel kinds of helicene-based Dy^{III} single molecules magnets (SMMs). The study of CD show that two enantiopure single molecule magnets display similar Cotton effect to free helicene ligands. The measurement of magnetic properties revealed that racemic enantiopure single molecule magnets showed different magnetic properties. For racemic SMM, it displayed antiferromagnetic properties, while for enantiopure SMMs, they showed ferromagnetic properties.



Scheme 3.1 Schematic represent of preparing single molecule magnets based on helicenes

A.1 Definitions

Magnets have fascinated human beings for a thousand years and played an important role in the development of society science, technology and daily life. In the 19th and 20th centuries, the nature of magnetism has been well understood, but the magnetic materials were structurally based on metals and oxides. At the end of the 20th century, the first magnetic material ¹ based on organic matters was discovered and a new research field single molecule magnets (SMMs) was opened.² The molecules which show slow relaxation of magnetization of purely molecular origin are termed single molecule magnets (SMMs). Before introducing the single molecule magnets, we would like to give a general introduction of the basic concepts of magnetism.

A.1.1 Magnetization and magnetic properties of materials

When a magnetic field H is applied to a material in vacuum, the response of the material is called magnetic induction B. In general, the magnetic field H and magnetic induction B are related by the equation:

$$\boldsymbol{B} = \boldsymbol{H} + 4\pi \boldsymbol{M}$$

, where M is the magnetization of the materials. The magnetization is defined as the magnetic moment per volume unit. M is the property of the material and depends on both the individual magnetic moments of ions, atoms, or molecules, and on how the dipole moments interact with each other.

In a diamagnetic material, all electrons are spin-paired. While in a paramagnetic material, one or more unpaired electrons exist. When the paramagnetic centers are close to each other, the interaction between the metal centers cannot be ignored and should be considered. So, paramagnetic materials can be further identified into these three types: ferrimagnetism, ferromagnetism and anti-ferromagnetism.

A.1.2 Paramagnetism

In paramagnetic material, the magnetic moments are slightly attracted to each other, thermal energy leads to random alignment of the magnetic moments, as illustrated in **Figure 3.1** (up left). When an external magnetic field is applied, the moments are induced to align, but only a small magnetization can be detected not all the magnetic moments align parallel to the applied magnetic field. When the magnetic field is removed, the magnetization will disappear.

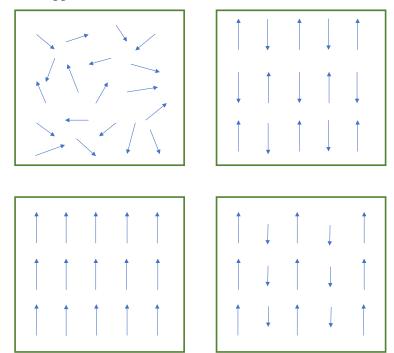


Figure 3.1 Magnetic ordering of paramagnetic (up left), anti-ferromagnetic (up right), ferromagnetic (down left), and ferrimagnetic (down right).

A.1.3 Anti-ferromagnetism

In the anti-ferromagnetic materials, the unpaired electron spins are aligned antiparallel to their adjacent moments, as illustrated in **Figure 3.1** (up right). The opposite direction of spins results in that the magnetic moments will cancel out and magnetic materials show diamagnetic behavior at absolute 0 K.

A.1.4 Ferromagnetism

In the ferromagnetic materials, the spins can be induced to align parallel to each other by the applied field, as illustrated in **Figure 3.1** (down left). Even when the external magnetic field is removed, the material can keep the alignment. Ferromagnetic materials usually display a net magnetic moment, which is because of parallel alignment of the spins.

A.1.5 Ferrimagnetism

In the ferrimagnetic materials, the exchange coupling between adjacent magnetic ions leads to anti-parallel alignment of the localized moments, like antiferromagnetic materials, as illustrated in **Figure 3.1** (down right). But ferrimagnetic materials show a net magnetic moment, which is due to the magnetization of one sublattice that is greater than that of oppositely directed sublattice.³ Ferrimagnetic materials display a magnetization upon applied field and can maintain the magnetic moment even when the external field is removed below some critical temperature.

However, the phenomenon of anti-ferromagnetism, ferromagnetism and ferrimagnetism can disappear for the thermal agitation. When the temperature is higher than a certain temperature, the thermal energy is large enough to make the magnetic ordering random. For ferromagnetic and ferromagnetic materials, this temperature is called Curie temperature, while for anti-ferromagnetic materials, that is called Neel temperature. When the temperature is high enough, all the magnetic materials will be changed into paramagnetic.

A.1.6 Susceptibility and permeability

The ration of *M* to *H* is defined as susceptibility, which is also the property of the material.

$$\chi = \frac{M}{H}$$

The susceptibility can reflect how responsive the material is to the applied magnetic field. In the thesis, we use the molar magnetic susceptibility χ_m . The molar magnetic susceptibility unit is cm³.mol⁻¹, while the unit of *H* is Oe. So, the unit of molar magnetization is cm³.Oe.mol⁻¹.

The ratio of B to H is defined as permeability, which indicates how permeable the material is to the applied field.

$$\mu = \frac{B}{H}$$

The unit of μ is gauss/Oe.

Based on the $B = H + 4\pi M$, we can obtain the relationship between permeability μ and susceptibility χ .

$$\mu = 1 + 4\pi\chi$$

A.1.7 Principles of magnetization

A.1.7.1 Curie law and Curie-Weiss law

In 1910, Pierre Curie found that the relationship between the molar magnetic susceptibility and temperature of paramagnetic materials, which fits Curie's law.

$$\chi = \frac{C}{T}$$

, where C is the Curie temperature or Curie constant, T is temperature. Curie constant is related to the spin multiplicity of the ground state.

In fact, many paramagnetic materials do not obey the Curie law, but follow a more general temperature dependence given by Curie-Weiss law.³

$$\chi = \frac{C}{T - \theta}$$

, where θ is the Weiss temperature or Weiss constant, *C* is the Curie temperature or Curie constant, *T* is the temperature. When θ is positive, there is ferromagnetic coupling interaction in the materials; when θ is negative, there is anti-ferromagnetic coupling interaction in the materials; while the θ is equal to 0, the materials are paramagnetic.

A.1.7.2 Magnetic susceptibility

To confirm the magnetic properties of the complexes, two key measurements should be carried out: *ac* susceptibility and hysteresis loop. Experimentally, the magnetic susceptibility is measured as a function of temperature, as illustrated in **Figure 3.2**.

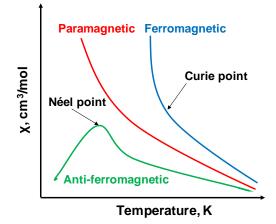
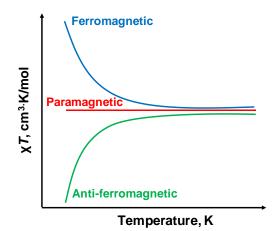


Figure 3.2 Magnetic susceptibility χ vs. temperature T.

In the magnetic susceptibility χ vs. temperature T plot, the temperature at which ferromagnetic materials become paramagnetic is called Curie temperature (T_c), while at which anti-ferromagnetic materials become paramagnetic is called Neel temperature (T_N).

Usually, we use the magnetic susceptibility multiplied by temperature χT as the function of temperature *T*, which is easy to distinguish one from the other (**Figure 3.3**).





In this diagram (**Figure 3.3**), ferromagnetism, anti-ferromagnetism and paramagnetism can be easily recognized. For ferromagnetic materials, the value of χT decreases with temperature increasing; while for anti-ferromagnetic materials, increases with temperature

increasing. The χT of paramagnetic materials keep the same all the way, and the value of it is equal to the Curie temperature.

Ferrimagnets show similar behavior to ferromagnets and display a spontaneous magnetization below critical temperature, T_c , even without an applied field. Nevertheless, the magnetization curve of typic ferrimagnets is different from that of ferromagnets (**Figure 3.4**).

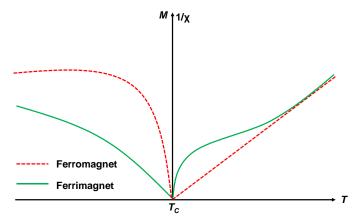


Figure 3.4 Comparison of magnetization and inverse susceptibility of ferromagnets and ferrimagnets.

Usually, the magnetic susceptibility consists of two components, the paramagnetic susceptibility (χ^{P} , positive) and diamagnetic susceptibility (χ^{D} , negative).

$$\chi = \chi^P + \chi^L$$

Diamagnetism is a property of matter and is always present, even in paramagnetic compounds. χ^{D} is essentially independent of temperature and field strength and so can be estimated based on the compound formula weight or by using Pascal's constants,³ for χ^{D} is additive.

A.1.7.3 Magnetic hysteresis loops

Magnetic hysteresis occurs when an external field is applied to the magnetic material, the atomic dipoles align to themselves with the field, magnetic moment will arrive at saturation at high field. When the applied field is removed, part of the alignment will be maintained. And the material is magnetized. When a reversal field is applied, the magnetization will be removed. Subsequently, the spin will be reversed and another saturation state will be reached again when the reversal field is increased (**Figure 3.5**).

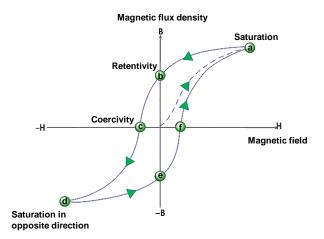


Figure 3.5 An example of hysteresis loop.

Hysteresis loop is another key measurement to confirm the magnetic properties of the complexes. Herein, what we should point out is that Superconducting Quantum Interference Device (SQUID) gives the significant contribution to measuring hysteresis loops of magnetic materials. The SQUID combines two physical phenomena: the quantization of the flux in a superconducting loop and Josephson tunneling (**Figure 3.6**).⁴ SQUID is the most sensitive detector of the magnetic flux. In general, there are two types of SQUIDs, the one is *dc*-SQUID, and the other one is *rf*-SQUID. They are operated by direct and alternating currents, respectively. In the *dc*-SQUID, there two Josephson junction is used.

Micro-SQUID was firstly developed at the beginning of 1990 in Grenoble, France (Chapelier *et al.* 1993;⁵ Wernsdorfer *et al.* 1995⁶). Subsequently, in 2001, Wernsdorfer at the L. Néel Laboratory in Grenoble extended and upgraded it (**Figure 3.7**).⁷ In the micro-SQUID, a superconducting ring of micrometric dimension is placed on the array of SQUID device. The micro-SQUID is pretty high sensitive, which allows us to detect the magnetic moments as small as 10^{-17} emu. In addition, the small size of the coils makes it possible to ramp the field fast and very short relaxation times can be measured. Even, we can use it to study the magnetic properties of single crystals in micrometric size and at very low temperature ($\ll 1$ K).⁷⁻⁹

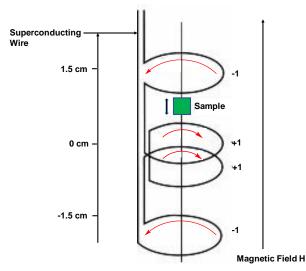


Figure 3.6 Schematic representation of SQUID equipment.

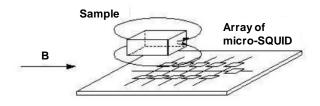


Figure 3.7 Schematic representation of magnetometer which is an array of micro-SQUID. (Reproduced from ref.⁷)

In an *ac* susceptibility measurement, the magnetic susceptibility χ_{ac} is equal to $\frac{dM}{dH}$. Compared to dc susceptibility, *ac* susceptibility has two advantages: one is that only a small applied field is needed with enough sensitivity; the other one is that it is easy to detect the dynamics of magnetization by changing the angular frequency (ω). We can measure the slow magnetization through *ac* susceptometry directly. The *ac* susceptibility is usually expressed as equation:

$$\chi(\omega) = \chi_s + \frac{\chi_T - \chi_s}{1 + i\omega\tau}$$

, where τ is the relaxation time; χ_T is the isothermal susceptibility under low frequency of ac field; χ_S is the adiabatic susceptibility under high frequency of ac field. The real and imaginary part of ac susceptibility are present as follow:

$$\chi'(\omega) = \chi_S + \frac{(\chi_T - \chi_S)}{1 + \omega^2 \tau^2}$$
$$\chi''(\omega) = \frac{(\chi_T - \chi_S)\omega\tau}{1 + \omega^2 \tau^2}$$

, where $\chi'(\omega)$ and $\chi''(\omega)$ are the real and imaginary components of susceptibility, respectively.

In the simplest case, the magnetic relaxation is related to the existence of a single model, in others words, to a Debye model.^{8, 10} The real and imaginary part of ac susceptibility can be approximated as equations given.

$$\chi'(\omega) = \frac{\chi_{dc}}{1 + \omega^2 \tau^2}$$
$$\chi''(\omega) = \frac{\chi_{dc} \omega \tau}{1 + \omega^2 \tau^2}$$

, where χ_{dc} is static magnetic susceptibility.

From the equation above, we can find that when $\omega \tau = 1$, the $\chi''(\omega)$ has the maximum value at a given temperature. At the same time, ω is equal to $2\pi v$ (v is the frequency at which the maximum of $\chi''(\omega)$ is observed). The relaxation time is determined as given equation below:

$$\tau = \omega^{-1}$$

or
$$\tau = \frac{1}{2\pi v}$$

The peak shifting in temperature *or* frequency dependence of $\chi''(\omega)$ plots is characteristic of SMMs behavior. Through fitting $\chi''(\omega)$ *vs. T* or $\chi''(\omega)$ *vs. v* data using calculations, the temperatures and frequencies at the maximum peaks can be determined. The relaxation time and the temperature obey the Arrhenius equation:

$$\tau = \tau_0 e^{\frac{U_{eff}}{kT}} \text{ or}$$
$$\ln(\tau) = \ln(\tau_0) + \frac{U_{eff}}{kT}$$

, where τ_0 is the pre-exponential factor, U_{eff} is the effective energy barrier, k is the Boltzmann constant and T is the temperature. From the equation, we can find that the energy barrier can be determined by fitting the experimental data. For example, by plotting $\ln(\tau)$ as the function of 1/T, the slope of the straight line is U_{eff}/k . Then, we can get the value of energy barrier U_{eff} .

A.1.8 Single molecule magnets (SMMs)

The molecules which show slow relaxation of magnetization of purely molecular origin are called single molecule magnets (SMMs). SMMs can maintain the magnetic moment at the molecular scale at low temperature due to its Ising-type anisotropy,⁸ which provides people an opportunity for high-density information storage, spintronics, and quantum computing.^{8, 11} The phenomenon of single molecule magnet was first discovered in early 1990 in the coordination complex made of 12 oxide and acetate bridged manganese ions (Figure 3.8).^{2, 12} After that, a new research field SMMs was opened. A SMM is a molecule which can be magnetized upon an applied magnetic field, and will remain magnetized even after removing the magnetic field. It should be pointed out that this is the property of the molecule itself. No interaction between the molecules is necessary for the phenomenon to occur, which makes the single molecule magnets different from the traditional magnetic materials. Even if you put the single molecule magnet in the solvent or fuse it into a matrix, such as a polymer, it will still display this property. SMMs have attracted increasing interest of scientists for decades. Because in SMMs, every molecule can be regarded as one bit, which results in unprecedented data densities.¹³⁻¹⁴ In addition, since traditional magnetic materials are reaching the superparamagnetic limit, SMMs can be a good alternative. Last but not the least, SMMs are in between classical and quantum magnetic systems and exhibit quantum properties.

There are two necessary requirements for materials to show SMM behavior. One is large spin ground state (S); the other one is negative uniaxial anisotropy (D), which generate the energy barrier U for the reversal of the magnetization vector. They fit the equation as follow:

$$U \approx S^2 |D|$$
 or $U \approx \left(S^2 - \frac{1}{4}\right) |D|$

The former is for integer S value, and the latter is for half-integer S value, respectively.

In 1993, R. Sessoli *et al.* reported a Mn₁₂ cluster showing highly anisotropic and long magnetization relaxation time below 4 K, as well as giving rise to hysteresis. This phenomenon is different from that of traditional bulk ferromagnets, in which the magnetization hysteresis results from the motion of domain walls.² In the Mn₁₂ cluster, four Mn^{IV} ions (green balls) stand in the inner cubic center, and are ferromagnetically coupled. Eight Mn^{III} ions (orange balls) stand in the outer shell, that are ferromagnetically coupled too (Figure 3.1). These two set of Mn ions also interact with each other, which

results in an anti-ferromagnetic coupling and a net spin ground state of $S_T = 10$. The value of S_T satisfies the requirement of large spin ground state. In addition, due to the near parallel alignment of Mn^{III} Jahn-Teller axes, the cluster Mn₁₂ show magnetic anisotropy. The two factors lead to large energy barrier U (about 60 K).

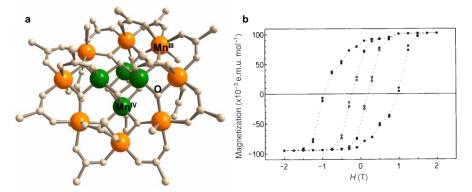


Figure 3.8 a) Structure of Mn_{12} ; b) hysteresis loop of Mn_{12} at 2.2 K (\bigcirc) and 2.8 K (\bigcirc) (picture from Ref.² Copyright of American Chemical Society).

A.1.9 Quantum tunneling of the magnetization (QTM)

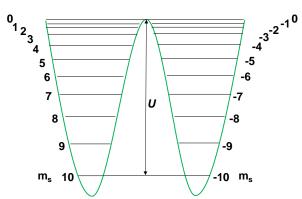


Figure 3.9 The energy barrier U for the reversal of spin directions.

The energy barrier $U = S^2 |D|$ will separate the two sub levels: one with positive m_s value stands for spin up and the other with negative m_s value stand for spin down, respectively (**Figure 3.9**). Because of thermal disturbance, when the temperature is increased, the thermal energy will be higher than the energy barrier between two sub levels, which could lead to paramagnetism and losing magnet properties. This is the main limiting factor of application of SMMs. So, we should increase the energy barrier for reversal of magnetization vector. In order to realize that, we can increase the spin ground state *S*, or increase the magnetic anisotropy |D|, or increase both of them at the same time.

There are three ways to convert the spin state. The first one is thermal relaxation, the second one is thermal-(or phonon)-assisted tunneling, the third one is ground state tunneling.

When energy levels of two sub-states coincide under an appropriate magnetic field and the states are brought to resonance, which leads to an experimental energy barrier relatively lower than the value $S^2|D|$. Because the quantum tunneling promotes the relaxation process.¹⁵ That tunneling phenomenon is the typical effect of quantum mechanism. The system can tunnel from one state to the other one when two states are separated by an energy barrier and are coupled and brought into resonance.⁸

A.1.10 Lanthanide single molecule magnets (SMMs)

Recently, lanthanide SMMs have attracted chemists' interests as the result of their high effective energy barrier (U_{eff}) and blocking temperature (T_B) (the blocking temperature T_B corresponds to the temperature at which the relaxation time of the magnetization equals the characteristic time of the experiment),⁴ which far surpasses that of transition metals SMMs.¹⁶

The lanthanide elements contain 15 elements, which are in the range from the atomic numbers 57 to 71. The electron configurations of lanthanide metals can be presented as $[Xe]4f = 6s^2$ (n=3-14 for Pr-Yb except Gd). It should be noted that 4f orbitals display extremely strong angular dependence, and lie deeply buried in core electron density (Figure 3.10).¹⁷ From Figure 3.10, we can find that the 4f orbitals are shielded by 5s and 5p orbitals and the angular momentums vary dramatically with the change in magnetic quantum number m_i , which result in the strong spin-orbit coupling interaction. Besides, because the 4f orbitals are shielded by 5s and 5p orbitals, the 4f orbitals cannot overlap with ligand orbitals and do not take part in the coordination, which leads to weak crystal field splitting. In this case, the spin-orbit coupling becomes more important. Compared to *d*-block metal, the crystal field splitting of lanthanide complexes is relatively smaller and the electronic spectra are pretty sharp. Consequently, the Ln^{III} ions except Gd^{III} (4f⁷, half filled) and Lu^{III} (4 f^{14} , full filled) show large unquenched orbital angular momentum and spin-orbital coupling, which leads to strong single-ion anisotropy, while for transition metal SMMs, the spin-orbit coupling is usually quenched. The strong anisotropy of Ln^{III} ions plays a key role in the their SMM properties. Compared to transition metal single molecule magnets (SMMs), we can find large numbers of lanthanide SMMs with relative high effective energy barriers.

To well describe the electron configuration of Ln^{III} ions, the Russell-Saunder scheme is applied, giving a multiplet denoted by ${}^{2s+1}L_J$ ($|L - S| \le J \le |L + S|$) (**Figure 3.10**). The coupling occurs between spin quantum number *S* and orbital angular momentum *L* which can be represented by the total angular momentum and the quantum number *J*. The value of *J* is in the region between (*L*+*S*) to (*L*-*S*). When the shell is less than half-filled, the ground state will be the lowest *J* value (*L*-*S*); while the shell is more than half filled, the *J* value of ground state will take the highest one (*L*+*S*). According to the Hund's rule, there is a large separation between the first exited states and the ground state *J* multiplet of lanthanide ions for the strong spin-orbital coupling except two ions Sm^{III} and Eu^{III} (Table 3.1).¹⁷ Usually, at low temperature, it may be sufficient to solely consider the ground state, which is characterized by angular momentum quantum number *J*, because of the separation of ground state and the first exited state. The interaction of the spin-orbit coupling *J* state and the crystal field generates the anisotropic character, which imposes an energy barrier to the reorientation for lanthanide based complexes.

Due to the existence of 4f orbitals, the physical and chemical properties of lanthanides are different from that of transition metals. The buried 4f orbitals are not affected by the ligand field, which leads to the result that the magnetic and spectroscopic properties are not strongly influenced by environment.

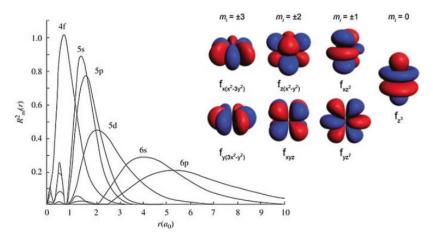


Figure 3.10 Radial distribution function of 4f, 5s, 5p, 5d, 6s, and 6p for cerium element. (picture from Ref.¹⁸ Copyright of Elesvier); *Inset* the 4f orbitals from highest magnitude m_l (left of inset, most oblate shape) to the lowest magnitude m_l (right of inset, most prolate shape). (picture from Ref.¹⁹ Copyright of The Royal Society of Chemistry).

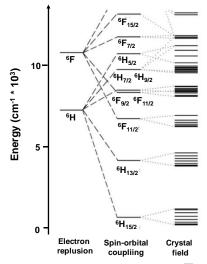


Figure 3.11 Level scheme of the electronic structures of Dy^{III} ion after the electron repulsion, spin-orbital coupling and crystal field. (Reproduced from ref.¹⁹)

Table 3.1 Ground state, g values, χT values at room temperature, first excited state, and energy separation between ground state and first excited state for Ln³⁺ ions.

Ln ³⁺	4f ⁿ	Ground state	gj	χ <i>T</i> (emu mol ⁻¹ K)	First exited state	Energy separation (cm ⁻¹)
Ce	f^1	² F _{5/2}	6/7	0.8	${}^{2}F_{7/2}$	2200
Pr	f^2	$^{3}H_{4}$	4/5	1.6	³ H ₅	2100
Nd	f^3	⁴ I _{9/2}	8/11	1.64	${}^{4}I_{11/2}$	1900
Pm	f^4	⁵ I ₄	3/5	0.9	⁵ I ₅	1600
Sm	f^5	⁶ H _{5/2}	2/7	0.09	⁶ H _{7/2}	1000
Eu	f^6	⁷ F ₀	0		$^{7}\mathrm{F}_{1}$	300
Gd	f^7	⁸ S _{7/2}	2	7.88	⁶ P _{7/2}	30,000
Tb	f^8	⁷ F ₆	3/2	11.82	${}^{7}F_{5}$	2000
Dy	f9	⁶ H _{15/2}	4/3	14.17	⁶ H _{13/2}	-
Но	f^{10}	⁵ I ₈	5/4	14.07	⁵ I ₇	-
Er	f^{11}	${}^{4}I_{15/2}$	6/5	11.48	${}^{4}I_{13/2}$	6500
Tm	f^{12}	³ H ₆	7/6	7.15	³ H ₅	-
Yb	f^{13}	${}^{2}F_{7/2}$	8/7	2.57	${}^{2}F_{5/2}$	10,000

Trivalent lanthanide ions contain unpaired electrons. They all show paramagnetic properties except for La^{III} and Lu^{III}. The magnetic moments of lanthanide ions are determined by the equation as follow:

$$\mu_{\text{eff}} = g_J \sqrt{J(J+1)}$$
or
$$\chi T = \frac{g_J \times J \times (J+1)}{8}$$

Where *J* is the total angular momentum of quantum number, and g_J can be represented as:

$$g_J = [S(S+1) - L(L+1) + 3J(J+1)]/2J(J+1)$$

It is worth to point out that Dy-SMMs easily outnumber others Ln-SMMs. Dy-SMMs have high U_{eff} value for that Dy^{III} ions have high magnetic anisotropy, and the energy gap between ground and first exited M_J levels is often large. Dy-SMMs are the most numerous because Dy^{III} is the Kramer's ion, which has an odd number of f-electrons, meaning that the ground state will always be bistable irrespective to the ligand field symmetry.²⁰

The origin of lanthanide SMMs can be dated back to 2003, when Ishikawa and his coworkers prepared a series of phthalocyanine double-decker complexes, $[Pc_2Ln]^- \cdot TBA^+$. (Ln = Tb, Dy, Ho, Er, Tm, or Yb; Pc = dianion of phtanlocyanine; $TBA^+ = N(C_4H_9)_4^+$) (**Figure 3.12**) They found that mononuclear lanthanide complexes showed slow relaxation of the magnetization, which resulted from a mechanism different from that of transition-metal-cluster SMMs .²¹

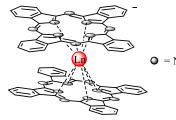


Figure 3.12 Structure of phthalocyanine double-decker complexes (Ln = Tb, Dy, Ho, Er, Tm, or Yb).

In 2006 Tang and his coworkers discovered the Dy₃ triangle complexes exhibited the coexistence of nonmagnetic ground states and SMMs behavior (anti-ferromagnetic properties) (**Figure 3.13**).²² After that, a large number of papers about lanthanide SMMs have been reported.^{20, 23-24}

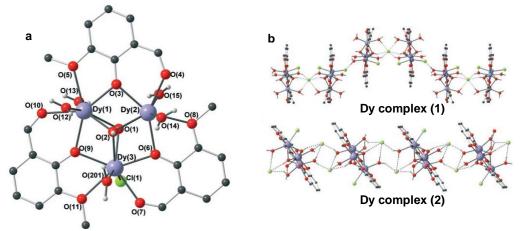


Figure 3.13 a) Crystal structure of the triangular units in Dy complex (1) and Dy complex (2) with numbering scheme. In Dy complex (1), there is 50:50 disorder of Cl and H2O at O (201) as described in the text. Intratriangle Dy...Dy distances: Dy complex (1) 3.50-3.53 Å; Dy complex (2) 3.51-3.54 Å. b) the hydrongen bonding is highlighted between trinuclear units in Dy complex (1) and Dy complex (2). Color scheme: blue Dy^{III}, red O, green Cl, dark gray C, white H.

(Reproduced from ref.²²)

A.1.11 Chiral single molecule magnets (SMMs)

The potential properties of SMMs such as ferroelectricity,²⁵⁻²⁶ conductivity,²⁷ luminescence,²⁸⁻³¹ chiroptical activity,³² and non-linear optical properties,³³ have been already explored. In comparision, the examples about combining the chirality and molecular magnetism (especially SMMs) are rarely reported. A breakthrough came from the synergy between chirality and molecular magnetism with the evidence of strong magneto-chiral dichroism in enantiopure 3D-ordered ferromagnets,³⁴ and in single chain magnets.³⁵

In 2011, Euan K. Brechin's group reported the first chiral SMM. This [Mn(III)₉] partial supertetrahedron was obtained from achiral starting materials (**Figure 3.14**). The energy barrier of the SMM for reversal of magnetization vector was about 30 K.³⁶

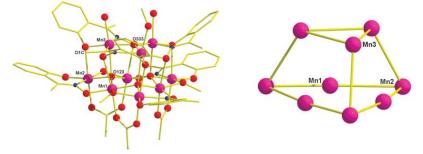


Figure 3.14 Structure of [Mn(III)₉] (left); partial supertetrahedron metallic skeleton (right). (Reproduced from ref.³⁶)

In 2013, Liu's group used enantiopure chiral β -diketonate ligands to construct homochiral Dy(III) single-ion magnets (SIMs) (**Figure 3.15**). The authors found that the capping diamine group (bipyridine for complexes *d*-1 and *l*-1; 1,10-phenanthroline (phen) for complexes *d*-2 and *l*-2) played an important role on the structure and magnetic properties (especially relaxation process) of two pairs of enantiopure Dy(III) complexes *d*-1, *l*-1, *d*-2 and *l*-2. This work revealed that it was was an efficient method to obtain homochiral lanthanide SIMs or SMMs to use enantiopure chiral β -diketonate ligands.³⁷

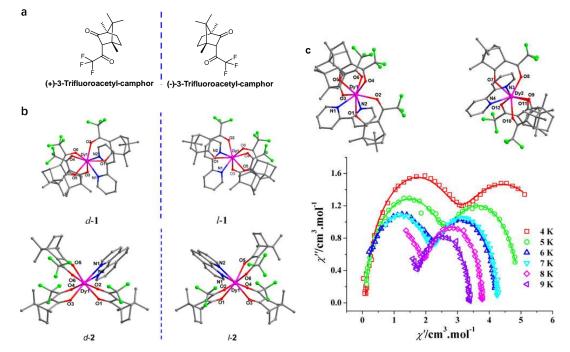


Figure 3.15 a) Molecular structures of ligands; b) crystal structures of Dy(III) single-ion magnets *d*-1, *l*-1, *d*-2, and *l*-2; c) magnetic behavior (two-step relaxation process) of cocrystal of *d*-1 and *l*-1. Color schemes: lilac Dy^{III}, red O, blue N, green F, gray C. (Reproduced from ref.³⁷)

In 2015, Long's group developed a high-temperature ferroelectric material based on chiral Zn^{2+}/Dy^{3+} complexes, which combined enantiopure Zn^{2+} -Schiff base antenna complexes and Dy^{III} ions and displayed single-ion magnet behavior and lanthanide luminescence (**Figure 3.16**).²⁸ The authors investigated the relationship between low-temperature magnetic slow relaxation and the optical properties as well as electric polarization and the crystal structure. At high temperature, the material showed paramagnetic property, while at low temperature, it exhibited superparamagnetic property.

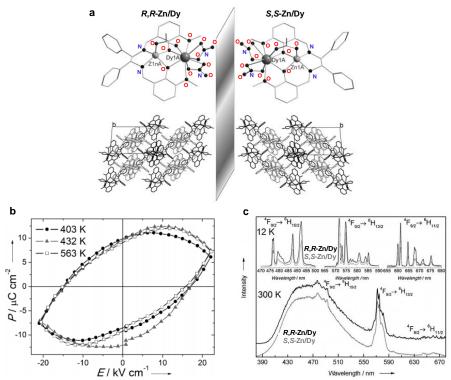


Figure 3.16 a) Molecular structures of *R*, *R*-Zn/Dy and *S*, *S*-Zn/Dy; b) dielectric hysteresis loop for *R*, *R*-Zn/Dy at different temperatures; c) luminescence spectra of *R*,*R*-Zn/Dy and *S*,*S*-Zn/Dy complexes at room temperature and at 12 K. (Reproduced from ref.²⁵)

B Design of chiral SMMs based on helicenes

So far, though chirality and SMM properties have been merged in the same molecule, differences between the SMM behavior of enantiopure and racemic forms have not been reported. So, in this part of work, we explain how we combined helicenes and SMMs to design and prepare racemic and enantiopure SMMs based on the 3-(2-pyridyl)-4-aza[6]-helicene **19** and compared the differences between their solid-state magnetic properties. We chose Dy^{III} as metal center for its large spin ground state and negative uniaxial anisotropy, which could generate the energy barrier for reversal of magnetization vector. Helicenes are chiral and configurationally stable and are known to display strong CD spectra and optical rotation values.³⁸⁻³⁹ In addition, 2-2'-bipyridine (bpy) derivatives are extensively used bidentate ligands in coordination chemistry.⁴⁰ Several Dy^{III} complexes with bpy ligand displayed SMM behavior for the well-adapted electronic distribution given by the N₂O₆ coordination sphere.⁴¹⁻⁴⁴ Accordingly, the stable 3-(2-pyridyl)-4-aza[6]-helicene **19** appears to be an appropriate chiral ligand for the coordination reaction to lanthanides, and promising for optimized magnetic and optical properties. The ligand **19**

has already been prepared in racemic and in enantiopure forms in our group, and has been used to prepare the first CPL-active rhenium(I) complexes⁴⁵ and cycloplatinated complexes behaving as acid-base triggered CPL switches.⁴⁶

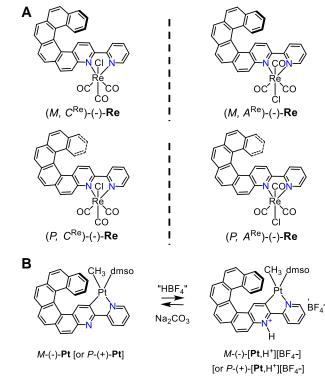
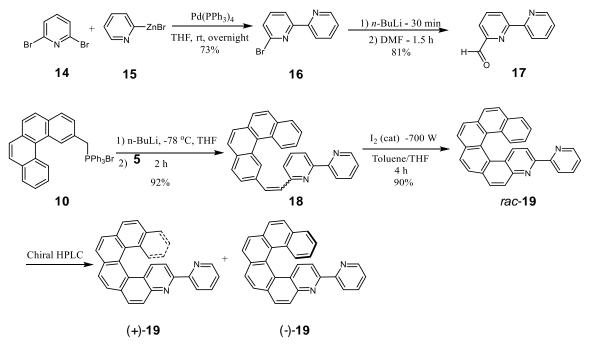


Figure 3.17 A) Structures of helicenes based rhenium (I) complexes; B) acid-base switchable helicene based platinated complexes.

The Dy^{III} complexes were well characterized by X-ray crystallography, CD spectroscopy, elemental analysis, temperature dependences of $\chi_m T$, temperature dependence of the relaxation time, magnetic hysteresis loops. *Ab initio* calculations were also performed to determine the intermolecular dipolar coupling and to interpret the different low-temperature magnetic behavior between enantiopure and racemic SMMs. This work has been performed in collaboration with chemists, physicists and theoreticians and has been published in Chemical Communications and Magnetochemistry journal.⁴⁷⁻⁴⁸

C Results and discussion

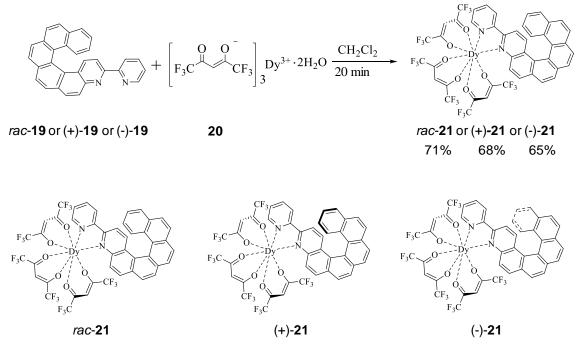
C.1 Synthesis of ligands



Scheme 3.2 synthesis process of ligands rac-19, (+)-19 and (-)-19.

The ligand 3-(2-pyridyl)-4-aza[6]helicene **19** was prepared according to the literature (**Scheme 2.2**).⁴⁶ Firstly, a Negishi coupling was employed between 2,6-dibromopyridine **14** and the 2-bromopyridine zinc complex **15**, giving 6-bromo-2,2'-bipyridine **16**. Then the formylation of 6-bromo-2,2'-bipyridine **16** was achieved by n-BuLi/DMF at low temperature to obtain [2,2'-bipyridine]-6-carbaldehyde **17**. The next step was a Wittig reaction between 2-methylbenzophenanthrenetriphenylphosphonium bromide **10**⁴⁹ and [2,2'-bipyridine]-6-carbaldehyde **17**, yielding a mixture of *cis*- and *trans*-stilbenoid precursor **18**. Finally, a photocyclization of compound **18** using a 700 W Hg lamp yielded helicenic bipy ligand **19**. In collaboration with Nicolas Vanthuyne in Aix Marseille University, two enantiopure ligands (+)-**19** and (-)-**19** were obtained by separation using chiral HPLC (Chromatographic condition: Chiralpak IC (250×10 mm), thermostated at 30 °C , hexane/ethanol/chloroform 90/5/5 as mobile phase, flow-rate = 5 ml/min, UV detection at 385 nm).

C.2 Synthesis of Dy^{III} SMMs



Scheme 3.3 Synthesis process of Dy^{III} complexes *rac*-21, (+)-21 and (-)-21.

*Rac-***19** ligand then was reacted with tris(1,1,1,5,5-hexafluoroacetyl-acetonate)-bis-(aqueous) Dy^{III} in CH₂Cl₂ solution for 20 min. Then slow diffusion of *n*-hexane in the mother solution afforded yellow single crystals of *rac-***21**. Crystals of (+)-**21** and (-)-**21** were prepared through the same process. This work was performed in collaboration with Dr. Fabrice Pointillart.

C.3 X-Ray diffraction analysis

Complex *rac*-21 crystallizes in the triclinic centrosymmetric space group P-1 (Figure 3.10), which is an achiral crystal. (+)-21 and (-)-21 were prepared through the same process. The space groups of crystals (+)-21 and (-)-21 were both P2₁2₁2₁, which were non-centrosymmetric,⁵⁰ and were applied to analysis of the coordination polyhedron around Dy^{III} ion in *rac*-21 • 0.5H₂O, (+)-21, and (-)-21. The unique Dy^{III} ion resides in a N₂O₆ triangular dodecahedron environment with D_{2d} symmetric factor. The six oxygen and two nitrogen atoms come from the three hfac⁻ anion and one helicene ligand, respectively. From crystal structure, we can find that, in *rac*-21, both enantiomers are present in the cell, and heterochiral dimers were formed in the presence of π - π interactions between bi-pyridyl fragments of *P*- and *M*-helicene ligands with distance of 3.390 Å (Figure 3.19a). The Dy-

Dy shortest intermolecular distance was measured to be 8.789 Å. The detail crystal structures of (+)-21 and (-)-21 can be seen in the experiment part (**Figure S1**, **S2** and **S3**). Form a macroscopic view, (+)-21 and (-)-21 formed *P*- and *M*- helical structure, respectively (**Figure 3.19b**). From a molecular point of view, the structures of (+)-21 and (-)-21 are similar to the one of **19** with a Dy^{III} ion in a N₂O₆ triangular dodecahedron environment (Table S2, Experiment part). However, crystal packing highlight drastic changes (**Figure 3.19 b**). The (-)-**19** and (+)-**19** ligands continuously interact through π - π interactions (head to tail style) to form (*M*) or (*P*) helical arrangements. The distance between bipyridyl fragment and helicene terminal fragment was 3.531 Å. The Dy-Dy shortest intermolecular distance was measured to be 10.127 Å, which was notably longer than the distance measured for the racemic mixture. It is worth mentioning that the Dy^{III} ion is not a stereogenic center, but is placed in a chiral environment due to the presence of the helicene moiety. The X-ray structures were solved by Vincent Dorcet and Fabrice Pointillart.

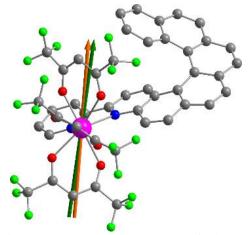


Figure 3.18 Representation of the crystallographic structure of 8 in *rac*-1·0.5C₆H₁₄. Experimental (dark green) and theoretical (orange) main anisotropy axes. Dy, O, N, C and F are shown in purple, red grey and green, respectively. Only the P enantiomer is shown and H atoms are omitted for clarity.

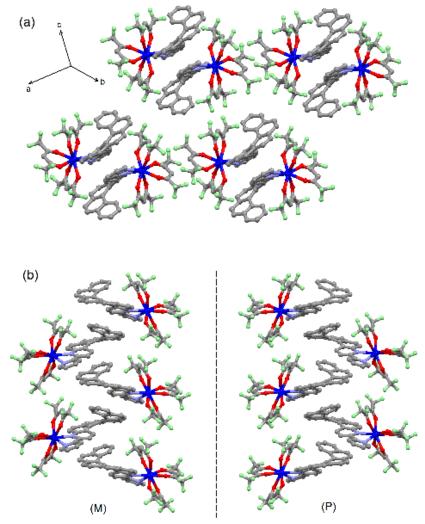


Figure 3.19 Crystal packing of (a) *rac*-1 and (b) (-)-1 (left) and (+)-1 (right), highlighting the (M) and (P) helicoidal arrangements. The dash line represents the mirror between both enantiomers.

C.4 Chiroptical spectroscopy

Because the complexes contained helicene unit which showed strong CD signal and optical rotation, we studied two enantiopure complexes' chiroptical properties. (+)-21 and (-)-21 showed mirror-image electronic dichroism spectra with Cotton effect of opposite signs at $\lambda_{max} = 370$, 354, 334, 275, 266 and 247 nm, which meant that they were configurationally stable in solution state (Figure 3.20). The ECD spectra of the complexes are very similar to those of the free ligands. No Cotton effect could be attributed to those of the hfac⁻ anions and main part of the optical activity came from the helicene ligand. The specific rotations of (-)-21 and (+)-21 were -1050 °cm² dmol⁻¹ and +1190 °cm² dmol⁻¹, respectively, which were lower than those for (-)-19 (-1800 °cm² dmol⁻¹) and (+)-19 (+1800 °cm² dmol⁻¹).

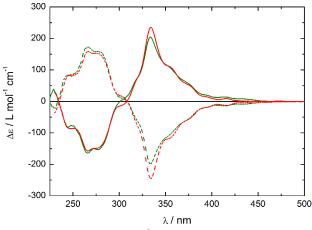


Figure 3.20 Experimental (CH₂Cl₂, ca. 5×10^{-5} M) ECD spectra of enantiopure (-)-19 (dash red line) and (+)-19 (full red line) and respective Dy^{III} complexes (-)-21 (dash green line) and (+)-21 (full green line).

C.5 Magnetic properties

The magnetic properties were measured by Dr. Olivier Cador and T. Guizouarn. The Dy^{III} complexes usually showed SMMs properties. The magnetic properties of complexes were studied in the solid state. In the region of high temperature, there were no major differences between the magnetic properties of the racemic and enantiomerically pure materials are observed. Down to 15 K, magnetic susceptibility multiplied by temperature $\chi_m T$ decreased monotonically from 13.95 cm³ K mol⁻¹ (14.17 expected for an isolated Dy^{III} ⁶H_{15/2} ground state).⁵¹ Only in the low temperature range difference emerged. When we decreased the temperature continually, for *rac*-21, the magnetic susceptibility multiplied by temperature $\chi_m T$ decreased continuously; while for (-)-21 and (+)-21, $\chi_m T$ increased slightly (**Figure 3.21**, and **Figure S5**). As we mentioned before, if the $\chi_m T$ increases with temperature increasing, it is anti-ferromagnetic; if the $\chi_m T$ decreases with temperature increasing, it is paramagnetic, thus, highlighting possible anti-ferromagnetic coupling in *rac*-21 • 0.5C₆H₁₄, whereas ferromagnetic coupling was expected for (+)-21 and (-)-21.

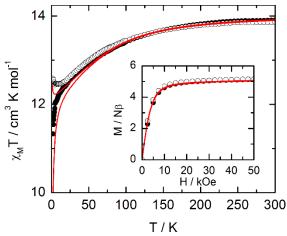


Figure 3.21 Temperatures dependences of $\chi_M T$ for compounds *rac*-**21**.0.5C₆H₁₄ (black circles) and (+)-**21** (white circles). In inset the field variations of the magnetization at 2 K. Full red lines correspond to the simulated curves from *ab-initio* calculations

The saturation magnetization (~ 5 N β for all the complexes, see Figure 3.21 inset) at 2 K confirmed that the ground state is essentially described by the Ising components $M_J = \pm$ 15/2. No evident pathway to promote super-exchange interactions between lanthanides emerges from the crystal structures, so only dipolar coupling can be supposed to operate here. To shed more light on the already reported results, rotating single-crystal magnetometries in synergy with quantum chemical calculations (CASSCF/SI-SO, see experiment part) have been performed on $rac-21 \cdot 0.5C_6H_{14}$. The orientation of the gtensor, considering the P-1 space group and an effective spin of S = 1/2, can be routinely determined by measuring the magnetization of a single crystal in three perpendicular planes (Figure S6 and Figure S7, Experiment part). ⁵²⁻⁵³ As expected, an Ising-type anisotropy with the largest g value of 18.9 (20 expected for a pure $M_J = \pm 15/2$ ground state) was revealed with the orientation of the main magnetic axis along the most negatively charged direction of the coordination polyhedron (Figure 3.18).⁵⁴ The calculated g-tensor accorded in magnitude as well as in orientation with the experimental data (Figure 3.18). The angle between experimental and calculated g_z value was 3.5° , while the magnitude of the calculated g_z is 19.8, confirming the Ising-type anisotropy. In addition, the composition of the wavefunction certified the $M_J = \pm 15/2$ nature of the ground state doublet. We also found that the energy gap between ground state and first exited $M_{\rm J}$ level was large.

Theoretical calculations performed by Boris Le Guennic and Guglielmo Fernandez Garcia enabled to interpret the magnetic properties. The space group of (+)-21 and (-)-21 were both $P2_12_12_1$, which leaded to four orientations of the molecules in the crystals, discarding easy experimental determination of the *g*-tensor. However, the excellent agreement between experimental and *ab initio* data for *rac*-21 ensured the reliability of the computational results on (+)-21. The orientation and amplitudes of the *g*-tensor are identical to those of *rac*-21 as well as the composition of the ground state doublet, in other words, mainly $M_J = \pm 15/2$ (Figure S8). However, a good agreement was found between the calculated and experimental field-dependences of the magnetization (inset Figure 3.21). As the magnetic susceptibility χ is equal to M/H ($M = \chi * H$), we can find some differences of magnetic susceptibility χ between *rac*- and enantiopure SMMs at 2 K. But it was relatively less straightforward than $\chi_M T vs$. *T* curves to distinguish them.

To well understand the different magnetic behavior shown in the low temperature regime by the racemic and enantiopure complexes, the calculation of an average isotropic dipolar coupling J_{dip} generated by the first neighbouring molecules was applied (computational approach is shown in Experiment part). In this framework, antiferromagnetic ($J_{dip} < 0$) and ferromagnetic ($J_{dip} > 0$) interaction between pair of molecules were computed in both racemic and enantiopure complexes. Due to the different stacking style in solid state, the Dy-Dy shortest distances are also different, which resulted in that in the case of *rac*-**21** $0.5C_6H_{14}$ the average dipolar coupling was antiferromagnetic ($J_{dip} = -0.055$ cm⁻¹), while it became ferromagnetic ($J_{dip} = 0.0033$ cm⁻¹). The magnitudes of the average Jdip are small with respect to the single pairwise dipolar couplings in both crystal packings, but the latter cancel each other in the averaging, leading to a weak coupling but of different nature. Accounting for this effect in the calculations, an excellent agreement between the ab initio results and the experimental data (**Figure 3.21**) is achieved.

The SMMs properties are only present at low temperature. As mentioned before, if the materials behave as SMM, we can find a maximum value of imaginary susceptibility χ'' , which is related to temperature to frequency. The maximum of χ'' will be observed when the frequency satisfies the relationship $\omega = \tau^{-1}$, so the relaxation time can be calculated by equation $\tau = \omega^{-1}$. Dynamic magnetic properties also reveal differences between the racemic and enantiomerically pure materials. *rac*-**1** • 0.5C₆H₁₄ can be seen as a fast SMM

with the characteristic maximum on the curves of the out-of-phase component (imaginary susceptibility) of ac susceptibility, $\chi_{M''}$, *vs.* frequency of the oscillating field lying outside the available time window (**Figure 322**) for *rac*-**21**•0.5C₆H₁₄ at 2 K. For **1**(+) and **1**(-), such maximum falls at 57 Hz in zero external dc field (**Figure 3.22** and **Figure S15**, **Table S5** and **S6**) at 2 K. The τ *vs.* T curves (τ being the relaxation time of the magnetic moment extracted from the ac vs. frequency curves with an extended Debye model) for (+)-**21** and (-)-**21** are shown on **Figure 3.23**.

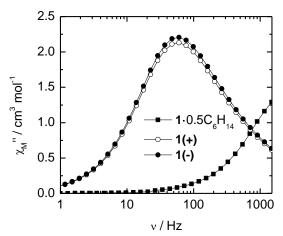


Figure 3.22 Frequency dependences of the out-of-phase component of the ac susceptibility, χ_M ", at 2 K measured in the absence of external dc field for *rac*-**21**.0.5C₆H₁₄, (+)-**21** and (-)-**21**.

Fitting with a modified Arrhenius law ($\tau^{-1} = \tau_0^{-1} \exp(-\Delta/kT) + \tau_{TT}^{-1}$) accounting for a temperature independent process provides $\tau_0 \approx 9.5(4) \times 10^{-6}$ s, $\Delta = 27(3)$ K and $\tau_{TT} = 2.0(2) \times 10^{-3}$ s. The application of an external field slows down the relaxation that appears, for (+)-**21** (Figure S14), to be the sum of two relaxation processes: one growing at the expense of the other. The slowest unique relaxation appears at the optimum field of 1 kOe (Figure S14). For both (+)-**21** and (-)-**21** the relaxation times follow two thermally activated regimes (reg0 and reg1). (Fig. 3.23 and Figure S15, Tables S4, S5, ESI[†]) with $\tau_0 = 6(6) \times 10^{-9}$ s, $\Delta_0 = 101(11)$ K, $\tau_1 = 1.4(2) \times 10^{-4}$ s and $\Delta_1 = 21(1)$ K for both (+)-**21** and (-)-**21**.⁵⁵⁻ At 1 kOe the relaxation time of the magnetic moment in *rac*-**21**.0.5C₆H₁₄ is tractable (Figure S16 and Table S7) with an extended Debye model. Like for the enantiomerically pure materials, two thermally activated regimes (reg0 and reg1) are identified with $\tau_0 \approx 9(7) \times 10^{-8}$ s and $\Delta_0 \approx 59(5)$ K for the fastest regime reg0 and $\tau_1 \approx 1.6(3) \times 10^{-4}$ s and $\Delta_1 \approx 17(1)$ K for reg1. Nevertheless, whatever the temperature and the magnetic field, the racemic SMM relaxes much faster than the enantiopure SMM. This is supported by the calculated

magnetic transition moments (**Figure S17** and **S18**) that show a transition probability between the ground-state Kramers doublets⁸ which is more than two times higher in the racemic compared to the enantiopure compound.

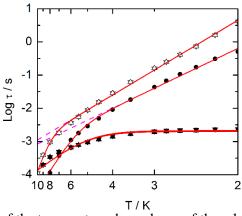


Figure 3.23 Log scale plots of the temperature dependence of the relaxation time for (+)-21 and (-)-21 in up and down triangles and *rac*-21.0.5C₆H₁₄ in circles. Empty symbols indicate measurements in zero external dc field while full symbols indicate measurements at 1 kOe. Red lines correspond to the best-fitted curves with modified Arrhenius laws (see text). Dashed pink lines are the high temperatures extension of the regime reg₁.

Hysteresis loops measured at the lowest temperature (500 mK) also suggest different relaxation rates. While the loop is closed at any field for the racemic form, it is opened infield for both enantiomerically pure materials (**Figure. 3.24**) with a maximum opening of 800 Oe centred at 900 Oe. Of course, all the curves shrink at zero field owing to the fast zero field relaxation. At a given field the magnetization of *rac*-**21**.0.5C₆H₁₄ is lower than (+)-**21** and (-)-**21** because of the observed anti-ferromagnetism in the racemic form versus ferromagnetism in the enantiomerically pure material. This example unambiguously illustrates that the enantiomerically pure material might show better magnetic properties than the racemic parent depending on the reorganization of the crystal structure between the various forms. As a matter of fact, dissolution of solid materials in non-coordinating solvent such as dichloromethane gives undiscernible magnetic properties for complexes *rac*-**21** and (+)-**21**.

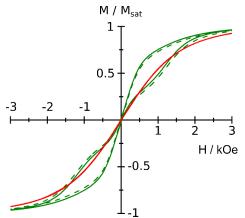


Figure 3.24 Magnetic hysteresis loops recorded at 500 mK and measured at a sweep rate of 16 Oe s⁻¹ for (+)-21 (full green line), (-)-21 (dashed green line) and *rac*-21.0.5C₆H₁₄ (red line).

D Experiment part

D.1 General Procedures and Materials.

The precursors $Dy(hfac)_{3}\cdot 2H_2O$ (hfac = 1,1,1,5,5,5-hexafluoroacetonate anion),⁵⁷ racemic **19** and optically pure 3-(2-pyridyl)-4-aza[6]-helicene₂ ((-)-**19** and (+)-**19**) were synthesized following previously reported methods. All other reagents were purchased from Aldrich Co., Ltd. and used without further purification

D.2 Synthesis of complexes

[**Dy**(hfac)₃(19)]·0.5C₆H₁₄ (*rac*-21·0.5C₆H₁₄). Dy(hfac)₃·2H₂O (16.4 mg, 0.02 mmol) were dissolved in 5 mL of CH2Cl2 and then added to a solution of 5 mL of CH2Cl2 containing 8.3 mg of ligand 19 (0.02 mmol). After 20 minutes of stirring, 35 mL of *n*-hexane were layered at room temperature in the dark. Slow diffusion leads to yellow single crystals which are suitable for X-ray studies. Yield: 17.5 mg (71 %). Anal. Calcd (%) for C₄₈H₂₈DyF₁₈N₂O₆: C 46.71, H 2.27, N 2.27; found: C 46.59, H 2.16 N, 2.29.

[**Dy**(**hfac**)₃((-)-**19**)] ((-)-**21**) and [**Dy**(**hfac**)₃((+)-19)] ((+)-**21**). The same experimental protocol than for the racemic complex is used except than (-)-**19** and (+)-**19** were used instead of **19**. Slow diffusions following by slow evaporations lead to light yellow single crystals which are suitable for X-ray studies. Yield: 15.5 mg (65 %) and 16.2 mg (68 %) respectively for (-)-**19** and (+)-**19**. Anal. Calcd (%) for C₄₅H₂₁DyF₁₈N₂O₆: C 45.37, H 1.76, N 2.35; found: C 45.39, H 1.81, N 2.38.

D.3 Crystallography.

Single crystals of *rac*-21·0.5C₆H₁₄, (-)-21 and (+)-21 were mounted on a APEXII Bruker-AXS diffractometer (MoK α radiation source, $\lambda = 0.71073$ Å, T = 150(2) K) for data collection, from the Centre de Diffractométrie (CDIFX), Université de Rennes 1, France. Structures were solved with a direct method using the SIR-97 program and refined with a full matrix least-squares method on F2 using the SHELXL-97 program for all the compounds. Crystallographic data are summarized in Table S1. Complete crystal structure results as a CIF file including bond lengths, angles, and atomic coordinates are deposited as Supporting Information.

D.4 Physical Measurements.

The elementary analyses of the compounds were performed at the Centre Régional de Mesures Physiques de l'Ouest, Rennes. Specific rotations (in deg cm² g⁻¹) were measured in a 1 dm thermostated quartz cell on a Perkin-Elmer- 341 polarimeter. Circular dichroism (in M-1 cm-1) was measured on a Jasco J-815 Circular Dichroism Spectrometer (IFR140 facility, Biosit platform, Université de Rennes 1). The dc magnetic susceptibility measurements were performed on solid polycrystalline sample with a Quantum Design MPMS-XL SQUID magnetometer between 2 and 300 K in an applied magnetic field of 200 Oe in the 2-20 K temperature range, 2 kOe between 20 and 80 K and 10 kOe above. These measurements were all corrected from the diamagnetic contribution of the sample holder as well as the intrinsic diamagnetism calculated with Pascal's constants. Ac measurements are performed with 3 Oe oscillating field amplitude. Hysteresis loops at 500 mK have been recorded with the help of a 3He insert (iHelium3) adapted to SQUID magnetometer. The magnetic field is then swept in hysteresis mode and the magnetic moment measured with RSO head. The sweep rate is estimated to be close to 16 Oe s-1. The dc and ac magnetic susceptibility of the dichloromethane solution have been measured with a modified NMR tube containing 0.2 mL of solution of concentration 6 mM. The ac data were corrected from the diamagnetism of dichloromethane and from the sample holder.

D.5 Computational Details.

For the calculation of the isotropic dipolar coupling between two molecules we employed the following formula:⁵⁸

$$J_{dip}^{12} = \frac{1}{3} Tr \left\{ \frac{\mu_B^2}{R_{12}^3} (g_1 \cdot g_2 - 3(g_1 \cdot R_{12})(R_{12} \cdot g_2)) \right\}$$

Where g_1 and g_2 are the *g*-tensors calculated *ab initio*, R_{12} is the distance vector between two Dy^{III} atoms and μ_B is the Bohr magneton. Since J_{dip} is proportional to R_{12}^{-3} , we only took into account the first neighbors to calculate the average coupling values. Figures S10 and S11 show the schematics maps of the dipolar couplings in the crystal structures. The corresponding J_{dip} for each couple are collected in Table S5. The temperature dependence of χ MT accounting for the average J_{dip} were calculated with the SINGLE_ANISO routine.

Compounds	$[Dy(hfac)_3(19)] \cdot 0.5C_6H_{14}$	[Dy(hfac) ₃ ((-)- 19)]	$[Dy(hfac)_3((+)-19)]$
1	$rac-21.0.5C_{6}H_{14}$	(-)-21	(+)-21
Formula	$C_{48}H_{28}DyF_{18}N_2O_6$	$C_{45}H_{21}DyF_{18}N_2O_6$	$C_{45}H_{21}DyF_{18}N_2O_6$
$M / g.mol^{-1}$	1233.22	1190.14	1190.14
Crystal system	Triclinic	Orthorhombic	Orthorhombic
Space group	-P-1 (N°2)	P2 ₁ 2 ₁ 2 ₁ (N°19)	P2 ₁ 2 ₁ 2 ₁ (N°19)
	a = 13.2160(5) Å	a = 11.1191(9) Å	a = 11.1110(6) Å
	b = 13.9132(6) Å	b = 17.6604(18) Å	b = 17.6697(12) Å
Cell parameters	c = 14.5959(6) Å	c = 22.693(2) Å	c = 22.3965(14) Å
Cell parameters	$\alpha = 67.984(2)^{\circ}$		
	$\beta = 72.454(2)^{\circ}$		
	$\gamma = 84.724(17)$ °		
Volume / Å ³	2371.7(2)	4456.2(7)	4456.0(5)
Z	2	4	4
T / K	150 (2)	150(2)	150(2)
2θ range / °	$3.14 \le 2\theta \le 54.92$	$2.92 \le 2\theta \le 54.98$	$2.92 \le 2\theta \le 54.96$
ρ_{calc} / g.cm ⁻³	1.727	1.774	1.774
μ / mm ⁻¹	1.698	1.804	1.804
Number of reflections	38886	25548	15348
Independent	10755	10112	9283
reflections	10733	10112	9283
R _{int}	0.0258	0.1334	0.0265
$Fo^2 > 2\sigma(Fo)^2$	9745	5232	8235
Number of variables	701	608	649
R_1 , w R_2	0.0369, 0.1012	0.0814, 0.1666	0.0377, 0.0803

Table S1. X-ray crystallographic data for the complexes 21.0.5C₆H₁₄, (-)-21 and (+)-21.

Table S2. SHAPE analysis of the coordination polyhedron around the Dy^{III} ion in *rac*-1.0.5C₆H₁₄, 1(-) and 1(+).

	CShM _{SAPR-8} (square antiprism) D _{4d}	CShM _{BTPR-8} (biaugmented trigonal prism) C _{2v}	CShM _{TDD-8} (triangular dodecahedron) D _{2d}
rac-21	1.613	2.288	0.784
(-)-21	2.429	2.081	0.504
(+)-21	2.348	2.057	0.486

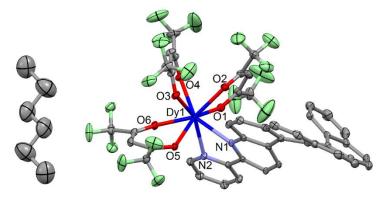


Figure S1. ORTEP view of the asymmetric unit for *rac*-21.0.5C₆H₁₄. Thermal ellipsoids are drawn at 30% probability. Hydrogen atoms are omitted for clarity.

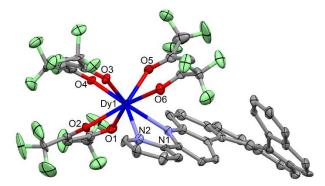


Figure S2. ORTEP view of the asymmetric unit for (-)-21. Thermal ellipsoids are drawn at 30% probability. Hydrogen atoms are omitted for clarity.

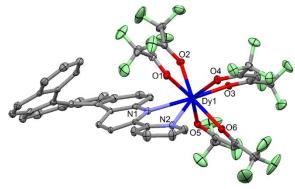


Figure S3. ORTEP view of the asymmetric unit for (+)-21. Thermal ellipsoids are drawn at 30% probability. Hydrogen atoms are omitted for clarity.

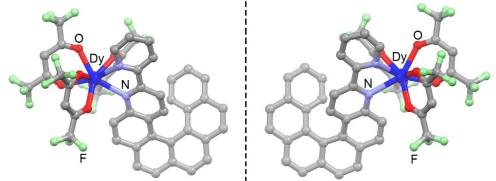


Figure S4. Molecular structures of (-)-21 (left) and (+)-21 (right) complexes. The dash line represents the mirror between both enantiomers. H atoms are omitted for sake of clarity.

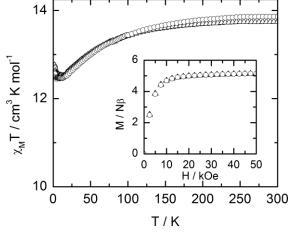


Figure S5. Temperatures dependences of $\chi_M T$ for (+)-21 (circles) and (-)-21 (triangles). In inset the field variations of the magnetization at 2 K.

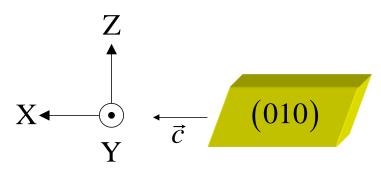


Figure S6. Oriented single crystal of *rac*-21.0.5C₆H₁₄ with the XYZ crystal reference frame.

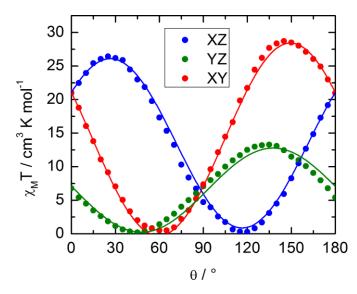


Figure S7. Angular dependence of $\chi_M T$ of a single crystal rotated of *rac*-21.0.5C₆H₁₄ in the three perpendicular planes XY, XZ and YZ with H = 1 kOe at 2 K. Best fitted curves in full lines (see here below).

Molar magnetic susceptibility was fitted with:

$$\chi_{M}T = \frac{MT}{H} = \chi_{\alpha\alpha}cos^{2}\theta + \chi_{\beta\beta}sin^{2}\theta + 2\chi_{\alpha\beta}sin\theta cos\theta$$

where α and β are the directions X, Y and Z and θ is the angle between H and α . After simultaneous least-square fitting of the three curves on Figure S7 the susceptibility tensor in the crystal frame (XYZ) is:

$$\chi_M T = \begin{pmatrix} 21.05 & -12.54 & 10.09 \\ -12.54 & 7.087 & -6.242 \\ 10.09 & -6.242 & 5.912 \end{pmatrix} \text{cm}^3 \text{ K mol}^{-1}$$

Principal values and direction of the susceptibility tensor in the XYZ crystal frame:

$$\chi_{M}T\begin{pmatrix}0.427\\0.883\\0.192\end{pmatrix} = -0.134, \chi_{M}T\begin{pmatrix}0.439\\-0.016\\-0.898\end{pmatrix} = 0.869, \chi_{M}T\begin{pmatrix}0.790\\-0.468\\0.394\end{pmatrix} = 33.53 \text{ cm}^{3} \text{ K mol}^{-1}$$

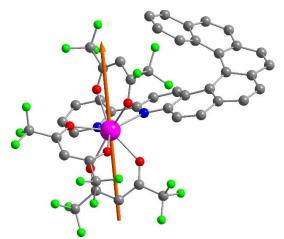


Figure S8. Representation of the crystallographic structure of (+)-21 (H atoms are omitted for clarity) with theoretical main anisotropy axis.

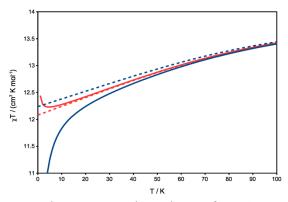


Figure S9. *Ab initio* computed temperature dependence of $\chi_M T$ between 0 and 100 K for *rac*-21 (blue lines) and (+)-21 (red lines). Dotted lines show the $\chi_M T$ in absence of J_{dip} , while full lines include the calculated dipolar coupling.

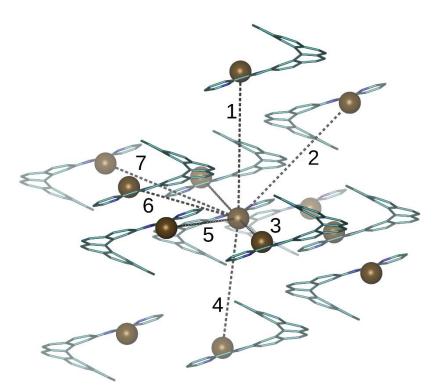


Figure S10. Schematic representation of the various dipolar coupling channels in *rac*-**21** \cdot 0.5C₆H₁₄. Corresponding *J*_{dip} values are given in Table S5.

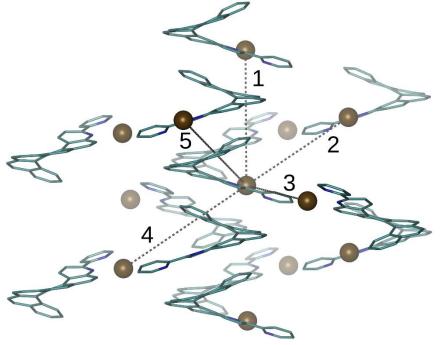


Figure S11. Schematic representation of the various dipolar coupling channels in (+)-21. Corresponding J_{dip} values are given in Table S5.

	$rac-21.0.5C_6H_{14}$	(+)-21
1	0.11	-0.22
2	-0.04	0.03
3	-0.20	0.09
4	0.18	0.19
5	0.03	0.03
6	0.09	
7	-0.06	
J_{dip}	-0.055	0.0033

Table S3. Calculated dipolar coupling values (in cm⁻¹) for the main pathways for *rac*-**21** \cdot 0.5C₆H₁₄ and (+)-**21**. Average *J*_{*dip*} values are also given.

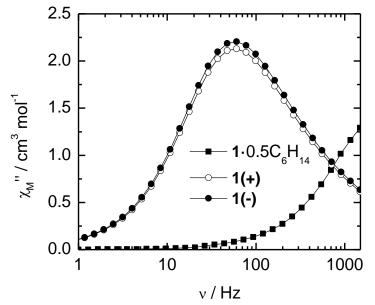


Figure S12. Frequency dependences of the out-of-phase component of the ac susceptibility, χ_M ", at 2 K measured in the absence of external dc field for *rac*-21.0.5C₆H₁₄, (+)-21 and (-)-21.

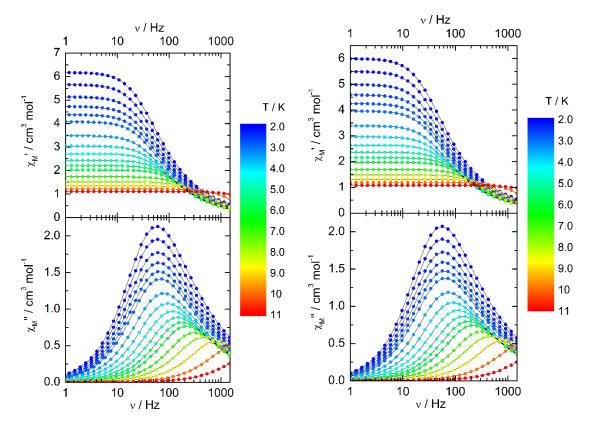


Figure S13. Frequency dependences of the in-phase, χ_M ' (top), and out-of-phase, χ_M '' (bottom), components of the ac susceptibility between 2 and 11 K for (-)-**21** (left) and (+)-**21** (right) measured at zero external dc field.

Extended Debye model.

$$\chi' = \chi_S + (\chi_T - \chi_S) \frac{1 + (\omega\tau)^{1-\alpha} \sin\left(\alpha \frac{\pi}{2}\right)}{1 + 2(\omega\tau)^{1-\alpha} \sin\left(\alpha \frac{\pi}{2}\right) + (\omega\tau)^{2-2\alpha}}$$
$$\chi'' = (\chi_T - \chi_S) \frac{(\omega\tau)^{1-\alpha} \cos\left(\alpha \frac{\pi}{2}\right)}{1 + 2(\omega\tau)^{1-\alpha} \sin\left(\alpha \frac{\pi}{2}\right) + (\omega\tau)^{2-2\alpha}}$$

With χ_T the isothermal susceptibility, χ_S the adiabatic susceptibility, τ the relaxation time and α the empiric parameter which describes the distribution of the relaxation time. For SMM with only one relaxing object α is close to zero. The extended Debye model was applied to fit simultaneously the experimental variations of $\chi_{M^{*}}$ and $\chi_{M^{**}}$ with the frequency *f* of the oscillating field ($\omega = 2\pi f$). Typically, only the temperatures for which a maximum on the $\chi_{M^{**}}$ vs. *f* curves have been considered (see figure here below for an example). The best fitted parameters τ , α , χ_T , χ_S are listed in tables here below with the coefficient of determination R².

T / K	χ_T / cm ³ mol ⁻¹	χ_S / cm ³ mol ⁻¹	А	τ / s	R²
2	6.14589	0.46922	0.19488	0.00237	0.99858
2.2	5.63111	0.43365	0.19404	0.00233	0.99858
2.4	5.11026	0.40238	0.1922	0.00227	0.99859
2.6	4.69973	0.37111	0.19123	0.0022	0.9986
2.8	4.3522	0.34749	0.18958	0.00212	0.9986
3	4.05399	0.32551	0.18786	0.00203	0.99864
3.5	3.4597	0.29868	0.17933	0.00176	0.99867
4	3.01634	0.2895	0.1632	0.00147	0.99879
4.5	2.67889	0.27133	0.14921	0.00119	0.99889
5	2.39349	0.27313	0.127	9.71E-04	0.99923
5.5	2.17094	0.26081	0.11061	8.00E-04	0.99939
6	1.9863	0.24816	0.09523	6.71E-04	0.99954
7	1.69859	0.21939	0.07048	4.87E-04	0.99977
8	1.48369	0.18948	0.05063	3.44E-04	0.9999
9	1.31687	0.15931	0.03938	1.99E-04	0.99997
10	1.18567	0.13039	0.04643	8.50E-05	0.99999

Table S4. Best fitted parameters (χ_T , χ_S , τ and α) with the extended Debye model for (+)-**21** at 0 Oe in the temperature range 2-10 K.

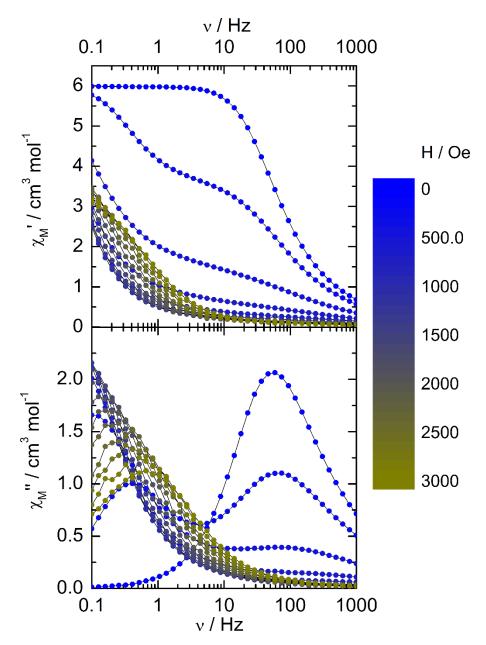


Figure S14. Frequency dependences of the in-phase, χ_M ' (top), and out-of-phase, χ_M '' (bottom), components of the ac susceptibility at 2 K for (+)-21 as a function of the external dc field.

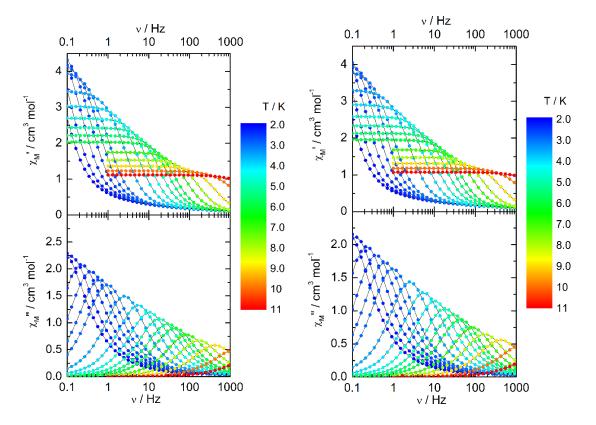


Figure S15. Frequency dependences of the in-phase, χ_M ' (top), and out-of-phase, χ_M '' (bottom), components of the ac susceptibility between 2 and 11 K for (-)-21 (left) and (+)-21 (right) measured at 1 kOe.

Table S5. Best fitted parameters (χ_T , χ_S , τ and α) with the extended Debye model for (+)-
21 at 1 kOe in the temperature range 2-10 K.

T / K	χ_T / cm ³ mol ⁻¹	χ_S / cm ³ mol ⁻¹	α	τ/s	R²
2	8.11525	0.17718	0.27621	4.10301	0.99562
2.2	6.19468	0.17773	0.21121	1.62892	0.99675
2.4	5.14851	0.17576	0.15562	0.73827	0.99774
2.6	4.60417	0.16893	0.12513	0.41423	0.99843
2.8	4.21454	0.16284	0.10534	0.25079	0.9989
3	3.90689	0.15738	0.09111	0.16033	0.9992
3.5	3.33199	0.14628	0.06948	0.06208	0.99965
4	2.9174	0.13696	0.05555	0.02881	0.99984
4.5	2.59334	0.12804	0.04463	0.01544	0.99988
5	2.33858	0.11871	0.04313	0.00885	0.99997

5.5	2.13082	0.10932	0.0408	0.00556	0.99996
6	1.9553	0.10371	0.03889	0.00372	0.99998
7	1.68262	0.09326	0.03908	1.87E-03	0.99998
8	1.47467	0.08415	0.04377	9.55E-04	0.99998
9	1.31242	0.06683	0.06566	3.90E-04	0.99999
10	1.18297	0.02224	0.1102	1.13E-04	0.99998

Table S6. Best fitted parameters (χ_T , χ_S , τ and α) with the extended Debye model for (-)-**21** at 1 kOe in the temperature range 2-10 K.

T / K	$\chi_T/\mathrm{cm}^3\mathrm{mol}^{-1}$	$\chi_S / \mathrm{cm}^3 \mathrm{mol}^{-1}$	α	τ / s	R²
2	8.88955	0.18188	0.28977	4.28414	0.99567
2.2	6.63483	0.18678	0.21929	1.6126	0.99664
2.4	5.49371	0.18677	0.16099	0.73007	0.99757
2.6	4.90716	0.18127	0.12888	0.41025	0.9983
2.8	4.41078	0.17437	0.10827	0.24938	0.9988
3	4.0822	0.16807	0.09483	0.1594	0.99912
3.5	3.47757	0.15801	0.07029	0.06171	0.9996
4	3.04025	0.14879	0.05592	0.02864	0.99984
4.5	2.70352	0.13814	0.04569	0.01539	0.99986
5	2.43672	0.12868	0.04328	0.00881	0.99997
5.5	2.21796	0.11946	0.04014	0.00554	0.99998
6	2.03605	0.10869	0.03938	0.00369	0.99998
7	1.7512	0.09906	0.03786	1.86E-03	0.99999
8	1.53493	0.08993	0.04184	9.51E-04	0.99999
9	1.36495	0.07197	0.06502	3.87E-04	0.99998
10	1.23104	0.0268	0.11079	1.13E-04	0.99999

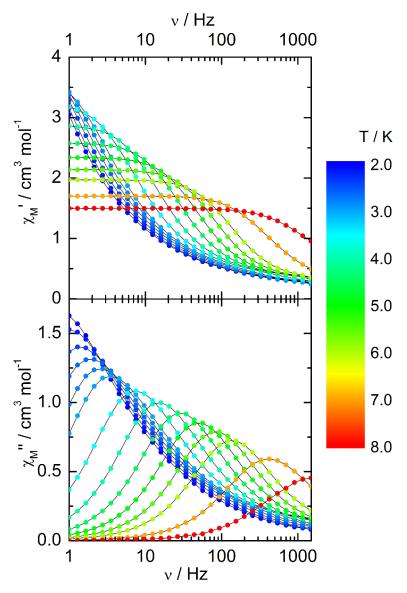


Figure S16. Frequency dependences of the in-phase, χ_M ' (top), and out-of-phase, χ_M '' (bottom), components of the ac susceptibility between 2 and 8 K for *rac*-**21**·0.5C₆H₁₄ measured at 1 kOe.

Table S7. Best fitted parameters (χ_T , χ_S , τ and α) with the extended Debye model for *rac*-**21**·0.5C₆H₁₄ at 1 kOe in the temperature range 2-8 K.

T / K	$\chi_T / \mathrm{cm}^3 \mathrm{mol}^{-1}$	χ_S / cm ³ mol ⁻¹	α	τ / s	R ²
2	8.62086	0.23959	0.47454	0.50976	0.9995
2.2	7.4378	0.22828	0.46179	0.30765	0.99927
2.4	6.32779	0.22755	0.44172	0.17253	0.99878
2.6	5.55667	0.23674	0.41934	0.10578	0.99815

2.8	4.9242	0.25371	0.38983	0.06692	0.99719
3	4.38714	0.28278	0.35067	0.04339	0.9964
3.5	3.49691	0.34665	0.25056	0.01811	0.9964
4	2.98133	0.3726	0.17657	0.0091	0.99784
4.5	2.62888	0.37061	0.13023	0.00499	0.999
5	2.36829	0.35409	0.10463	0.00292	0.99949
5.5	2.15779	0.33666	0.08871	0.00178	0.99968
6	1.98315	0.32184	0.08224	0.0011	0.99978
7	1.71005	0.3076	0.10012	3.72E-04	0.99987
8	1.5005	0.43115	0.10942	1.14E-04	0.99996

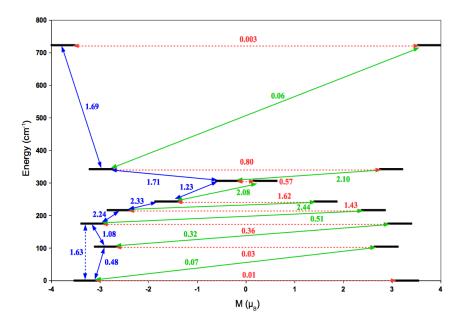


Figure S17. *Ab initio* magnetization blocking barrier for *rac*-21, computed by means of magnetic transition moments. The black thick lines correspond to all the spin–orbit states. The full green lines show possible Orbach processes dotted red lines quantum tunneling processes, full blue lines direct vertical transitions to the first-neighbor multiplet, dotted blue lines direct vertical transitions to the second-neighbor multiplet.

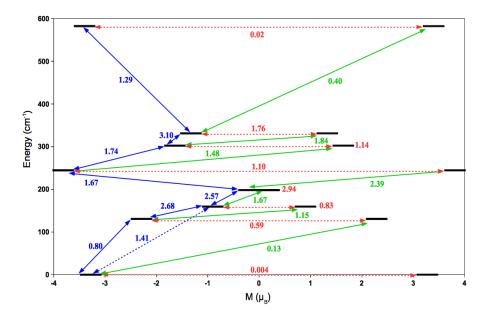


Figure S18. *Ab initio* magnetization blocking barrier for (+)-**21**, computed by means of magnetic transition moments. The black thick lines correspond to all the spin–orbit states. The full green lines show possible Orbach processes, dotted red lines quantum tunneling processes, full blue lines direct vertical transitions to the first-neighbor multiplet, dotted blue lines direct vertical transitions to the second-neighbor multiplet.

E Conclusion

In this part of work, we designed and prepared a novel class of chiral lanthanide SMMs, the chirality being introduced by a 3-(2-pyridyl)-4-aza[6]helicene ligand. The SMMs were characterized by X-ray, element analysis, CD spectroscopy, and magnetic behavior. Most important is that racemic and enantiopure Dy^{III} SMMs showed different magnetic properties. For *rac*-21, it exhibited anti-ferromagnetic properties, while for (+)-21 and (-)-21, it displayed ferromagnetic properties, which was also the first example about comparing the different magnetic properties between *rac*- and enantiopure SMMs. In future, such high configurationally stable chiral molecular magnets may be modified on purpose to be grafted on the surface and applied into storage materials and quantum computing.¹¹ Due to character emission properties of lanthanide complex, circularly polarized luminescence can also be envisioned.⁵⁹⁻⁶¹

F References

- 1. Sessoli, R.; Tsai, H. L.; Schake, A. R.; Wang, S.; Vincent, J. B.; Folting, K.; Gatteschi, D.; Christou, G.; Hendrickson, D. N., *J. Am. Chem. Soc.* **1993**, *115*, 1804-1816.
- 2. Sessoli, R.; Gatteschi, D.; Caneschi, A.; Novak, M. A., *Nature* **1993**, *365*, 141-143.

3. Spaldin, N. A., *Magnetic materials: fundamentals and applications*. Cambridge University Press: 2010.

4. Gatteschi, D.; Sessoli, R.; Villain, J., *Molecular nanomagnets*. Oxford University Press on Demand: 2006; Vol. 5.

- 5. Mailly, D.; Chapelier, C.; Benoit, A., *Phys. Rev. Lett.* **1993**, *70*, 2020.
- 6. Wernsdorfer, W.; Hasselbach, K.; Mailly, D.; Barbara, B.; Benoit, A.; Thomas, L.; Suran,
- G., J. Magn. Magn. Mater. 1995, 145, 33-39.
- 7. Wernsdorfer, W., Adv. Chem. Phys. 2001, 118, 99-190.
- 8. Gao, S., Molecular nanomagnets and related phenomena. Springer: 2015; Vol. 164.
- 9. Wernsdorfer, W., *Supercond. Sci. Technol.* **2009**, *22*, 064013.
- 10. Cole, K. S.; Cole, R. H., J. Chem. Phys. **1941**, 9, 341-351.
- 11. Bogani, L.; Wernsdorfer, W., Nat. Mater. 2008, 7, 179-186.

12. Clérac, R.; Winpenny, R. E. P., Single-Molecule Magnets and Related Phenomena. In *50 Years of Structure and Bonding – The Anniversary Volume*, Mingos, D. M. P., Ed. Springer International Publishing: Cham, 2016; pp 35-48.

13. Leuenberger, M. N.; Loss, D., *Nature* **2001**, *410*, 789-793.

14. Ardavan, A.; Rival, O.; Morton, J. J.; Blundell, S. J.; Tyryshkin, A. M.; Timco, G. A.; Winpenny, R. E., *Phys. Rev. Lett.* **2007**, *98*, 057201.

- 15. Gatteschi, D.; Sessoli, R., Angew. Chem. Int. Ed. 2003, 42, 268-297.
- 16. Zhang, P.; Zhang, L.; Tang, J., *Dalton Trans.* **2015**, *44*, 3923-3929.
- 17. Tang, J.; Zhang, P., Lanthanide single molecule magnets. Springer: 2015.
- 18. Goldschmidt, Z. B., *HPCRE* **1978**, *1*, 1-171.
- 19. Rinehart, J. D.; Long, J. R., *Chem. Sci.* **2011**, *2*, 2078-2085.
- 20. Woodruff, D. N.; Winpenny, R. E. P.; Layfield, R. A., Chem. Rev. 2013, 113, 5110-5148.
- 21. Ishikawa, N.; Sugita, M.; Ishikawa, T.; Koshihara, S.-y.; Kaizu, Y., J. Am. Chem. Soc.

2003, *125*, 8694-8695.

22. Tang, J.; Hewitt, I.; Madhu, N.; Chastanet, G.; Wernsdorfer, W.; Anson, C. E.; Benelli,

C.; Sessoli, R.; Powell, A. K., Angew. Chem. Int. Ed. 2006, 45, 1729-1733.

- 23. Sessoli, R.; Powell, A. K., *Coord. Chem. Rev.* **2009**, *253*, 2328-2341.
- 24. Sorace, L.; Benelli, C.; Gatteschi, D., Chem. Soc. Rev. 2011, 40, 3092-3104.
- 25. Long, J.; Rouquette, J.; Thibaud, J. M.; Ferreira, R. A.; Carlos, L. D.; Donnadieu, B.;
- Vieru, V.; Chibotaru, L. F.; Konczewicz, L.; Haines, J., Angew. Chem. Int. Ed. 2015, 54, 2236-2240.

26. Wang, Y.-X.; Shi, W.; Li, H.; Song, Y.; Fang, L.; Lan, Y.; Powell, A. K.; Wernsdorfer, W.; Ungur, L.; Chibotaru, L. F., *Chem. Sci.* **2012**, *3*, 3366-3370.

27. Coronado, E.; Day, P., Chem. Rev. 2004, 104, 5419-5448.

28. Pedersen, K. S.; Dreiser, J.; Weihe, H.; Sibille, R.; Johannesen, H. V.; Sørensen, M. A.;

Nielsen, B. E.; Sigrist, M.; Mutka, H.; Rols, S., Inorg. Chem. 2015, 54, 7600-7606.

29. Long, J.; Vallat, R.; Ferreira, R. A.; Carlos, L. D.; Paz, F. A. A.; Guari, Y.; Larionova, J., *Chem. Commun.* **2012**, *48*, 9974-9976.

30. Pointillart, F.; Le Guennic, B.; Golhen, S.; Cador, O.; Maury, O.; Ouahab, L., *Chem. Commun.* **2013**, *49*, 615-617.

31. Pointillart, F.; Le Guennic, B.; Cador, O.; Maury, O.; Ouahab, L. n., *Acc. Chem. Res.* **2015**, *48*, 2834-2842.

32. Chorazy, S.; Podgajny, R.; Nitek, W.; Fic, T.; Görlich, E.; Rams, M.; Sieklucka, B., *Chem. Commun.* **2013**, *49*, 6731-6733.

33. Train, C.; Nuida, T.; Gheorghe, R.; Gruselle, M.; Ohkoshi, S.-i., *J. Am. Chem. Soc.* **2009**, *131*, 16838-16843.

34. Train, C.; Gheorghe, R.; Krstic, V.; Chamoreau, L.-M.; Ovanesyan, N. S.; Rikken, G. L. J. A.; Gruselle, M.; Verdaguer, M., *Nat. Mater.* **2008**, *7*, 729-734.

35. Sessoli, R.; Boulon, M.-E.; Caneschi, A.; Mannini, M.; Poggini, L.; Wilhelm, F.; Rogalev, A., *Nat. Phys.* **2015**, *11*, 69-74.

36. Inglis, R.; White, F.; Piligkos, S.; Wernsdorfer, W.; Brechin, E. K.; Papaefstathiou, G. S., *Chem. Commun.* **2011**, *47*, 3090-3092.

37. Liu, C.-M.; Zhang, D.-Q.; Zhu, D.-B., *Inorg. Chem.* **2013**, *52*, 8933-8940.

38. Shen, Y.; Chen, C.-F., *Chem. Rev.* **2012**, *112*, 1463-1535.

39. Chen, C.-F.; Shen, Y., *Helicene Chemistry: From Synthesis to Applications*. Springer: 2016.

40. Saleh, N.; Shen, C.; Crassous, J., *Chem. Sci.* **2014**, *5*, 3680-3694.

41. Li, D.-P.; Wang, T.-W.; Li, C.-H.; Liu, D.-S.; Li, Y.-Z.; You, X.-Z., *Chem. Commun.* **2010**, *46*, 2929-2931.

42. Norel, L.; Bernot, K.; Feng, M.; Roisnel, T.; Caneschi, A.; Sessoli, R.; Rigaut, S., *Chem. Commun.* **2012**, *48*, 3948-3950.

43. Pointillart, F.; Jung, J.; Berraud-Pache, R.; Le Guennic, B.; Dorcet, V.; Golhen, S.;

Cador, O.; Maury, O.; Guyot, Y.; Decurtins, S., Inorg. Chem. 2015, 54, 5384-5397.

44. Bi, Y.; Guo, Y. N.; Zhao, L.; Guo, Y.; Lin, S. Y.; Jiang, S. D.; Tang, J.; Wang, B. W.; Gao, S., *Chem. Eur. J.* **2011**, *17*, 12476-12481.

45. Saleh, N.; Srebro, M.; Reynaldo, T.; Vanthuyne, N.; Toupet, L.; Chang, V. Y.; Muller, G.; Williams, J. A. G.; Roussel, C.; Autschbach, J.; Crassous, J., *Chem. Commun.* **2015**, *51*, 3754-3757.

46. Saleh, N.; Moore, B.; Srebro, M.; Vanthuyne, N.; Toupet, L.; Williams, J. A. G.; Roussel, C.; Deol, K. K.; Muller, G.; Autschbach, J.; Crassous, J., *Chemistry – A European Journal* **2015**, *21*, 1673-1681.

47. Ou-Yang, J. K.; Saleh, N.; Fernandez Garcia, G.; Norel, L.; Pointillart, F.; Guizouarn, T.; Cador, O.; Totti, F.; Ouahab, L.; Crassous, J.; Le Guennic, B., *Chem. Commun.* **2016**, *52*, 14474-14477.

48. Fernandez-Garcia, G.; Flores Gonzalez, J.; Ou-Yang, J.-K.; Saleh, N.; Pointillart, F.; Cador, O.; Guizouarn, T.; Totti, F.; Ouahab, L.; Crassous, J., *Magnetochemistry* **2016**, *3*, 2.

49. Lightner, D. A.; Hefelfinger, D. T.; Powers, T. W.; Frank, G. W.; Trueblood, K. N., *J. Am. Chem. Soc.* **1972**, *94*, 3492-3497.

50. Flack, H. D., *Helvetica Chimica Acta* **2003**, *86*, 905-921.

51. Kahn, O., VCH Publishers, Inc.(USA), 1993 1993, 393.

52. Boulon, M. E.; Cucinotta, G.; Luzon, J.; Degl'Innocenti, C.; Perfetti, M.; Bernot, K.;

Calvez, G.; Caneschi, A.; Sessoli, R., Angew. Chem. 2013, 125, 368-372.

53. Cucinotta, G.; Perfetti, M.; Luzon, J.; Etienne, M.; Car, P. E.; Caneschi, A.; Calvez, G.; Bernot, K.; Sessoli, R., *Angew. Chem.* **2012**, *124*, 1638-1642.

54. da Cunha, T. T.; Jung, J.; Boulon, M.-E.; Campo, G.; Pointillart, F.; Pereira, C. L.; Le Guennic, B.; Cador, O.; Bernot, K.; Pineider, F., *J. Am. Chem. Soc.* **2013**, *135*, 16332-16335.

55. Guo, Y.-N.; Xu, G.-F.; Gamez, P.; Zhao, L.; Lin, S.-Y.; Deng, R.; Tang, J.; Zhang, H.-J., *J. Am. Chem. Soc.* **2010**, *132*, 8538-8539.

56. Guo, Y.-N.; Ungur, L.; Granroth, G. E.; Powell, A. K.; Wu, C.; Nagler, S. E.; Tang, J.; Chibotaru, L. F.; Cui, D., *Sci. Rep.* **2014**, *4*.

57. Richardson, M. F.; Wagner, W. F.; Sands, D. E., *J. Inorg. Nucl. Chem.* **1968**, *30*, 1275-1289.

58. Gatteschi, D.; Bencini, A., Electron Paramagnetic Resonance of Exchange Coupled Systems. Springer, Berlin: 1990.

59. Bunzli, J.-C. G.; Piguet, C., Chem. Soc. Rev. 2005, 34, 1048-1077.

- 60. Tsukube, H.; Shinoda, S., Chem. Rev. 2002, 102, 2389-2404.
- 61. Carr, R.; Evans, N. H.; Parker, D., Chem. Soc. Rev. 2012, 41, 7673-7686.

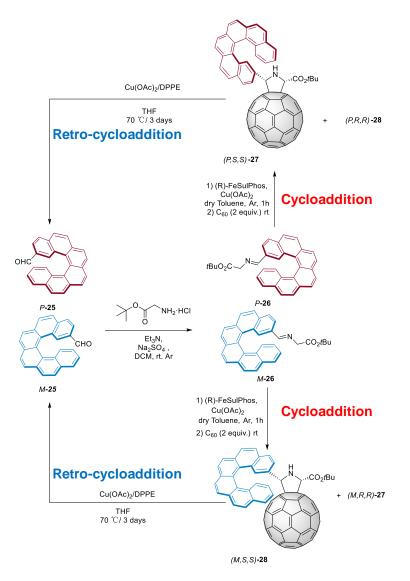
Chapter IV



RENNES 2017

A Introduction

In this part of work, we prepared and characterized a series of chiral fullerene derivatives based on helicenes. We can control the reaction to selectively obtain the different chiral fullerene isomers. The absolute configurations of chiral fullerenes were determined by CD spectra according to corrected Sector Rule. Moreover, the cycloaddition was reversible, under catalysis condition, chiral fullerene could go back to helicene aldehyde precursors without loss of *ee* value. It is also the first time to employ helicenes to develop a novel kind of reversible stereodivergent cycloaddition onto fullerenes for preparing chiral fullerene derivatives and efficient racemates separation (**Scheme 4.1**).



Scheme 4.1 Reversible stereodivergent cycloaddition onto fullerenes.

A.1 General features of fullerenes

A.1.1 History of the fullerenes

The fullerenes, the first molecular allotropes of carbon, were discovered in 1985 by Robert F. Curl, Sir Harold W. Kroto, and Richard E. Smalley,¹ who shared the Nobel chemistry prize in 1996 for their contribution on fullerenes research. Fullerenes are different from the other reticular allotropes of carbon, diamond and graphite, and they have defined number of carbon atoms and are highly symmetric closed cages.²⁻⁴ These molecules were named after the architect Buckminster Fuller for his designed geodesic domes.⁴

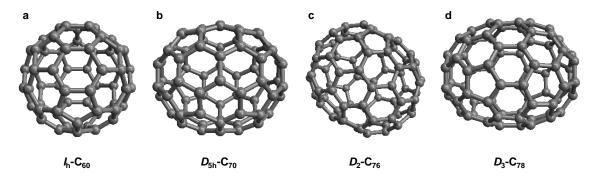


Figure 4.1 Molecular structure of $I_{\rm h}$ -C₆₀, $D_{5\rm h}$ -C₇₀, D_2 -C₇₆, D_3 -C₇₈. (Reproduced from ref.⁵)

A.1.2 Physical and spectroscopic properties

The investigations of physical properties are mainly carried on the C_{60} and partly on C_{70} , because these two are the abundant fullerenes. Only little of higher fullerenes are available for study, resulting from their longer production cycle (about 250 hours).⁶

Solubility of fullerenes in various solvents is an important issue. Because the modification of fullerenes is normally performed in the solution state. It also plays a key role for extraction or chromatographic separations of fullerenes. Usually, fullerenes are insoluble in polar and H-bonding solvent. In alkanes solvents, fullerenes are partly soluble, but the solubility increases with the number of atoms increasing. In aromatic and in carbon disulfide, the solubility is appreciable. Especially, in benzene, toluene or naphthalene solvents, the solubility increases significantly.

 C_{60} and C_{70} display some strong absorption bands between 190 nm and 410 nm as well as in the visible region through forbidden transition.⁷ The absorption bands between 190 to 410 nm are attributed to the allowed ${}^{1}T_{1u}$ - ${}^{1}A_{g}$ transitions, while those in the visible area are due to the forbidden singlet-singlet transitions.⁸⁻⁹ In solution state, the C_{60} and C_{70} show purple and red color, respectively.

The ¹³C NMR spectra of C₆₀ and C₇₀ exhibit big differences. For the truncated icosahedral symmetric $I_{\rm h}$ -C₆₀, only one signal at 143.2 ppm is observed, while for $D_{\rm 5h}$ -C₇₀, five peaks can be observed with a ratio of 1:2:1:2:1, which is due to the five different sets of carbon atoms.¹⁰

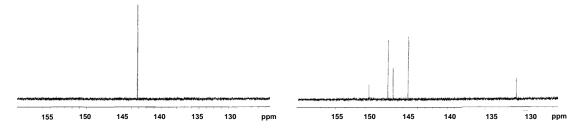


Figure 4.2 ¹³C NMR spectra of C₆₀ (left) and C₇₀ (right). (Reproduced from ref.⁴)

The UV-vis spectra of C60 and C70 were characterized by several stronger absorption between 190 and 410 nm as well as by some forbidden transitions in the visible part of spectrum (**Figure 4.3** and **Figure 4.4**).⁷ The band between 190 to 410 nm are assigned to allowed ${}^{1}T_{1u}$ - ${}^{1}A_{g}$ -transition, while those between 410 and 620 nm due to orbitally forbidden singlet-singlet transitions. The absorptions in the visible are responsible for the purple color of C₆₀ and the red color of C₇₀.⁶

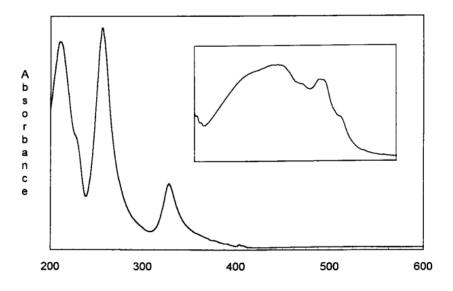


Figure 4.3 Electronic absorption spectrum of C_{60} in hexane. The inset is the 420-400 nm region (Reproduced from ref.⁷)

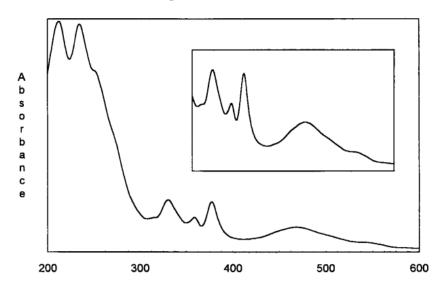


Figure 4.4 Electronic absorption spectrum of C_{70} in hexane. The inset is the 300-600 nm region (Reproduced from ref.⁷)

In the solid state, C_{60} can form a face-centered-cubic (FCC) structure at ambient temperature. Each cubic unit contains four C_{60} molecules. The edge length of cubic is 14.198 Å. The density of FCC is 1.69 g·cm⁻³.¹¹⁻¹³

A.1.3 Chiral fullerenes

The first chiral fullerenes, D_2 -symmetric C₇₆ and D_3 -symmetric C₇₈, were reported by Diederich in 1991.¹⁴⁻¹⁵ One year after that, the first enantiopure fullerene derivative based on achiral C₆₀ was reported.¹⁶ Chiral Fullerenes derivatives can be prepared from chiral

carbon cages (**Figure 4.5**) or from added groups. Except the inherently chiral fullerenes, from the origin of chirality, chiral fullerenes derivatives can be divided into three categories as follows:³ 1. The parent fullerenes are achiral, while the derivatization creates a chiral functionalization on the fullerenes skeleton. They have an inherently chiral functionalization pattern; 2. The parent fullerenes are achiral, nonidentity of all substitutions leads to chirality. They have a non-inherently chiral functionalization pattern; 3. The parent fullerenes are achiral addition groups do not create chiral pattern on fullerenes skeleton, while the chiral elements are located in the addends.³

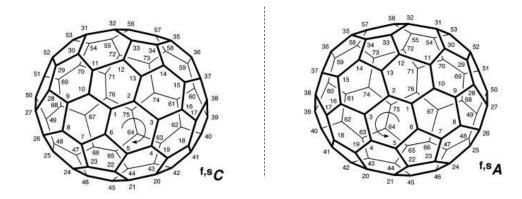
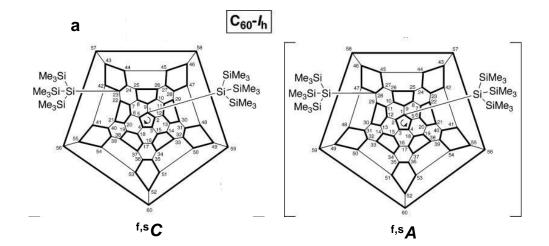
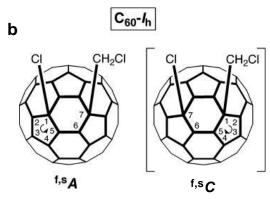
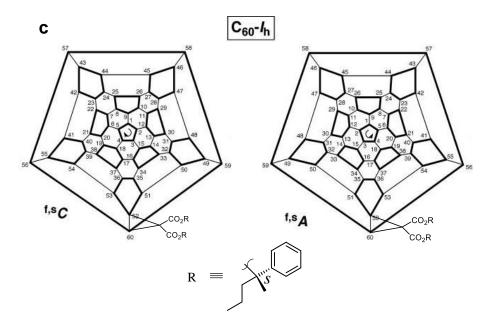
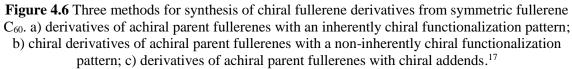


Figure 4.5 Two enantiomers of inherently chiral fullerenes C₇₆-D₂ (Reproduced from ref.³)









For example, in the first case, the parent fullerene C_{60} is achiral (**Figure 4.6 a**). The number of C-atom on the achiral fullerene can be achieved with two mirror-symmetric numbering schemes, named Schlegel diagrams,³ with clockwise and anticlockwise numbering. But for the fullerene derivatives with an inherently chiral functionalization pattern, only one of the two numbering schemes afford the lowest set of locants, which is preferred. As diagram below, the left one with clockwise numbering scheme afford "1,23" as lowest set of locant, which is lower than the right set "1,28", and in accordance with IUPAC conventions.

In the second case, the symmetric arrangement of substitution groups on the achiral parent fullerene has no distinction in two mirror-symmetric numbering schemes (**Figure 4.6 b**). In other words, they have the same lowest set of locant in two schemes. While the priority of addends is different according to the CIP rule. Usually, the atom or group with higher CIP ranking being assigning a lower locant is preferred. As shown in the diagram below, two addends have the same overall set of locant in their two mirror-symmetric numbering schemes. While the priority of group (CH₂Cl) is lower than that of atom (Cl). Thus, the ^{f,s}A (^f stands for fullerene; while ^s stands for systematic numbering) form defines the left molecule in **Figure 4.6 b**.

In the last case, the addends are chiral, but will not lead to chiral addition pattern on the fullerene surface (**Figure 4.6 c**). As diagram below, the addends have the same overall set of locant in two mirror-symmetric numbering schemes. There is no chiral addition pattern on the fullerene surface. The chiral elements are exclusively located on the addends parts.

We will focus on the last case and introduce the chiral fullerenes from asymmetric catalysis. The chirality in fullerenes are considered fundamental issue, besides, chiral fullerenes display an important role in the field of materials science¹⁸ and medicinal chemistry.¹⁹⁻²⁰ Usually, chiral fullerenes derivatives are obtained by highly expensive and time consuming HPLC or prepared from chiral starting materials. So, developing an efficient and selective synthesis of chiral fullerenes attracts the interests of chemists.

A.1.4 Chiral fullerenes from asymmetric catalysis

In the past two decades, the asymmetric catalytic 1,3-dipolar cycloaddition of azomethine has become an atom-economical and powerful method to synthesis optical active pyrrolidines.²¹⁻²² Most importantly, the 1,3-dipolar cycloaddition of azomethine ylides on C₆₀ can afford pyrrolidino[3,4:1,2][60]fullerenes, which are widely used due to their stability, versatility and availability of the starting materials. Usually, the azomethine ylides are synthesized by heating aldehydes and amino acids²³⁻²⁴ or imino esters.²⁵ Salvatore Filippone and Nazario Martin's group did a lot of work about asymmetric metal catalysis for the synthesis of pyrrolidinofullerenes. We will introduce several methods about preparation of chiral fullerenes derivatives by enantioselective catalytic 1,3-dipolar cycloadditions of dipoles on C₆₀. The asymmetric functionalization of [70]fullerenes,²⁶⁻²⁷ metallofullerenes²⁸⁻³¹ and H₂-containing endofullerens³² will not be discussed here. Because the [70]fullerenes have four different double bonds, which show different reactivities, the reaction is more complex. While for metallofullerenes and H₂-containing fullerenes, no modification of chemical reactivity on carbon cage was observed, just high enantiomeric excesses was revealed. More details can be found in Filippone and Martin's Accounts (2014)²

A.1.4.1 Asymmetric [3+2] cycloaddition onto [60]fullerenes

[60]fullerene has curved double bonds and displays deficient electron character resulting from the presence of sole sp²-hybridized carbon atoms, which leads to non-coordinating character and makes the reaction with 1,3-dipoles (α -imino esters or azalactones) challenging. In the [3+2] cycloaddition (Prato reaction), [60]fullerene usually acts as the dipolarophile, and metals play the role of catalysts. The [3+2] cycloaddition products have a N-containing five members ring and their stereocenters can be tuned by reaction conditions. According to the type of 1,3-dipoles used, we will discuss the reaction from α imino esters and azalactones two aspects.

A.1.4.2 Asymmetric [3+2] cycloaddition with α-imino esters onto [60]fullerenes

The reaction of α -imino ester and [60]fullerene under thermal conditions leads to a mixture of *trans* and *cis* isomers of the 2-alkoxycarbonyl-5-arylpyrrolidino[3,4:1,2][60]fullerene. In general, obtaining the products with a good

stereoselectivity is challenging for the synthesis of four enantiomers. Hence, developing a stereoselective synthetic method of chiral fullerene becomes demanded. The metal-ligand pairs are chosen to induce the stereoselective formation of the 1,3-dipole, then carrying out the process under milder conditions and controlling the stereochemical outcome in terms of diastereo- and enantioselectivity.²

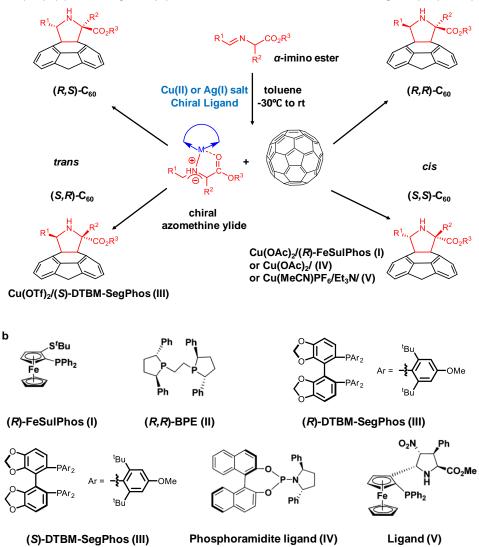
In 2009, Filippone and Martin's group reported the first efficient enantioselective catalytic synthesis of chiral pyrrolidinofullerenes.³³ In this work, the authors combined the metal catalyst Ag(I) or Cu(II) and a chiral ligand to direct the cycloaddition of [60]fullerene to opposite enantiofaces of *N*-metallated azomethine ylides. The [60]fullerene acted as non-coordinating dipolarophile in the reaction. After that, they developed this catalytic system and performed the stereodivergent synthesis of pyrrolidinofullerenes "à la carte".³⁴⁻³⁵ They found that when Cu(OAc)₂/(*R*)-FeSulphos (I) or phosphoramidite (IV) catalysis are used, the (*S*,*S*)-cis-C₆₀ form of product can be obtained; while for AgOAc/(*R*,*R*)-BPE (II) catalysis pair, the opposite enantiomer, (*R*,*R*)-cis-C₆₀ form of product can be obtained. But the enantiomeric excesses (*ee* value) of products in these reactions are relatively lower than those of non-fullerene dipolarophiles. Maybe the non-ligand character of C₆₀ influences the results. It is worth noting that the acetate counterion plays an important role in both the formation of the azomethine ylide and the high enantioselectivities. Moreover, Cu(MeCN)PF₆/Et₃N/chiral ligand (V) catalytic pairs can also afford the (*S*,*S*)-*cis*-C₆₀ with high *ee* values at lower catalyst loadings.

When $Cu(OTf)_2/(R)$ -DTBM-SegPhos or (*S*)-DTBM-SegPhos catalytic pairs are applied in the reaction, (*R*,*S*)-*trans*-C₆₀ and (*S*,*R*)-*trans*-C₆₀ are obtained, respectively. In these reactions, the Et₃N base is indispensable for optimal yields, due to the fact that the triflate anion cannot trigger the formation of the azomethine ylide.

The reactivity and enantioselectivity among different substituted α -imino esters. The arylsubstituted α -imino esters display better reactivity than those alkyl-substituted α -imino esters, since the latter are easily hydrolyzed. To deeply understand the [3+2] cycloaddition onto C₆₀, Filippone and Martin tested reactivities and stereoselectivities of different electronegative groups in the aromatic moiety at the *meta* or *ortho* positions of the phenyl ring.² Even some chiral α -imino amides acting as 1,3 dipoles were studied.

a Cu(OTf)₂/(R)-DTBM-SegPhos (III)





Scheme 4.2 a) [3+2] cycloaddition of *N*-Metallated azomethine ylides onto C_{60} ; b) molecular structures of chiral ligands.

Because of the difficulty in obtaining suitable crystal of fullerene derivatives for X-ray analysis, the circular dichroism (CD) is widely used to assign the absolute stereochemistry of chiral fullerenes. In 1996, a proposed sector rule for chiral absolute configuration was first reported by Stephen R. Wilson' group (Figure 3.6).³⁶ The axis system defines positive and negative region of space for which asymmetric perturbation of the intrinsically symmetric chromophore may be defined. In general, the greatest number of atoms are located in the - sector causing a negative sign of Cotton effect at 430 nm, which severs as

the fingerprint for 6-6 substitution on C_{60} .³⁶ Otherwise, it affords a positive Cotton effect at 430 nm.

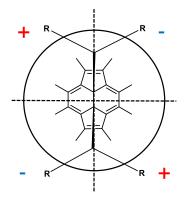


Figure 4.7 Sector rule of C_{60} derivatives. The vertical axis is drawn through the 6-6 $C(sp^3)$ - $C(sp^3)$ bond. Location of the greatest number of atoms in + or – sectors defines he sign of Cotton effect at 430 nm which is used to determine the absolute configuration of attached group.

According to the sector rule, the *cis* products catalyzed by Ag(I)/(R,R)-BPE (II) complex display a positive Cotton effect in their CD spectra in the region from 425 to 430 nm, which is in accordance with a (2R,5R) configuration. Similarly, the *cis* product formed from the Cu(II)/chiral ligand (I), (III), (IV), (V) systems show negative Cotton effect, which is in consistence with the (2S,5S) stereochemistry.

The *trans* derivatives also obey the sector rule. In contrast to *cis* derivatives, those in *trans* form afford an additive contribution in the corresponding signal, resulting in a higher intensity band at about 430 nm.

Later on, in 2013, Filippone and Martin's group successfully obtained a crystal of chiral fullerene and determined its absolute configuration, which was opposite to the one analyzed by empirical way sector rule.³⁷ Consequently, a corrected sector rule for the assignment of absolute configuration of chiral fullerenes was proposed as follow (**Figure 4.8**).

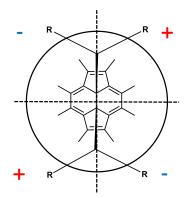
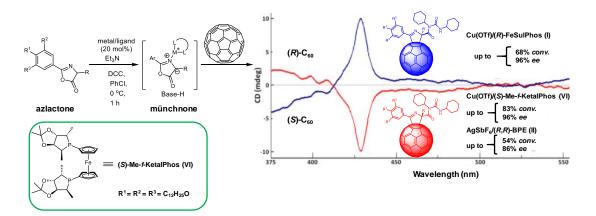


Figure 4.8 Corrected Sector Rule of C_{60} Derivatives. The vertical axis is drawn through the 6-6 $C(sp^3)$ - $C(sp^3)$ bond. Location of the greatest number of atoms in + or – sectors defines he sign of Cotton effect at 430 nm which is used to determine the absolute configuration of attached group.

A.1.4.3 Asymmetric [3+2] cycloaddition with azlactones onto [60]fullerenes

Due to the existence of different reactive sites (acidic, electrophilic or Lewis acid active site) of oxazol-5-(4H)-ones (azlactones), the versatile chemistry of this family of substrates has been reported in the literature.³⁸ Extraordinarily, azlactones can react as 1,3-dipoles (so-called münchnones) with alkenes in the presence of a Lewis acid. Nevertheless, so far, just Tepe's and Toste's group reported stereoselective preparation of Δ^1 -pyrrolines by the silver-mediated reaction³⁹ and enantioselective gold-catalyzed synthesis,⁴⁰ respectively. Filippone and Martin's group explored the catalysis strategy with combination of available chiral phosphine ligands and nonprecious metals, and found that, after dicyclohexyl carbodiimide (DCC) addition, the catalysis pair (±)-BINAP/AgOAc can afford a racemic mixture of 5-carbamoylpyrrolino-[3,4:1,2][60]fullerene derivatives (R)-C₆₀ and (S)-C₆₀.⁴¹ In the reaction, the azlactones play as monodentate ligands, and show a preference for lesscoordinating nonbasic counterions, which leads to a tighter interaction between the metal and the monodentate azlactone. When the anion SbF_6^- acts as counterion of Ag(I)/(R,R)-BPE (II) complex in company with Et_3N , pyrroline (S)-C₆₀ can be obtained with 86% ee. The same product can be obtained with 96% ee by employing Cu(OTf)/(S)-Me-f-KetalPhos (VI) pair along with triflate anion as counterion and Et_3N as base. While the catalysis pair Cu(OTf)/(R)-FeSulPhos (I) was applied in the cycloaddtion reaction, the opposite enantiomer (S)-C₆₀ was achieved (Scheme 4.3). The authors prepared different azlactones with different substitutions and from different amino acids to explore the scope

of the reaction. In addition, they found that the solubility could influence the conversions of ee values. The soluble derivatives would perform better than those with less solubility. Usually, metal-chiral ligand complexes catalysts afford pyrrolinofullerenes in moderate to good yields along with high *ee* values. It was also the first example of enantioselective cycloaddition of münchnones catalyzed by a copper salt. What should be noted is that the asymmetric induction is fully controlled and switched by choosing suitable catalysts pair, and not influenced by the substitution of starting azlatones.



 $\begin{array}{c} \mbox{Scheme 4.3 Metal-catalyzed enantioselective [3+3] cycloaddtion of azlatones onto C_{60}. \\ \mbox{Reproduced from ref.}^{41} \end{array}$

The absolute stereochemistry of pyrrolinofullerenes is determined by CD analysis according to corrected sector rule (**Figure 4.8**). The catalyst pair Cu(OTf)/(*R*)-FeSulPhos (I) leads to the (*R*)-C₆₀ derivatives. The greatest group of (*R*)-C₆₀ is located in + sector, and the sign of cotton effect at 430 nm is positive. However, the catalyst pair Cu(OTf)/(S)-Me-f-KetalPhos (VI) results in opposite enantiomer (*S*)-C₆₀, which shows negative cotton effect at 430 nm (**Figure 4.9**).

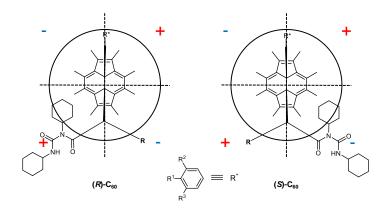


Figure 4.9 Top view of pyrrolinofullerenes (*R*)- C_{60} (left) and (*S*)- C_{60} (right) according to corrected sector rule.

Filippone and Martin's group also developed asymmetric organocatalysis in [3+2] cycloaddition onto C_{60} . Herein, we will not focus on it, which can be found in literatures.^{37, 42-43}

A.2 Divergent reactions on racemic mixtures (Divergent RRM)

Before the introduction of divergent reactions on racemic mixtures, we should mention simple kinetic resolution,⁴⁴⁻⁴⁸ which relies on a difference in reaction rate between enantiomers to obtain enatioenriched product (**Figure 4.10** left).⁴⁹ In this strategy, a chiral, non-racemic agent reacts with one enantiomer faster than with the other one. The selectivity factor (s) is defined as the flowing equation:

$$s = \frac{k_{fast}}{k_{slow}}$$

,where k_{fast} and k_{slow} are reaction rates. When *s* is equal to 1, there is no selectivity in the reaction, and only racemic products can be obtained. In the ideal case, when *s* is large (usually $s \ge 200$), enantioenriched products can be obtained in a 50% yield, at the same time, enantioenriched starting material can be recovered in 50% yield. However, a disadvantage of this mode is that if we want to get high yield (~50%) of each compound with excellent *ee* value, high selectivity factor is necessary, but hard to get.

The resolution mode of divergent reaction on a racemic mixture (divergent RRM) can avoid the necessity for extremely high selectivity factors (**Figure 4.10** middle). In this strategy, both enantiomers react with chiral reagent (X*) at similar rates to form nonenantiomeric products (P(R) and Q(R), in Figure 4.9 middle) which are separable. In contrast to simple kinetic resolutions, the mode of divergent RRM does not matter the relative rates as long as complete reagent control is achieved.⁵⁰ With excellent reagent control, both products can be obtained in high yield (up to 50%) and enantiomeric enrichment.⁴⁹

Parallel kinetic resolutions are defined as a special case of divergent RRM. In this mode, there are two chiral agents (X^* and Y^* , in **Figure 4.10** right), which each react preferentially with on enantiomer. The products are also separable.

More details about divergent RMM can be seen in the references.^{49, 51}

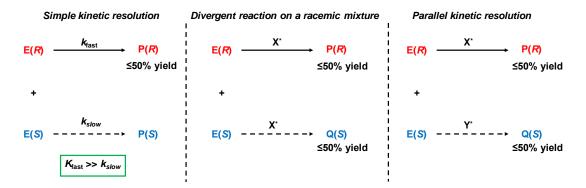


Figure 4.10 Simple kinetic resolution compared to a parallel kinetic resolution and a divergent reaction on a racemic mixture.

B Design of the project

This work has been performed in collaboration with Rosa M. Girón Rubio, Dr. Salvatore Fillipone and Prof. Nazario Martín at the Universidad Complutense de Madrid (UCM). The helicenic precursors **25** have been prepared in Rennes and their stereoselective addition to C_{60} through a Prato-type reaction, followed by a retro-Prato reaction to obtain enantio-enriched samples of **27** and **28** has been achieved in Madrid. This work has highlighted the use of divergent reactions on racemic mixtures (RRM) to obtain enantioenriched samples of carbo[6]helicene-2-carbaldehyde.

Asymmetric (chemical or enzymatic) synthesis, chiral chromatographic separation, kinetic resolution or crystallization methods, are the main methodologies to access to optically active compounds. Each one of these strategies are still developing new alternative tools in order to face new challenging chemical problems as well as the constantly high demand of enantiopure chiral compounds.

In this regard, the use of divergent reactions on racemic mixtures (RRM) constitutes an alternative to afford enantiopure compounds when all other methods fail.^{49, 52} In this

strategy both enantiomers of a racemate chemically interact with a chiral substrate (reagent, catalyst or solvent, etc.) giving rise to non-enantiomeric products that could eventually be diastereoisomers (stereodivergent), constitutional isomers (regiodivergent) or different chemical compounds (chemodivergent). Although, neither different reaction rates for both enantiomers are necessary, as in the kinetic resolution, nor stoichiometric amounts of chiral reagents, efficient divergent RRM require high selectivity and easily separable products.

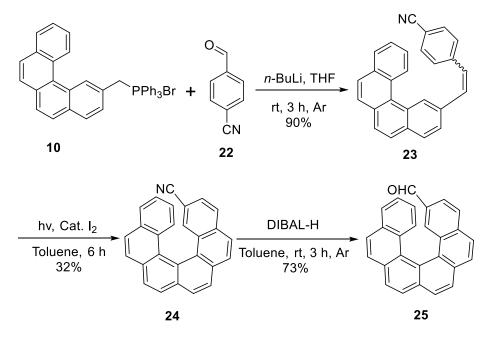
On the other hand, chirality has experienced an increasing interest in new fields such as, for instance, nanoscience.⁵³⁻⁵⁴ In particular, carbon-based nanostructures such as helicenes,⁵⁵ fullerenes,⁵⁶ or curved polyaromatic hydrocarbons,⁵⁷⁻⁵⁸ feature new optoelectronic properties such as charge-carrier mobility or chiroptical properties, stemming from their chiral arrangement. Actually, for these types of compounds, often lacking functional groups, the enantiomeric chromatographic separation is the only available path to obtain optically active compounds.

Thus, we decided to take advantage of the "reversible" covalent chemistry of [60]fullerene as a mean to carry out the resolution of racemic helicenes. Therefore we report a stereodivergent RRM on C_{60} employing only catalytic amounts of chiral agents, followed by a retro-cycloaddition process (see **Scheme 4.1**). In a first step, racemic helicene-iminoesters underwent an enantioselective azomethine ylide cycloaddition reaction to [60]fullerene by using catalytic amounts of Cu(II)/Fesulphos or Ag(I)BPE. Thanks to the high enantiocontrol on the two new formed stereocenters, two diastereomeric helicene-pyrrolidino[3,4:1,2][60]-fullerenes were formed in good enantiomeric excesses and easily separated by conventional silica-gel chromatography. The chiroptical properties of these derivatives, resulting from the curved C_{sp2} helicene and fullerene moieties, were studied. Finally, by the use of a metal-catalyzed retro-cycloaddition reaction under mild conditions⁵⁹ afforded both starting formylhelicene enantiomers which were obtained in very good yield and optical purity.

In this chapter, we want to combine the helicenes and fullerenes to prepare a kind of helicenes fused fullerenes by asymmetric catalysis. The compounds are characterized by multi NMR spectra, mass spectrommetry, CD spectroscopy and so on. The novel strategy paves a new road for selectively preparing chiral fullerenes.

C. Result and discussion

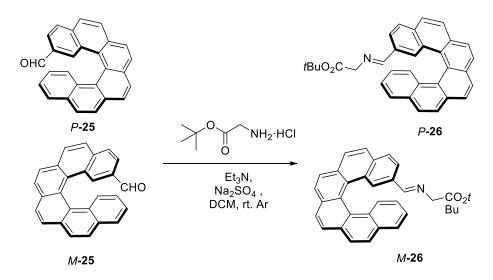
The formyl-helicene racemate **25** were synthesized from starting compound **10**.⁶⁰ The first step was a Witting reaction between the 2-methylbenzophenanthrenetriphenylphosphonium bromide salt **10** and 4-formylbenzonitrile **22**. In the reaction, *n*butyllithium was used as the strong base to deprotonate the phosphonium salt and form a phosphorus ylide. The temperature was controlled at -78 °C to avoid the formation of byproducts. Then the aldehyde **22** was added into the reaction dropwise and a mixture of trans and cis isomers of stilbene **23** were obtained. Subsequently, photocyclization of stilbene **23** was performed using with 700 W mercury lamp and catalytic I₂, and racemic 2-cyano-carbo[6]helicene **24** were obtained with 32% yield. The cyano group was reduced to an aldehyde by using DIBAL-H in toluene at 30°C, giving racemic carbo[6]helicene-2carbaldehyde **25** with 73% yield (**Scheme 4.3**). In collaboration with Nicolas Vanthuyne at Aix Marseille University, we obtained two enantiopure isomers *P*- and *M*carbo[6]helicene-2-carbaldehyde (*P*- and *M*-**25**) by separation through chiral HPLC.



Scheme 4.3 Synthesis route of compound 25.

Due to the chemical structure of helicenes based only on aromatic sp^2 carbon atoms and without functional groups, we considered helicenes as useful racemic benchmark to prove the efficiency of stereodivergent reversible reactions by the use of [60]fullerene. In

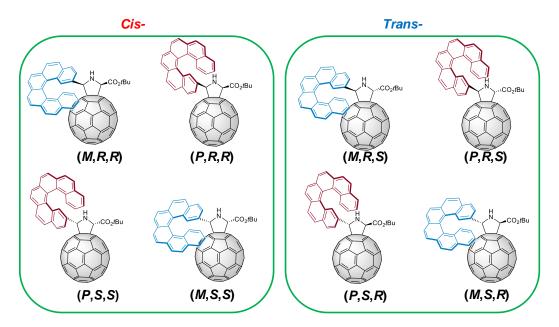
particular, we used formyl-helicene racemate **25** as starting material to carry out the synthesis of the respective helicene-iminoester racemate **26**.



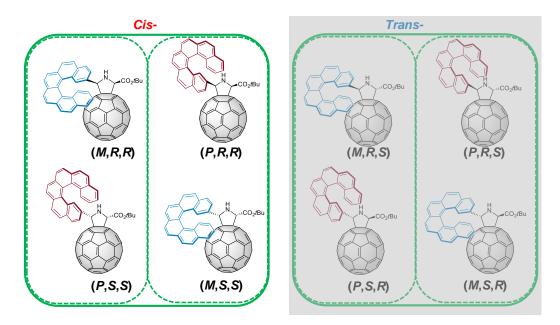
Scheme 4.4 Synthesis of racemic *P/M* iminoester 26 from racemic aldehyde 25.

In order to assess the ability of the catalytic system to maintain the sense of asymmetric induction in the presence of an additional chiral element, we started our study with both enantiomers (P and M) of 25, and 26, previously separated by HPLC.

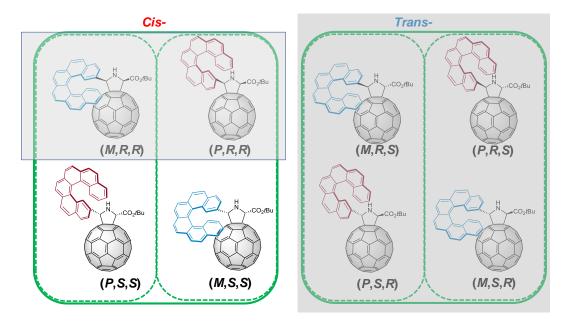
When we carry out the reaction from racemic helicene iminoester without stereoselectivity, there would be $2^3 = 8$ isomers, which include 4 *cis*-isomers and 4 *trans*-isomers (**Scheme 4.5**). The system would be very complicated and the products are pretty difficult to separate. So, if we could control the reaction selectively form *cis* products, which means that we just obtain 4 *cis*-isomers, which contain 2 pairs of diastereomers (**Scheme 4.6**). Moreover, if the reaction can stereoselectively form *cis*-(*S*,*S*) isomer, in theory, with starting materials of racemic helicene iminoester, we can obtain two diastereoemers (*P*,*S*,*S*) and (*M*,*S*,*S*) chiral fullerenes (**Scheme 4.7**), which can be separated by column chromatography. It may provide alternative mode for the racemate resolution.



Scheme 4.5 Molecular structure of 8 isomers in case of non-selective condition.



Scheme 4.6 Four *cis*-isomers in case of *cis*-selective reaction condition.



Scheme 4.7 Two diasteromers in the case of *cis*-(*S*,*S*) selective condition.

Among the available catalytic systems, the pair Cu(II) acetate/ Fesulphos was chosen and revealed similar efficiency as in previous studies *i.e.* directed to the formation of the (2S,5S)-pyrrolidino[3,4:1,2][60]fullerene with *ee* values up to 92%.⁶¹ The catalyst proved to maintain the expected selectivity affording mainly the diasteroisomer (M,S,S)-**28** or the diastereomer (P,S,S)-**27**, when *M*-**26** or *P*-**26** was used, respectively. The diastereomeric ratio between (P,S,S)-**27** and (P,R,R)-**28** (92/8) was higher than (M,S,S)-**28**/(M,R,R)-**27** (83/17) as a result of the matching between *P* chirality and chirality of the catalyst Cu(II)acetate/ Fesulphos and a mismatching with the *M* chirality. It is important to note that diastereoisomers **27** and **28** could be easily separated by conventional silica-gel chromatography fulfilling a very important requirement for the separation of racemates by stereodivergent RRM.

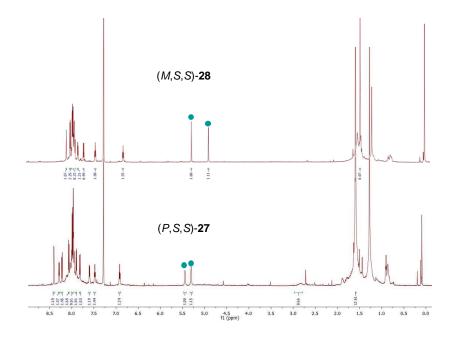
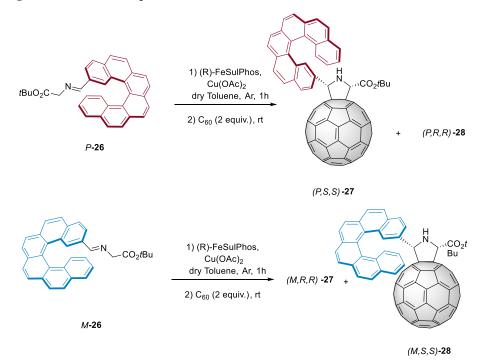


Figure 4.11 ¹H NMR spectra of (*M*,*S*,*S*)-28 and (*P*,*S*,*S*)-27 (in CDCl₃, 700 MHz).



Scheme 4.8 Cycloaddition of iminoester P-26 and M-26 onto C₆₀.

Thus, when the same catalytic system was employed for directing the cycloaddition of the racemic mixture **25** onto [60]fullerene, the two diastereoisomers **27** and **28** were obtained in a 80% yield (with respect to helicenes **26**) and in a 47/53 ratio. Each separated diasteroisomer was analysed by chiral HPLC and circular

dichroism (CD). Thus, diasteroisomer **28** was obtained in a highly enantioenriched form, being 96/4 the ratio between (M,S,S)-**28** and (P,R,R)-**28**, while for diasteroisomer **27** the enantiomeric ratio, (P,S,S)-**27** to (M,R,R)-**27**, was slightly lower (92/8). The CD spectra of the four stereoisomers feature both the characteristic peaks of helicene and of [60]fullerene monoadduct. Thus, at 330nm the helicene moiety gives rise to an intense peak, with the positive or negative sign corresponding to the enantiomers *M* or *P*, respectively, while the peak at 427 nm is the fingerprint of the [60]fullerene monoadducts chirality,⁶² which show a lower intensity.

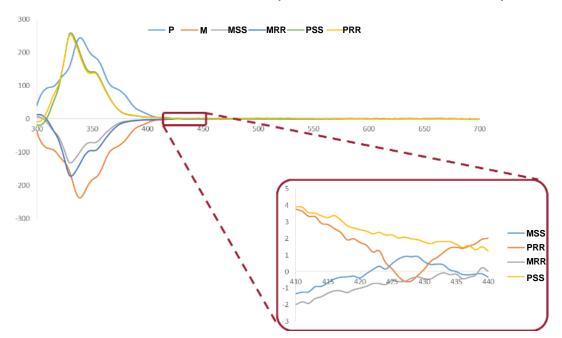


Figure 4.12 Circular dichroism (CD) spectra of *P*-26, *M*-26, (*M*,*R*,*R*)-27, (*P*,*S*,*S*)-27 (*M*,*S*,*S*)-28, and (*P*,*R*,*R*)-28,. Inset peak corresponding to [60]fullerene chirality.

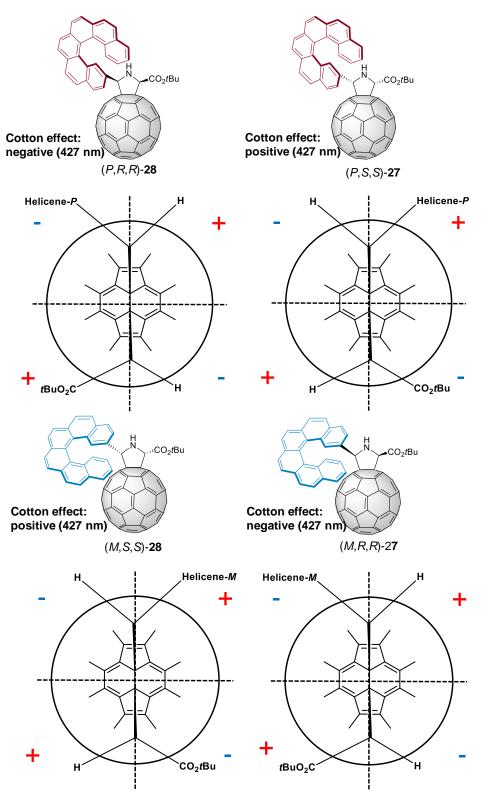
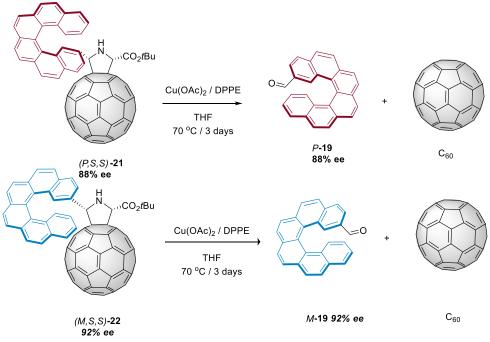


Figure 4.13 Corrected Sector Rule for (*P*,*R*,*R*)-**28**, (*P*,*S*,*S*)-**27**, (*M*,*R*,*R*)-**27**, and (*M*,*S*,*S*)-**28**.

Once proved the efficiency of the chiral catalytic system to carry out the stereodivergent RRM, we extended the scope of such functionalization in order to

assess the singular reversible covalent chemistry of fullerenes as a useful platform to carry pristine [60]fullerene and iminoester starting materials in refluxing toluene, we had to change the experimental conditions in order to avoid a racemization of chiral aldehydes **25**.

We eventually found in the pair $Cu(Ac)_2/dppe$ in refluxing THF the suitable conditions to reverse the cycloaddition in good yields and maintaining the enantiomeric excess. Thus, helicene starting material *P*-1 was obtained in a good yield and with an 88% *ee* from the separated enantioenriched diastereoisomer 3, thus maintaining unchanged the optical purity. Analogously, the retro-cycloaddition of 4 (92% *ee*, (*M*,*S*,*S*)) afforded the helicene *M*-1 with good yield and unchanged *ee*.



Scheme 4.9 Reversibility of cycloaddition of (*P*,*S*,*S*)-27 and (*M*,*S*,*S*)-28.

D Conclusion

In this chapter, we prepared and characterized kinds of chiral fullerenes from helicene aldehyde. According to corrected Sector Rule, their absolute configurations were determined by Cotton effect at around 430 nm in the CD spectra. In addition, we found that, with catalysis pair $Cu(OAc)_2/DPPE$, chiral fullerenes can go back to helicene aldehyde without loss of *ee* value, which meant that it is a retro-cycloaddition process. In general, we reported for the first time on the use of the reversible sterodivergent

cycloaddition of racemic helicenes onto [60]fullerene with its subsequent retrocycloaddition as a general and efficient alternative strategy for the racemate resolution.

E Experiment part

E.1 General information

All experiments were performed under an atmosphere of dry argon using standard Schlenk techniques. Commercially available reagents were used as received without argon further purification. Solvents were freshly distilled under from sodium/benzophenone (tetrahydrofuran, diethyl ether) or from phosphorus pentoxide (pentane, dichloromethane). Preparative separations were performed by gravity column chromatography on basic alumina (Aldrich, Type 5016A, 150 mesh, 58 Å) or silica gel (Merck Geduran 60, 0.063-0.200 mm) in 3.5-20 cm columns. ¹H, ¹³C, and ³¹P NMR spectra were recorded on Bruker Ascend 300 and 400. Assignment of proton atoms is based on ¹H-¹H COSY experiment. Assignment of carbon atoms is based on HMBC, HMQC and DEPT-135 experiments. Mass analyses were performed by the CRMPO, University of Rennes 1. Specific rotations (in deg $\text{cm}^2 \text{ g}^{-1}$) were measured in a 1 dm thermostated quartz cell on a PerkinElmer Model 341 polarimeter. Circular dichroism (in M⁻¹ cm⁻¹) was measured on a Jasco J-815 Circular Dichroism Spectrometer (IFR140 facility - Bosit. Université de Rennes 1).

E.2 Synthetic Procedures and Characterizations of helicene aldehydes.

Materials and Reagents. THF was distilled from sodium. Commercially available reagents were used as received without further purification. Compound **24** was prepared as the reported procedure.^{60, 63}

Synthesis of compound 25. To a toluene solution (60 ml) of 2-cyanocarbo[6]helicene compound 24 (200 mg, 0.56 mmol) under argon, 1 M DIBAL-H (0.85 mL, 0.85 mmol) was added. The mixture was stirred for 3 hours at 30°C, and the methanol was added. The solution was filtrated, evaporated with vacuum and purified with silica gel (DCM/heptane 1:3). The Carbo[6]helicene-2-carbaldehyde was obtained as yellow solid (148 mg, 0.41 mmol, 72%). Two enantiomers *P*-5 and *M*-5 were separated by HPLC. ¹H NMR (300 MHz, CDCl₃) δ 9.08 (s, 1H), 8.14-7.99 (m, 6 H), 7.98-7.94 (m, 3H), 7.91 (d, *J* = 8.3 Hz, 1H),

7.81 (dd, J = 8.1, 1.4 Hz, 1 H), 7.71 (dd, J = 8.3, 1.5 Hz, 1 H), 7.50 (dd, J = 8.1, 1.2 Hz, 1 H), 7.18 (ddd, J = 8.1, 6.9, 1.2 Hz, 1 H), 6.65 (ddd, J = 8.4, 6.9, 1.4 Hz, 1 H). ¹³C NMR (75 MHz, CDCl₃) δ 191.9, 135.2, 135.0, 133.4, 132.7, 131.8, 131.6, 131.5, 129.7, 129.3, 129.2, 128.6, 128.1, 128.1, 127.8, 127.8, 127.8, 127.7, 127.55, 127.3, 127.2, 127.1, 126.3, 125.8, 124.8, 123.8, 122.1. HRMS: m/z calcd for C₂₇H₁₆ONa: 379.10933 [M+Na]⁺; found: 379.1092 (0 ppm). Specific rotation: *P*-**25** $[\alpha]_D^{20}$: +4575 °dm⁻¹cm³g⁻¹; *M*-**25** $[\alpha]_D^{20}$: -4640 °dm⁻¹cm³g⁻¹.

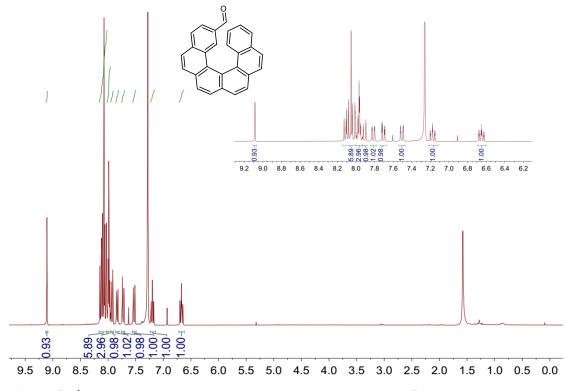
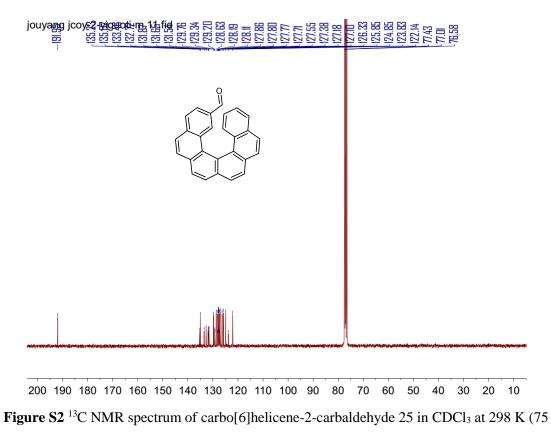


Figure S1 ¹H NMR spectrum of carbo[6]helicene-2-carbaldehyde **25** in CDCl₃ at 298 K (300 MHz).



MHz).

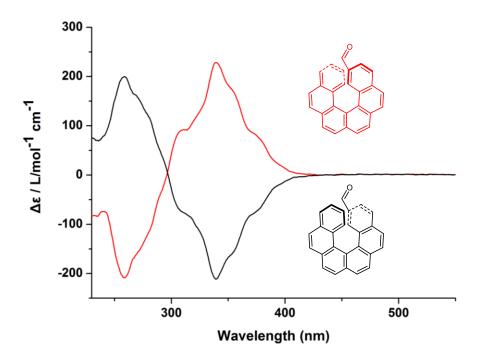


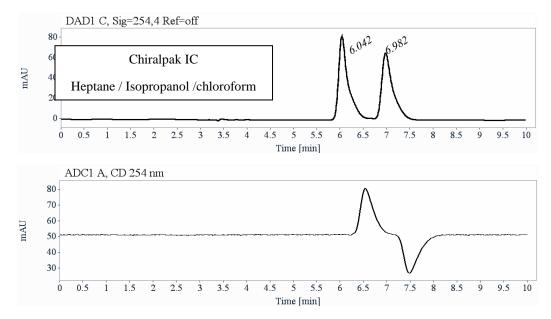
Figure S3 Circular dichroism spectra of *P*-25 and *M*-25 in CH₂Cl₂ at 298 K.

E.3 Analytical chiral HPLC separation for compound 25

• The sample is dissolved in chloroform, injected on the chiral column, detected with an UV detector at 254 nm and with CD at 254 nm. The flow-rate is 1 ml/min.

and

Column	Mobile Phase	t1	k1	t2	k2	α	Rs
Chiralpak IC	Heptane / Isopropanol /chloroform (80/10/10)	6.04(+)	1.05	6.98(-)	1.37	1.30	2.64



Signal: DAD1 C, Sig=254,4 Ref=off

RT [min]	Area	Area%	Capacity Factor	Enantioselectivity	Resolution (USP)	
6.04	1204	52.02	1.05			
6.98	1111	47.98	1.37	1.30	2.64	
Sum	2315	100.00				

Semi-preparative separation for compound 25:

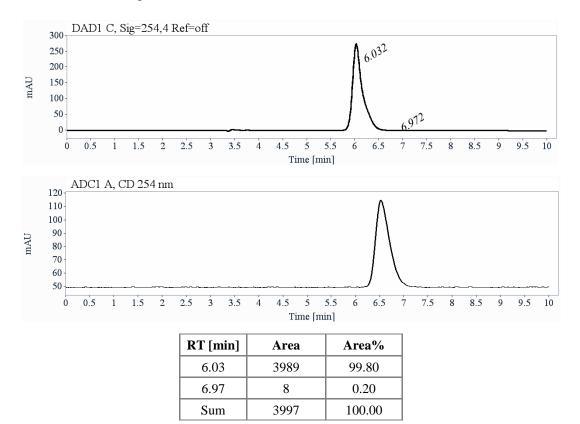
• Sample preparation: About 240 mg of compound **25** are dissolved in 27 mL of a mixture of hexane/isopropanol/chloroform 45/5/50.

• Chromatographic conditions: Chiralpak IC (250 x 10 mm), hexane / isopropanol / chloroform (80/10/10) as mobile phase, flow-rate = 5 mL/min, UV detection at 254 nm.

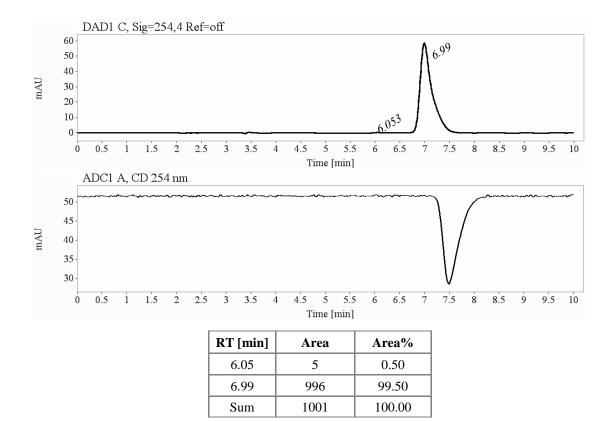
• Injections (stacked): 180 times 150 µL, every 2.5 minutes.

• Collection: the first eluted enantiomer is collected between 6 and 6.3 minutes and the second one between 7.1 and 7.5 minutes.

• First fraction: 71 mg of the first eluted enantiomer with ee > 99.5%



• Second fraction: 65 mg of the second eluted enantiomer with ee > 99%



E.4 Synthesis of chiral fullerene derivatives.

This part of work was accomplished and written by Rosa M. Girón, Salvatore Filippone, and Nazario Martín in Universidad Complutense de Madrid, Spain.

E.4.1 General Methods and Materials

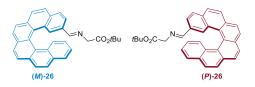
The commercially available reagents and solvents were used without further purification. Iminoesters were previously described in the literature. ¹H NMR and ¹³C NMR spectra were recorded on a BRUKER AVANCE-300 and -700 in CDCl₃, or a BRUKER AVANCE AMX-700 in CDCl₃ at 23 °C, and referenced to CDCl₃; coupling constants (*J*) are reported in Hz and the chemical shifts (δ) in ppm. Mass spectra were reported on a BRUKER-ULTRAFLEX III (MALDI-TOF). Reactions were monitored by thin-layer chromatography carried out on 0.2 mm TLC-aluminium sheets of silica gel (Merck, TLC Silica gel 60 F₂₅₄). Flash column chromatography was performed using silica gel (230-400 mesh). For conversions, HPLC column *Buckyprep* (Waters) (4.6 × 250 mm) was used and

for enantiomeric excesses, chiral HPLC *Chiralpak IC*. All these values were monitored in a 320 nm spectrophotometer detector. Circular Dichroism (DC) measurements were carried out on a JASCO J-815 DC SPECTROMETER.

E.4.2 General procedure for the synthesis of helicene α-iminoesters

The α -iminoesters 2 were synthesized according to the method described in literature.

Synthesis of racemic tert-butyl (E)-N-[(2-carbo[6]helicene)methylene]glycinate



The racemic iminoester **26** was prepared according to the general procedure by using carbo[6]helicene-2-carbaldehyde (20 mg, 0.056 mmol,) *tert*-butyl glycinate hydrochloride (14 mg, 0.080 mmol), triethylamine (12 μ L, 0.080 mmol), and anhydrous sodium sulfate. Isolated yield: 99% (26 mg). ¹H NMR (300 MHz, CDCl₃) δ 8.04 – 7.78 (m, 11H), 7.68 (s, 1H), 7.58 (d, *J* = 8.5 Hz, 1H), 7.36 (s, 1H), 7.21 (t, *J* = 7.0 Hz, 1H), 6.69 (t, *J* = 7.7 Hz, 1H), 4.09 (dd, *J* = 38.3, 16.1 Hz, 2H), 1.48 (s, 9H). ¹³C NMR (75 MHz, CDCl₃) δ 165.20, 133.88, 133.79, 133.67, 132.86, 132.11, 131.92, 131.80, 130.10, 130.06, 129.92, 129.70, 128.92, 128.82, 128.63, 128.28, 128.21, 128.02, 127.87, 127.80, 127.69, 127.65, 127.44, 126.63, 126.33, 125.27, 123.26, 81.61, 77.87, 77.44, 77.02, 62.88, 28.51.

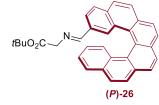
Synthesis of tert-butyl (E)-N-[M-(2-carbo[6]helicene)methylene]glycinate M-26



The iminoester *M*-26 was prepared according to the general procedure by using *M*-carbo[6]helicene-2-carbaldehyde (20 mg, 0.056 mmol,) *tert*-butyl glycinate hydrochloride (14 mg, 0.080 mmol), triethylamine (12 µL, 0.080 mmol), and anhydrous

sodium sulfate. Isolated yield: 96% (25.5 mg). ¹H NMR (300 MHz, CDCl₃) δ 8.03 – 7.86 (m, 10H), 7.80 (d, J = 8.0 Hz, 1H), 7.68 (s, 1H), 7.58 (d, J = 8.5 Hz, 1H), 7.36 (s, 1H), 7.21 (ddd, J = 8.0, 6.9, 1.1 Hz, 1H), 6.69 (ddd, J = 8.4, 6.9, 1.4 Hz, 1H), 4.09 (ddd, J = 37.8, 16.0, 1.2 Hz, 2H), 1.48 (s, 9H).

Synthesis of *tert*-butyl (E)-*N*-[*P*-(2-carbo[6]helicene)methylene]glycinate *P*-26



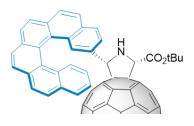
The iminoester **P-26** was prepared according to the general procedure by using *P*-carbo[6]helicene-2-carbaldehyde (20 mg, 0.056 mmol,) *tert*-butyl glycinate hydrochloride (14 mg, 0.080 mmol), triethylamine (12 μ L, 0.080 mmol), and anhydrous

sodium sulfate. Isolated yield: 94% (25 mg). ¹H NMR (300 MHz, CDCl₃) δ 8.03 – 7.83 (m, 10H), 7.80 (d, J = 8.0 Hz, 1H), 7.68 (s, 1H), 7.58 (d, J = 8.5 Hz, 1H), 7.36 (s, 1H), 7.21 (ddd, J = 8.0, 7.0, 1.1 Hz, 1H), 6.69 (ddd, J = 8.4, 7.0, 1.3 Hz, 1H), 4.09 (dd, J = 37.4, 16.5 Hz, 2H), 1.48 (s, 9H).

E.4.3 General procedure for catalytic 1,3-dipolar cycloaddition of heliceneazomethine ylides and [60]fullerene.

Chiral ligand (0.0022 mmol) and metal salt (0.0022 mmol) were dissolved in toluene (3 mL). The solution was stirred for 1h at room temperature, and then, a solution of α -iminoester (0.0074 mmol). Finally, C₆₀ (0.0149 mmol). The reaction mixture was stirred for 2.5 h, and afterwards, it was quenched with a saturated ammonium chloride solution (20 mL). The mixture was extracted with toluene (3 x 20mL), and the combinated extracts were washed with brine (30 mL). The organic layer was dried over MgSO₄ and concentrated in vacuo. The crude product was purified by silica gel flash chromatography (the eluent is indicated in each case).

Synthesis of (2*S*,5*S*)-tert-butoxycarbonyl-5-(*M*-2-carbo[6]helicene)pyrrolidino-[3,4:1,2][60]ful-lerene (*M*,*S*,*S*-28)

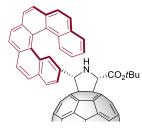


The adduct (*M*,*S*,*S*)-**28** was prepared according to the general procedure by using the catalytic system (0.0022 mmol) (R_p)-Fesulphos (1 mg) and Cu(OAc)₂ (4 mg), *tert*-butyl (E)-N-[*M*-(2-carbo[6]helicene)methylene]glycinate *M*-**26** (3.5 mg, 0.0074 mmol,) and C₆₀ (11 mg, 0.0149

mmol). Isolated yield: 83% (7.2 mg). ¹H NMR (700 MHz, CDCl₃) δ 8.40 (s, 1H), 8.28 (d, J = 7.9 Hz, 1H), 8.22 (d, J = 8.4 Hz, 1H), 8.07 (d, J = 8.4 Hz, 1H), 8.00 – 7.94 (m, 6H), 7.90 (d, J = 8.1 Hz, 1H), 7.82 (d, J = 8.4 Hz, 1H), 7.60 (d, J = 8.0 Hz, 1H), 7.48 (t, J = 7.4 Hz, 1H), 6.92 (t, J = 7.5 Hz, 1H), 5.43 (s, 1H), 5.30 (s, 1H), 2.80 (s, 1H), 1.59 (s, 9H).

¹³C NMR (176 MHz, CDCl₃) δ 167.55, 153.40, 153.06, 151.61, 150.85, 147.02, 146.91, 146.83, 146.34, 146.30, 146.17, 146.02, 145.96, 145.95, 145.90, 145.79, 145.71, 145.65, 145.38, 145.33, 145.26, 145.18, 145.12, 145.07, 145.05, 145.02, 144.46, 144.36, 144.34, 144.11, 144.08, 143.11, 142.81, 142.60, 142.58, 142.48, 142.45, 142.24, 142.22, 142.08, 142.00, 141.83, 141.71, 141.65, 141.55, 141.23, 139.78, 139.43, 139.29, 138.80, 137.25, 135.66, 135.54, 135.14, 133.08, 131.89, 131.79, 131.66, 131.27, 130.09, 129.49, 129.26, 129.05, 128.33, 128.16, 128.07, 128.01, 127.71, 127.53, 127.50, 127.46, 127.16, 127.06, 126.90, 126.33, 125.75, 125.33, 123.93, 83.12, 76.51, 73.72, 28.32.

Synthesis of (2*S*,5*S*)-tert-butoxycarbonyl-5-(*P*-2-carbo[6]helicene)pyrrolidino-[3,4:1,2][60]fullerene (*P*,*S*,*S*-27)



The adduct (*P*,*S*,*S*)-**27** was prepared according to the general procedure by using the catalytic system (0.0022 mmol) (R_p)-Fesulphos (1 mg) and Cu(OAc)₂ (4 mg), *tert*-butyl (E)-*N*-[*P*-(2-carbo[6]helicene)methylene]-glycinate *P*-**26** (3.5 mg, 0.0074 mmol,) and C₆₀ (11 mg, 0.0149 mmol). Isolated yield: 92% (9.8

mg). ¹H NMR (700 MHz, CDCl₃) δ 8.12 (s, 1H), 8.03 (d, *J* = 8.3 Hz, 2H), 8.01 – 7.92 (m, 8H), 7.86 (d, *J* = 7.3 Hz, 1H), 7.73 (d, *J* = 8.5 Hz, 1H), 7.49 – 7.46 (m, 1H), 6.86 – 6.83 (m, 1H), 5.31 (s, 1H), 4.93 (s, 1H), 1.54 (s, 9H).

E.4.4 Representative NMR spectra of α-iminoesters M-26 and P-26

¹H NMR, DEPT 135, and ¹³C NMR spectra of racemic *tert*-butyl (*E*)-*N*-[(2-carbo-[6]helicene)-methylene]glycinate **26**

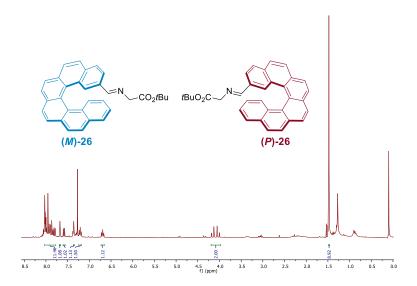


Figure S4 ¹H NMR (700 MHz, CDCl₃) of spectra of racemic *tert*-butyl (*E*)-*N*-[(2-carbo[6]helicene)-methylene]glycinate **26**

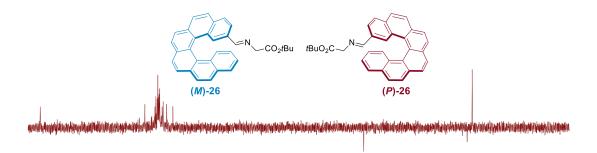
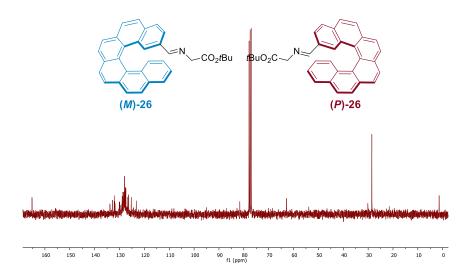
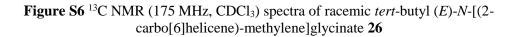


Figure S5 DEPT-135 (175 MHz, CDCl₃) spectra of racemic *tert*-butyl (*E*)-*N*-[(2-carbo[6]helicene)-methylene]glycinate **26**





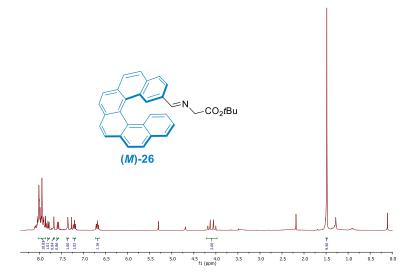


Figure S7 ¹H NMR (700 MHz, CDCl₃) spectrum of *tert*-butyl (*E*)-*N*-[(*M*-2-carbo[6]helicene)methylene]glycinate (*M*)-**26**

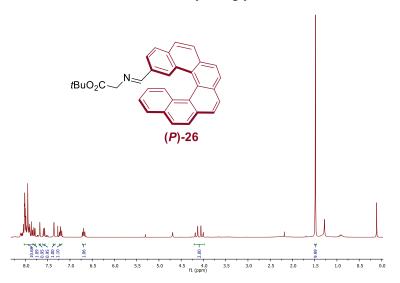


Figure S8 ¹H NMR (700 MHz, CDCl₃) spectrum of *tert*-butyl (*E*)-*N*-[(*P*-2-carbo[6]helicene)methylene]glycinate *P*-**26**

E.4.5 Representative NMR spectra of pyrrolidino[3,4:1,2][60]fullerene derivative (*M*,*S*,*S*)-28

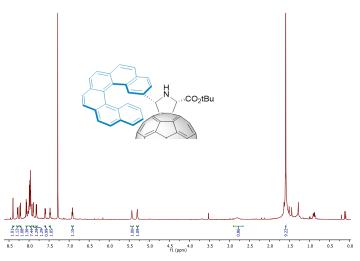


Figure S9 ¹H NMR (700 MHz, CDCl₃) spectrum of (2*S*,5*S*)-tert-butoxycarbonyl-5-(*M*-2-carbo[6]helicene)-pyrrolidino[3,4:1,2][60]fullerene (*M*,*S*,*S*)-**28**

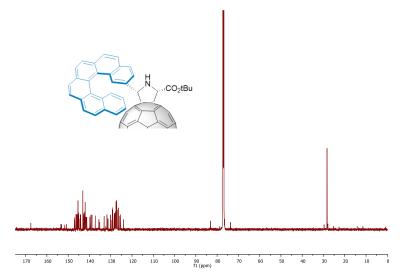


Figure S10 ¹³C NMR (175 MHz, CDCl₃) spectrum of (2*S*,5*S*)-tert-butoxycarbonyl-5-(*M*-2-carbo[6]helicene)-pyrrolidino[3,4:1,2][60]fullerene (*M*,*S*,*S*)-**28**

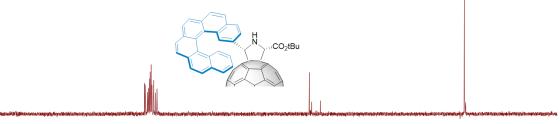


Figure S11 DEPT (175 MHz, CDCl₃) spectrum of (2*S*,5*S*)-tert-butoxycarbonyl-5-(*M*-2-carbo[6]helicene)-pyrrolidino[3,4:1,2][60]fullerene (*M*,*S*,*S*)-**28**

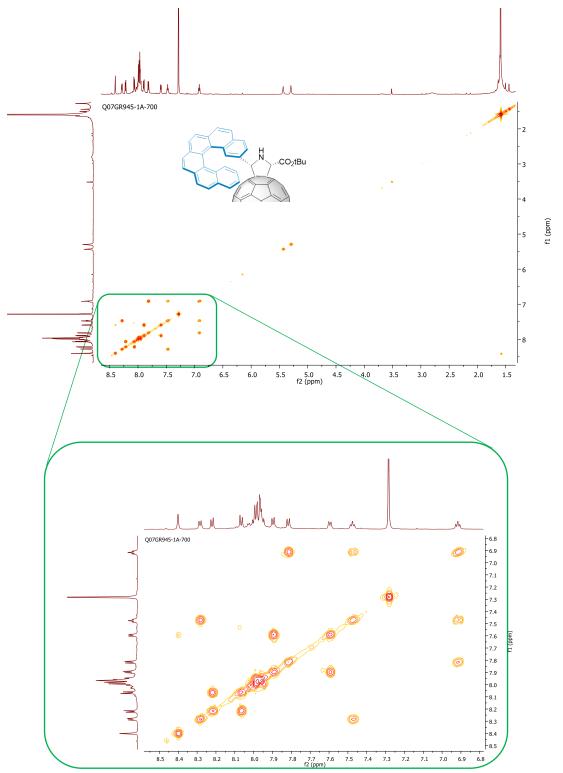


Figure S12 COSY spectrum of (2*S*,5*S*)-tert-butoxycarbonyl-5-(*M*-2-carbo[6]helicene)pyrrolidino[3,4:1,2][60]fullerene (*M*,*S*,*S*)-**28**

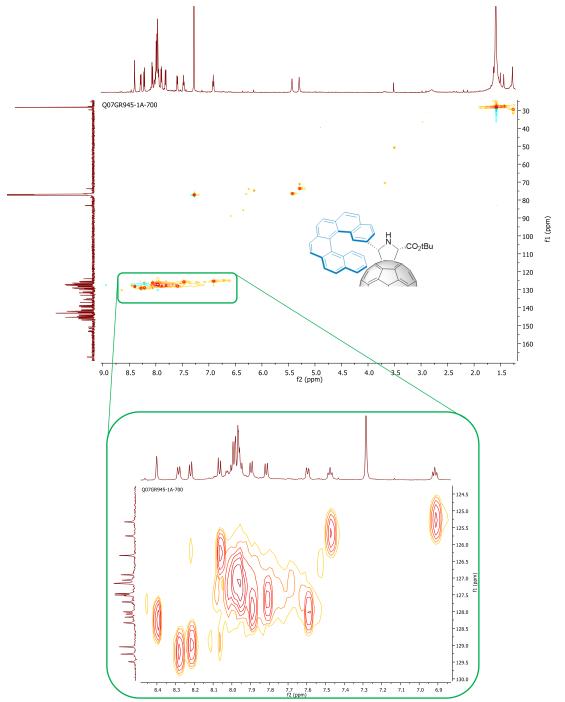


Figure S13 HMQC spectrum of (2*S*,5*S*)-tert-butoxycarbonyl-5-(*M*-2-carbo[6]helicene)pyrrolidino[3,4:1,2][60]fullerene (*M*,*S*,*S*)-**28**

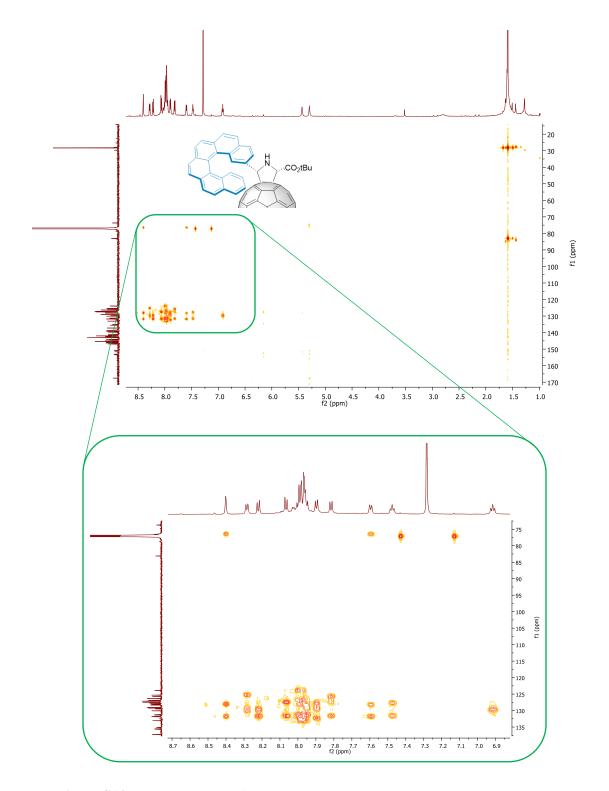


Figure S14 HMBC spectrum of (2*S*,5*S*)-tert-butoxycarbonyl-5-(*M*-2-carbo[6]helicene)pyrrolidino[3,4:1,2][60]fullerene (*M*,*S*,*S*)-**28**

F References

1. Kroto, H. W.; Heath, J. R.; O'Brien, S. C.; Curl, R. F.; Smalley, R. E., *Nature* **1985**, *318*, 162-163.

2. Maroto, E. E.; Izquierdo, M.; Reboredo, S.; Marco-Martínez, J.; Filippone, S.; Martin, N., *Acc. Chem. Res.* **2014**, *47*, 2660-2670.

3. Thilgen, C.; Diederich, F., *Chem. Rev.* **2006**, *106*, 5049-5135.

4. Hirsch, A., *The chemistry of the fullerenes*. John Wiley & Sons: 2008.

5. Stephens, P. W., *Physics & chemistry of fullerenes: a reprint collection*. World Scientific: 1993; Vol. 1.

6. Taylor, R.; Walton, D. R., *Nature* **1993**, *363*, 685-693.

7. Ajie, H.; Alvarez, M. M.; Anz, S. J.; Beck, R. D.; Diederich, F.; Fostiropoulos, K.;

Huffman, D. R.; Kraetschmer, W.; Rubin, Y., J. Phys. Chem. 1990, 94, 8630-8633.

8. Gasyna, Z.; Schatz, P.; Hare, J.; Dennis, T.; Kroto, H.; Taylor, R.; Walton, D., *Chem. Phys. Lett.* **1991**, *183*, 283-291.

9. Leach, S.; Vervloet, M.; Desprès, A.; Bréheret, E.; Hare, J. P.; Dennis, T. J.; Kroto, H. W.; Taylor, R.; Walton, D. R., *Chem. Phys.* **1992**, *160*, 451-466.

10. Johnson, R. D.; Meijer, G.; Salem, J. R.; Bethune, D. S., *J. Am. Chem. Soc.* **1991**, *113*, 3619-3621.

11. Yannoni, C. S.; Bernier, P. P.; Bethune, D. S.; Meijer, G.; Salem, J. R., *J. Am. Chem. Soc.* **1991**, *113*, 3190-3192.

12. Yannoni, C.; Johnson, R.; Meijer, G.; Bethune, D.; Salem, J., *J. Phys. Chem. Lett.* **1991**, *95*, 9-10.

13. Krätschmer, W.; Lamb, L. D.; Fostiropoulos, K.; Huffman, D. R., *Nature* **1990**, *347*, 354-358.

14. Ettl, R.; Chao, I.; Diederich, F.; Whetten, R. L., *Nature* **1991**, *353*, 149-153.

15. Diederich, F.; Ettl, R., *Science* **1991**, *252*, 548.

16. Vasella, A.; Uhlmann, P.; Waldraff, C. A.; Diederich, F.; Thilgen, C., *Angew. Chem. Int. Ed.* **1992**, *31*, 1388-1390.

17. Thilgen, C.; Diederich, F., *Chem. Rev.* **2006**, *106*, 5049-5135.

18. Nishimura, T.; Tsuchiya, K.; Ohsawa, S.; Maeda, K.; Yashima, E.; Nakamura, Y.;

Nishimura, J., J. Am. Chem. Soc. 2004, 126, 11711-11717.

19. Friedman, S. H.; Ganapathi, P. S.; Rubin, Y.; Kenyon, G. L., *J. Med. Chem.* **1998**, *41*, 2424-2429.

20. Zhu, Z.; Schuster, D. I.; Tuckerman, M. E., *Biochemistry* **2003**, *42*, 1326-1333.

21. Gothelf, A. S.; Gothelf, K. V.; Hazell, R. G.; Jørgensen, K. A., Angew. Chem. 2002, 114, 4410-4412.

22. Adrio, J.; Carretero, J. C., *Chem. Commun.* **2011**, *47*, 6784-6794.

23. Maggini, M.; Scorrano, G.; Prato, M., J. Am. Chem. Soc. **1993**, 115, 9798-9799.

24. Prato, M.; Maggini, M., Acc. Chem. Res. 1998, 31, 519-526.

25. Wu, S.-H.; Sun, W.-Q.; Zhang, D.-W.; Shu, L.-H.; Wu, H.-M.; Xu, J.-F.; Lao, X.-F., J.

Chem. Soc., Perkin Trans. 1 1998, 1733-1738.

26. Meier, M. S.; Wang, G.-W.; Haddon, R. C.; Brock, C. P.; Lloyd, M. A.; Selegue, J. P., *J. Am. Chem. Soc.* **1998**, *120*, 2337-2342.

27. Wilson, S. R.; Lu, Q., J. Org. Chem. 1995, 60, 6496-6498.

28. Chai, Y.; Guo, T.; Jin, C.; Haufler, R. E.; Chibante, L. F.; Fure, J.; Wang, L.; Alford, J.

M.; Smalley, R. E., J. Phys. Chem. Lett. 1991, 95, 7564-7568.

29. Lu, X.; Akasaka, T.; Nagase, S., Chem. Commun. 2011, 47, 5942-5957.

30. Wakahara, T.; Nikawa, H.; Kikuchi, T.; Nakahodo, T.; Rahman, G. A.; Tsuchiya, T.;

Maeda, Y.; Akasaka, T.; Yoza, K.; Horn, E., J. Am. Chem. Soc. 2006, 128, 14228-14229.

- 31. Sawai, K.; Takano, Y.; Izquierdo, M.; Filippone, S.; Martín, N.; Slanina, Z.; Mizorogi,
- N.; Waelchli, M.; Tsuchiya, T.; Akasaka, T., J. Am. Chem. Soc. 2011, 133, 17746-17752.
- 32. Maroto, E. E.; Izquierdo, M.; Murata, M.; Filippone, S.; Komatsu, K.; Murata, Y.; Martín, N., *Chem. Commun.* **2014**, *50*, 740-742.
- 33. Filippone, S.; Maroto, E. E.; Martín-Domenech, Á.; Suarez, M.; Martín, N., *Nat. Chem.* **2009**, *1*, 578-582.
- 34. Maroto, E. E.; Filippone, S.; Martín-Domenech, A.; Suarez, M.; Martín, N., *J. Am. Chem. Soc.* **2012**, *134*, 12936-12938.
- 35. Maroto, E. E.; Filippone, S.; Suárez, M.; Martínez-Álvarez, R.; de Cózar, A.; Cossío, F. P.; Martín, N., *J. Am. Chem. Soc.* **2014**, *136*, 705-712.
- 36. Wilson, S. R.; Lu, Q.; Cao, J.; Wu, Y.; Welch, C. J.; Schuster, D. I., *Tetrahedron* **1996**, *52*, 5131-5142.
- 37. Marco-Martínez, J.; Marcos, V.; Reboredo, S.; Filippone, S.; Martín, N., *Angew. Chem. Int. Ed.* **2013**, *52*, 5115-5119.
- 38. Fisk, J. S.; Mosey, R. A.; Tepe, J. J., Chem. Soc. Rev. 2007, 36, 1432-1440.
- 39. Peddibhotla, S.; Tepe, J. J., J. Am. Chem. Soc. 2004, 126, 12776-12777.
- 40. Melhado, A. D.; Luparia, M.; Toste, F. D., J. Am. Chem. Soc. 2007, 129, 12638-12639.
- 41. Marco-Martínez, J.; Reboredo, S.; Izquierdo, M.; Marcos, V.; López, J. L.; Filippone, S.;
- Martín, N., J. Am. Chem. Soc. 2014, 136, 2897-2904.
- 42. Zhang, C.; Lu, X., J. Org. Chem. 1995, 60, 2906-2908.
- 43. O'Donovan, B. F.; Hitchcock, P. B.; Meidine, M. F.; Kroto, H. W.; Taylor, R.; Walton,
- D. R., Chem. Commun. 1997, 81-82.
- 44. Eliel, E. L.; Wilen, S. H., *Topics in stereochemistry*. John Wiley & Sons: 2009; Vol. 21.
- 45. Keith, J. M.; Larrow, J. F.; Jacobsen, E. N., *Advanced Synthesis & Catalysis* **2001**, *343*, 5-26.
- 46. Cook, G. R., *Curr. Org. Chem.* **2000**, *4*, ii-ii.
- 47. Eliel, E. L.; Wilen, S. H.; Doyle, M. P., *Basic organic stereochemistry*. Wiley-Interscience: 2001.
- 48. Eliel, E. L.; Wilen, S. H., *Stereochemistry of organic compounds*. John Wiley & Sons: 2008.
- 49. Miller, L. C.; Sarpong, R., *Chem. Soc. Rev.* **2011**, *40*, 4550-4562.
- 50. Vedejs, E.; Jure, M., Angew. Chem. Int. Ed. 2005, 44, 3974-4001.
- 51. Kumar, R. R.; Kagan, H. B., Advanced Synthesis & Catalysis 2010, 352, 231-242.
- 52. Todd, M. H., Separation of Enantiomers: Synthetic Methods. John Wiley & Sons: 2014.
- 53. Wang, Y.; Xu, J.; Wang, Y.; Chen, H., Chem. Soc. Rev. 2013, 42, 2930-2962.
- 54. Brandt, J. R.; Salerno, F.; Fuchter, M. J., **2017**.
- 55. Jeanne, plese put the references that you consider suitables
- 56. Hizume, Y.; Tashiro, K.; Charvet, R.; Yamamoto, Y.; Saeki, A.; Seki, S.; Aida, T., *J. Am. Chem. Soc.* **2010**, *132*, 6628-6629.
- 57. Rickhaus, M.; Mayor, M.; Juricek, M., Chem. Soc. Rev. 2016, 45, 1542-1556.
- 58. Rickhaus, M.; Mayor, M.; Juricek, M., Chem. Soc. Rev. 2017, 46, 1643-1660.
- 59. Martín, N.; Altable, M.; Filippone, S.; Martín-Domenech, A.; Echegoyen, L.; Cardona,
- C. M., Angew. Chem. Int. Ed. 2006, 45, 110.
- 60. Moussa, M. E. S.; Srebro, M.; Anger, E.; Vanthuyne, N.; Roussel, C.; Lescop, C.; Autschbach, J.; Crassous, J., *Chirality* **2013**, *25*, 455-465.
- 61. Filippone, S.; Maroto, E. E.; Martín-Domenech, A.; Suárez, M.; Martín, N., *Nat. Chem.* **2009**, *1*, 578.
- 62. Marco-Martínez, J.; Marcos, V.; Reboredo, S.; Filippone, S.; Martín, N., *Angew. Chem. Int. Ed.* **2013**, *52*, 5115-5119.
- 63. Ben Hassine, B.; Gorsane, M.; Geerts-Evrard, F.; Pecher, J.; Martin, R.; Castelet, D., *Bull. Soc. Chim. Belg* **1986**, *95*, 547-556.



RENNES 2017

Résumé

1 Introduction générale sur les hélicènes et leurs applications

Les hélicènes sont des composés hélicoïdaux composés de noyaux aromatiques ou hétéroaromatiques *ortho*-fusionnés et possèdant un système π - conjugué étendu. Deux facteurs importants pour évaluer ces composés chiraux sont le pouvoir rotatoire et le dichroïsme circulaire (CD) qui s'avèrent très élevés. En outre, grâce à leur bonnes propriétés de luminescence, leur stabilité chimique et thermique, et leur environnement chiral unique, les hélicènes trouvent des applications potentielles comme commutateurs chiroptiques, filtres de spin, comme composés à luminescence polarisée circulairement (CPL) pour les diodes électroluminescentes organiques (OLED), en reconnaissance moléculaire et en catalyse asymétrique. Au cours de mon doctorat, j'ai développé de nouvelles applications des hélicènes en tant que systèmes moléculaires chiraux photocommutables, aimants moléculaires chiraux et dérivés de fullerènes chiraux.

2 Systèmes chiraux photocommutables à base d'hélicènes

Les commutateurs moléculaires peuvent être convertis de manière réversible d'un état à un autre par un stimulus externe tel que la lumière, l'électricité, la chaleur ou une réaction chimique. En particulier, le développement de molécules photocommutables est devenu un domaine actif de recherche en chimie car ils permettent une activation et un contrôle à distance sans générer de déchets chimiques dans les systèmes. Le stilbène rigide est l'une des unités de commutation photosensibles, qui a été signalé pour la première fois par Majerus *et al.* en 1967. Le stilbène rigide présente deux isomères *trans* (*E*) et *cis* (*Z*) stables distincts, qui présentent une barrière d'activation élevée de 43 kcal.mol⁻¹ (une demi-vie d'environ 103 ans à 300 K), mais peuvent être facilement interconvertis par un processus photochimique avec un rendement quantique élevé.

Afin de préparer une nouvelle série de molécules chirales photocommutables, nous avons voulu combiner l'unité de stilbène rigide avec des unités hélicèniques (**Schéma 1**). Profitant des propriétés photoactives du stilbène rigide et des propriétés chiroptiques fortes

des hélicènes, nous avons pu réaliser des commutateurs chiroptiques sensibles à un stimulus lumineux. Comme le montre le Schéma 1, le stilbène rigide présente deux isomères *trans* et *cis* distincts. Lorsque le commutateur passe d'un état à un autre, le système π -conjugué et la géométrie changent, ce qui peut influencer les propriétés de l'ensemble du système. C'est-à-dire que les propriétés d'absorption et chiroptiques de l'unité hélicène seront modifiées en fonction de l'état différent du stilbène rigide. Le processus de lecture peut être examiné par spectroscopie ultraviolet-visible (UV-vis) et par CD.

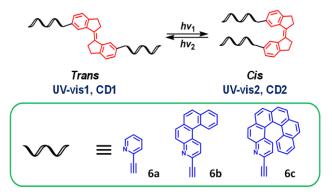


Schéma 1 Représentation schématique des commutateurs photosensibles étudiés.

Après avoir préparé ces composés, nous avons étudié leurs processus d'isomérisation *cis-trans* par spectroscopies RMN (Figure 1), UV-visible et CD. Dans le cas du dérivé stilbène rigide *trans-***6a** possédant 2 unités pyridine, nous avons montré qu'une irradiation lumineuse à 365 nm permettait d'atteindre un état photostationnaire (*trans-cis* 57:43) puis un retour à un état *trans-cis à* 66:34 par une irradiation à 419 nm.

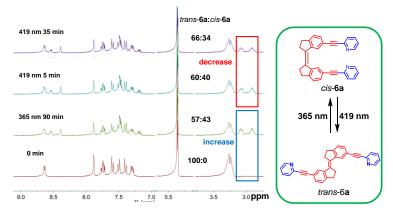


Figure 1 Reversibilité de la photocommutation *trans-cis* du composé 6a observée par RMN ¹H (CD₂Cl₂, 300 MHz, 298 K).
 De la même manière, l'irradiation lumineuse à 350 nm du composé énantiopur *trans-(M,M)*-6c a donné une isomérisation sélective. Les intensités d'absorption des spectres UV-

vis changent de manière continue jusqu'à ce qu'un état photostationnaire soit atteint après 60 min (Figure 2). Bien que les changements soient modestes par rapport à la forte absorption intrinsèque des systèmes hélicéniques, un point isobestique clair a été observé à 285 nm, ce qui a révélé que l'isomérisation du *trans-(M,M)*-**6c** à *cis-(M,M)*-**6c** était un processus unimoléculaire. Lors de l'irradiation du *cis-(M,M)*-**6c** avec une lumière de longueur d'onde de 320 nm à 20 °C pendant 30 minutes, des changements opposés ont été observés.

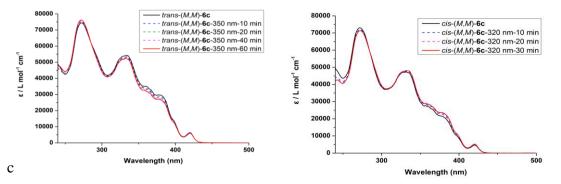


Figure 2 Gauche: changements spectraux UV-vis du *trans-(M,M)-6*c dans du dichlorométhane dégazé après irradiation à 350 nm pendant 60 min; droite: modifications spectrales UV-vis du *cis-(M,M)-6*c dans le dichlorométhane dégazé après irradiation à 320 nm pendant 30 min.

Concernant les spectres CD, pour les cis(M,M)-6c et cis(P,P)-6c, nous avons constaté que les intensités de bande actives étaient légèrement modifiées. Un point isobestique à 285 nm a été observé. Pour les composés trans(M,M)-6c et trans(P,P)-6c, les changements opposés ont été observés (Figure 3).

De plus, nous avons observé que nous pouvions moduler clairement les propriétés d'absorption et d'émission UV-vis des commutateurs moléculaires en ajoutant de l'acide et de la base. Pour les interrupteurs *cis* et *trans* **6c** à fragments [6]hélicéniques, en ajoutant un excès de 18-couronne-6-HBF₄-H₂O dans une solution de dichlorométhane (DCM), la bande d'absorption à 325 nm diminue, tandis que la bande à 380 nm augmente; une nouvelle bande d'absorption large apparaît à 475 nm (**Figure 4**). La fluorescence de ces composés est éteinte après l'ajout d'acide. Puis en ajoutant du carbonate de sodium solide, nous avons retrouvé les spectres UV-vis et de fluorescence initiaux.

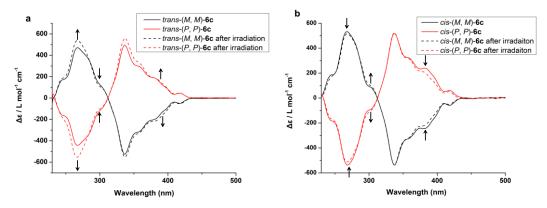
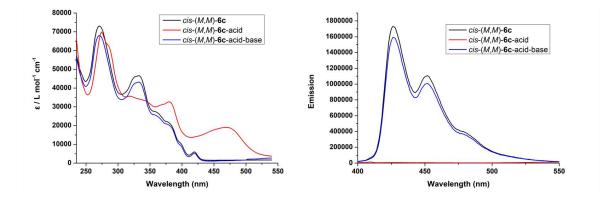


Figure 3 Spectres de dichroïsme circulaire (CD) de a) *trans-(M,M)-6***c** (noir) et *trans-(P, P)-6***c** (rouge) avant (trait plein) et après (pointillés) après irradiation à 350 nm et b) *cis-(M,M)-6***c** (noir) et *cis-(P,P)-6***c** (rouge) avant (trait plein) et après (ligne tiretée) irradiation à 320 nm dans du CH_2Cl_2 dégazé.

En conclusion, nous avons synthétisé une série de nouveaux systèmes chiraux photocommutables basés sur des hélicènes. Les études de leurs propriétés de photocommutables par les spectres RMN ¹H, les spectres UV-vis et les spectroscopies CD ont montré qu'ils pouvaient réaliser une isomérisation photochimique avec une bonne réversibilité. Nous avons trouvé que l'acide 18-crown-6-HBF₄-H₂O et la base carbonate de sodium pouvaient moduler les propriétés d'absorption UV-vis et de fluorescence. De plus, le processus de protonation et de déprotonation est réversible



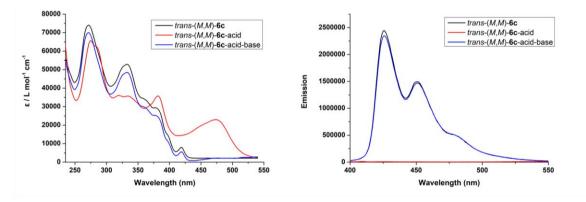


Figure 4 Gauche: réversibilité des spectres UV-vis de *cis-(M,M)*-**6c** et *trans-(M,M)*-**6c**; droite: réversibilité des spectres de fluorescence de *cis-(M,M)*-**6c** et *trans-(M,M)*-**6c** avant d'ajouter de l'acide (18-couronne-6•HBF₄•H₂O)---ligne noire; après addition d'acide (18-couronne-6•HBF₄•H₂O)---ligne rouge; après l'ajout de base (carbonate de sodium)---ligne bleue.

En se basant sur le même système stilbènique rigide, nous avons préparé des complexes or(I)-alcynyl (**Schéma 2**), dans lesquels la distance entre les atomes d'or est modifiée dans les deux différentes conformations *cis* et *trans*. Nous voulions vérifier s'il existait une interaction or-or dans la forme *cis* des complexes alcynyles d'or(I).

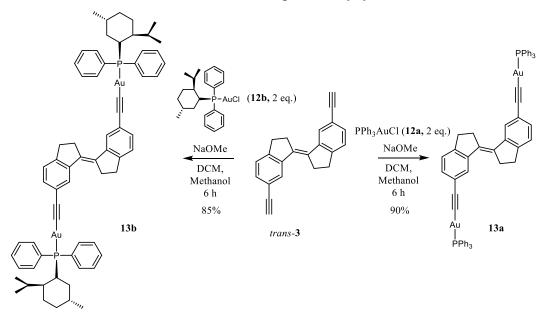


Schéma 2 Synthèse des complexes d'or(I) 13a et 13b.

Leur processus d'isomérisation a été étudié et est apparu efficace, soulignant la valeur ajoutée d'avoir un métal lourd dans une telle structure. Sous irradiation avec une lumière de longueur d'onde de 365 nm et de 420 nm, les complexes d'or peuvent effectuer un processus réversible, tel qu'observé par RMN ¹H, RMN ³¹P et spectroscopie UV-vis (**Figure 5**). Cependant, aucune interaction or-or n'a pu être établie dans les formes *cis* de **13a, b**.

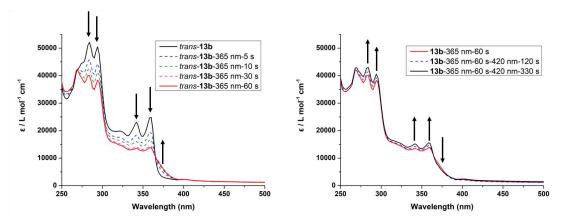


Figure 5 Spectres UV-vis d'isomérisation du composé d'or 13b à 365 nm (a) et 420 nm (b) dans du dichlorométhane dégazé.

3 Premiers aimants à molécule unique à base d'hélicène Dy^{III}

Dans ce sujet, nous avons synthétisé et caractérisé de nouveaux types d'aimants moléculaires (SMMs) de Dy(III) à base d'un ligand hélicène-bipyridine **19** (Schéma **3**). L'étude du CD montre que les complexes de Dy(III) énantiopurs présentent un effet Cotton similaire à celui des ligands hélicène-bipy libres (Figure 6). La mesure des propriétés magnétiques à l'état solide a révélé que les aimants à molécule unique énantiopurs et racémique présentaient des propriétés magnétiques différentes. En effet, les SMM racémiques présentent des propriétés ferromagnétiques, tandis que les SMM énantiopurs présentent des propriétés ferromagnétiques. C'est ainsi la première fois que l'on étudie la différence de comportement magnétique entre les complexes racémiques et énantiopurs.

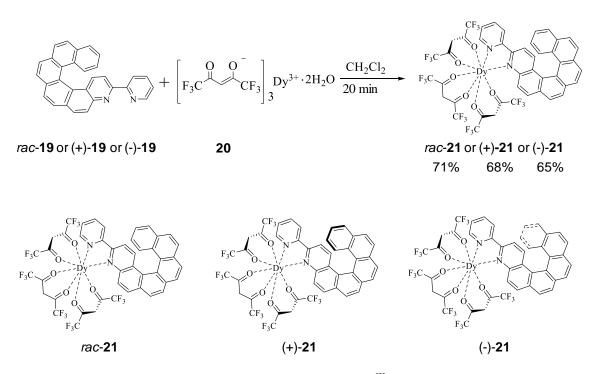


Schéma 2 Synthèse des complexes hélicène-bipy-Dy^{III} rac-21, (+)-21 et (-)-21.

Les complexes hélicène-bipy-Dy^{III} racémique et énantiopurs ont tous montré des propriétés de type SMMs. Dans la région de température élevée, il n'y avait pas de différences les propriétés magnétiques des matériaux majeures entre racémiques et énantiomériquement purs. Jusqu'à 15 K, la susceptibilité magnétique multipliée par la température $\chi_m T$ diminue de façon monotone de 13,95 cm³ K mol⁻¹. Seulement dans la gamme de basses températures une différence est apparue. Lorsque nous réduisons continuellement la température, pour *rac*-21, la susceptibilité magnétique multipliée par la température $\chi_m T$ diminue continuellement; alors que pour (-)-21 et (+)-21, $\chi_m T$ augmente légèrement (**Figure 7**). Comme nous l'avons mentionné précédemment, si le $\chi_m T$ augmente avec l'augmentation de la température, il est anti-ferromagnétique; si le $\chi_m T$ diminue avec l'augmentation de la température, il est ferromagnétique; si le $\chi_m T$ reste le même tout le temps et est égal à la constante de Curie, il est paramagnétique, mettant ainsi en évidence un couplage anti-ferromagnétique en rac-21.0.5C₆H₁₄, alors qu'un couplage ferromagnétique était observé pour (+)-21 et (-)-21.

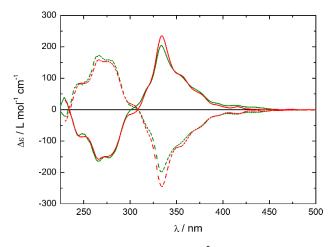


Figure 6 Spectre CD expérimentaux (CH₂Cl₂, C ~5 10^{-5} M) de (-)-**19** (pointillés rouge) et (+) - 19 (trait plein rouge) et des complexes de Dy^{III} respectifs (-)-**21** (pointillés vert) ligne) et (+)-**21** (trait plein vert).

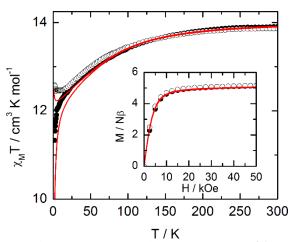


Figure 7 Dépendances thermiques de $\chi_M T$ pour les composés *rac*-**21**-0.5C₆H₁₄ (cercles noirs) et (+)-**21** (cercles blancs). Insertion: les variations de champ de l'aimantation à 2 K. Les lignes rouges pleines correspondent aux courbes simulées à partir des calculs *ab initio*.

Les boucles d'hystérésis mesurées à la température la plus basse (500 mK) suggèrent également des taux de relaxation différents. Alors que la boucle est fermée à n'importe quel champ pour la forme racémique, elle est ouverte pour les deux matériaux énantiomériquement purs (**Figure 8**).

En conclusion, dans ce sujet, nous avons conçu et préparé les premiers aimants à molécule unique de Dy à base de ligands hélicène-bipyridine. Les spectres CD et les propriétés maginétiques des complexes Dy^{III} ont été étudiés. C'est aussi la première fois que l'on compare la différence de propriétés magnétiques entre les SMM racémiques et énantiopurs. Ce travail a été publié en 2016 dans le journal *Chemical Communications*.

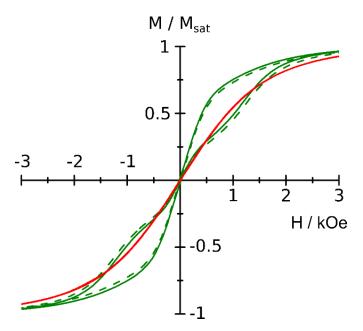
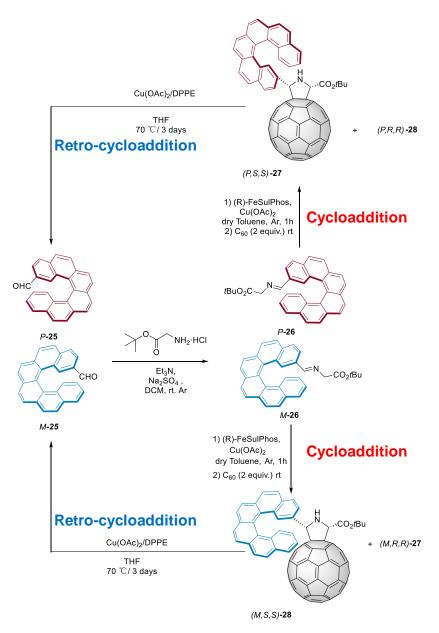
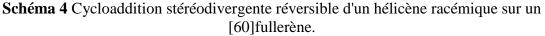


Figure 8 Boucles d'hystérésis magnétiques enregistrées à 500 mK et mesurées à un taux de balayage de 16 Oe.s⁻¹ pour (+)-**21** (ligne verte pleine), (-)-**21** (ligne verte en pointillés) et *rac*-**21**- $0.5C_6H_{14}$ (ligne rouge).

4 Dérivés de fullerène chiraux à base d'hélicènes

Dans cette partie du travail, nous avons préparé et caractérisé une série de dérivés de fullerène chiraux à base d'hélicènes, de type hélicènyl-(2*S*,5*S*)-pyrrolidino[3,4:1,2]-[60]fullerene (**Schéma 4**). Nous avons pu contrôler la stéréosélectivité de la réaction pour obtenir sélectivement les différents isomères des fullerènes chiraux. Les configurations absolues des fullerènes chiraux ont été déterminées par leurs spectres CD selon la règle corrigée des secteurs. De plus, la cycloaddition étant réversible dans des conditions catalytiques, les fullerènes chiraux ont pu redonner les précurseurs d'hélicène-aldéhyde sans perte de valeur d'excès énantiomérique. C'est également la première fois que des hélicènes sont utilisés pour développer un nouveau type de cycloaddition stéréodivergente réversible sur des fullerènes pour préparer des dérivés de fullerène chiraux et une séparation efficace des racémates.





Parmi les systèmes catalytiques disponibles, le couple Cu (II) acétate/Fesulphos a été choisi et a révélé une efficacité similaire à celle des études précédentes, c'est-à-dire permettant la formation du (2S,5S)-pyrrolidino[3,4:1,2]-[60]fullerene avec des valeurs d'*ee* jusqu'à 92%. Le catalyseur s'est avéré maintenir la sélectivité attendue en donnant principalement le diastéréoisomère (M,S,S)-**28** ou le diastéréoisomère (P,S,S)-**27**, lorsque M-**26** ou P-**26** est utilisé, respectivement. Le rapport diastéréomérique entre (P,S,S)-**27** et (P,R,R)-**28** (92/8) est supérieur à (M,S,S)-**28** / (M,R,R)-**27** (83/17) à la suite d'un bon match entre la chiralité P et la chiralité du catalyseur Cu (II) acétate/Fesulphos et d'un mismatch

avec la chiralité M. Il est important de noter que les diastéréoisomères 27 et 28 peuvent être facilement séparés par une chromatographie sur gel de silice classique répondant à une exigence très importante pour la séparation des racémates par RRM stéréodivergente (réaction stéréodivergente de racémiques).

Ainsi, lorsque le même système catalytique a été utilisé pour diriger la cycloaddition du mélange racémique **25** sur le [60]fullerène, les deux diastéréoisomères **27** et **28** ont été obtenus avec un rendement de 80% (par rapport aux hélicènes **26**) et dans un rapport 47/53. Chaque diastéréoisomère séparé a été analysé par HPLC chirale et par dichroïsme circulaire (CD). Ainsi, le diastéréoisomère **28** a été obtenu sous une forme énantio-enrichie élevée, soit 96/4 pour le rapport entre (M,S,S)-**28** et (P,R,R)-28, alors que pour le diastéréoisomère **27**, le rapport énantiomérique, (P,S,S)-**27** à (M,R,R)-**27**, était légèrement plus faible (92/8).

En raison de la difficulté à obtenir des cristaux de fullerènes appropriés pour l'analyse aux rayons X, le dichroïsme circulaire (CD) est largement utilisé pour attribuer la stéréochimie absolue des fullerènes chiraux. Les spectres CD des quatre stéréoisomères présentent à la fois les pics caractéristiques de l'hélicène et du monoadduit [60]fullerène. Ainsi, à 330 nm, la partie hélicènique donne lieu à un pic intense, avec le signe positif ou négatif correspondant respectivement aux énantiomères P ou M, tandis que le pic à 427 nm est l'empreinte de la chiralité [60]fullerène du monoadduit chiral (**Figures 9** et **10**).

Dans ce sujet, nous avons préparé et caractérisé des nouveaux types de fullerènes chiraux à partir d'un hélicène carboxaldéhyde. Selon la règle de secteur corrigée, leurs configurations absolues ont été déterminées par l'effet Cotton vers 430 nm dans les spectres CD. De plus, nous avons trouvé que, avec la paire catalytique Cu(OAc)₂/DPPE, les fullerènes chiraux peuvent redonner l'hélicène aldéhyde sans perte de l'*ee*, ce qui signifie qu'il s'agit d'un processus de rétro-cycloaddition utilisé ici pour dédoubler un dérivé hélicènique.

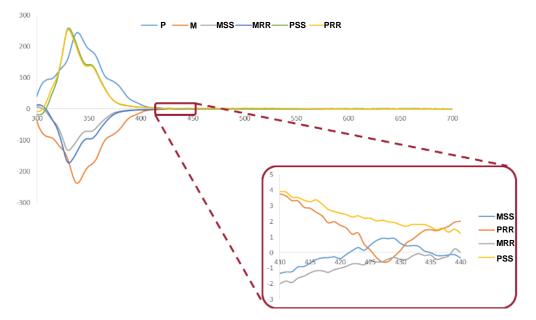


Figure 9 Les spectres de dichroïsme circulaire (CD) de *P*-26, *M*-26, (*M*,*R*,*R*)-27, (*P*,*S*,*S*)-27 (*M*,*S*,*S*)-28 et (*P*,*R*,*R*)-28. Insertion correspondant à la chiralité du [60]fullerène.

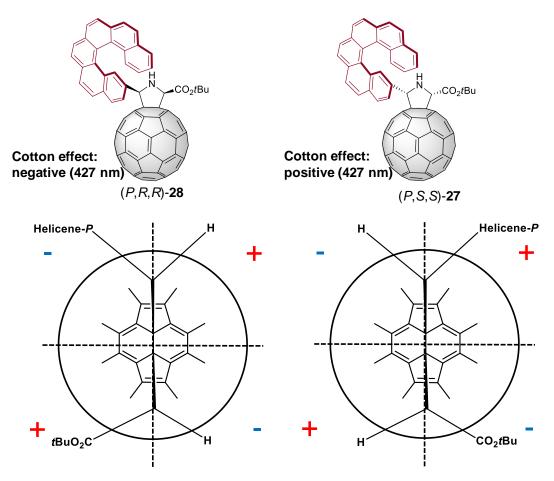


Figure 10 Règle de secteur corrigée pour (P,R,R)-28 et (P,S,S)-27.

Summary

In this PhD work, we firstly developed two studies based on the so-called 'stiff stilbene' units that are known to reversibly interconvert between two *trans* and *cis* forms through light. The first study corresponds to photoresponsive chiral switches based on helicenes, the other one to photoresponsive gold(I) complexes. Then, we dealt with the synthesis and characterization of helicene-bipyridine based Dy(III) complexes as novel kinds of chiral single molecule magnets (SMMs) and compared the difference of the magnetic properties between racemic and enantiopure SMMs. Finally, we developed the first use of the reversible sterodivergent cycloaddition of racemic helicenes onto [60]fullerene with its subsequent retro-cycloaddition as an efficient alternative strategy for the enantiomeric resolution of a helicene-carboxaldehyde.

<u>Résumé</u>

Dans ce travail de thèse, nous avons d'abord développé deux études basées sur des unités dites «stilbène rigide» qui sont connues pour s'interconvertir de manière réversible entre deux formes *trans* et *cis* grâce à la lumière. La première étude correspond à des photocommutateurs chiraux à base d'hélicènes, l'autre à des complexes photocommutables alcynyles d'or(I). Ensuite, nous avons examiné la synthèse et la caractérisation de complexes de Dy(III) à base d'hélicène-bipyridine comme nouveaux types d'aimants moléculaires (SMM) chiraux et comparé la différence des propriétés magnétiques entre les SMM racémique et énantiopurs. Enfin, nous avons développé la première utilisation de la cycloaddition réversible d'hélicènes racémiques sur le [60]fullerène et de sa rétrocycloaddition ultérieure comme une stratégie alternative efficace pour le dédoublement énantiomérique d'un hélicène-carboxaldéhyde.

Key words :

Helicenes, Photoresponsive chiroptical switches, Gold complexes, Chiral single molecule magnets, Chiral helicene-fullerene derivatives.